Fatigue Properties and Reliability of Solder Joints in BGA Assembly

By

Xin Wei

A dissertation submitted to the Graduate Faculty of
Auburn University
in partial fulfillment of the
requirements for the Degree of
Doctor of Philosophy

Auburn, Alabama
Dec 10, 2022

Keywords: lead-free solder, fatigue, stress-controlled, strain-controlled, reliability

Approved by

Sa'd Hamasha, Chair, Associate Professor of Industrial and Systems Engineering

John Evans, Charles D. Miller Endowed Chair Professor of Industrial and Systems Engineering

Sean Gallagher, Hal N. and Peggy S. Pennington Associate Professor of Industrial and Systems Engineering

Jia Liu, Assistant Professor of Industrial and Systems Engineering

Michael Bozack, Professor of Physics

Abstract

Lead-free near-eutectic Sn-Ag-Cu (SAC) solder system has raised increasing attention in the electronics industry since the hazardous effects of SnPb solders. One of the critical considerations for the reliability of an electronic product is the fatigue failure of interconnected solder joints. Numerous studies have investigated fatigue properties of SAC solder materials using large bulk samples, and later the more realistic individual solder joints. However, solder joints in BGA components would suffer from more complex situations and thus make the fatigue life of the component different from the individual solder joints. This dissertation includes two types of test vehicles: the individual solder joint and the customized solder joints in BGA assembly. The latter test vehicle has 3×3 solder joints interconnected between two substrates to represent a realistic chip.

The first study of the research focused on the reliability of SAC-based individual solder joints. Low-temperature solder (LTS) alloys have recently received considerable attention because of their inexpensive price and the reduced defects in complex assemblies. The shear and fatigue properties of individual solder joints were tested using an Instron micromechanical testing system. Two LTS (Sn-58Bi-0.5Sb-0.15Ni and Sn-42Bi) with low melting temperatures were examined and compared with Sn-3.5Ag and Sn-3.0Ag-0.8Cu-3.0Bi. The surface finish was electroless nickel-immersion gold (ENIG) during the test. Sn-3.5Ag solder with organic solderability preservative (OSP) surface finish was tested as well, for comparison. Shear testing was conducted at three strain rates, and the shear strength of each solder alloy was measured. A constant strain rate was used for the cyclic fatigue experiments. The fatigue life of each alloy was determined for various stress amplitudes. The failure mechanism in shear and

fatigue tests were characterized using scanning electron microscopy/energy-dispersive spectroscopy (SEM/EDS). The results revealed that Sn-3.0Ag-0.8Cu-3.0Bi had superior shear and fatigue properties compared to other alloys but was more susceptible to brittle failure. The shear strain rate affected the failure modes of Sn-3.0Ag-0.8Cu-3.0Bi, Sn-58Bi-0.5Sb-0.15Ni, and Sn-42Bi; however, Sn-3.5Ag was found to be insensitive. Several failure modes were detected for Sn-3.5Ag in both shear strength and fatigue tests. For Sn-3.5Ag solder alloy, the OSP surface provided better interfacial toughness than the ENIG surface finish.

In the second part of the research, customized sandwich test vehicles with 3×3 solder joints connected between two substrates were manufactured. Instron Micromechanical Tester is used to test the SAC305 solder joints using both the stress-controlled and strain-controlled methods at room temperature. The testing was conducted at a constant strain rate of $0.05s^{-1}$. Four stresses and four strain levels of the solder alloy Sn-3.0Ag-0.5Cu (SAC305) were examined using organic solderability preservative (OSP) and electroless nickel-immersion silver (ENIG) surface finishes. The work per cycle and plastic strain range were computed based on a systematic recording of the stress-strain (hysteresis) loops of each sample. A novel approach based on inelastic work is developed to calculate the fatigue life of a BGA assembled test vehicle. The results of the stress-controlled and strain-controlled tests indicated that the OSP surface finish outperformed the ENIG surface finish. Regardless of the testing process and surface finish, the Coffin-Manson and Morrow energy models were acceptable for SAC305.

The third study investigated the fatigue performance of some other micro-alloying solder alloys besides Sn-3.0Ag-0.5Cu (SAC305). These lead-free solder alloys are Sn-3.5Ag-0.7Cu-3Bi-1.5Sb0.125Ni (SAC-I), Sn-3.41Ag-0.52Cu-3.3Bi (SAC-Q), and Sn0.92Cu-2.46Bi (SAC-R). The fatigue performance of these solder alloys was

compared considering the effects of surface finishes (OSP and ENIG) and testing approaches (stress-controlled and strain-controlled). The SEM and EDS were utilized to determine the microstructure and failure mechanism of each solder alloy. The results showed that OSP surface finish outperformed the ENIG surface finish, regardless of testing methods and solder alloys. The interfacial IMC layer of SAC305 with the OSP surface finish was scallop-like Cu_6Sn_5, whereas smoother layers were observed in the SAC-R, SAC-Q, and SAC-I solder joints. SAC-Q and SAC-I associate with ENIG surface finish performed the brittle failure. They are more susceptible to changes in strain and stress, particularly strain. The composition of the IMC layer was dependent on the concentration of Cu in the solder alloys.

The final study proposed a mechanical fatigue test method under low temperature (248K), room temperature (298K), and elevated temperature (348K). The same solder joints were assembled in the BGA configuration. The investigated solder alloys were SAC305 (Sn-3.0Ag-0.5Cu) and SnPb (Sn-37Pb). Two types of surface finishes (OSP and ENIG) were utilized for all the testing solder alloys to study the effect of surface finish. Strain-controlled tests were performed using the Instron Micromechanical Tester. It was found that the characteristic fatigue life decreased with the increase of strain level or testing temperature because the solder joint experienced more damage every cycle. The higher testing temperature also led to the larger plastic strain range, the more inelastic work, and decreased peak stress for solder joints in BGA assembly. The temperature of 348K tends to amplify this effect. The OSP surface finish outperformed the ENIG surface finish regardless of strain level or testing temperature due to the failure mechanisms. An empirical model was suitable to describe the effects of strain level on the fatigue behavior of SAC305 and SnPb solder joints at the temperature of 248K, 298K, and 348K. The modified empirical model was proposed to correlate

fatigue life, strain level, and testing temperature. The failure mode in each case was identified.

Acknowledgments

I would like to express my deepest appreciation to my advisor Dr. Sa'd Hamasha. This endeavor would not have been possible without his years of help, guidance, and support. His dynamism, vision, sincerity, and motivation have deeply inspired me. I would also like to thank him for his friendship, empathy, and great sense of humor. I am extending my heartfelt thanks to his wife, Dr. Haneen Ali, for her impressive suggestions and encouragement on my daily life.

I'm also extremely grateful to my committee members, Dr. John L. Evans, Dr. Sean Gallagher, Dr. Jia Liu, and Dr. Michael Bozack, for their valuable insights and precious time. Meanwhile, I would like to thank all my lab-mates, co-workers, and friends: Dr. Sinan Su, Dr. Minghong Jian, Dr. Francy Akkara, Dr. Mohammed Abueed, Mohamed El Amine Belhadi, Palash Vyas, Arvind Karthikeyan, Sufyan Tahat, and Abdallah Alakayleh, Qais Qasaimeh, Anyi Li.

Many thanks to my parents, Cancheng Wei and Xiuhong Zhu. I could not have undertaken this journey without their inspiration and support. I can still remember the moments you encourage me.

Finally, I would like to save the best for my wife, Linghui Zhu, and my newborn daughter, Celeste Wei, whom I will protect for the rest of my life. I am deeply indebted to your understanding, accompany, and support.

Finally, I would like to offer my best respect to Auburn University and Industrial & System Engineering Department!

Endless love to Auburn University and land of Alabama for hosting me for 6 years. War Eagle!

Table of Contents

List of Tables

List of Figures

List of Abbreviations

ALT	Accelerated Life Testing
AOI	Automated Optical Inspection
BGA	Ball Grid Array
CDF	Cumulative Density Function
CFR	Constant Failure Rate
CTE	Coefficient of Thermal Expansion
DoD	Department of Defense
DIP	Dual In-line Package
DFR	Decreasing Failure Rate
DNP	Distance to Neutral Point
EDS	Energy Dispersive X-Ray Spectroscopy
ENIG	Electroless Nickel Immersion Gold
HASL	Hot Air Solder Leveling
IFR	Increasing Failure Rate

ImAg	Immersion Silver
ImSn	Immersion Tin
I/O	Inputs/Outputs
IMC	Intermetallic Compound
LTS	Low Temperature Solder
NPTH	Non-Plated Through Holes
NSMD	Non-Solder Mask Defined
OSP	Organic Solderability Preservative
PCA	Printed Circuit Assembly
PCB	Printed Circuit Board
PDF	Probability Density Function
PTH	Plated Through Holes
RoHS	Restriction of the Use of Certain Hazardous Substances
SAC	SnAgCu
SEM	Scanning Electron Microscope

SMD	Solder Mask Defined
SMT	Surface Mount Technology
SoC	System on Chip
SiP	System in Package
THMT	Through-hole Mount Technology
TSV	Through Silicon Via
WEEE	Waste Electrical and Electronic Equipment

Chapter 1 General Introduction

1.1 Electronic Packaging

Electronic packaging refers to production and enclosures for electronic devices ranging from microchips up to electronic systems. The electronic packaging industry is one of the largest industries in the world [1]. The electronic packaging market was valued at USD 1020.13 million in 2019, and is expected to reach USD 2825.42 million by 2025 [2]. Consumer electronics, such as TVs, laptops, digital cameras, and the processes are more suitable for mass production due to the rising demand these years. The desired performance of electronic products highly attributes to the housing and interconnection characteristics provided by electronic packaging. The major functions of electronic packaging are:

1. Signal distribution
2. Power distribution
3. Heat dissipation
4. Protection

Besides that, the design of electronic packaging should include more considerations in addition to above-mentioned functions, including topological and electromagnetic effects for signal distribution; electromagnetic, structural, and materials aspects for power distribution; structural and materials selection for heat dissipation; and mechanical, chemical, electromagnetic protection for components and interconnections. The hierarchy of electronic packaging is shown in Figure 1.1, which consists of mainly four levels (level zero, one, two, and three).

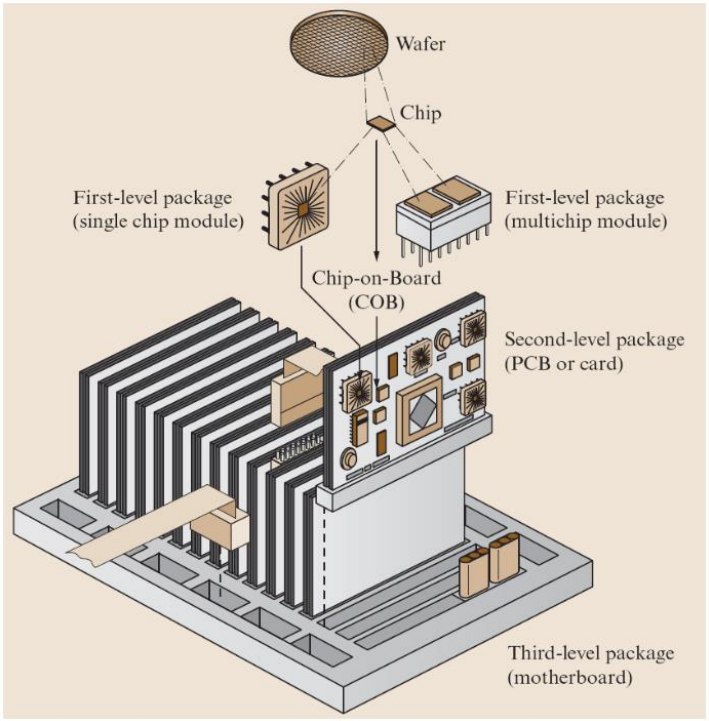

Figure 1-1 Hierarchy of electronic packaging

Level 0 refers the gate-to-gate interconnections on the silicon die, which is diced from a single-crystal silicon wafer. There are millions of solid-state semiconductor devices (transistors, capacitors, inductors, and resistors) connected to form functional electrical circuitry in one single silicon die. It ensures the essential and fundamental processing of semiconductor device.

Level 1 describes the connections between silicon die and package. They include both mechanical connections and electrical connections. The silicon die is mechanically affixed to a lead-frame or interposer layer, and at the same time wire bonding or flip chip Ball Grid Array technology would build up electrically connection between silicon die and the chip carrier. A vast variety of chip carriers is available in the market now, differentiated by factors such as shape, size, lead pitch, internal structure, and materials used for construction. In general, components are categorized as either passive components or active components. Passive components lend their electrical

characteristics to the circuit, but provide no active control over a signal; while active components can amplify an electrical signal and produce power.

Level 2 donates the connection between package and Printed Circuit Board (PCB). This is also called Printed Circuit Assembly (PCA). The Printed Circuit Board is typically a rigid laminate constructed of layers of fiberglass-epoxy composite. The PCB or substrate provides electrical connection and isolation, thermal dissipation, and a flat mounting surface for soldering components [3][4]. Technically, components can be attached to the substrate using two mounting technologies: Through-hole Mount Technology (THMT), and Surface Mount Technology (SMT).

Level 3 is the connection between circuit boards, such as mounting a daughter card to a mother board. This kind of PCB is usually installed to give some additional capabilities to the device. For example, anyone can install a new powerful graphics card in personal computer to have better visual experience and performance.

The electronics industry is keeping moving towards smaller size, lighter weight, faster processing speed, increased circuit density, higher power density, larger semiconductor die with more complicated functionality, more Inputs/Outputs (I/O's), more reliable working life, and less expensive price. Semiconductor manufacturers are making their every effort to minimize the size of chips in order to reduce power consumption and improve the performance. Meanwhile, solder joint, which is widely used to form connection in level 1 and level 2, have been proven to be the major concern to cause failure of electronic products. Since Pb-containing solder alloys present toxic characteristic despite many advantages, directives such as Waste Electrical and Electronic Equipment (WEEE) and Restriction of the Use of Certain Hazardous Substances (RoHS) were adopted in European to solve the problem [5]. In the United

States, the electronics industry has also been pushed towards the adoption of lead-free practices by market force although no law or regulation is issued by the government.

1.2 Reliability of Electronic Packaging

Reliability is the probability that a component or system will perform a required function for a given period of time when used under stated operating conditions. The word can be traced back to 1816, and it was first coined by the poet Samuel Taylor Coleridge [6]. The rise of the new discipline - reliability engineering, attributed to the birth of statistics, and the development and the adoption of mass production. The unreliability of the vacuum tube around 1905 served as the catalyst to accelerate the coming of this discipline. Nowadays reliability has grown into an omnipresent attribute with qualitative and quantitative connotations that pervades every aspect of the world, including electronic packaging.

There is obvious difference between quality and reliability. Quality describes the static measure of product that meets its specification, while reliability is the dynamic measurement of product performance under the service life conditions such as temperature, load, stress, time, and so on. Reliability actually demonstrates the quality of product performance over time - it extends quality into the time domain.

IPC-STD-001B classifies electronic products into three major classes, each comes with its own reliability requirement [7]:

Class I: Consumer products. Service life of products in class I usually falls less than five years and the cost of failure is relatively low. Examples are laptops, cell phones, and cameras.

Class II: Dedicated/Industrial/Telecom products. Service life for products in this class is longer than class I and the failure cost is higher. For example, failure of large industrial machine would result in production line halts and thus financial loss.

Class III: Critical or High-performance products. Products in this category play important roles and any failure could be life threatening. Examples are wing controller of airplane and ventilator machine. Service life of these products should be more than twenty years.

The failure of any component in the electronic product could result in the reliability issue. Considering thousands/millions of components functioning in the system, it is vital to optimize design configuration to ensure the reliability of the system as well as simplify the configuration. Components in the system could be connected in series, parallel, or combined series-parallel, each has its own advantages. In addition, redundancy of critical components has necessity working as a backup or fail-safe to improve the reliability of the system. The reliability of component itself is unneglectable - scientists and engineers are investigating every way to improve the reliability of one single component. In practical service life, the reliability of a component is typically limited by the failure of any interconnected solder joint, which makes it essential and significant to study the reliability of different lead-free solder joints commercially available on the market. Materials, designs, and manufacturing processes are optimized as a trade-off between cost, quality, and reliability.

1.3 Electronic Packages in Realistic Applications

Electronic packages in real service applications could be exposed to high temperature changes due to the operation of high power-density devices or the exposure of various ambient environments. The large mismatches in the coefficients of thermal expansion

of the various materials in the package would induce thermal stresses to interconnected solder joints. Usually the corner joints are supposed to suffer more thermo-mechanical stresses and thus have more chance to fail earlier [8]. The cause of this observation lies in the fact that the distance between the corner joints and the neutral point is larger than the other solder joints. The plastic shear strain during loading could be predicted using the Distance to Neutral Point (DNP) Equation 1-1:

$$\Delta\gamma_p = \frac{\left(\alpha_{PCB} - \alpha_{component}\right) * \Delta T}{h} * [D.N.P] \qquad 1\text{-}1$$

Where $\Delta\gamma_p$ is plastic shear strain during loading temperature change, α_{PCB} is the Coefficient of Thermal Expansion (CTE) of PCB or substrate, $\alpha_{component}$ is the CTE of component, *h* is the height between the component and the PCB, and [D.N.P] donates the distance to neutral point, as shown in Figure 1-2.

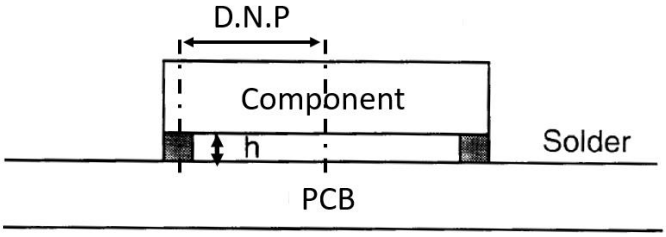

Figure 1-2 Distance to Neutral Point (DNP) Approximation

Besides that, stresses could also occur due to the external mechanical loading or the vibration applied to electronic products. The desired smaller size of the interested structure and materials makes experimental measurements more difficult to realize. Typical reliability concerns and failure modes include solder joint fatigue, die fracture, severing of interconnections, wire bond failure, delamination of material interfaces, and encapsulant cracking.

Extensive research has been conducted to investigate the behavior of solder joint under thermal cycling conditions, together with a multitude of models developed to predict the corresponding reliability. However, limited work has focused on the fatigue properties of solder joints in isothermal shear fatigue cycling, which is meaningful to understand the performance of solder joints at different temperatures.

The reliability of an electronic package/component/product could be quantified using the Accelerated Life Testing (ALT). ALT is the process of testing a product or a component by subjecting it to extreme conditions beyond the normal requirements in order to identify the potential failure modes and the withstanding limit of the product in a short span of time [9][10]. The underlying assumption of ALT is that components showing better performance in the tests would reveal the same advantages in real applications [11], which is not always true. A proper reliability model should consider all the critical factors without oversimplifying real working conditions. The data collected from ALT might fit well with some commonly used distributions, where the Weibull distribution and lognormal distribution are the most widely used ones.

1.4 Problem Statement

Solder joints are often exposed to temperature-changing environments, drop, or vibration in real service conditions, which make them subject to both thermal and/or mechanical stresses for a long period of time. Many studies have investigated the mechanical properties of solder materials by simplifying a solder joint as a large bulk sample, which are typically machined, cast, or prepared form tubes, wires, or rods, with rectangular or circular cross-section [12]. Mechanical fatigue tests such as uniaxial tension-tension [13], simple-shear [14], thermomechanical shear [15], and multiaxial tension-torsion test [16] were conducted previously using the bulk samples. However,

the mechanical properties of large bulk sample should in actual differ from that of solder joints in BGA components because:

- Solder joints in BGA components have smaller size thus finer microstructure;
- The Intermetallic Compound (IMC) layer is formed between bulk solder and Cu pad during reflow process, which might have detrimental effect on the properties of solder joints and even result in different failure modes [17];
- Surface finishes applied could alter the composition of IMC layer;
- Precipitate distribution in bulk samples and in solder joints varies significantly [18];
- Microstructure evolution and damage accumulation of solder joints were found different from that of bulk samples [17].

Previous research [19][20][21][22] has studied the effect of solder materials, surface finish, stress amplitude, and aging on the mechanical properties of various individual SnAgCu (SAC) solder joints. However, the research on the new generation of Low Temperature Solder (LTS) still leave blanks for fulfill.

Electronic packages undergo both shear deformation caused by mismatch of CTE, and warpage and distortion during thermal excursions encountered in manufacturing process and actual operation conditions. In addition, various mechanical and environmental stresses (drop, vibration) could be applied to solder joints in real life service. Therefore, solder joints are subject to the combination of shear and tensile loading in most applications [23]. It is well worthy to note that the mechanical properties of solder joints in BGA components could vary significantly from that of individual solder joints because they might suffer from more complex situations. On one hand, fatigue failure of any solder joint would result in component failure; on the

other hand, stress applied to the component would distribute to all the solder joints. In other words, any solder joint with microcracks would potentially undertake less stress thus mitigate the fatigue of itself but accelerate the failure of the other solder joints. There is an absence of research on the fatigue performance of solder joints in BGA assembly considering different testing approaches.

Another critical factor for isothermal cyclic test is the testing temperature. Some research has studied the effect of temperature on the fatigue properties of solder alloys using bulk samples [13][24], while limited work employed individual solder joints [25][26]. Most of the studies focused on the effects of frequency and strain level on the fatigue behavior of solder alloys [23][27][28]. Despite the superiority of SAC-based solder alloys compared to eutectic SnPb [29], Department of Defense (DoD) is still using SnPb solder alloy mainly because of its predictability. Recently, the Solder Reliability and Assurance Project was launched to ensure the safe transition from SnPb alloy to lead-free solder alloys. Until now, no literature has compared the fatigue properties between SAC305 and SnPb solder joints considering the effect of surface finish and testing temperature. There is indeed a need to conduct a comprehensive study to investigate the fatigue properties of SAC305 and SnPb solder joints in BGA assembly.

Most of the current prediction models were developed for SnPb solders many years ago. These models were then adapted to lead-free solders by fitting the accelerated test data to extract new values for the various constants. However, there is usually a very limited number of data available to extrapolate the real service life from the test results considering the test vehicles have different combinations of process parameters, pad design, surface finish, printed circuit board, and so on. In addition to this, the failure mechanism in thermal cycling and isothermal cycling varies significantly. In thermal

cycling, the coarsening of precipitates and strain-induced stress led to the global recrystallization, followed by crack propagation along the new network of grain boundaries. In contrast, the intergranular microcracks are formed along the subgrain boundaries within dendrites during the isothermal cycling, resulting the link-up of microcracks to form larger transgranular cracks. In some cases, IMC interfacial cracks are observed since the stronger solder ball compared to IMC strength. Nevertheless, this dissertation focused on the modeling of solder joints' fatigue life in isothermal cycling condition. Prediction of service life based on accelerated test results can be misleading without proper constitutive relations and an understanding of the behavior of damage accumulation throughout the solder joint fatigue life. The satisfactory accuracy of life prediction using models cannot be achieved without considering the transferability from testing specimens to realistic components. The finite element analysis is thus necessary to estimate the true parameters, such as plastic strain, inelastic work, and stress, of interested samples with their specific geometries in working conditions. These true parameters can then be fitted in models for the more accurate predictions.

1.5 Research Objectives

The motivation of this research work is to investigate the shear and fatigue properties of commercially available SAC-based solder alloys using individual solder joints, and to study the fatigue properties of solder joints in BGA assembly considering the effect of solder alloys, surface finish, testing method, and testing temperature. Various prediction models, including empirical model, Coffin-Manson model, and Morrow energy model, are expected to be developed for each situation. The following targets are achieved in this research:

- Develop appropriate testing procedures, including test vehicle design, fixture design, experimental setup, and testing profile, to conduct shear and fatigue tests for various solder materials under different conditions.
- Study the effects of stress amplitude and surface finish on the shear and fatigue performance of SAC-based solder alloys by testing individual solder joints at room temperature.
- Study the effect of stress level, strain level, and surface finish on the fatigue performance of micro-alloying SAC solder joints in BGA assembly using stress-controlled and strain-controlled methods at room temperature.
- Study the effect of temperature and surface finish on the fatigue performance of SAC305 and SnPb solder joints in BGA assembly.
- Examine microstructure and failure mechanism of the specimens and perform metallurgical analysis using Scanning Electron Microscope (SEM) and Energy Dispersive X-Ray Spectroscopy (EDS).
- Develop reliability models to predict fatigue life of various SAC-based solder alloys regarding their service conditions.

1.6 Proposed Dissertation Organization

This dissertation consists of nine chapters. Chapter 1 provides introduction of electronic packaging including general concepts, reliability of electronic packaging, service environment of electronic packaging, together with problem statement and detailed research objectives. Chapter 2 introduces relevant concepts and methods that are used later in this research for easy of reading and comprehending. Chapter 3 covers literatures about fatigue properties of solder alloys in both thermal cycling and isothermal cycling, main effects on the reliability of solder alloys, and common

constitutive models proposed to predict fatigue life of solder joints. Chapter 4 includes test vehicle preparation, experimental setup, testing profile and research methodology. Chapter 5 addresses the effect of shear strain rate on the shear properties and the effect of stress amplitude on the fatigue properties of SAC-based individual solder joints, including two LTS. Parameters in empirical models, Coffin-Manson model, and Morrow energy model are examined. Chapter 6 studies the effects of stress level, strain level and surface finish on the reliability of SAC305 solder joints in BGA assembly. Coffin-Manson model and Morrow energy model are found suitable for the sandwich specimens. Chapter 7 explores the fatigue performance of SAC305, SAC-R, SAC-Q, and SAC-I solder joints assembled with OSP and ENIG surface finish. Their microstructure and failure mechanisms are shown and compared. Chapter 8 investigates the fatigue properties of SAC305 and SnPb solder joints at different testing temperature. A modified model is proposed to predict the fatigue life given strain level and testing temperature. Chapter 9 summarizes the dissertation work and concludes the results. Future work is listed in the end of this dissertation.

Chapter 2 Background

2.1 PCB and Substrate

A PCB is usually a rigid structure that consists of non-conductive substrate and metal traces. The electronic components are soldered mechanically to the flat substrate and electrically to the traces. In other words, PCB with flat surface provides mechanical support for electronic components and the metal traces build up electrical connections between the components. In addition, the PCB is responsible for thermal dissipation and electrical isolation (non-conductive substrate). The board may be composed of either a single layer of circuitry (on top or bottom) or multiple layers of circuitry stacked together. Various layers could be electrically connected through vias. Types of vias include through hole vias which electrically connect top layer and bottom layer, blind vias which are exposed on one side of the board, and buried vias which is embedded inside the PCB to connect internal layers. Sometimes thermal vias are designed in certain application to help speed up heat dissipation.

2.1.1 Substrate Material

A PCB is built with a dielectric core material with poor electrical conducting properties to make the circuitry transmission as pure as possible, and then interspaced with additional layers of metal and dielectric as needed. Common dielectric materials used for substrates include polymer (phenolic, epoxy, polyimide, polyester, Teflon) and reinforcement (paper, glass fabric, Kevlar). One should carefully consider glass transition temperature when selecting the appropriate substrate material in real applications – property of substrate material could change from brittle to elastic, and CTE also changes at glass transition temperature. Taking account of this, operating

temperature limits of FR-4 and polyimide are 120°C and 230°C (their glass transition temperature). In addition, CTE of substrates varies significantly from horizontal to vertical. Added glass reinforcement allows for constrained expansion in x-y plane, but the CTE can be anisotropic. CTE of laminate substrate in x-y plane is typically around 14-18 ppm/°C to match well with 16 ppm/°C of copper, while in Z direction its CTE is 100-200 ppm/°C, which is 10 times larger. It is vital to design reasonable thickness of substrate to avoid possible reliability issues.

The standard dielectric material used for PCB is FR-4, which is a flame-resistant material composite of woven fiberglass cloth and epoxy resin. 'FR' means flame retardant and number '4' indicates woven glass reinforced epoxy resin [30]. Glass fibers here are the base material which provides laminate stability, while epoxy resin enables extra ductility. Besides, ceramic substrate is also available in harsh-environment applications such as military and aerospace. Although the price of ceramic substrate is much higher, the characteristics of higher thermal conductivity and lower CTE are preferred by designers since more options are available.

2.1.2 Solder Mask

Solder mask is a thin lacquer-like polymer layer covered on the PCB to protect the copper traces against oxidation and corrosion. Solder bridges that could form between closely spaced solder pads can be prevented with solder mask. Commonly used solder mask materials are acrylic or epoxy polymers. Copper pads on the PCB can be 'defined' in two kinds of manners, namely Solder Mask Defined (SMD) pads and Non-Solder Mask Defined (NSMD) pads. SMD pads have the solder mask apertures specified such that the opening is smaller than the diameter of the copper pad, as is shown in the left side of Figure 2-1. In this format the overlapping on the copper pad would help prevent

delamination between the pad and substrate, which is called pad lifting and is usually caused by thermal or mechanical stress [3][31]. Also, alignment of electronic components would be much easier in this way. For NSMD pads, no contact is made between solder mask and the copper pad, leaving a gap between the two as shown in the right side of Figure 2-1. NSMD pads have been proven to have better fatigue properties in thermal-mechanical tests because of the stronger bond created for solder-pad interface, but with pad lifting issues in drop shock tests.

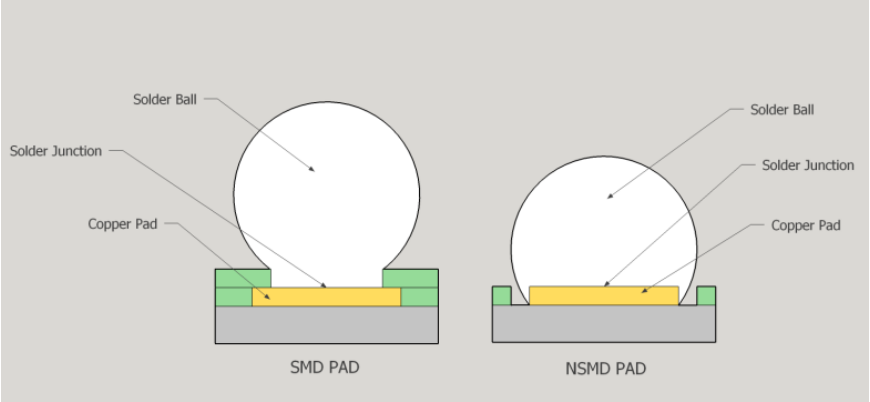

Figure 2-1 Cross-section view of SMD and NSMD pads

2.1.3 Surface Finish

The two kinds of solder mask mentioned in session 2.1.2 can only cover copper traces (NSMD) or part of copper pads (SMD), leaving some or all of the contacting area exposed to the air, which might result in reliability issues due to corrosion or oxidation prior to assembly. To deal with this problem, surface finish is applied to protect the exposed circuitry and ensure solderability in the following reflow steps. In general, surface finish can be classified as two main types: electroless plating and electroplating. The former one in also known as chemical plating or autocatalytic plating. This process creates a metal layer deposit on the surface by autocatalytic chemical reduction of metal cations in a liquid bath, such that the plating and substrate is physically bonded. Using

the latter method, a metallurgical bond is formed between the plating and substrate by applying an externally generated electric current. Compared with electroless plating, the bond formed in this process is much stronger and with higher ductility. Besides that, contaminants could be another potential problem during electroless plating. There are a variety of different surface finishes developed over the past few decades:

1. Hot Air Solder Leveling (HASL): This process has been dominating the market for decades because of the low cost and its excellent wetting characteristic. In this process, the PCB is immersed into a bath of molten solder (SnPb or Lead-Free) to cover exposed metal surface with specified solder. Excessive solder is then removed using hot air knives. Complex surface mount technology nowadays has revealed and exaggerated the shortcomings of the uneven surfaces in this process. It is found unsuitable for fine pitch components.
2. Organic Solderability Preservative (OSP): It is a water based organic compound that selectively bonds to copper. OSP is environment friendly, unlike the other surface finishes that are metal based. Advantages of OSP include low cost, excellent coplanarity and solderability, as well as multiple reflow capabilities. However, it is less robust than HASL and could degrade easily with the change of temperature.
3. Immersion Tin (ImSn): The RoHS compliant Immersion Tin surface finish is a thin deposit layer of tin on copper, which would form a Sn-Cu intermetallic structure during the process. The process continues and results in a limited shelf for the surface finish. The occurrence of tin whiskers and sensitivity of handling are additional drawbacks. ImSn is ideal for fine geometries and fine pitch surface mount components because it allows excellent flatness and smoothness.

4. Immersion Silver (ImAg): This process is very similar to ImSn but with a higher cost. For most applications, it can be a good alternative to ENIG which is introduced later. Moderate shelf life, solderability performance, and simple process control are benefits of this choice, but it could be sensitive to contaminants both in the air or in the board, thus need a highly qualified working space for this process.
5. Electroless Nickel Immersion Gold (ENIG): ENIG could be the answer for most of the applications in the PCB industry since the growth and implementation of the lead-free requirements. It is a two-layer metallic coating of 2 -8 μin Au over 120-240 μin Ni. The nickel layer works as a barrier to protect copper from oxidation and a surface for soldering. The gold layer protects the nickel layer during storage with very low electrical resistance. ENIG provides excellent shelf life, solderability, wettability, and flat surface. Shortcomings of ENIG could be the higher cost and sometimes the occurrence of black pad syndrome, which is a buildup of phosphorous between the gold and nickel layers. This feature could result in fractured surfaces and faulty connections.

In summary, one should always consider the requirements for durability, environment impact, and cost when choosing surface finish for specific applications. Each surface finish has its own superiorities and drawbacks. Reliability of surface finish, together with different solder materials, is gaining increasing interests for manufacturers all over the industry.

2.2 Solder Alloy

Solder alloys are compounds of different metals, which are used to provide permanent metallurgical bond between electronic components and the PCBs. Some common elements used for solder alloys in the electronic industry are tin, lead, copper, silver, bismuth, nickel and so on. Solder joints are the formed connections between the components and the PCB during soldering process to provide electrical, mechanical, and thermal connections. They are considered vital to the quality, performance, and reliability of electronic assemblies.

2.2.1 Tin-Lead Solder

Tin-lead solders have been developed by the Romans thousands of years ago. With the emerging and popularity of electronics, tin-lead solders quickly became the choice for the electronic industry for its superior features until very recently. The advantages of tin-lead solders include the inexpensive and plentiful of lead, low surface tension, strong formed intermetallic bond, and good mechanical properties.

The most popular tin-lead solder used in the industry is the mixture of 63% tin and 37% lead, which formed the eutectic tin-lead solder. Eutectic alloys have a specific temperature at which the alloys would melt immediately when increasing temperature and solidifies immediately when decreasing temperature. Other solder alloys would typically have a pasty range within which the alloy would be partially solid and partially solid, but the compositions of solid part and liquid part are different. Eutectic Sn-37Pb performs a wide range of advantages, including:

- Eutectic composition (the single transition temperature)
- Low melting point (183°C)

- Low cost (made from relatively abundant/cheap elements)
- Good wetting and manufacturability
- Adequate fatigue resistant
- Good joint integrity
- Excellent electrical conductivity

2.2.2 Lead-Free Solder

The predominating eutectic Tin-Lead solder has been gradually replaced by lead-free solder alloys because of the hazardous effect of lead on both humans and the environment. The adoption of WEEE and RoHS directives in early 2003 greatly raised people's interests in lead-free solder alloys. The two directives came into effect on July 1, 2006, aims to restrict the inclusion of lead in consumer products in the EU. In the US, no regulation is proposed by government to ban the use of lead, but the market force is pushing the US electronic industry towards the adoption of lead-free practice. Many lead-free solder alloys have been developed and researched since then.

To meet the current requirement of the industry, new-developed solder alloys should have improved wettability, suitable melting temperature, good mechanical properties, good resistance to thermal fatigue, good corrosion resistance, availability, and reasonable material cost.

Sn-Ag-Cu alloys

Nowadays SAC solders have been regarded as the most promising solders owing to the good soldering performance and the good reliability characteristics (e.g., good creep resistance, thermal fatigue reliability). Typical SAC alloys contain 3.0-4.0 wt.% silver (Ag), 0.5-1.0 wt.% copper (Cu), and the balance of 95 wt.%+ tin (Sn) [32], which makes them near eutectic. A variety of SAC alloys have been proposed and investigated,

including SAC305 (Sn-3.0Ag-0.5Cu), SAC105 (Sn-1.0Ag-0.5Cu), SAC387 (Sn-3.8Ag-0.7Cu), SAC396 (Sn-3.9Ag-0.6Cu) and so on. They are used in different applications.

Many methods have been applied to improve the performance of SAC solder, such as alloying it with additional elements and add nanoparticles to enhance the properties. The difference is that the added elements tend to undergo a diffusion process which produces an alloy of the SAC systems or act as a solid solution strengthener, while the addition of nanoparticles does not involve a diffusion process, instead act as discrete particles in the solder system.

The melting temperature of SAC solder alloys ranges from 217°C to 221°C depending on the composition of Ag and Cu. The reduction of Ag content for SAC alloys would offer a cheaper price at the expense of the lower ductility and the higher melting point. Doped elements such as Ti, Bi, Zn, Mg, Ce, Mn, La, and Co would help decrease the melting temperature, while the added nanoparticles (Al_2O_3, ZrO_2, TiO_2, $SrTiO_3$) would slightly increase the melting temperature.

SAC solder alloys have a higher wetting force than the eutectic Sn-Ag solder due to the addition of Cu element. Some other additional elements also tend to create better wettability properties, but except elements like Mg, which would cause degradation due to the vulnerability to oxidation. Minor addition of nanoparticles (Al_2O_3) would also enhance the wettability, but excessive amount (>1 wt.%) appears to degrade the wetting properties.

In the SAC solder system, the microstructure of the solder mainly consists of primary Sn grains, eutectic structure particles and IMC particles. A thin IMC layer is preferable because it provide strong bonding to enhance joint strength. However, an excessive

IMC layer thickness degrades the mechanical properties and can promote a brittle failure mode during crack propagation. As such, the addition of elements and nanoparticles can reduce the self-diffusion of Sn and thus have an influence in producing a thinner IMC. In addition, better mechanical properties are found by adding proper elements and nanoparticles.

Tin-Zinc alloys

The Sn-Ag, Sn-Cu and Sn-Ag-Cu solders are promising lead-free alloys, but their higher melting temperature compared to that of the eutectic Sn-Pb solder alloy may require a modification of the existing production lines. The presence of silver in the composition almost triples the price of solder material. Fortunately, eutectic Sn-Zn solder alloys show a low melting point very close to that of Sn-Pb solder and could provide satisfied mechanical properties as well. The problem tells that Zn-containing alloys exhibit poor wetting properties and are prone to oxidation and corrosion. New Sn-Zn based alloys are still under development to be widely used in the industry. In the other way, because of the drastic improvement of flux technology, the Sn-Zn based solder pastes have been applied in many commercial products, such as laptops, printers, TV tuners and more.

Sn-Bi alloys

Sn-Bi solder alloys were proposed as one of the most popular alloys a long time ago due to its low melting temperature (eutectic point: 139°C) and inexpensive price. However, they were not widely used previously because of the lower wettability, fatigue resistance, and elongation [33]. Recently, LTS Sn-Bi attract much attention from the industries for flexible PCB applications. Sn-Bi solders avoid warpage wherein PCB and electronic parts deform or deviate from the initial state due to their CTE

mismatch. One of the effective approaches to improve the properties, microstructure, and wettability of Sn-Bi solders is to have additional micro-alloying elements or nanoparticles [34].

2.3 Printed Circuit Assembly

Semiconductor packaging is evolving with an increased demand for maximum possible functionality, finer size, and added utility. In order to build up both electrical and mechanical connections between PCB and electronic components in the second level of electronic packaging, modern PCA prompted two methods: Through-Hole Mount Technology (THMT) and Surface Mount Technology (SMT), each with their designated PCB components to mount on the board.

2.3.1 PCB Components

PCB components are made up of a variety of complex electrical units, which could be typically categorized as active components and passive components. Passive components are unable to change their character when applying electrical impulses. Single or repeatable reaction can be provided by them. Active components are devices capable by themselves of controlling voltages and currents to produce gain or switching actions. They are able to change their basic character in react to an applied signal.

Material

Active components can be further classified as ceramic packages or plastic packages depending on the material of chip carriers. Plastic packages are by far the most common in use today for its cheaper price. Ceramic packages are much more expensive but provide excellent performance – they are widely used in military, aerospace, and other

ultra-high-performance required areas. Examples of plastic packages and ceramic packages are shown in Figure 2-2.

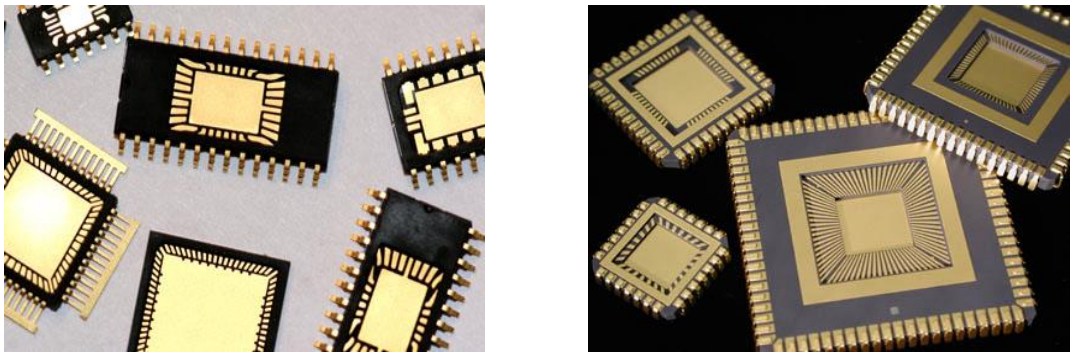

Figure 2-2 Plastic Package (left) and Ceramic Package (right)

Ceramic packages are superior to plastic packages in hermeticity, exceptional planarity, high temperature stability/resistance, thermal conductivity, and built-in passive feature. Drawbacks of ceramic package include more complicated lead routing and much higher cost. Ceramic packages constitute two thirds of the total packaging market despite far less number manufactured each year.

Lead type

Packages could also be sorted using the criteria of mounting type used, as is shown in Figure 2-3 [31]. Typical package examples for through hole mounting and surface mounting are shown in Figure 2-4. The left example is a Dual In-line Package (DIP) used for through hole mounting. The right example exhibits many surface mount packages assembled on the PCB board. Specifically, leaded packages, the most widely used package format, are electrically and mechanically connected with PCB land dictated by either lead or attachment solder materials.

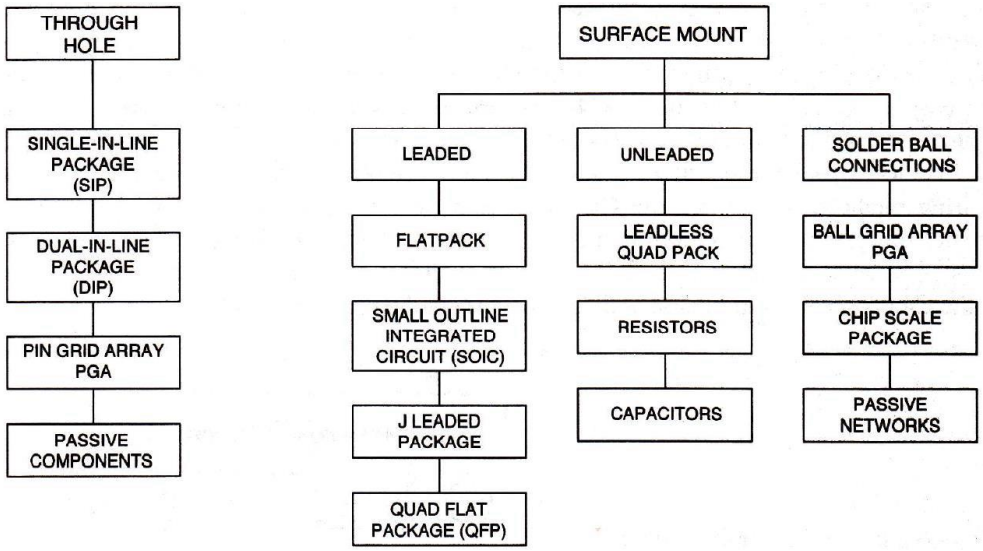

Figure 2-3 Types of Packaging

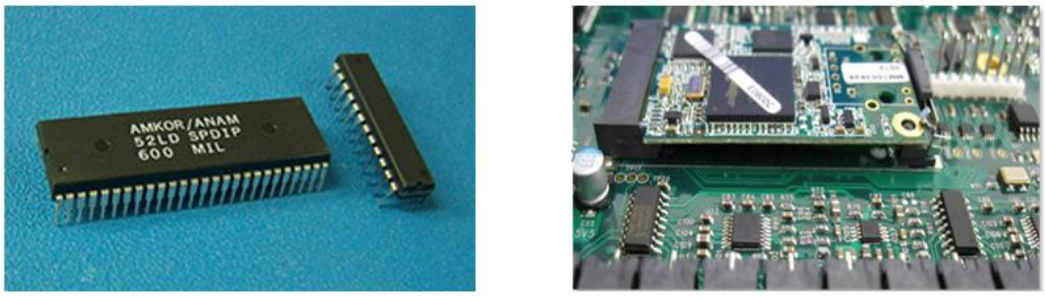

Figure 2-4 Through hole mounting package and surface mounting package

Leaded packages include mainly three lead types: Gull Wing Lead, J Lead, and Solder Ball Area Array. Gull Wing Lead, as the name says, has the shape of gull wing; while J Lead expands in the opposite way, which makes it look like alphabet J. The geometry of each type is illustrated in Figure 2-5. Note that the main solder fillet on the Gull Wing joint reaches back toward the component body, while the main solder fillet on the J-Lead joint goes outward the component body. The other lead type – Solder Ball Area Array will be detailed discussed in the next session.

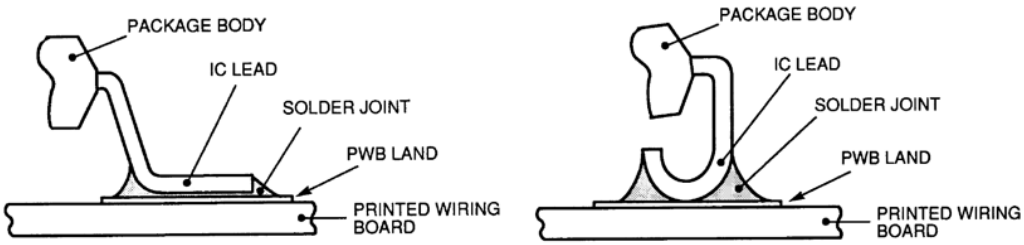

Figure 2-5 Gull Wing Lead and J Lead

BGA Components

The continuing need of more I/O for advanced integrated circuit components called for finer pitch I/O. However, there are limits to make finer pitch at some point as the pitch reaches very fine. Possible problems include coplanarity, wicking, and shorting [35]. In order to get rid of this situation, industry was looking for new technologies. Fortunately, area array as a solution has been around for some time to increase number of I/O.

The appearance of SMT made the I/O placed under the surface mount component possible. In this way I/O can be installed in a full 2-dimensional lattice rather than limited to the perimeter of one component. In other words, the number of I/O increases from 4n to n^2 (although sometimes only part of the allowable area is covered). Figure 2-6 illustrates the schematic of a typical Ball Grid Array (BGA) component. There are many small solder spheres applied to the grid contact pads (copper pads) built on the bottom of the component. These solder spheres are then precisely attached to the solder paste deposits on the copper pads which are located on the PCB boards. This process is typically completed using a pick and place machine. After that, during reflow process, the solder spheres would reflow and wet with solder paste to form robust burger-shaped solder joints.

BGA components do exhibit some superior characteristics such as finer pitch, better electrical performance (shortest path between component and PCB board), and superlative thermal dissipation capability [36]. However, reliability concerns would come up when exposed to harsh environment, especially under drastic temperature changes. Some typical types of BGA packages available in the market are listed in Table 2-1 [37].

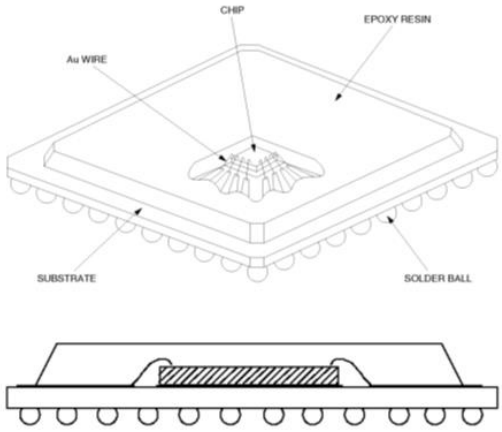

Figure 2-6 Ball Grid Array Component

Table 2-1 Types of Ball Grid Array

PBGA Plastic Ball Grid Array	Can be either 2-layer or 4-layer substrates, with pitch ranges from 1.0-1.27mm and body size greater than 23mm × 23mm.	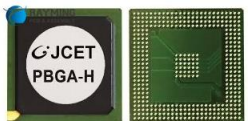
CBGA Ceramic Ball Grid Array	Multi-layer ceramic substrate, C4 (Controlled Collapse Chip Connection) approach is applied, with higher cost but extreme reliability.	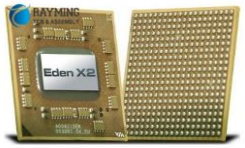
TBGA Tape Ball Grid Array	Flexible polyimide film (tape) with copper metallization is used, with better heat dissipation and superlative electrical properties.	
EBGA Enhanced Ball Grid Array	Plastic Ball Grid Array with additional heat sink options - a dam is built on the boundaries and liquid components are added to make sealing.	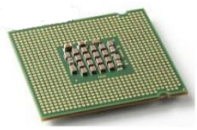

FC-BGA Flip Chip Ball Grid Array	Flip Chip technology is used in this component thus shorter electrical pathways – better electrical connectivity and faster performance.	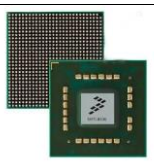
MBGA Metal Ball Grid Array	Also known as Super Ball Grid Array, a metal heat sink is applied to dissipate extra heat generated by chip.	

2.3.2 Through-hole Mount Technology (THMT)

The use of rigid substrate from 1940s that can provide mechanical support for electronic components promoted hand-wiring, which was the fundamental process for through-hole mounting at the beginning. Actually, THMT appeared from the second generation of computers in the 1950s. It was extensively used in PCA as a substitute for Point-To-Point constructions during the 1970s and early 1980s. Earlier electronic assembly techniques had been almost completely replaced by THMT until SMT became popular in the late 1980s.

Through-hole mounting is the process by which component leads are placed into drilled holes on the PCB. The holes can be plated or non-plated - with Plated Through Holes (PTH) there is a conductive path (thin copper layer) plated onto the walls of the holes during the manufacturing process; with Non-Plated Through Holes (NPTH), no copper is plated on the hole barrel, as is shown in Figure 2-7. It is obvious the manufacturing process of NPTH is simpler and quicker, but considering most PCBs are double sided or multi-layered nowadays, PTHs are widely used to provide connections between the components and the required layers in the board.

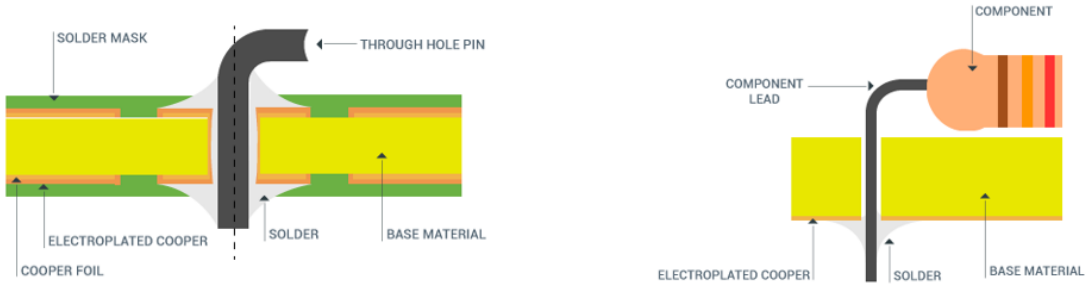

Figure 2-7 PTH vs. NPTH scheme

The basic form of an electronic component used for THMT is shown in Figure 2-8. The THMT process includes passing component leads through the drilled holes, crimping these leads on the backside, and soldering the leads firmly attached to PCB, which would build links between the component and copper traces with lower resistance and better mechanical stability. The soldering process was first completed by hand soldering, then the invention of wave solder machine eliminates hand soldering, leading to faster production and higher quality. After that, with the demanding for higher component densities, automated placement machines were developed for quick pick and place process including crimping, forming, and wire cutting.

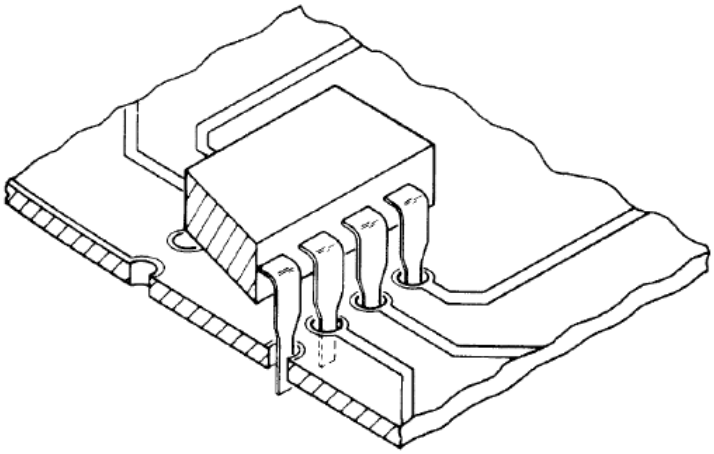

Figure 2-8 Through-hole Mounting Technology (THMT)

Through-hole mounting is best used for products with high-reliability requirement of the connections since it provides stronger bonds than SMT. It is commonly used in military and aerospace, where the excellent reliability of solder connections is preferred - components would experience extreme accelerations, collisions, or high temperatures and undergo excessive mechanical stress. Also, through-hole mounting is available in test and prototyping applications for the benefit of easy manual adjustment and replacement.

On the downside, required drilling holes in THMT limits available routing area on any multilayer boards, plus the much lower placement rate compared to SMT, making THMT prohibitively expensive. In addition, lead pitch is limited by the I/O connections placed along two edges of the components.

In all, despite a severe drop in popularity since the emerging of SMT in 1980s, the disappearance of THMT from PCA is a wide misconception. There still exists some circumstances where THMT is preferred including solder connections requiring strain relief, test and prototyping applications, and bulky/heavy components. Availability and cost are also critical factors when considering components (through-hole package or surface mount package) to assembly.

2.3.3 Surface Mount Technology (SMT)

Unlike THMT, SMT is a process where components are mounted directly onto the surface of PCB, as shown in Figure 2-9. This method was originally called ‘planar mounting’ and developed in the 1960s. By the 1990s, it has grown increasingly popular and dominated high-tech electronic PCAs.

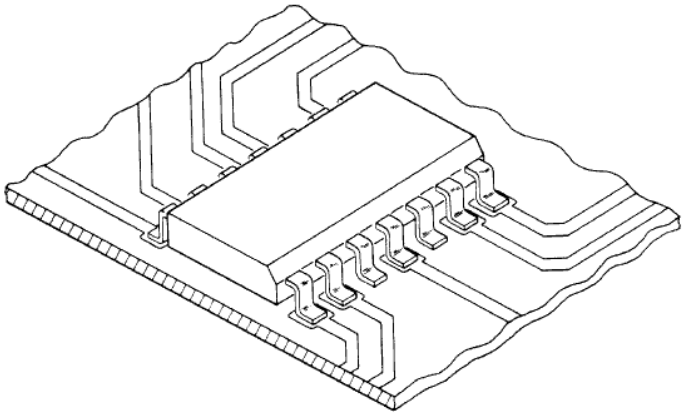

Figure 2-9 Surface Mount Technology

The key difference between SMT and THMT is that there is no need to drill holes on PCB for SMT since the through-hole component leads have been replaced by “vias”, which are small components creating conductive connections between different PCB layers. In addition, surface mount components can be mounted on both sides of the PCB, significantly increasing the useable surface area in the PCB. Besides, surface mount components are smaller with finer pitch size. These advanced feathers have allowed the design of PCB with more density, higher performance, and smaller size. Moreover, surface mount components can be placed at rates of 1000~10000 per hour using pick-and-place machine, which is much faster than the rate for through-hole components - less than 1000 per hour. At last, reduced lead length improves the electrical performance of components but in contrary makes the thermal management more complicated.

Overall, SMT has proved to be more efficient and economic than THMT in many ways - it is dominating the PCAs with more than 90% usage today, despite some reliability considerations related to mechanical, electrical, and thermal. As mentioned before, it is important to select the appropriate technology in real applications.

Future Trends

Modern electronics is more and more miniature, but with more complex configuration. The requirement of reduced cost per integrated circuit and enhanced performance is pushing the development of new generation of electronic packaging to achieve higher integration through different ways such as utilizing new materials, processes and configurations. All this leads to the emerging phenomena that an increasing number of components, semiconductor chips and passives are placed inside the system. And at the same time more complex interconnections are designed to address electrical and electromagnetic interference with close signal proximity, thermal issues with high current and a proper thermal management and heat dissipation without sacrificing coupling efficiency, and mechanical issues with miniaturized structures. The scaling of electronic packaging has reached the limit after following Moore's Law for over thirty years. Also, the functional diversification of electronics, physical limits and growth of costs in the future reveal that 'more Moore' structure is impracticable. New technologies are desired to build high density circuits and cope with potential problems in a competitive cost. Fortunately, System on Chip (SoC) and System in Package (SiP) [38][39][40] are proposed to continue the improvement in performance, size, power, and cost. The trends in scaling are shown in Figure 2-10.

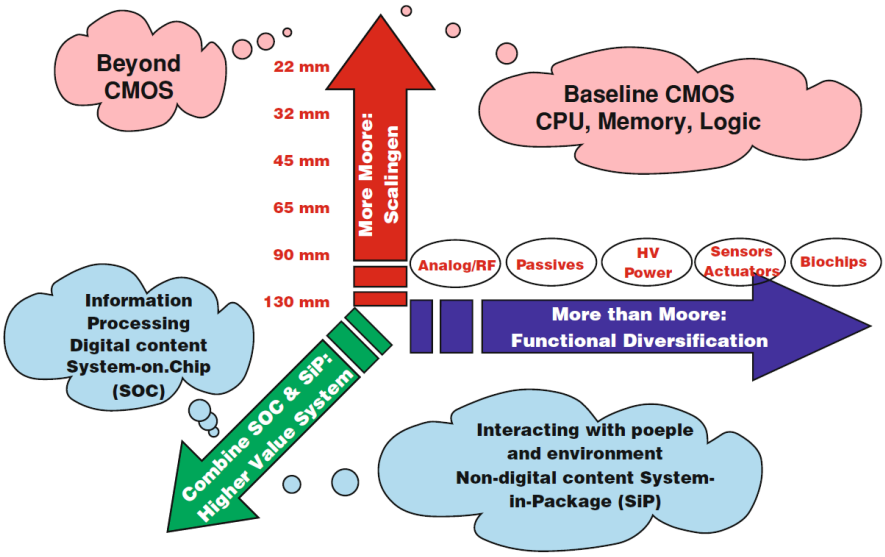

Figure 2-10 Scaling trends of electronics industry

System on Chip Technology

SoC is a way to increase functional integration by including sub-systems on a single chip. It is developed from the willingness of constructing high volume custom devices by integrating design elements from different semiconductor devices. Main advantages of this technology include high function density, high on-chip frequencies, strong reliability, and moderate unit cost. On the other hand, significant shortcomings are selected chips would restrict system function, high costs, less competitive in low-end or middle-end market since long period of design and testing. The adopted application of this technology mainly lies in multicore processing and portable consumer electronics.

System in Package Technology

SiP combines multiple active electronic components of different functionality assembled in a single unit, which enables multiple functions inserted into a system or subsystem. This technology integrates circuits and discrete components to enhance the performance and reduce the overall size. Existing technologies, such as lead frames,

package on package and die stacking, are promoting the development of SiP. 3D-integration technologies offer a novel approach to further enhance the performance through stacking semiconduction elements on top of each other, and vertical room is better utilized than 2D-integration. Three technologies are used in 3D-integration (Figure 2-11.):

- Stacking of package dies (package on package)
- Stacking of dies, chip to chip (3D-Packaging)
- Wafer level 3D integration, chip to wafer, wafer to wafer (3D-WL)

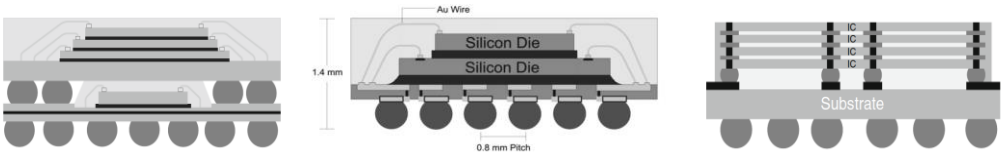

Package on package　　3D-Packaging　　3D-WL integration

Figure 2-11 3D-integration technologies

Among the three technologies, 3D-WL packaging is probably the best considering the exhibited performance, as shown in Table 2-2. But problems lie in the fact that even 3D packaging is on the way to overcome challenges like die yield, thermal management and 3D design tools. When it comes to 3D-WL packaging, problems will be further amplified. Fortunately, technologies such as Through Silicon Via (TSV) and coreless substrate have been proposed to address these potential problems [41].

Table 2-2 Features of 3D-integration

Technology	3D packaging	3D-WL integration
Infrastructure	Packaging	Foundry
3D interconnect	Bond wires, FC	Through silicon vias
Active layer thickness	>50 μm	<50 μm
I/O density (cm^{-2})	10^4–10^5	10^5–10^8

2.3.4 SMT Assembly Process

Although THMT is still in use for some applications, the interest of this paper mainly focuses on SMT - samples tested in the experiments later in the dissertation are also prepared using SMT. The process of SMT assembly is clearly shown in Figure 2-12.

The first step is material preparation and examination. During the process, surface mounting components and PCB are prepared and inspected to find any flaw that could lead to unsuccessful assembly.

The second step is stencil preparation. The stencil is often made of stainless steel or nickel with a series of precisely cut apertures on it. These apertures are produced according to the position of copper pads located on the PCB. The aim of applying stencil is to provide fixed position for next step - solder paste printing.

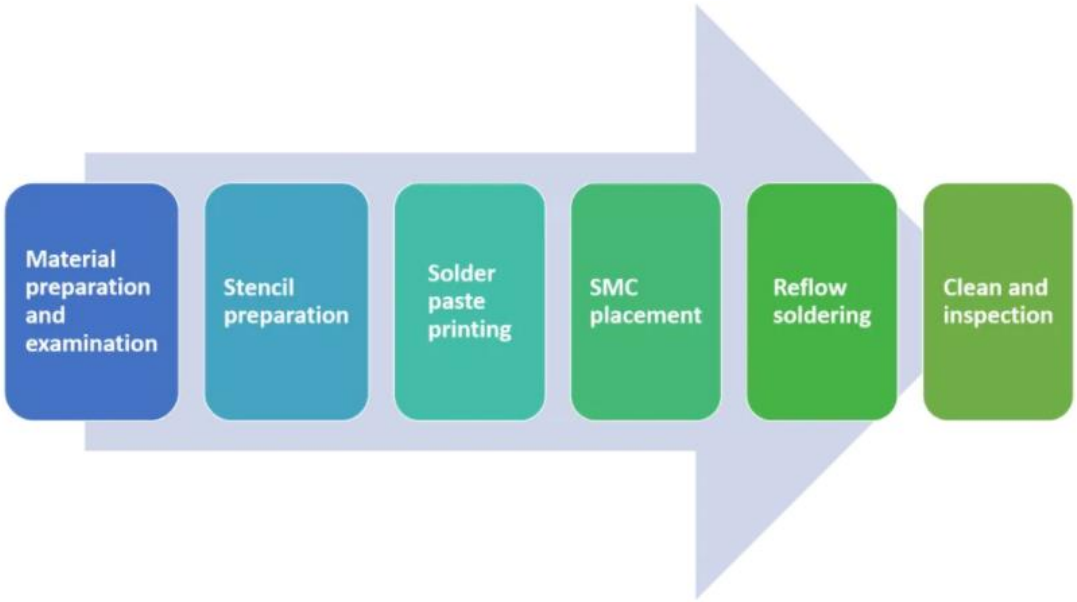

Figure 2-12 Flow Chart of SMT process

The third step is solder paste printing. As the name indicates, during this step solder paste is printed on the copper pad through the apertures of the stencil. Solder paste is a toothpaste-like sticky paste, used to temporarily hold the components to be placed in the next step. The composition of solder paste is mainly powder of metal particles and

a thick medium suspension called flux. The most common method of depositing solder paste through stencil apertures is squeegee blade printing. In the process, a squeegee is used to apply suitable force to push the solder paste across the stencil and onto the copper pad on an angle range from 45° to 60°.

The fourth step is component pick and placement. The PCBs then proceed to the pick-and-place machines. Basic placement process includes picking components using vacuum nozzles, inspection and positioning by camera, and placement with force to embed component in solder paste. A variety of pick-and-place machines are available in the market, with different types of feeders and heads, and with different machine capability.

The next step is the reflow process. After the components are placed, the boards are conveyed into the reflow soldering oven. The reflow oven can be designed as either infrared or convection, and it contains multiple zones in which temperature can be individually controlled. Typical zones for a reflow oven are:

- Pre-heat zone: In this zone the temperature of the PCB together with all the components is raised simultaneously and gradually until reaches soak temperature. Temperature ramp-up rate is slow in the zone, usually at 1.0°C – 2.0°C per second. Excessive heating rate would result in component cracking and solder paste splattering.
- Soak zone: The board is then kept in this zone within soak temperature for 20-120 seconds to remove solder paste volatiles and activate the flux. By the end of the zone the entire board should have thermal equilibrium.
- Reflow zone: The temperature ramps up at 1.0°C - 2.0°C per second until reaches programmed peak temperature. The time above liquidus temperature is

usually controlled between 30-60 seconds. This process ensures the wetting of the solder paste and the bonding of components to the copper pads on the PCB. The components are supposed to be kept in place during the process because of the surface tension of molten solder, but the movement during the process could result in poor connection quality or even complete lack of connection.

- Cooling zone: The board is cooled down to solidify the solder in this zone. Cooling rate has a significant effect on the microstructure of solder joints.

The last step is clean and inspection. After reflow soldering, the boards are cleaned and then inspected. Some defects could be reworked or repaired at repair station. Common inspection equipment includes magnifying lens, Automated Optical Inspection (AOI), X-ray machine, flying probe tester, etc.

The whole SMT assembly process is clearly illustrated in Figure 2-13.

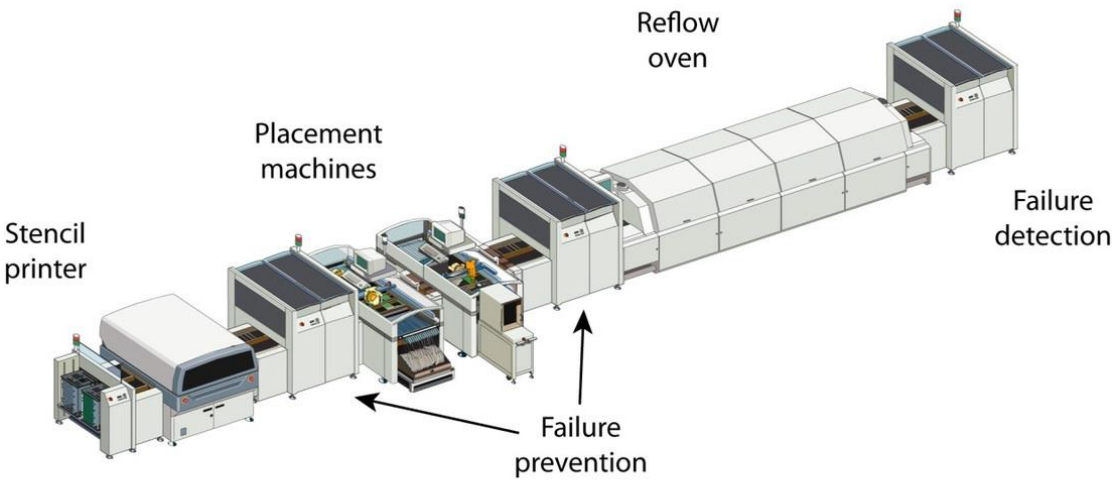

Figure 2-13 SMT Assembly Production Line

2.4 Mechanical Properties of Solder Materials

Mechanical property is defined as a property that involves a relationship between stress and strain, or a reaction to an applied force. The applied force to an object is also known as loading. Depending on the loading conditions, a material can be subject to different loading scenarios. Figure 2-14 illustrates five fundamental loading conditions: tension, compression, bending, shear, and torsion. The force applied to the object can also be either constant or fluctuating, namely static loading and cyclic loading. Mechanical properties of solder materials generally describe the physical properties that solder materials exhibit upon the application of forces.

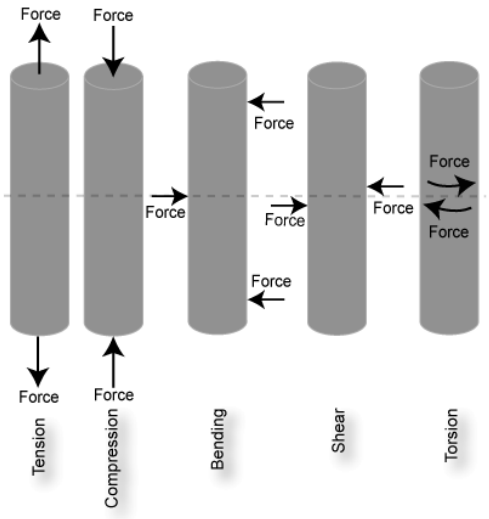

Figure 2-14 Fundamental loading conditions

Since the geometry of material varies, the more common way to describe the loading applied to it is tress. The term stress is used to express the loading in terms of force applied to a certain cross section area of the material. In this way stress can also be defined as a physical quantity that expresses the internal forces that neighboring particles of a continuous material exert on each other. Equation 2-1 describes the relation:

$$\sigma = \frac{Force}{Cross\ Section\ Area} = \frac{F}{A} \qquad 2\text{-}1$$

Strain is the response of the material to an applied stress - stress tends to deform the body. In engineering field, strain is defined as the amount of deformation in the direction of the applied force divided by the initial length of the material. The relation is shown in Equation 2-2:

$$\varepsilon = \frac{Elongation}{Initial\ Length} = \frac{\Delta L}{L} \qquad 2\text{-}2$$

Electronic packages are subject to both thermal and mechanical stress in real service applications. On one hand, during operation the temperature of the electronic package would increase, not to mention the influence of ambient environment. On the other hand, external mechanical loading has a undenied effect on solder joints inside the package. To make a better pair between solder alloy selection and application environment, it is essential to investigate the mechanical properties of solder materials by conducting tensile test, shear test, creep test, and fatigue test.

2.4.1 Tensile Property

Tensile properties indicate the reaction of the material when applying tension force. A tensile test is a fundamental mechanical test to measure the applied load and the elongation of the specimen over some distance until breaking. The result of a tensile test is represented in a load versus elongation curve, which can be converted into a stress versus strain curve. The stress-strain curve relates the applied stress to the resulting strain. Each material has its own unique stress-strain curve. Typical stress-strain curves are shown below in Figure 2-15.

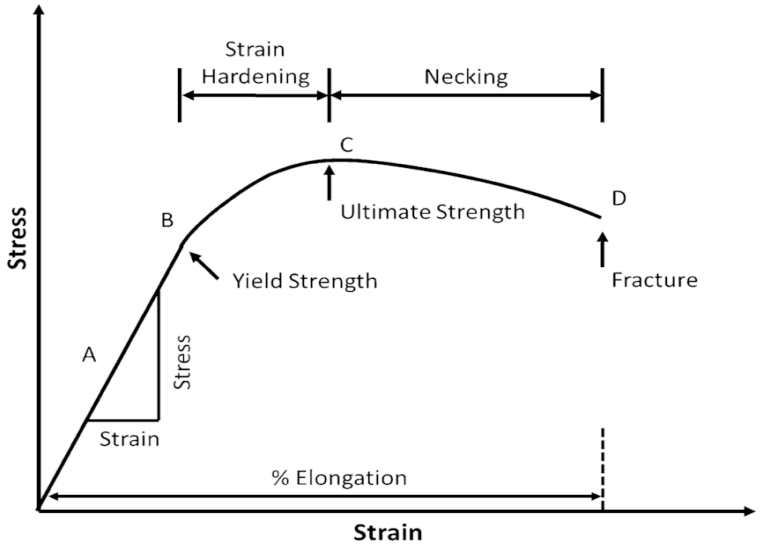

Figure 2-15 Typical tensile stress-strain curve for ductile material

The stress and strain initially increase with a linear-elastic relationship and no plastic deformation is induced in this region. When stress is reduced, the testing material will return to original shape. Hooke's Law describes the relation of stress and strain in this region:

$$\sigma = E * \varepsilon \qquad 2\text{-}3$$

Where *E* is called the modulus of elasticity or Young's modulus. It indicates the stress is proportional to strain in the region and it's actually the slope of the line. Young's modulus defines the properties of a material to return to its original shape after the removing of the stress. It is a mechanical property that measures the tensile stiffness of a solid material.

The yield strength is the stress corresponding to the yield point at which the material begins to deform plastically. It represents the upper limit of allowable force without producing permanent deformation. For ductile materials, from point B in Figure 2-15, the curve deviates form line relationship and permanent deformation occurs in the specimen, which means the specimen is not able to return to original shape after the

release of applied loading force. For brittle materials, little or no plastic deformation occurs and the material fractures near yield point B.

The ultimate strength is the ability of a material to withstand external forces without breaking. For ductile materials, the ultimate strength (point C) is outside of the elastic portion and higher than yield strength (point B). For brittle materials, the ultimate strength is close to the yield strength.

The ductility of a material is a measure of the extent to which a material can deform before fracture. This property is an aspect of plasticity of material and is temperature dependent. The ductility of a material increases with the rising of temperature. It is expressed as percent elongation of the testing specimen, shown in Equation 2-4:

$$EL = \frac{Fracture\ Length - Initial\ Legth}{Initial\ Length} = \frac{L_f - L_0}{L_0} \qquad 2\text{-}4$$

Tensile properties of solder materials are normally tested using bulk samples. These properties should be fully understood for design purpose, although solder joints are barely exposed to pure tensile loadings in realistic operations.

2.4.2 Shear Property

As mentioned before, electronic packages are subject to temperature change during operation. The substrate with relatively higher CTE tends to expand more than PCB components with lower CTE. The mismatch of CTE result in the deformation of solder joints and thus shear strain, as shown in Figure 2-16.

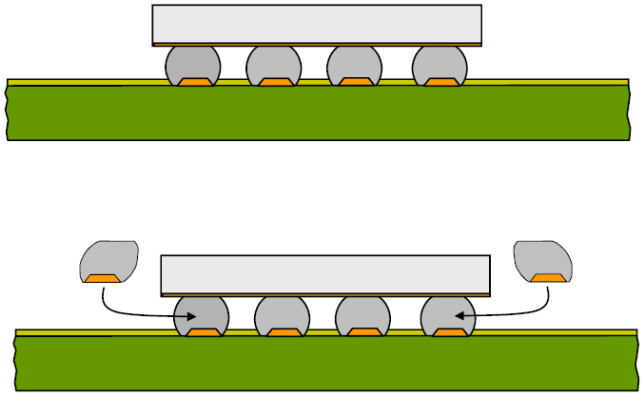

Figure 2-16 Shear stress of solder joints induced by temperature change

Shear stress-strain curve is quite similar to that of tensile stress-strain curve (Figure 2-15). Shear stress increases linearly first until reaching yield point τ_{ys}. Then strain hardening stage appears, resulting the continuous increasing of shear stress to maximum value τ_{uts}. The shear stress decrease after that until fracture. Here shear stress τ and shear strain Υ is defined by equation 2-5 and 2-6:

$$\tau = \frac{F}{A} \qquad 2\text{-}5$$

$$\Upsilon = \frac{\Delta x}{h} \qquad 2\text{-}6$$

where F is the shear force applied, A is the area parallel to the applied force, Δx is the transverse displacement, and h is the shear height of the specimen.

The linear relation of shear stress and shear strain is shown in equation 2-7:

$$\tau = G * \Upsilon \qquad 2\text{-}7$$

Where G is the shear modulus of testing material, indicated by the slope in the graph. Shear modulus of a material is given by equation 2-8:

$$G = \frac{E}{2(1+v)} \qquad 2\text{-}8$$

Where E is Young's modulus and ν is Poisson's ratio.

2.4.3 Fatigue Property

Fatigue is the weakening of a material caused by cyclic loading. The name 'Fatigue' originated from Latin expression which means 'to tire'. Fatigue is commonly associated with physical and mental weariness in people, but it has become a widely accepted terminology in engineering nowadays. The form of fatigue varies in different conditions: fluctuations of external applied stresses or strains result in mechanical fatigue; deformation caused by repeated stresses at high temperatures is creep-fatigue; recurring loads applied to chemical aggressive environment cause corrosion fatigue; temperature fluctuating together with cyclic loads produce thermomechanical fatigue.

The fatigue life of a solder material can be expressed as the number of cycles required to initiate a fatigue crack and to propagate the crack sub-critically to some final crack size. The cyclic loading stress are carefully selected below ultimate tensile stress, or even yield stress in order to guarantee sufficient fatigue life. Fatigue failure occurs in the following stages:

- Nucleation of permanent damage caused by substructure and microstructure change;
- The creation of microscopic cracks;
- The growth and coalescence of microscopic flaws to form dominant cracks;
- Stable propagation of the dominant cracks;
- Complete fracture.

Figure 2-17 demonstrates the deformation and propagation of fatigue cracks in the aged SAC solder material [42].

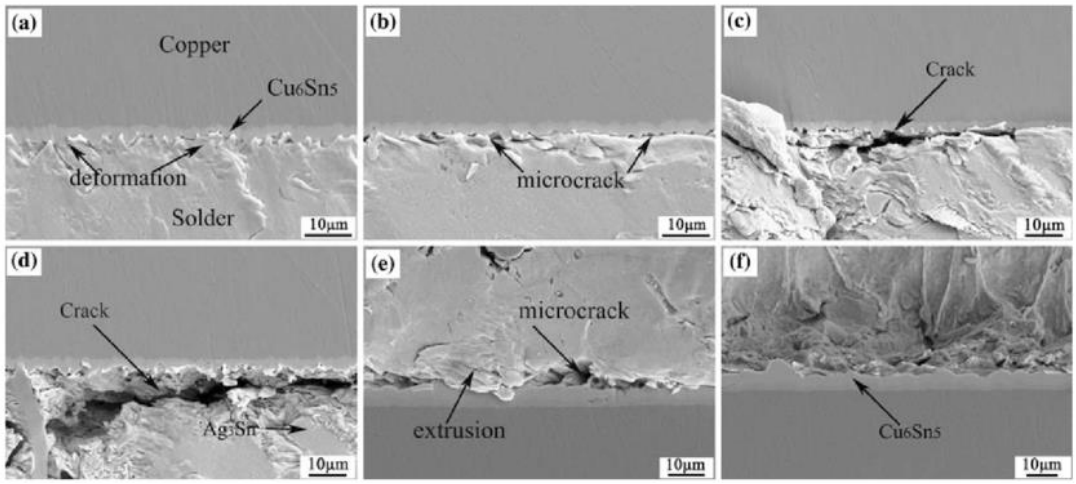

Figure 2-17 Evolution of fatigue cracks shown in SAC solder sample

Mechanical, microstructural and environmental factors are of great significance for the nucleation of microdefects and the rate of dominant fatigue crack propagation. The main obstacle of developing life prediction models lies in the different choices for the definition of crack initiation. Materials scientists are likely to consider the nucleation of flaws in micrometer scale as the crack inception stage. These cracks are commonly found along slip bands and grain boundaries. On the other hand, engineers prefer relating a wide range of crack detection equipment, which has differentiated resolution limit, with the nucleation of fatigue crack and with the initial crack size.

Despite there exists a fracture mechanics approach to fatigue design, where the testing specimens are inherently flawed and the useful fatigue life is defined as the number of cycles to propagate the dominant crack from its initial size to some critical dimension, classical approaches are more commonly applied. The difference between the two is that the latter aims to figure out the total fatigue life in terms of the cyclic stress range or the strain range. In other words, the total fatigue life incorporates the number of stress or strain cycles to induce fatigue failure in initially uncracked specimens under controlled stress or strain amplitudes.

Depending on the fatigue cycles to failure, high-cycle fatigue test and low-cycle fatigue test are characterized. Under high-cycle, low-amplitude loading is imposed thus mainly cause elastic deformation. In this case fatigue life has been traditionally expressed in terms of stress range, as shown in Figure 2-18. Strain hardening materials under constant loading amplitudes tend to exhibit a plateau in the stress-life plot beyond about 10^6 fatigue cycles. Indefinitely cycles are expected if stress below plateau level. This stress level is defined as the fatigue limit or endurance limit. Under low-cycle, the loadings are generally high enough to exert sufficient plastic deformation prior to crack initiation. Fatigue life is found to be precisely predicted in terms of strain range.

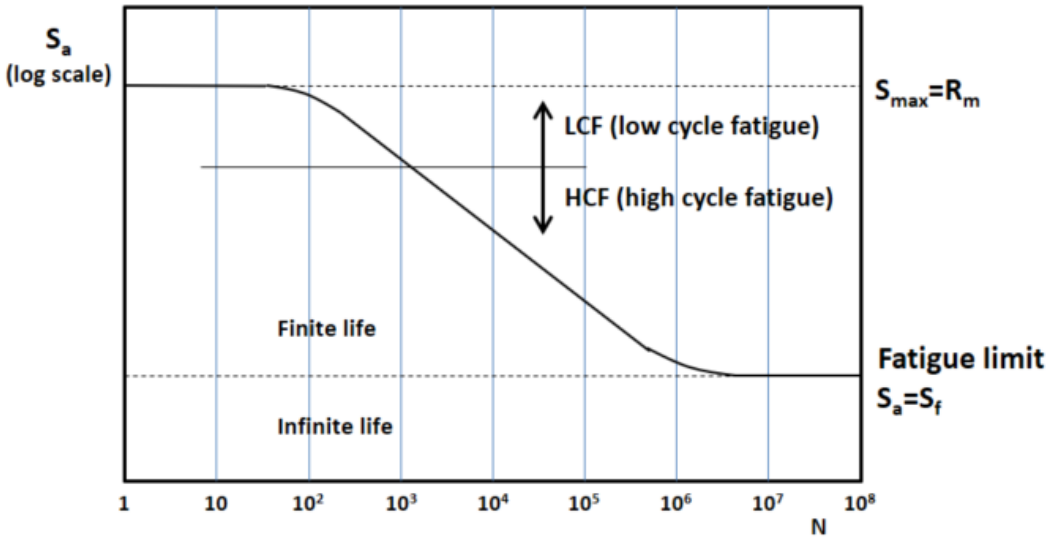

Figure 2-18 Typical S-N diagram for strain hardening materials

2.5 Reliability of Solder Materials

Reliability, as defined in Chapter 1, is the probability of proper function over time. The implicit feature of the definition lies in the underlying assumption that the survival time, or say life length, is usually dispersed as a probability distribution function. Given a population of identical specimens, the dispersing in the failure time is distributed as a

probability function. Denoting life length by *T*, the distribution function on *T* is represented by *F(t)*:

$$F(t) = \Pr\{T < t\} \qquad 2\text{-}9$$

For a given time value *t*, *F(t)* is the Cumulative Density Function (CDF) that describes the failure probability occurs less than time *t*. In the similar manner, reliability function *R(t)* can be expressed as the life length equals or exceeds *t*:

$$R(t) = 1 - F(t) = \Pr\{T \geq t\} \qquad 2\text{-}10$$

The Probability Density Function (PDF) of failure, *f(t)*, can be derived from CDF, or vice versa:

$$f(t) = \frac{d}{d(t)} F(t) \qquad 2\text{-}11$$

$$F(t) = \int_0^t f(u)\, d(u) \qquad 2\text{-}12$$

Another function derived from the distribution function to describe the instantaneous conditional probability of failure per given survival time is the hazard function. Hazard function, *λ(t)*, is actually the instantaneous failure rate. In order to avoid the misleading conception of failure rate in other failure phenomena, the function *λ(t)* is named as the hazard function. The algebraic form of the hazard function is expressed as:

$$\lambda(t) = \lim_{\Delta t \to 0} \{\frac{1}{\Delta t} \frac{F(t + \Delta t) - F(t)}{R(t)}\} = \frac{f(t)}{R(t)} \qquad 2\text{-}13$$

Any of the four above mentioned reliability measures can be used as a basis for distinguishing failure patterns of a device or system, since they are four equivalent algebraic descriptors of longevity – they are functionally related and comprise alternate description of the life length dispersion. However, the hazard function is viewed as the

most informative descriptor of failure behavior. The distribution function selected to model life length is usually determined in this step. Further classify the hazard function comes with Increasing Failure Rate (IFR), where the failure rate increases with time goes on; Decreasing Failure Rate (DFR), where the failure rate is decreasing; and Constant Failure Rate (CFR), which is an interesting special case where the failure rate stays stable. Note the concept that a population of devices displays a 'bathtub-shaped' hazard over their life length. The 'bathtub curve' is shown in Figure 2-19. The curve is intended to illustrate the general phases of hazard rates through working time. Early in the life, failure happens at a relatively high rate owing to the population of devices with material flaws, manufacturing defects, or other physical anomalies. The shape of early failure is quite similar to that of early infant mortality, which is characterized by DFR. Random failures, plotted in straight line, exhibits the natural failure characteristic of devices during working life. The failure rate is recognized as a CFR. The wear-out failure curve reveals the 'wear out' phenomena, where devices tend to fail more easily toward the end of lives, thus an IFR. Combining these three failure modes comes a bathtub curve showing three phases: burn-in period, useful life period, and wear out period. Burn-in failures can be significantly reduced by taking actions such as burn-in testing, quality control, and acceptance testing. Extending useful life is also possible by providing redundancy parts and excess strength. Wear-out of devices is prevented by derating, maintenance, and parts replacement.

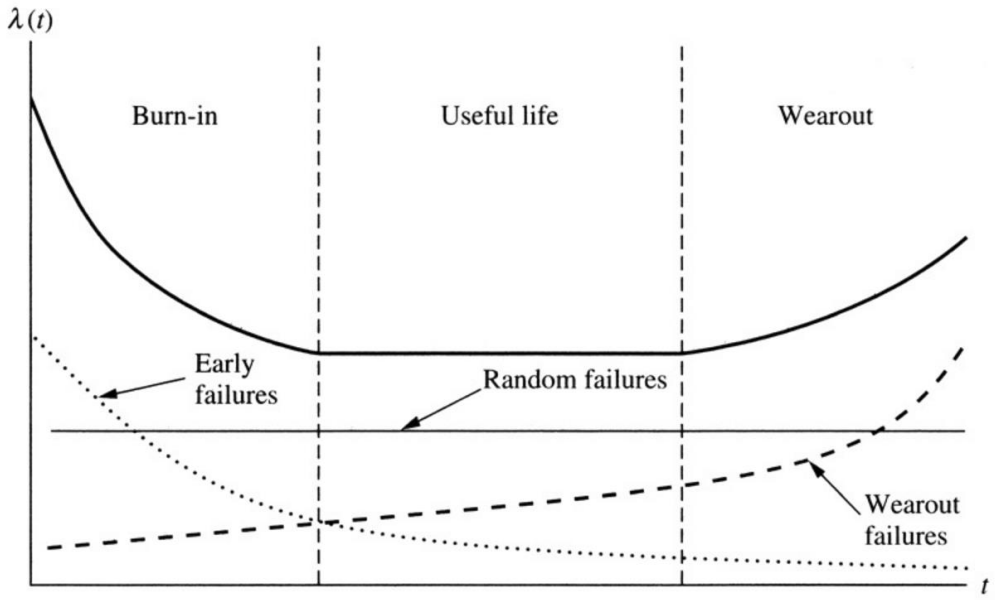

Figure 2-19 Example of a bathtub curve

A number of life distribution models have been developed to characterize the life of interested devices, including the Exponential distribution, the Weibull distribution, the Normal distribution, the Lognormal distribution, the Gamma distribution, etc.

With regard to lead-free solder materials, such as doped solder materials, extensive research has been carried out since the restriction on the use of lead-based solders. Driven by the necessity to improve the reliability of lead-free electronic products, intensive efforts have been devoted into improving the mechanical properties of Sn-based solders. It has been proved that the addition of minor elements, such as Ni, Co, and Ti, would have positive effect on the mechanical properties of solder material, including shear strength, tensile strength, impact resistance, and creep resistance. It is imperative to investigate the reliability of commercial or promising solder alloys for different applications.

In order to identify the potential failure modes and the withstanding limit of a product in a short period of time, extreme conditions (temperature, stress, vibration, etc.) beyond its operation requirements are adopted without the inducing of other unexpected

outside disruptive factors for the purpose of conducting ALT, that is carefully designed to figure out the quality or reliability of a product in correlation with preconceived interested factors. The reliability of solder materials exposed to differentiated environments is widely researched by conducting the following ALT reliability tests:

- Thermal Cycling Test
- Vibration Test
- Thermal Shock Test
- Drop Test
- Low-Cycling Fatigue Test

The specific description of actual failure characteristics of solder materials is naturally based on the analysis of collected and observed failure. The reliability of solder materials can be statistically estimated using either 'nonparametric' methods or 'parametric' methods. The former statistical methods do not require any assumption concerning the identity or the form of the life distribution. The computation and manipulation of the methods are easier. These methods are generally applied where no potentially confining restrictions on behavior are assumed and the choice of life distribution model is difficult. However, the estimated reliability contains less information since no inferences about the identities of the hazard or distribution functions is provided. Parametric statistical methods, on the contrary, start with the assumption that the form of life distribution is known. The choice of life distribution model is based on experience or knowledge about the specimen or product. Once the assuming of life distribution model, parameters are estimated. For solder materials, Weibull distribution is widely assumed to characterize fatigue life.

Named for its developer, Waloodi Weibull, Weibull distribution was first proposed to describe the specimen strength of tensile test. Subsequent research revealed that the distribution provides a reasonable model for the life lengths of many devices, especially electronic products. The most general Weibull distribution is expressed in the three-parameter form:

$$F(t) = 1 - e^{-\left(\frac{t-\delta}{\theta-\delta}\right)^{\beta}} \qquad 2\text{-}14$$

where δ is a minimum-life parameter. Before time δ, no failure is supposed to occur. Since δ is simply a coordinate location parameter, the Weibull distribution can be simplified as the two-parameter form:

$$F(t) = 1 - e^{-\left(\frac{t}{\theta}\right)^{\beta}} \qquad 2\text{-}15$$

where the parameter θ is called scale parameter, which determines the range of dispersion. Note the value of the distribution at $t=\theta$ is independent of the other parameter β, so θ is also named as 'characteristic life'. The parameter β is the shape parameter, which determines the relative shape of the distribution. The shape of Weibull PDF is distinguished differentiable with various shape parameter β. The value of shape parameter β provides informative insight into the behavior of failure process, as is shown in Figure 2-20. Table 2-3 summarizes the property of failure process with most commonly used shape parameters.

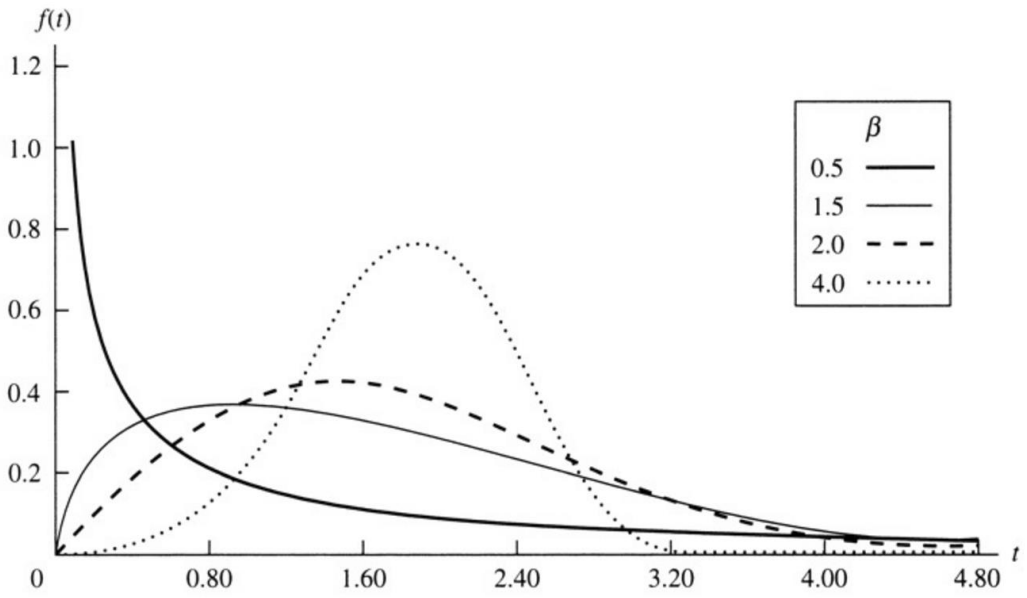

Figure 2-20 PDF of Weibull distribution with various shape parameters

Table 2-3 Property of failure process for given shape parameters

Value	Property
0<β<1	Decreasing Failure Rate
β=1	Exponential Distribution (Constant Failure Rate)
1<β<2	Increasing Failure Rate - Concave
β=2	Rayleigh Distribution (Linear Failure Rate)
β>2	Increasing Failure Rate - Convex
3<=β<=4	Approaches Normal Distribution

Chapter 3 Literature Review

3.1 Introduction

Reliability has become part of our everyday life in an implicit way – most people recognize the fact but not always fully perceive the implications of reliability. The equipment, manufactured products, and fabricated infrastructure that contribute substantially to improve quality of daily life actually have finite longevity. With respect to electronic products, reliability is subdivided into wafer level reliability, chip level reliability, and board level reliability, corresponding to hierarchy of electronic packaging as mentioned in Section 1.1. Specifically, this dissertation focuses on board level reliability, which is also known as interconnection reliability. Reliability of interconnections, or say solder joints, is evaluated by a number of reliability tests, such as thermal cycling test, drop test, fatigue test, etc., as mentioned in Section 2.5. Failure mechanism of solder joints differs significantly with a variety of reasons, including solder material, solder mask, and service environment. During a product life cycle, solder joints inside the electronic package are exposed to an environment of thermal-mechanical fatigue (temperature excursions, vibration, drop, shock). A scientific reliability research of solder joints can be conducted by ALT, which includes standard sample preparation, designed experimental setup, and flexible control variate method.

3.2 Accelerated Thermal Cycling Test

The majority of fatigue failures of solder joints in surface mount assemblies is due to the CTE mismatch induced damage. For near-eutectic SAC alloys, the Sn phase grows rapidly with a dendritic growth morphology during the solidification process, characterized by copious branching. Under thermal cycling, SAC solder joints are

subject to cyclic thermomechanical strain. The recrystallization of Sn phase in the higher deformation regions results in the production of a much small grain size, which causes grain boundary sliding and diffusion in these recrystallized regions and leads to extensive grain boundary damage. The damage accumulates to form fatigue crack initiation and then the crack grows along the recrystallized Sn grain boundaries [43][44]. To date, a number of studies have confirmed the effect of surface finish on the recrystallization of Sn in SAC alloys. Mattila et al. [45] reported that the incubation time for recrystallization on OSP surface finish is shorter than that on Ni/Au (ENIG) surface finish because of the large primary Cu_6Sn_5 particles. The addition of Ni to SAC solder joints, on contrary, has been proved to suppress grain growth after recrystallization, leading to increased reliability. A significant analysis and discussion on the recrystallization behavior of SAC solder joints was presented by Sundelin et al. [46], finding that recrystallization nucleates at the locations where the strain is concentrated during thermomechanical fatigue, i.e. in the neck region and in the vicinity of voids. Besides, it's found that solder joints with hypoeutectic composition tend to recrystallize more readily than joints with eutectic or hypereutectic composition.

The addition of bismuth to SAC-based pastes has been studied by different research groups and the results indicates improved fatigue resistance and mitigated aging effect [47][48][49][50][51]. Liu et al. [47] reported that Bismuth increases tensile strength of solder alloy, and thus improves endurance of stress and prevents deformation during thermal cycling. Bismuth concentration effect at the interface of IMC improves modulus and hardness to ensure better thermal fatigue properties. Solderability was also found to be improved with the addition of Bismuth by Zhang et al. [48].

Effect of surface finish in thermal cycling was also widely investigated. Akkara et al. [52] carried out a number of investigations into reliability of doped solder alloys and

effect of surface finish in thermal cycling, concluding that Bismuth slows down the adverse effect of aging because Bismuth atoms stay in the Sn solid solution and create distortion to the crystalline cell structure which stops the movement of dislocations. ENIG surface finish was found to have the best reliability owing to its double layer protection, compared with OSP surface finish and ImAg surface finish [53].

3.3 Drop Test

Portable devices such as cell phones are prone to accidental drops during handling due to the preferred slim design and tiny size. Survey commissioned by T-Mobile indicates that 29% of cell phone failures were from accidental drop. However, cell phone manufacturers try to improve this situation by using materials that could absorb more energy on impact and by taking efforts to have better housing designs, thereby increasing the device price and making the device heavier, rather than addressing the main issue to improve the reliability of solder joints. Chung et al. [54] investigated the reliability of BGA components in drop test and the results show that thinner BGA components defects more thus has shorter characteristic life, and the failure mode mostly occurs at the most outer solder joints.

The desired feature of portable devices to provide reliable lead-free solder joints under both thermal cycling and drop impact loading conditions are facing challenging since the developed SAC alloys, which provide good thermal cycling reliability, have poor drop reliabilities. SAC105 solder alloy shows better performance than SAC305 under drop loading conditions, yet reversed trending is observed for thermal cycling test [55]. To further improve the drop reliability, micro-alloying elements are added into the solder alloys. Low temperature SAC alloy with Ca or Ce exhibits softer intermetallic layer ($CaSn_3$, $CeSn_3$), which are characterized by void formation nucleation in the IMC

and reduction of strain localization along with Cu_6Sn_5 that results in enhanced ductility of solder alloy [56]. In addition, Sn-Bi solder alloys containing small amounts of elements such as Zn can significantly enhance the ductile property. Moreover, it was found that the addition of elements such as 0.5 wt.% Zn (Zinc), 1.0 wt.% Ag (Silver), or 0.5 wt.% In (Indium) and Nickel (Ni) to Sn-Bi baseline increased the average grain size of Sn-Bi, resulting in the longer grain boundaries [57][58][59]. Therefore, the ductility is improved due to the high occurrence of grain boundary sliding phenomenon of crystals within large grains.

3.4 Fatigue Test

Although the principle aiming of applying solder joints is to provide both electrical connections and mechanical attachments, it is the latter that generally gives cause for concern. Fatigue failure is one of the most common failure modes in realistic manufacturing, test, handling and service conditions. Stronger materials that could resist more fatigue damage, would result in an unacceptable change in failure mode - form ductile to brittle, with failures occurring in the component body or in the substrate rather than in the solder [60].

In order to predict the fatigue life of an electronic component, accelerated isothermal cycling tests are generally conducted in two manners: stress control mode and strain control mode. Since reliability of electronic assemblies is commonly limited by the fatigue failure of one of the solder joints, research on the fatigue life of individual solder joints has been widely investigated, including different types of solder materials [18], effect of cycling amplitudes, strain rate, surface finish, and aging [61][21][62]. It is found that larger stress amplitude leads to more damage per cycle, thus a faster failure process and decreased fatigue life. Regarding solder materials, it has been revealed that

solder alloy containing both high Bi and high Ag demonstrated better fatigue life than alloys containing single high Bi or high Ag. Su et al. [22] studied the effect of surface finish and pointed out that ENIG surface finish is not as good as OSP and ImAg surface finishes for the reason that brittle failure is prone to occur. Extensive research focused on the variations of amplitude during real service life since Miner's rule overestimates the fatigue life of lead-free solder materials. Data from several studies have identified that variations in cycling amplitude would lead to permanent changes in the rigidity of lead- free solder joints [61][63]. Lower-Ag alloys, which tend to be less fatigue-resistant, are also less sensitive to variations in amplitude [18]. Besides, strain rate has been proven to have non-negligible effects on the solder joint fatigue life in both single and varying amplitude cycling [64]. It is now well established from a variety of studies that cycling with a high strain rate at the mild amplitude and a low strain rate at the harsh amplitude leads to the most damage acceleration and thus the fastest failure [65]. In addition, many recent studies have shown that aging plays a crucial role in the fatigue behavior of solder joints. A significant reduction in the fatigue life and shear strength of solder joints are observed with increased aging time or aging temperature [66].

In strain-controlled test, which is also known as displacement-controlled test or low cycle fatigue test, the fatigue behavior generally follows the Coffin-Manson equation. Kanchanomai et al. [27] studied the effect of strain rate (frequency) and the failure modes under several strain rates. The result indicates that multiple surface cracks predominantly initiated in an intergranular manner along the boundary steps of Sn-dendrite for low strain rate tests, while along the boundaries of sub-grains in Sn-dendrites for high strain rate tests. These multiple cracks would link-up to form macroscopic cracks and propagate to grow up after a certain fatigue cycles. Another study conducted by Kanchanomai et al. [24] considered the effect of temperature in

isothermal tests. Increased plastic strain range and decreased stress range was found with the increasing of temperature. The main deformation mechanism is pipe-diffusion-controlled dislocation climb at elevated temperature. Lee et al. [67] studied the effect of SAC solder joint geometry, finding that hourglass-type solder joints exhibited better fatigue performance than barrel-type joints. Different failure modes were identified when testing the two different geometries. Lee et al. [68] also reported that the addition content of Sb improves the fatigue performance. Sn-Ag-Sb solder with 10.05 wt.% Sb content appears the greatest fatigue life. The plastic strain decreases as Sb content increases. Fu et al. [73] investigated the effect of long-term isothermal aging, reporting that the effect of aging was much more significant within the first few days after correlating with the microstructural changes. It is found that aging causes weakening of dendrite structure and coarsening of IMC layers. Moreover, Park and Lee [74] estimated the fatigue life of BGA solder joints under mixed loading conditions. The result shows that stress-strain responses vary with different loading angles. SAC307 has a longer fatigue life than SnPb at room temperature.

3.5 Solder Doping and IMC Layer

The reliability of solder joints is highly dependent on the formation and growth of IMC layer at the interface. Mainstream lead-free solders, such as Sn-Ag, SAC, Sn-Cu, and Sn-Zn, contain a high amount of Sn, which leads to brittle fracture because of more rapid formation and growth of IMCs [75]. The interfacial reaction of SAC solder and Cu substrate actually includes the formation of IMCs during soldering and the growth of IMCs in the later conditions such as thermal aging. During the aging process, the morphology of the Cu_6Sn_5 phase changes from scalloped to planar. Extended aging time result in the formation of a thin Cu_3Sn layer between the Cu_6Sn_5 layer and the Cu

substrate. The growth of Cu_3Sn layer continues by consuming the Cu_6Sn_5 layer due to the thermodynamic instability of the Cu_6Sn_5 layer ($9Cu + Cu_6Sn_5 \rightarrow 5Cu_3Sn$) [76]. The schematic diagram of IMC growth is shown in Figure 3-1. Excessive growth of Cu_6Sn_5 IMCs reduces the thermal fatigue life, tensile strength, fracture toughness and isothermal shear fatigue life of the solder joint [77]. The Cu_3Sn layer further results in the formation of microvoids [78]. Micro-alloying elements that have beneficial effects on the metallurgy of materials have been widely researched to improve the wettability of solders and refine the microstructure [79][80].

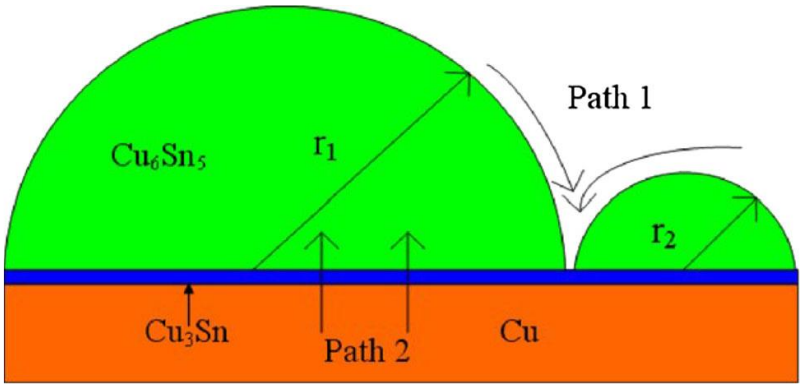

Figure 3-1 Schematic diagram of Cu atom diffusion during solid state aging

Cerium (Ce)

Zhang et al. [81]investigated the effect of Ce on the IMC growth behavior of Sn-3.8Ag-0.7Cu solder. The addition of 0.03 wt.% Ce inhibited the growth of the interfacial IMC. The inhibitory effect of $CuSn_3$ was even more pronounced from the study. Tu et al. [69] also reported the reduced growth rate of interfacial IMC by adding Ce into SAC305 solder. However, there is a lack of evidence that the addition of Ce inhibited the growth of Cu_6Sn_5 in a short time soldering.

Praseodymium (Pr)

An appropriate content of Pr in solders can improve the combined solder properties such as solderability, refine the microstructure, and inhibit the IMC growth rate [83][84][85]. The refined microstructure enhances the mechanical properties of solder joints [86]. Gao et al. [87] reported that 0.05 wt.% content of Pr leaded a 31% reduction of IMC thickness for Sn-3.8Ag-0.7Cu solder. Figure 3-2 depicts the effect of Pr on the microstructure of IMC interface. Pr reacts with Sn to form a Sn-Pr phase, which reduces the activity of the Sn atom. The stabilized $PrSn_3$ IMC particles also act as heterogeneous nucleation sites and accelerates the solidification of the solder [88]. However, excessive content of Pr causes the aggregation of small Pr-containing particles to form large $PrSn_3$ IMCs.

The addition of Pr also results in the growth of Sn whiskers during aging due to the reaction of Pr IMC and oxygen: $4PrSn_3 + 3O_2 \rightarrow 2Pr_2O_3 + 12Sn$. The conductive Sn whiskers could cause electronic short circuits and mechanical damage.

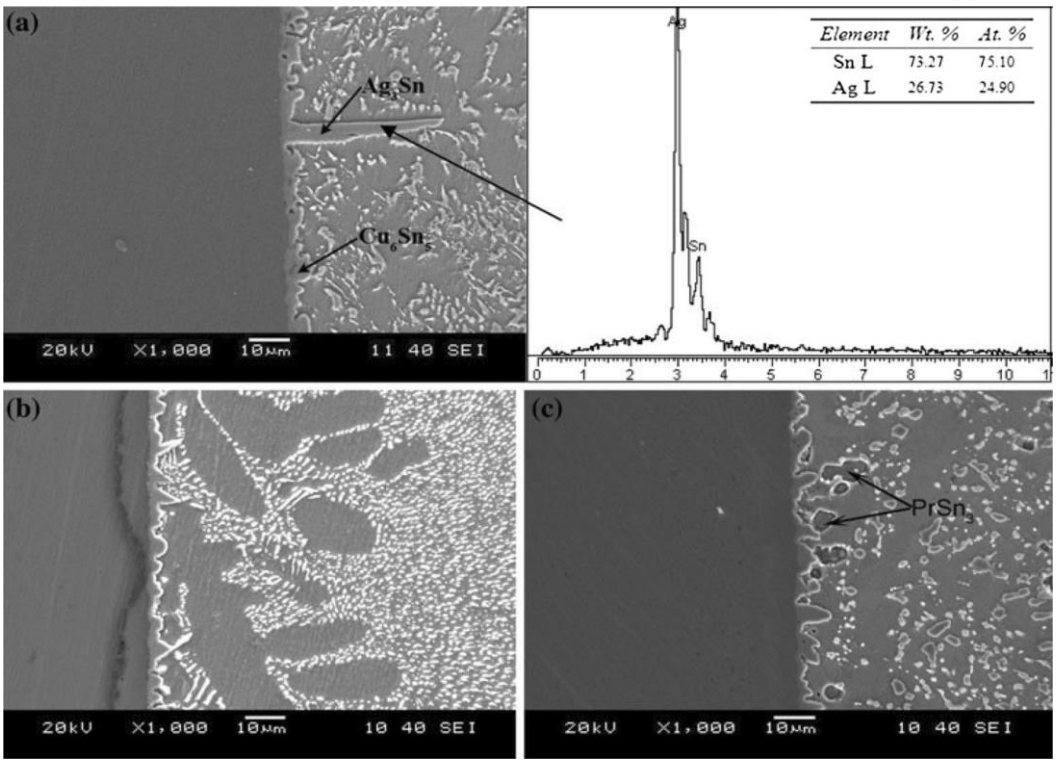

Figure 3-2 Microstructure of the joint interface, (a) SAC/Cu, (b) SAC0.05Pr/Cu, and (c) SAC0.5Pr/Cu

Nickel (Ni)

Two kinds of IMC layers were formed at Sn3.8Ag0.7Cu-xNi/copper after isothermal aging - one $(Cu, Ni)_6Sn_5$ layer adjacent to the SAC solder and one Cu_3Sn layer near the Cu substrate [90]. The radius of the Cu atom (0.128 nm) is quite close to that of the Ni atom (0.125 nm), and both of them are face-centered cubic structures. Ni atoms are able to occupy the Cu atoms in the Cu_6Sn_5 IMC lattice to form $(Cu, Ni)_6Sn_5$ phase. The thermodynamic affinity of Ni-Sn is higher than that of Cu-Sn, resulting in the better stability of $(Cu, Ni)_6Sn_5$ phase than Cu_6Sn_5 [91]. Besides, lower Gibbs free energy of ternary IMC than binary IMC leads to retarded growth of Cu_3Sn layer [92]. The addition of Ni also refines the grain size of IMC layer. Cheng et al. [93] found that 0.05 wt.% Ni addition remarkably enhances the growth rate of Cu_6Sn_5 phase and inhibits the growth rate of Cu_3Sn phase for Sn-1.2Ag-0.5Cu-0.05Ni solder material. The nucleating rate of Cu_6Sn_5 phase is increased, together with the formation of a significant number of small Cu_6Sn_5 phases near the interface. The accelerated reaction speed between Cu and Sn and the accelerated growth rate of Cu_6Sn_5 phase during aging are found owing to the high grain boundary as well as the triple junction density of Cu_6Sn_5 layer.

Tay et al. [94] revealed that Ni nanoparticles and Ni alloy addition function similarly on IMC growth, as is shown in Figure 3-3. Ni nanoparticles also affect the growth rate of IMC layer during reflow and aging.

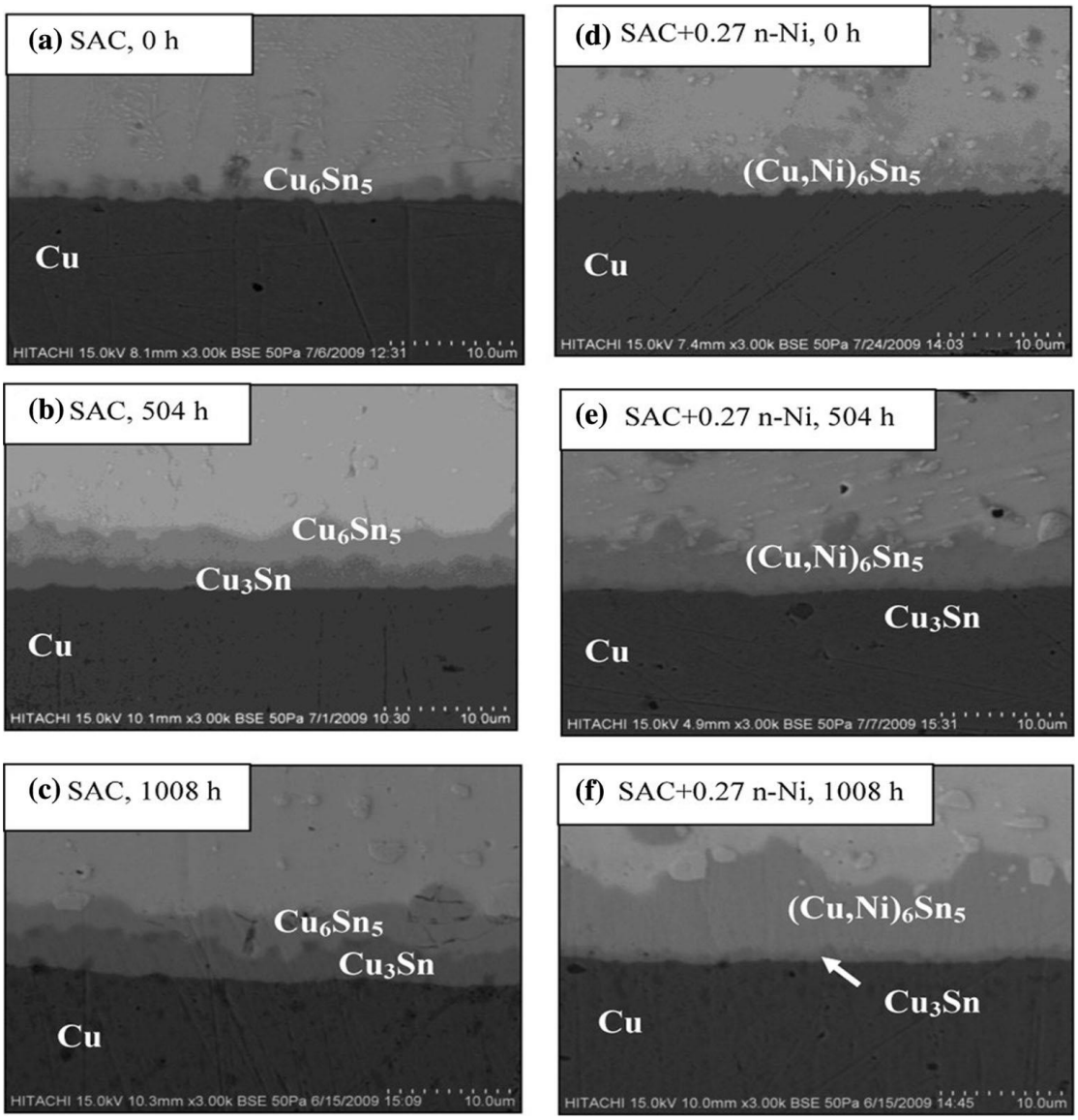

Figure 3-3 SEM backscattered electron micrograph of the solder joint interface with and without Ni nanoparticles

Zinc (Zn)

Many researchers have investigated the effect of Zn addition since Zn can refine the microstructure, reduce the melting temperature, and enhance the creep lifetime [95][96]. Cho et al. [97] suggested 0.4 wt.% of Zn addition into solder materials to inhibit the growth of Cu_3Sn phase. The addition of Zn suppressed the IMC layer and accumulated at the junction of Cu and Cu_3Sn to form a Cu-xZn compound. Cu atoms in the Cu-xZn alloy exhibit less activity thus lower diffusion rate of Cu atoms and lower growth rate

of Cu_3Sn. Mayppan at al. [98] investigated the interface of SAC solder alloys after sintering at 150 °C for 2 hours. Cu_6Sn_5, Cu_3Sn, β-Sn, Cu-Zn, and Ag_3Sn phases were found in XRD observation. The total IMC growth rate of SAC, SAC-0.1Zn, SAC-0.4Zn, SAC-0.7Zn was 6.25×10^{-14}, 4.41×10^{-14}, 4.00×10^{-14}, 5.76×10^{-14} cm^2/s, respectively, indicating the optimal Zn content of 0.4 wt.%.

With more content of Zn (1.5 wt.%), Cu_5Zn_8 IMC nucleates at the interface and then flake off to form a barrier layer which hinders the diffusion of Cu and Sn [99][100][101]. El-Daly et al. [102] reported that the small $(Cu, Ag)_5Zn_8$ IMCs formed in low silver Sn-2.0Ag-0.7Cu solder alloys inhibits the growth rate of Cu_6Sn_5 and Ag_3Sn IMCs because they have a dispersion strengthening effect. With higher Zn content (3.0 wt.%), less Ag_3Sn particles are formed, causing slight strength deterioration of solder alloys.

Antimony (Sb)

The addition of Sb to SAC solder alloys can also suppress the IMC growth rate and provide finer grain size. Tang et al. [103] identified the diffusivity of Cu atomic to be the lowest with around 1.0 wt.% Sb concentration in SAC305-*x*Sb solder joints. With the addition of Sb, the average grain size of the scallop-like Cu_6Sn_5 was reduced from 14.2 μm to 11.9 μm. The result is in line with the findings of Chen et al. [104], who observed more uniformly distributed IMC crystal grains after adding Sb. The reason lies in the fact that Sb is more affinitive to Sn, which results in the formation of Sn-Sb compounds and the decreased growth rate of Cu-Sn IMC. Besides, the Sn-Sb IMC particles provide heterogeneous nucleation sites for Cu_6Sn_5, thus finer and more uniform crystal grains.

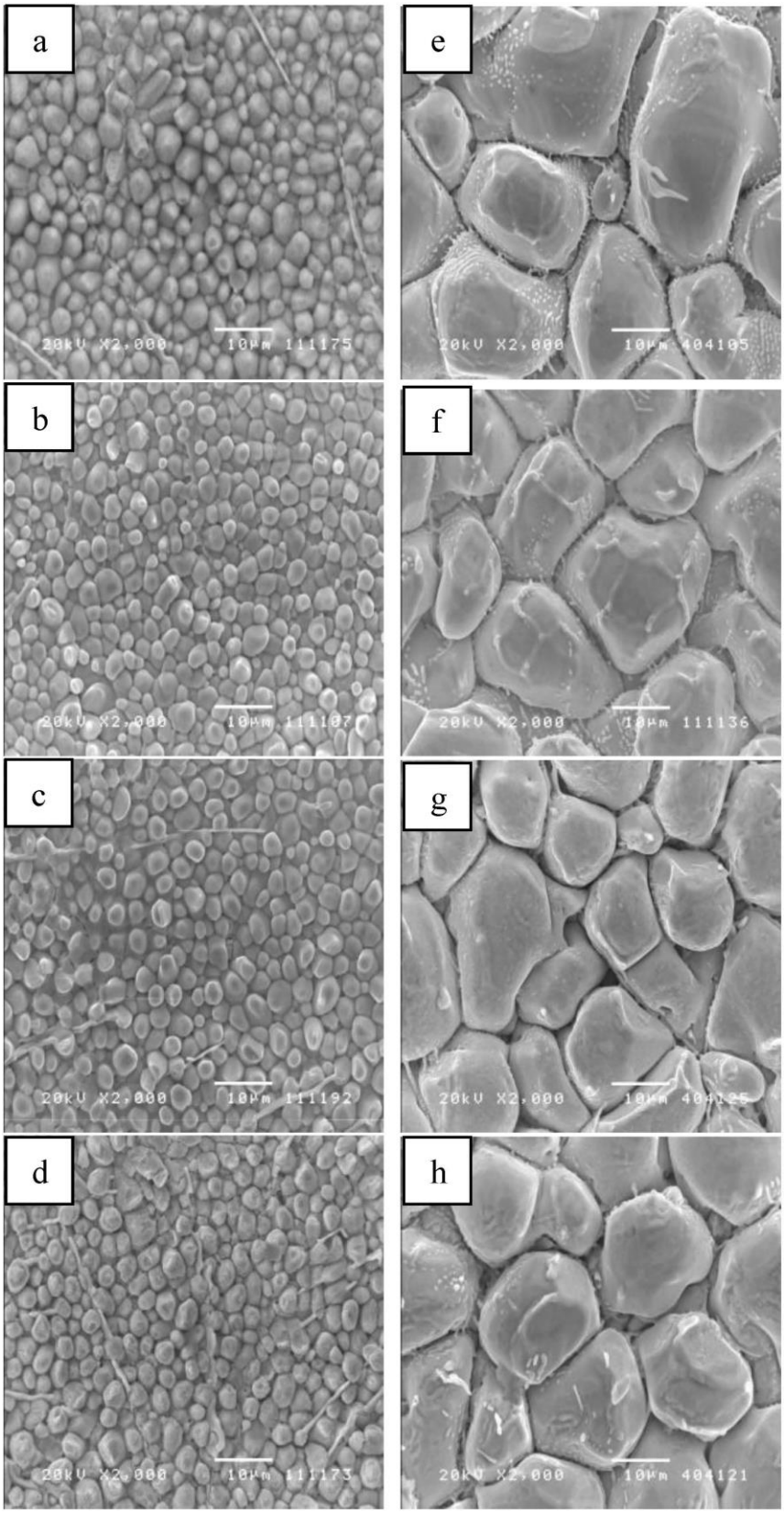

Figure 3-4 SEM micrographs of top view of IMC layer of Sn-3.5Ag-0.7Cu-xSb solder joints reflowed for 48s (a, b, c, d) and 7200s (e, f, g, h): (a, e) x=0, (b, f) x=0.5, (c, g) x=1.0, and (d, h) x=2.0

Bismuth (Bi)

It is reported that 3 wt.% Bi addition to SAC solder alloys significantly increase the creep resistance by 126.1 times and the creep life by 23.7 times [105]. The addition of Bi also retards the propagation of IMCs and reduces the density of cavities during aging, as is shown in Figure 3.4 [106]. Solid solution of Bi causes lattice distortion in the Sn-rich phase, affecting the self-diffusion of the atoms and migration of interstitial impurities [107]. Little effect of Bi addition on Cu_3Sn layer was observed, while an apparent inhabitation effect on the growth rate of Cu_6Sn_5 has been reported by Qi et al. [108].

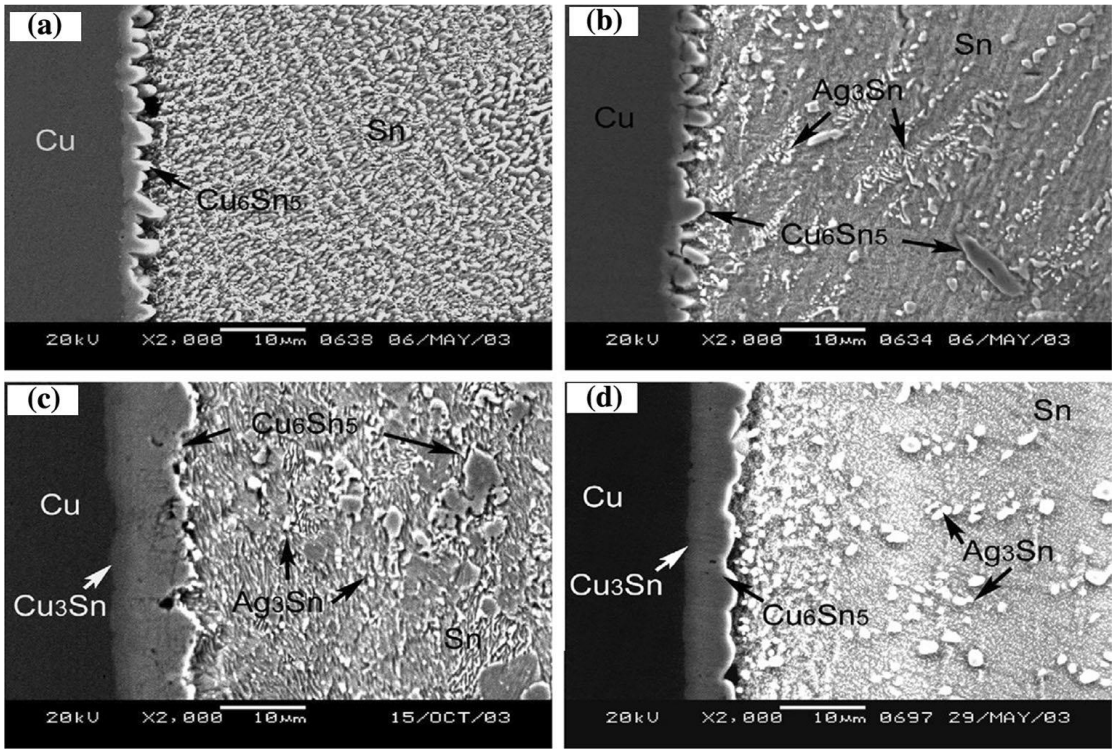

Figure 3-5 Microstructure evolution of SAC/Cu (a, c) and SAC-3Bi/Cu (b, d) solder joints: (a, b) as soldered; (c, d) aged for 1000 h

Li et al. [109] studied the growth rate of IMCs in SAC305 solders with different amount of Bi addition (1.0 - 5.0 wt.%), finding the slowest IMC growth rate in SAC305-1.0Bi. Ag_3Sn, Cu_6Sn_5 and Bi-rich particles on the Cu_6Sn_5 grain boundary retarded the

diffusion of Cu and Sn atoms passing through the layer [110]. The phenomena are also called grain boundary pinning mechanism.

3.6 Fatigue Life Prediction Model

ASTM International defines solder joint failure as “the process of progressive localized permanent structural change occurring in a solder joint subjected to conditions which produce fluctuating stresses and strains at some points which may culminate in cracks or complete fracture” [111]. With the understanding of basic failure mechanism and proper assumptions, many researchers have proposed models to predict the fatigue life of solder joints since the early 1960s. These models are categorized into four groups based on the factor hypothesized to contribute more to fatigue damage, which are damage accumulation-based models, plastic strain-based models, creep damage-based models, and energy-based models.

3.6.1 Damage Accumulation-Based Fatigue Models

As mentioned in Section 2.4, applied stress or load below the material fatigue limit causes plastic deformation and infinite fatigue life. With increased stress or load, damage occurs and accumulates in the material until fatigue failure. Depending on whether the damage per cycle is dependent of load, damaged accumulation-based models are classified as linear damage cumulative theory and nonlinear damage cumulative theory. The former one is usually applied assuming the damage caused by a stress cycle is independent of load sequence and the ratio of damage accumulation is independent of stress level. Main benefits of using linear damage models are its simplicity and approximately accuracy [112].

Among many of the linear damage models, the Miner's rule has been the most popular one to predict the fatigue life of solder joints under cyclic loading test with varying stress amplitudes [113]

$$\sum_{i=1}^{k} \frac{n_i}{N_i} = 1 \qquad 3\text{-}1$$

where n_i is the number of cycles accumulated at a given stress amplitude and N_i is the number of cycles to failure at the same stress amplitude. The sum of the fractional damage from 1 to k stress amplitudes equals 1.

However, the Miner's linear damage rule is inevitable to miscalculate fatigue life of solder alloys due to the assumption that the cumulative damage per cycle is independent of load. Hamasha et al. [114][115] have proved that solder materials are stress dependent, which means the accumulated damage after a specified fraction of fatigue life varies for different stress amplitudes. Besides, previous applied stress could change the way of damage accumulation such as the formation of microcracks. Zhang et al. [116] carried out a multitude of investigations into damage accumulation and life prediction with load below fatigue limit. According to their result, low stress amplitude below the fatigue limit still contributes to damage accumulation depending on the existing damage. The more initial damage, the more effect. A Cauchy MF based damage model was proposed to provide the most satisfying prediction, which follows nonlinear damage rules to correlate the damage accumulation with loading parameters. Corten and Dolan [117] suggested a modified nonlinear accumulation damage model to account for the effect of load interaction during fatigue cycling. In the model, damage can propagate at both high stress amplitudes and low stress amplitudes

$$\sum_i \left(\frac{n_i}{N_1}\right)\left(\frac{\sigma_i}{C}\right)^d = 1 \qquad 3\text{-}2$$

where N_1 is the fatigue life at the highest stress amplitude σ_1, n_i is the number of cycles at stress amplitude σ_i, and d is the material constant.

Further research revealed a higher exponent d at a higher stress amplitude, which is supposed to be constant all the time. This indicates modification of d in Corten-Dolan's model. Zhu et al. [118] proposed a dynamic Corten-Dolan's equation, where exponent d is expressed as a function of stress amplitude

$$d(\sigma_i) = \mu \frac{{\sigma_i}^{\lambda} \delta_f^{1-\lambda}}{\sigma_i} \qquad 3\text{-}3$$

where λ is a load interaction factor, μ is material constant, δ_f is initial static strength, σ_i is the ith level stress amplitude. The fatigue life of Corten-Dolan's model can be given as

$$N_g = \frac{N_1}{\sum_{i=1}^{k} \alpha_i \left(\frac{\sigma_i}{\sigma_1}\right)^{d(\sigma_i)}} \qquad 3\text{-}4$$

where N_g is the number of cycles to failure and N_1 is the number of cycles to failure at σ_1.

Combining Miner's rule with Corten-Dolan's model, Hamasha et al. [115] proposed a modified model to predict fatigue life of two alternating amplitudes

$$\sum_{i=0}^{s} f(i) \frac{n_{mi}}{N_m} + \frac{n_{hi}}{N_h} = 1 \qquad 3\text{-}5$$

where n_{mi} is the number of cycles at low amplitude, N_m is the life at low amplitude, n_{hi} is the number of cycles at high amplitude, N_h is the life at high amplitude. The amplitude factor $f(i)$ is the hysteresis energy in the low amplitude cycles after

exposure to i sets of n_{hi} high amplitude cycles divided by the hysteresis energy in the low amplitude cycles before exposing to high amplitude cycles.

3.6.2 Plastic Strain-Based Fatigue Models

Electronic assemblies are exposed to cyclic temperature changes in real service life. CTE mismatch between electronic components and substrate materials results in the plastic deformation of interconnected solder joints. Low-cycle fatigue failure caused by plastic deformation is one of the dominant factors that affect the reliability of electronic assemblies. Many models have been proposed to predict the fatigue life as a function of plastic strain, in which Coffin-Manson model [119] is most widely used:

$$N_f^m \Delta\varepsilon_p = C \qquad 3\text{-}6$$

where N_f represents the fatigue life, $\Delta\varepsilon_p$ is the plastic strain range, m is the fatigue exponent, and C is the ductility coefficient.

Solomon et al. [120] proposed a similar fatigue prediction model which relates the plastic shear strain to the fatigue life for SnPb solder joints at four temperature levels ranging from -50°C to 125°C, finding no obvious difference observed between fatigue behavior at testing temperatures:

$$\Delta\gamma_p N_f^\alpha = \theta \qquad 3\text{-}7$$

where $\Delta\gamma_p$ is the plastic shear strain range, α and θ are constants independent of testing temperature.

Further studies investigated the effect of cycling frequency. Shi et al. [121] have proved the variance of fatigue life with differentiated frequency – the fatigue life decreases with the decreasing of frequency at a low rate above 10^{-3} Hz, drastically decreasing ratio of fatigue life appears with higher frequency such as from 10^{-3} to 10^{-4} Hz. To

include the frequency factor in the Coffin-Manson model, the frequency-modified Coffin-Manson model was proposed to predict the fatigue life of solder alloys with specified cycling frequency:

$$[N_f v^{(k-1)}]^m \Delta\varepsilon_p = C \qquad 3\text{-}8$$

where *v* is the frequency, and *k* is the frequency exponent.

Engelmaier et al. [122] incorporated parameters such as cyclic frequency, solder, and substrate temperature into the Coffin-Manson model, known as the Engelmaier model:

$$N_f = \frac{1}{2}\left(\frac{\Delta\gamma}{2\varepsilon_f'}\right)^{\frac{1}{c}} \qquad 3\text{-}9$$

where N_f is the mean cycle to failure, $\Delta\gamma$ is the cyclic shear strain range, ε_f' is the fatigue ductility coefficient, and c is the fatigue ductility exponent, which can be calculated by solder material, cycling frequency, and mean temperature.

Norris and Landzberg [123] proposed another fatigue life prediction model based on Coffin-Manson model, which includes three factors: the maximum temperature T_{max}, the frequency of temperature cycle f, and the thermal excursion range ΔT. The ratio of fatigue life in field N_{field} and test N_{test} is defined as acceleration factor:

$$AF = \frac{N_{field}}{N_{test}} \qquad 3\text{-}10$$

$$AF = \left(\frac{\Delta T_{test}}{\Delta T_{field}}\right)^a \times \left(\frac{f_{field}}{f_{test}}\right)^b e^{[(Ea/k)(\left(\frac{1}{T_{max}},field\right)-\left(\frac{1}{T_{max}},test\right))]} \qquad 3\text{-}11$$

where Ea is the activation energy, k is Boltzmann's constant, a and b are exponent parameters of different solder alloys.

3.6.3 Creep Damage-Based Fatigue Models

The constant load below yield strength applied to a material would induce the occurrence of time-dependent deformation, which causes material deformation over time to reduce load applied. The creep behavior of solder joints is normal when exposed to a constant elevated temperature – the closer to the melting point of solder alloy, the heavier the creep. It has been found that fatigue endurance is significantly reduced when considering both fatigue effects and creep effects.

Syed et al. [124] proposed a new life prediction model by combining Monkman-Grant equation [125] with Miner's rule [126]:

$$N_f = \left(\frac{E_{cr}}{C}\right)^{-1}_{per\ cycle} \tag{3-12}$$

where E_{cr} is the accumulated creep strain for the whole cycle, and C is the creep ductility for the creep mechanism. If there are two creep mechanisms, accordingly the equation becomes:

$$N_f = \left(\frac{E_1}{C_1} + \frac{E_2}{C_2}\right)^{-1}_{per\ cycle} \tag{3-13}$$

Based on Eq. (3.13), fatigue life can also be predicted based on both creep strain and creep energy density [127] . Creep strain-based model is:

$$N_f = (C_{\mathrm{I}}\varepsilon^{\mathrm{I}}_{acc} + C_{\mathrm{II}}\varepsilon^{\mathrm{II}}_{acc})^{-1} \tag{3-14}$$

where N_f is the number of cycles to failure. C_{I} and C_{II} are constants related to creep mechanisms. $\varepsilon^{\mathrm{I}}_{acc}$ and $\varepsilon^{\mathrm{II}}_{acc}$ are accumulated creep strain per cycle.

Assuming damage accumulated in the solder joints is mainly from the steady-state creep strain accumulation, the energy density model is proposed:

$$N_f = (W_{\mathrm{I}} w_{acc}^{\mathrm{I}} + W_{\mathrm{II}} w_{acc}^{\mathrm{II}})^{-1} \quad \text{3-15}$$

where W_{I} and W_{II} represent constants related to dissipated creep energy density. w_{acc}^{I} and w_{acc}^{II} are accumulated creep energy density per cycle for each creep mechanism.

Manson et al. [128] provided a creep-based fatigue prediction method – where any one cycle of a completely reversed inelastic strain is partitioned into three out of four strain range components: $\Delta\epsilon_{pp}$ - completely reversed plasticity, $\Delta\epsilon_{pc}$ - tensile plasticity reversed by compressive creep or $\Delta\epsilon_{cp}$ – tensile creep reversed by compressive plasticity, and $\Delta\epsilon_{cc}$ – completely reversed creep. The first subscript letter refers to the type of strain imposed in the tensile portion of the cycle, and the second subscript letter refers to the type of strain imposed during the compressive portion of the cycle.

Yoshiharu et al. [129] proposed a partitioning equation based on Manson's method, where $\Delta\varepsilon_{pp}$ is time-independent plasticity reversed by time-independent plasticity, $\Delta\varepsilon_{pc}$ is time-independent plasticity reversed by creep, $\Delta\varepsilon_{cp}$ is creep reversed by time-independent plasticity, and $\Delta\varepsilon_{cc}$ is creep reversed by creep:

$$\Delta\varepsilon_{ij} = A_{ij} \times N_{ij}^{-m_{ij}} \quad \text{3-16}$$

where subscript i and j corresponds to p and c, respectively. N_{ij} is the cyclic life corresponding to partitioned strain range $\Delta\varepsilon_{ij}$ and m is the slope of Coffin-Manson plot. By utilizing Miner's rule, the creep-fatigue life is given by:

$$\frac{1}{N_f} = \frac{1}{N_{pp}} + \frac{1}{N_{cc}} + \frac{1}{N_{cp}} + \frac{1}{N_{pc}} \quad \text{3-17}$$

3.6.4 Energy-Based Fatigue Models

During cyclic stress-strain test, damage is accumulated in the solder joint until to some point large enough to cause a fracture or crack. The damage can be indicated using hysteresis energy assuming that energy is absorbed cycle by cycle from the plastic deformation. The idea of developing energy-based model comes from the fact that energy reflects the change of both stress and strain, thus a better parameter to be correlated with fatigue life than creep or plastic strain [130].

One of the earliest fatigue life prediction models was proposed by Stowell et al. [131], relying on the assumption that the energy to the fracture of a specific material (W_f) is a known value, which can be calculated by summing up the energy losses of each cycle (W_m) from the static stress-strain hysteresis loop. The model is given by:

$$N_f \times W_m = W_f \tag{3-18}$$

Kujawski et al. [132] proposed a model to predict the fatigue life in both low and cycle fatigue, assuming the strain energy density as a constant damage parameter:

$$\Delta W_t = W_f \, (2N_f)^d + \Delta W_{end} \tag{3-19}$$

where ΔW_t is the total cyclic energy that can also be expressed by $\Delta W_t = (1/2)\Delta W + (1/2)\Delta\sigma\Delta\varepsilon$ – the combination of the enclosed cyclic plastic strain energy and the linear elastic energy. ΔW_{end} is the elastic strain energy density. W_f and d can be acquired by fitting the equation.

Oldham et al. [133] proposed a similar creep-fatigue life prediction method by assuming an "intrinsic material property" $E_{intrinsic}$, the average of the hysteresis energy density. Total number of cycles to failure N_f can be expressed by:

$$N_f = \frac{E_{intrinsic}}{w} \quad \text{3-20}$$

where w is the energy density dissipated in one cycle.

The most widely used model to predict the fatigue life of solder joints is Morrow's energy model [134]:

$$N_f^m W_p = C \quad \text{3-21}$$

where m is the fatigue exponent and C is material ductility coefficient. W_p represents the plastic strain energy density of steady state.

Solomon et al. [135] introduced a frequency modified energy model based on Morrow's energy model:

$$[N_f v^{(k-1)}]^m \frac{W_p}{v^n} = C \quad \text{3-22}$$

where v is frequency, and k is frequency exponent determined from the relationship between fatigue life and frequency. n is another frequency exponent determined from the relationship between strain energy density and frequency.

Shi et al. [136] further proposed a modified Morrow energy model that includes both the effect of frequency and temperature. A temperature-dependent material parameter should be introduced since material ductility coefficient C is more dependent on temperature. It was found the increasing of temperature would result in the decrease of C without the temperature-dependent parameter. To maintain the constancy of C, the material parameter should decrease with the increasing of temperature. Interestingly, flow stress of the material σ_{flow} was found to decrease with the increasing of temperature. The modified model is thus given as:

$$[N_f v^{(k-1)}]^m \frac{W_p}{2\sigma_{flow}} = C \qquad \text{3-23}$$

Chapter 4 Experimental Methodology

4.1 Introduction

The reliability of electronic assemblies is found to be limited by the fatigue life of solder joints. Commonly, fatigue properties of solder materials are investigated using large bulk samples without considering the effects of IMC layer and surface finish. To better quantify the fatigue behavior of solder alloys in real service life, various methods, customized test vehicles, and special experimental setups were designated to a set of proposed test plans. This chapter mainly includes four topics: test vehicle preparation, experimental setup, test plan, and failure analysis.

The first topic demonstrates the test vehicle design and assembly. Two different types of customized test vehicles were manufactured to accomplish the designated goals in the test plan. One of the types was individual solder joints with specific surface finish. The other type was customized sandwich test vehicle with 3×3 solder joints connected between the two substrates. A brief sample assembly process is also introduced.

The second topic tells the experimental setup used in all the tests, including testing profiles, equipment, and customized fixtures. Differentiated testing profiles and fixtures were designed to satisfy the requirements of each testing method. Each experimental setup is introduced in detail in Section 4.3.

The third topic identifies the test plans for each of the four studies. A test matrix, including testing solder material, surface finish, testing environment, and replicates, is developed in each study to characterize the fatigue behavior of our test vehicles.

The last topic introduces sample preparation procedures prior to microscopic examination. Further inspection was completed by SEM and EDS to figure out the microstructure and failure modes in each condition.

4.2 Test Vehicle Preparation

4.2.1 Individual Test Vehicle

Test Board Design

The test board consists of FR-4 glass epoxy substrates and full arrays of individual solder joints. One test board can be split into 12×10 smaller package pieces via the designed v-scoring divisions. Each smaller package piece (test vehicle) is full array of 0.6-mm Solder Mask Defined (SMD) solder joints with size 10mm ×10mm. The pitch size of solder joints is 3mm and the opening of SMD pad is 22 mils. There are nine solder joints arrayed on each test vehicle. The same surface finish is applied on each test board – either OSP surface finish or ENIG surface finish.

Solder Materials Selection

Four commercially available lead-free solder alloys were provided by NXP semiconductors. Table 4.1 summaries all the test solder materials as well as surface finish applied. Micro-alloying elements mainly include Bi and Sb. The schematic of the individual test vehicle and the cross-section view are shown in Figure 4-1.

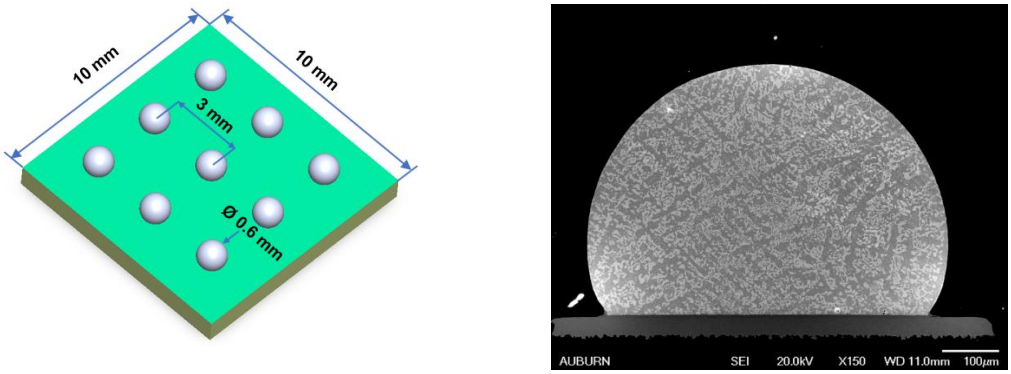

Figure 4-1 Schematic of the test vehicle and the cross-section view

Table 4-1 Solder material selection for study 1

Solder Materials	Compositions	Solidus Line	Liquidus Line
Sn-Ag	Sn-3.5Ag	221	223
SAC-Bi	Sn-3.0Ag-0.8Cu-3.0Bi	205	215
Sn58Bi	Sn-58Bi-0.5Sb-0.15Ni	139	145
Sn42Bi	Sn-42Bi-0.5Sb	138	151

Test Vehicle Assembly

The assembly process was completed in the Electronic Packaging Lab, including the following steps:

1) Alignment of #1 stencil on the top of solder mask, leaving copper pads exposed through apertures of #1 stencil, as shown in Figure 4-2(a).

2) Tacky flux was printed on the copper pad using the squeegee with desired squeegee angle, print speed, etc.

3) # 2 stencil was aligned on top of the PCB with wider apertures, as is shown in Figure 4-2(b).

4) Solder spheres were brushed to fill into the apertures of #2 stencil. Each solder sphere would occupy only one aperture. Figure 4-2(c) demonstrates the

schematic after this step. The above processes were completed with DEK Galaxy stencil printing machine, as is shown in Figure 4-3.

5) After inspection, test boards were arranged to reflow in the Vitronics Soltec Refow Oven within a nitrogen environment. Figure 4-4 shows the reflow oven. Two reflow profiles were employed. For SAC-based solders, the reflow profile includes a preheat stage and a peak temperature of 245°C with 45-60s above liquidus, as shown in Figure 4-5; for LTS, a similar reflow profile was utilized but with peak temperature of 170°C.

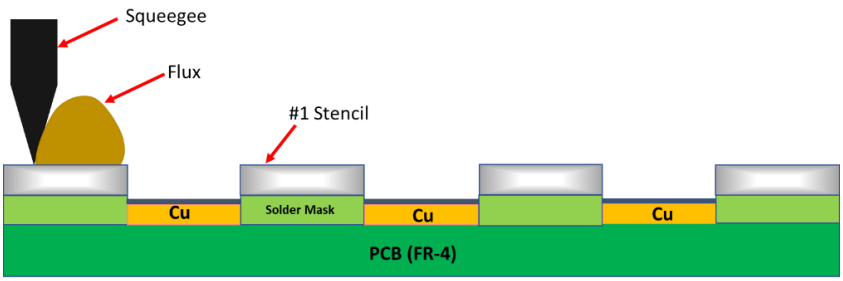

(a) Alignment of #1 stencil

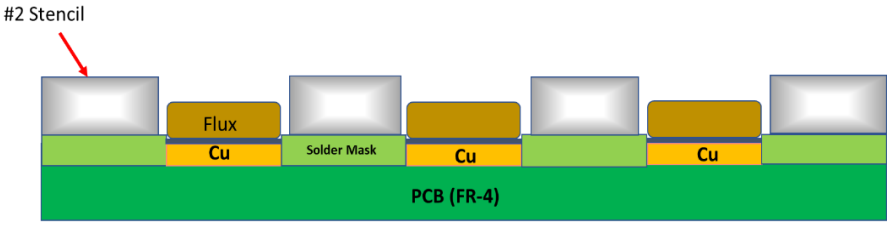

(b) Alignment of #2 stencil

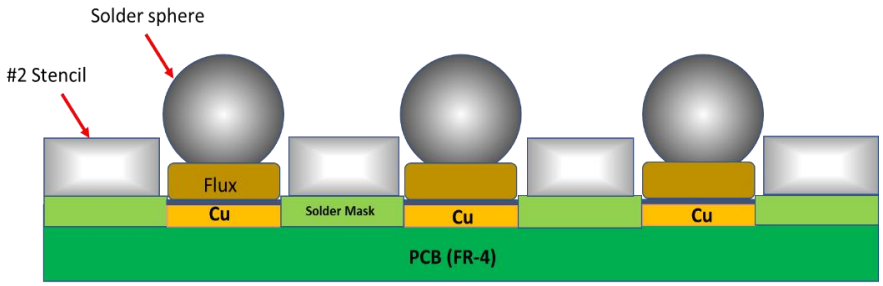

(c) Assemble solder spheres

Figure 4-2 Assembly process of individual solder joints

Figure 4-3 DEK Galaxy Printing Machine

Figure 4-4 Vitronics Soltec Reflow Oven

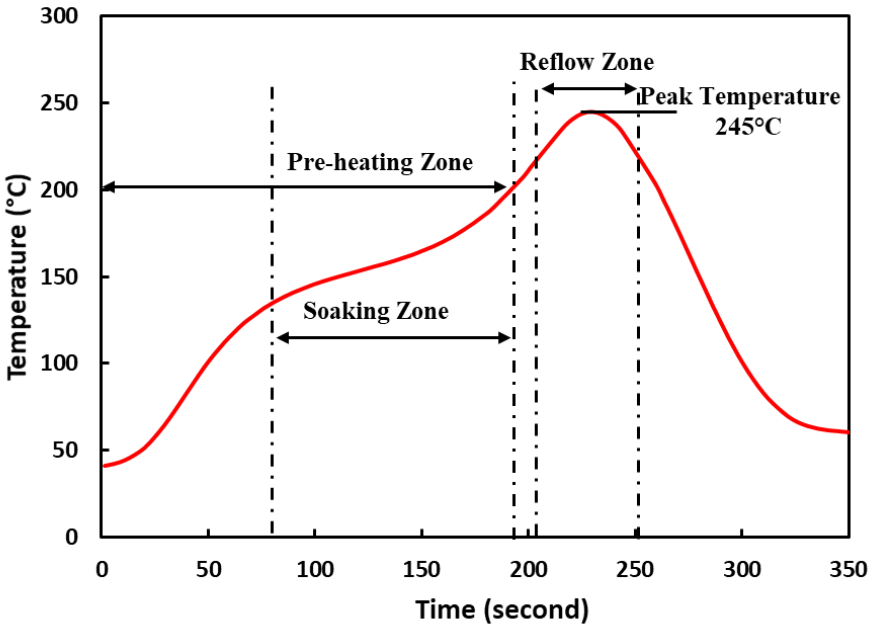

Figure 4-5 Reflow profile of individual solder test board

4.2.2 Sandwich Test Vehicle

Test Board Design

To better represent realistic chips, customized sandwich BGA test vehicles were manufactured, as is shown in Figure 4-6. The test vehicle consists of two FR4 glass-epoxy PCBs and nine interconnected solder spheres. This design is quite similar with the former one: the dimension of the test vehicle is 10mm × 10mm × 1mm, with a 3-mm pitch size. The diameter of the nine solder balls connected between the two substrates is 0.762 mm. The gauge distance between the two substrates is measured around 0.50 mm. Compositions of solder alloys and surface finishes investigated for sandwich test vehicles are listed in Table 4-2. The PCB surface finishes studied in this test were OSP and ENIG, both reflowed on the 0.559 mm solder mask defined (SMD) Cu pads.

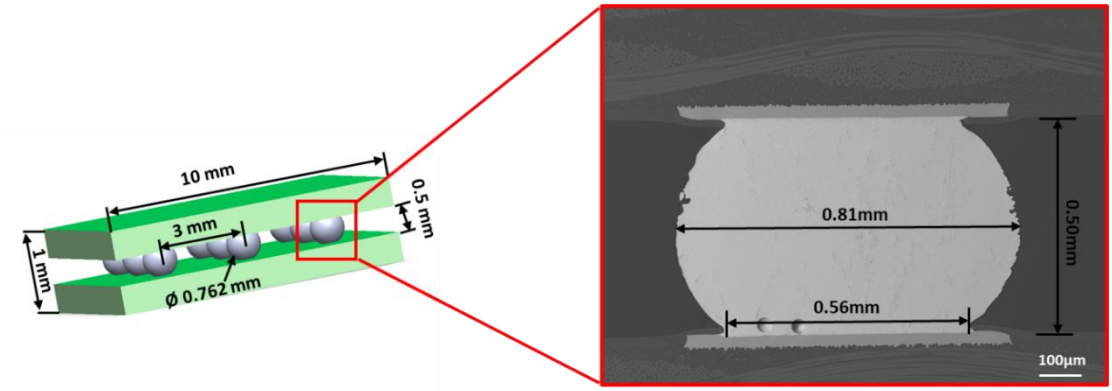

Figure 4-6 Sandwich Test Vehicle

Table 4-2 Solder Joints Composition

Solder Alloy	Compositions	Surface Finish
SAC305	Sn-3Ag-0.5Cu	OSP, ENIG
SnPb	Sn-37Pb	OSP, ENIG
SAC-Q	Sn-3.41Ag-0.52Cu-3.3Bi	OSP, ENIG
SAC-R	Sn-0.92Cu-2.46Bi	OSP, ENIG
SAC-I	Sn-3.5Ag-0.7Cu-3Bi-1.5Sb-0.125Ni	OSP, ENIG

Test Vehicle Assembly

The assembly process was also accomplished in the Electronic Packaging Lab, as is shown in Figure 4-7, which includes the following steps:

1) A stencil made of stainless steel was aligned on the top of solder mask, leaving copper pads exposed through apertures of the stencil.

2) Tacky flux was printed on the copper pad using the squeegee with desired squeegee angle, print speed, etc.

3) Solder spheres were brushed to fill into the apertures of another stencil. Each solder sphere would occupy only one aperture. The flux would temporarily retain the solder spheres in the following steps.

4) Some smaller package pieces were split via the v-scoring divisions. These pieces were then precisely arranged on the other complete PCB boards using the pick-and-place machine, as is shown in Figure 4-8.

5) After inspection, test boards were sent to reflow in the Vitronics Soltec Reflow Oven within nitrogen environment. Different reflow profiles were employed for selected solder alloys. A 242 °C peak temperature profile was utilized for lead-free sandwich test vehicles, as is shown in Figure 4-9. For Sn-Pb specimens, the BGA soler joints were reflow soldered using a 215°C peak temperature profile, indicated in Figure 4-10.

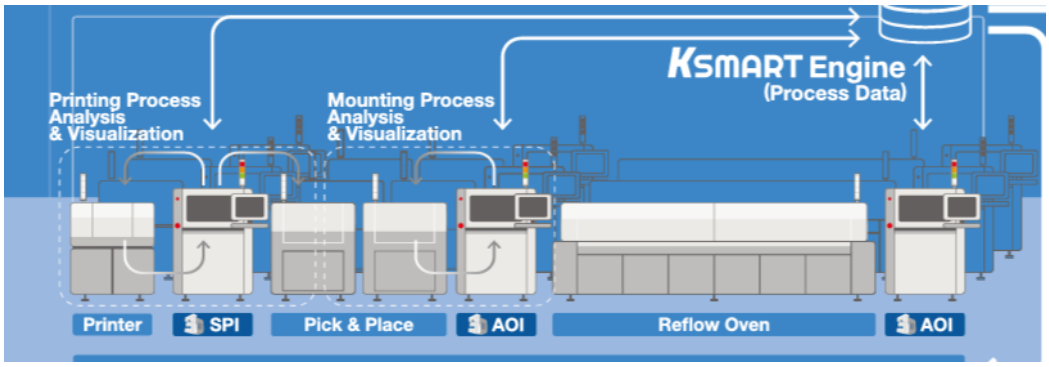

Figure 4-7 Assembly line in the Electronic Packaging Lab

Figure 4-8 Fuzion platform pick and place machine

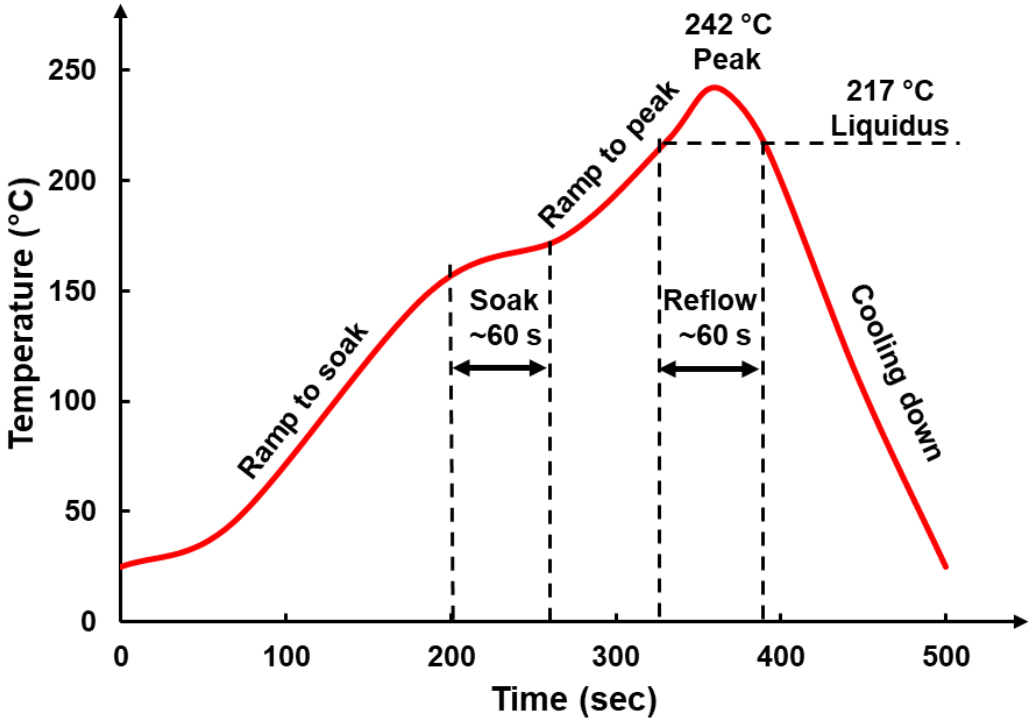

Figure 4-9 Typical reflow profile for assembling SAC305 BGA solder joints

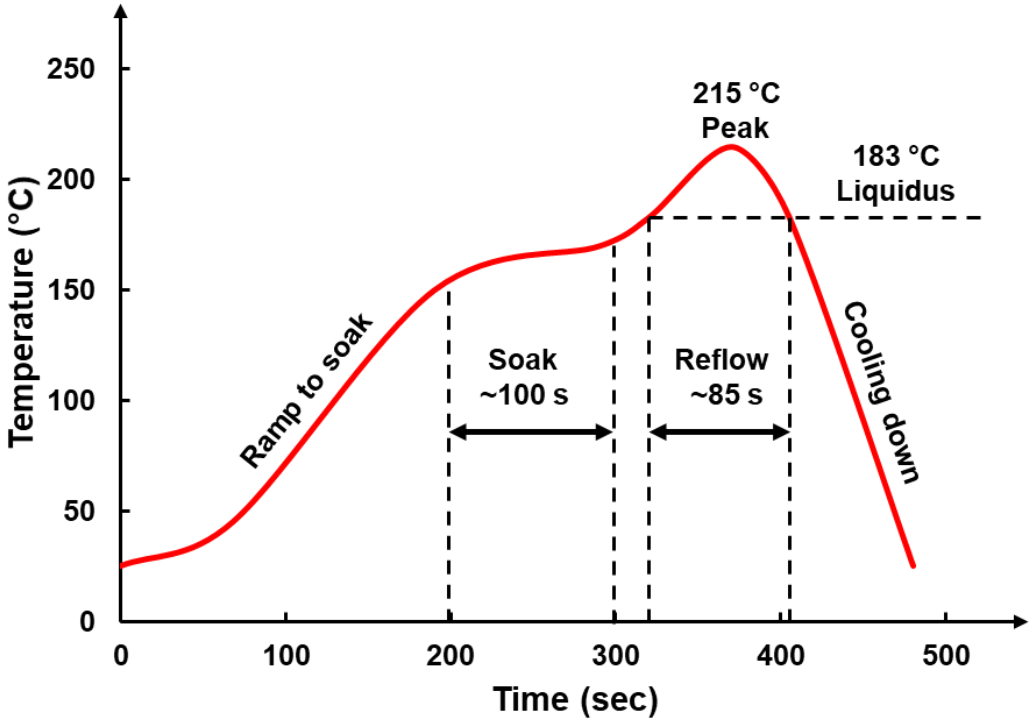

Figure 4-10 Typical reflow profile for assembling SnPb BGA solder joints

4.3 Experimental Setup

All the tests in this dissertation were conducted using the multifunctional Insrtron 5948 Micromechanical Tester. The 5948 model MicroTester can perform tension, compression, shear, and low-cycle fatigue tests with a load force range of less than 2mN up to 2kN, which is preferred to test small assemblies or miniature specimens by combining an ultra-high precision drive system with high-accuracy load measurement. The desired function of exhibiting micro-position displacement control is obtained using preloaded ball-screw drive system that is equipped with both a rotary encoder and a 10nm resolution encoder. The reading of load and displacement was reset as zero before starting any experimental test. The calibration of load cell, displacement control, and moving speed is required to ensure the accuracy of the testing results. The technical from Instron calibrated these parameters previously. The accurate reading of the load cell was verified by applying various constant load (weight).

4.3.1 Study I

In the first study, high-accuracy Instron 5948 micromechanical testing equipment was employed to measure the shear strength of four types of solder alloys. Shear strength analysis was performed to quantitatively assess the durability of the interconnects between the pads on the substrate and the solder joints. The applied force was divided by the pad-opening area to compute the shear stress, since the solder balls were assembled on the SMD pads. The displacement of a shear probe after contacting the solder ball was divided by the center of force to pad (approximated as 0.8 times solder radius) to measure the shear strain. The maximum shear stress during the shear test was considered as the shear strength. The integrity of a solder joint cannot be assessed just by its shear strength. In order to examine the solder joint quality, both shear strength

and displacement data should be used [70]. Figure 4-11 displays the Instron testing system with specific fixtures. The vertical displacement was measured using a ball screw drive mechanism with pre-load and 20-nm extension resolution. The actuator was attached with a 50-N load cell to detect the shear stress applied to the solder sphere. The load measurement accuracy was confirmed within ± 0.5% of reading down to 0.1 N. The shear procedure was performed according to JEDEC standard JESD22-B117. Figure 4-12 demonstrates a shear test schematic diagram. The test vehicle was glued to the sample holder with a superglue that provided a shear strength of $0.1N/mm^2$. The tip of the shear probe was machined as a hollow cylinder made of stainless steel. The inner diameter of the hollow was 0.75mm and the outer diameter was 1.5mm, as shown in Figure 4-11. The shear probe was moved from the top side to the bottom side until the solder joint and copper pad were completely sheared off. Because both shear speed and shear height have a considerable influence on the shear strength of solder joints, all shear tests utilizing the X-Y positioning stage used a constant shear height of 0.05 mm. For the shear fatigue test, the same test vehicles, testing equipment, and experimental setup as in the preceding shear strength test were used. Rather than shearing off the solder joints in one direction, the shear probe moves downwards at a strain rate of 0.5 s^{-1} until it reaches the predetermined stress extreme, and then reverses the movement for the cyclic shear fatigue test.

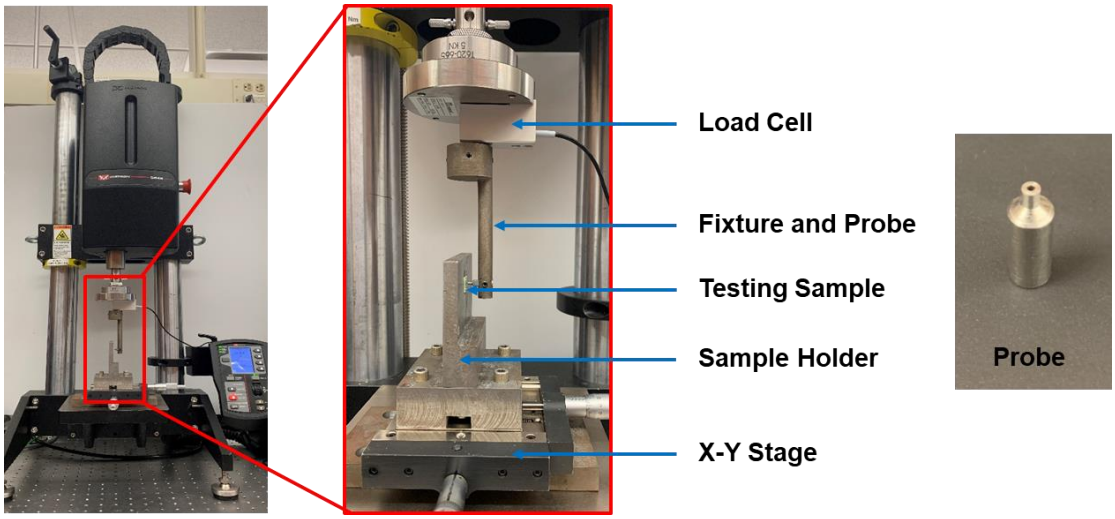

Figure 4-11 Instron Micro Tester fixture design

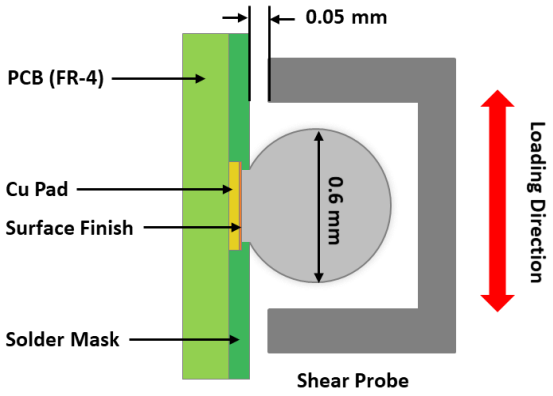

Figure 4-12 Schematic of shear fatigue test with individual solder joint

4.3.2 Study II

An Instron 5948 micromechanical tester, depicted in Figure 4-13, was used to perform the isothermal accelerated shear fatigue experiments. It was equipped with a ball screw-driven rail table with a servo motor to provide an axial displacement resolution of 20nm. Figure 4-14 shows a schematic of the setup. An epoxy adhesive (cyanoacrylate) was used to bond the BGA test vehicle between the two fixtures. The thickness of the glue was precisely controlled using the x-y stage. The load cell with a capacity of 2 kN was mounted with a fixed fixture to detect the applied force. The top fixture mounted with

the actuator created an axial movement. A base beam detects and sends the actuator displacement to the Instron feedback system. In the stress-controlled test, the moving direction of the actuator was altered once the maximum stress was detected by the load cell. This caused an overshooting of the maximum stress value, which was highly dependent on the moving speed of the actuator. To minimize the overshooting effect while accelerating the fatigue test, the strain rate was kept at 0.05 s^{-1}. The instantaneous load-displacement data were recorded based on programmed data acquisition. Both the stress-controlled and strain-controlled profiles were used in this study. In the stress-controlled method, the actuator changes its direction once the load cell detects the desired force, in the strain-controlled method, the actuator moves within a fixed displacement range. The applied stress was obtained by dividing the applied force by the total pad-opening area of the nine solder joints, while the strain was computed by dividing the displacement by the gauge length between the two substrates (0.50 mm).

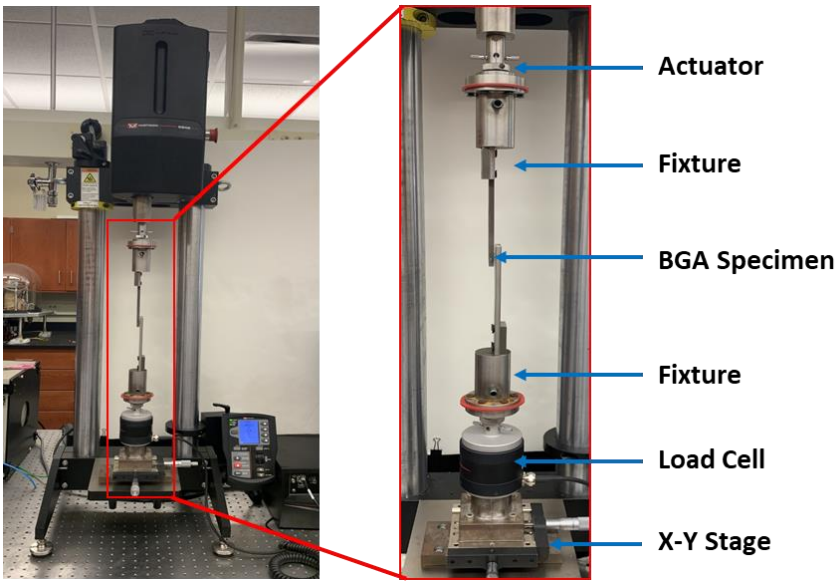

Figure 4-13 Fatigue test with sandwich test vehicle at room temperature

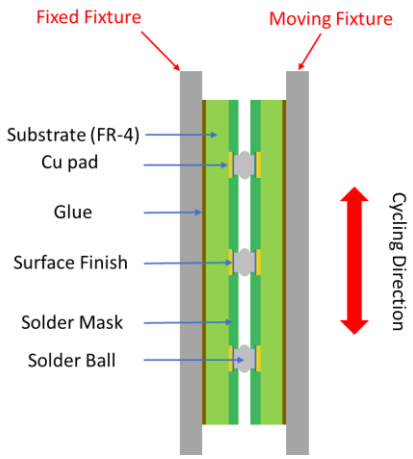

Figure 4-14 Schematic of shear fatigue test with sandwich test vehicle

4.3.3 Study III

The Instron 5948 micromechanical tester was used to perform the isothermal accelerated shear fatigue experiments. The experimental setup is the same as that discussed in study II. Both stress-controlled profiles and strain-controlled profiles were utilized for different third generation solder alloys (SAC305, SAC-R, SAC-Q, and SAC-I).

4.3.4 Study IV

The Instron 5948 Micromechanical testing system was utilized in this study. Fixtures, together with the chamber, Nitrogen cylinder, and the chilling system, were assembled to enable the isothermal tests at various testing temperatures ranging from 248K to 348K, as shown in Figure 4-15 and Figure 4-16. The top fixture, which is assembled to the actuator of the Instron Micro Tester, has the capability of controlling vertical displacement of the nanometer level. The sandwich test vehicle was precisely mounted between the two fixtures using an epoxy adhesive (cyanoacrylate), and the thickness of the epoxy adhesive was adjusted by the x-y positioning stage. The instantaneous change of load applied to the test vehicle was detected by assembling the bottom fixture to the

load cell with the capacity of 2kN. To enable various testing temperature, an EC1637 Micro Fatigue Chamber was framed on the Instron machine. The built-in heater served as the hot source and the nitrogen cylinder provided liquid nitrogen. The hot or cold air flow was then blow into the chamber through the isolation hose connection to control the temperature. The testing temperature inside the chamber was monitored by the type J-K-T thermometer and the AH1637 Air Handler System. The variation of testing temperature was confirmed to be within ± 1°C. In order to prevent the overheating of fixtures at elevated temperature, a chilling system was employed to pump cool circulated water through the fixtures, as is shown in Figure 4-15. The cooling effect of the chilling system was verified by the thermal simulation, and this assured the effectiveness of the system even when the testing temperature was 398K.

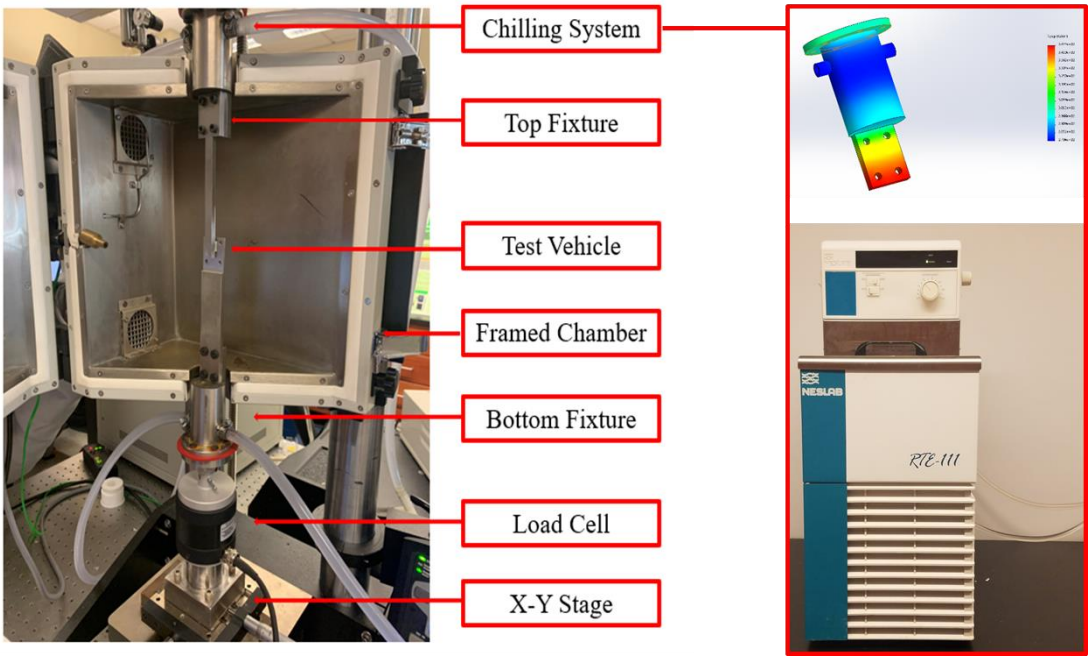

Figure 4-15 Shear fatigue test with sandwich test vehicle in the chamber

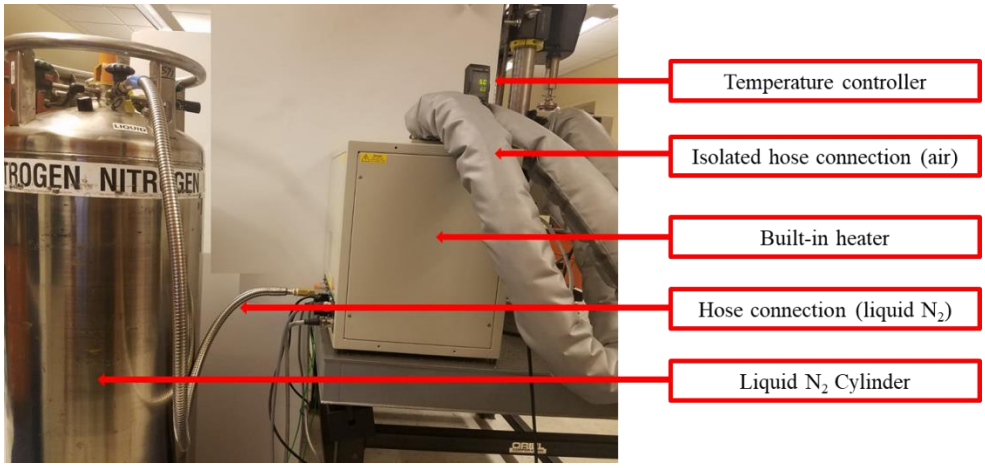

Figure 4-16 Heating source and nitrogen cylinder

The schematic diagram shown in Figure 4-19 demonstrates the detailed setup for our customized sandwich test vehicle. The bottom fixture was mechanically assembled with the load cell and x-y stage, and it was then screwed in and fixed to the base of the Instron machine. After the test vehicle was glued and the epoxy adhesive was cured, the experiment was conducted by controlling the movement of the top fixture, which is assembled to the actuator. A base beam was able to detect the displacement of the actuator, thus cycling the test with a feedback system. The instantaneous value of load and displacement was simultaneously recorded by the Instron machine with programmed data acquisition. The fatigue tests were performed using strain-controlled profiles, where the displacement traveled between upper and lower extremes with the same magnitude. Specimens were mechanically cycled at a constant strain rate of 0.05 sec^{-1}.

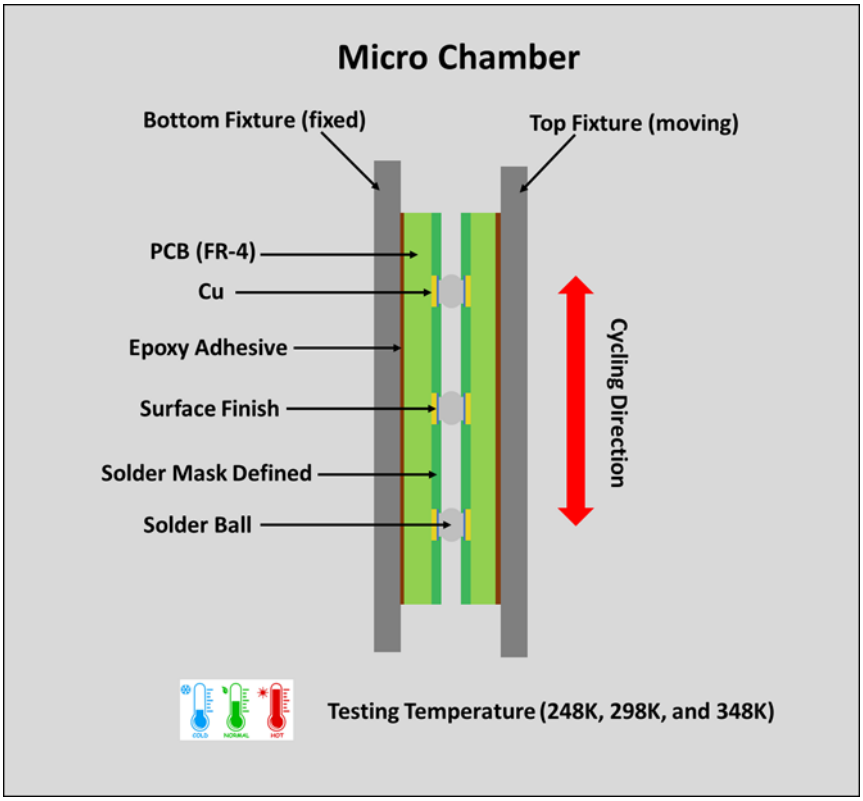

Figure 4-17 Schematic diagram of sandwich sample in the chamber

4.4 Test Plan

4.4.1 Study I

The first study is collaboration with NXP Semiconductor and the goal is to study the shear and fatigue performance of different solder alloys. The shear tests were carried out at room temperature with three rates of shear strain (0.01, 0.1, and 1 s-1) and seven identical specimens. Table 4-3 summarizes the test matrices.

Table 4-3 Shear test matrix for study I

Solder Materials	**Shear Strain Rate (sec^{-1})**		
	0.01	0.1	1
Sn-Ag	7 samples	7 samples	7 samples
SAC-Bi	7 samples	7 samples	7 samples
Sn-58Bi	7 samples	7 samples	7 samples

Sn-42Bi	7 samples	7 samples	7 samples

The isothermal shear fatigue test was utilized to assess the fatigue characteristics of individual solder joints at room temperature. To guarantee that the cycle fatigue life fell within a tolerable range, four stress amplitudes were carefully selected. Seven test vehicles were used to characterize the fatigue life at each stress amplitude using a two-parameter Weibull distribution. The test matrix is presented in Table 4-4.

Table 4-4 Fatigue test matrix for study I

Alloys	Surface Finish	16 MPa	20 MPa	24 MPa	28 MPa	32 MPa	36 MPa	40 MPa
Sn-Ag	ENIG	7	7	7	7	-	-	-
SAC-Bi	ENIG	-	-	-	7	7	7	7
Sn-58Bi	ENIG	-	-	7	7	7	7	-
Sn-42Bi	ENIG	-	7	7	7	7	-	-
Sn-Ag	OSP	-	7	7	7	7	-	-

For each stress amplitude, characteristic fatigue life of individual solder joints was calculated using the data from seven samples. The results of the seven samples were fitted in a 2-parameter Weibull distribution to figure out the characteristic life, which is the scale parameter θ. We have chosen one typical replicate out of the seven, which has the closet fatigue life to the characteristic life. Figure 4-20 illustrates a typical hysteresis loop for Sn-Ag solder joints with ENIG surface finish under 20 MPa. Plastic strain range and inelastic work per cycle can be measured from the hysteresis loop for each cycle. Models (Morrow energy model and Coffin-Manson model) were developed to predict the fatigue life of each solder alloys using plastic strain range and work per cycle.

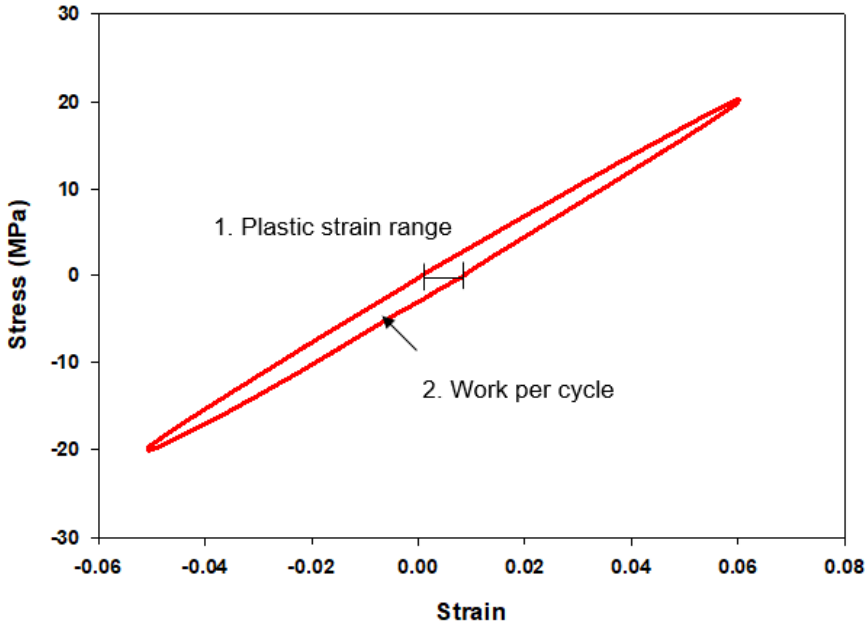

Figure 4-18 Typical hysteresis loop for Sn-Ag solder joint under 20 MPa

4.4.2 Study II

The second study aims to investigate the fatigue behavior of SAC305 solder joints in BGA assembled with both stress-controlled and strain-controlled profiles. The SAC305 test vehicles were assembled with either OSP surface finish or ENIG surface finish to compare the fatigue performance in each case. In stress-controlled test, two predefined extreme stresses (maximal and minimal) were programmed for the cyclic test, similar with the method used in study 1; in strain-controlled test, minimum strain and maximum strain were selected.

Pilot tests were performed to estimate the fatigue life for each case. The stress and strain levels in Table 4-5 ensure a reasonable range of fatigue life in each case. They generated significant differences in fatigue life at each level, while confining the fatigue life within 6,000 cycles. The test matrices are presented in Table 4-5. Five samples were tested at each testing conditions. Representative samples with fatigue life closest to the

characteristic fatigue life were selected to illustrate the evolution of inelastic work and plastic strain range per cycle in subsequent sessions.

Table 4-5 Test matrix for study II

Solder Alloy	Method	Level	OSP Surface Sample No.	ENIG Surface Sample No.
SAC305	Stress-controlled	20MPa	5	5
		24MPa	5	5
		28MPa	5	5
		32MPa	5	5
	Strain-controlled	2.4%	5	5
		3.0%	5	5
		3.6%	5	5
		4.2%	5	5

Evolution of hysteresis loops in stress-controlled test and strain-controlled test were plotted for each solder alloy. Enclosed area of hysteresis loop for each cycle, counting as work per cycle, was calculated according to the in-situ stress-strain data pointed recorded by the Instron machine. Plastic strain range per cycle was also measured from the hysteresis loop. Empirical models were utilized to study the correlation between fatigue life of each solder alloy with stress amplitude and strain level. Work per cycle and plastic strain range per cycle were calculated for Morrow Energy model and Coffin-Manson Model, respectively.

4.4.3 Study III

In the third study, SAC305 and three micro-alloying solder spheres were assembled in BGA test vehicles to represent realistic chips. Table 4-6 lists the composition of the

investigated solder alloys as well as the applied surface finish. Both the stress-controlled and strain-controlled profiles were used in this study. The composition of the solder joints has a substantial effect on their fatigue characteristics. Consequently, pilot tests were conducted to evaluate the stress and strain levels so that the characteristic life could potentially fall within an acceptable range (less than 3000 cycles). Two stress levels and two strain levels were chosen for each solder alloy after the pilot tests. Higher stress and strain levels are employed in certain situations due to their improved reliability (SAC-Q and SAC-I with OSP surface finish). In addition, the fatigue life of the SAC-Q and SAC-I solder alloys with ENIG surface finish was very sensitive to strain variation. It ranged from a few hundred cycles at a strain level of 2.4% to over ten thousand cycles at a comparatively lower strain level of 1.8%. Therefore, only one strain level was measured for the two SAC-Bi solder joints with the ENIG surface finish. The test matrices are listed in Table 4-7, and five identical BGA test vehicles were used for each test condition.

Table 4-6 Composition of solder materials in Study III

Solder Alloy	**Compositions**	**Surface Finish**
SAC305	Sn-3Ag-0.5Cu	OSP, ENIG
SAC-Q	Sn-3.41Ag-0.52Cu-3.3Bi	OSP, ENIG
SAC-R	Sn-0.92Cu-2.46Bi	OSP, ENIG
SAC-I	91.8Sn-3.5Ag-0.7Cu-3Bi-1.5Sb-0.125Ni	OSP, ENIG

Table 4-7 Test matrix for Study III

Solder Alloy	**Surface Finish**	**Stress-controlled**		**Strain-controlled**	
		Low level (MPa)	**High level (MPa)**	**Low level**	**High level**
SAC305	OSP	24	32	3.0%	4.2%

	ENIG	24	32	3.0%	4.2%
SAC-R	OSP	24	32	3.0%	4.2%
	ENIG	24	32	3.0%	4.2%
SAC-Q	OSP	36	40	4.2%	4.8%
	ENIG	24	32	N/A	2.4%
SAC-I	OSP	36	40	4.2%	4.8%
	ENIG	24	32	N/A	2.4%

After the test, a comprehensive microstructure analysis was conducted to investigate the effects of micro-alloying elements, surface finish, and stress/strain level on the fatigue properties. The microstructure of the four solder alloys, along with the formation of IMC layers and failure modes, were compared and researched.

4.4.4 Study IV

The objective of this study is to systematically investigate the fatigue performance of sandwich test vehicles in isothermal strain-controlled test. SAC305 and SnPb solder alloys were assembled in the customized sandwich test vehicles to compare the fatigue performance. Both OSP surface finish and ENIG surface finish were reflowed on the solder mask defined copper pads to study the effect of surface finish on the fatigue performance. The testing method utilized in this study is strain-controlled test and the testing setup has been illustrated previously. Low temperature of 248K and elevated temperature of 348K in the isothermal shear fatigue tests were accomplished by framing the chamber on the Instron machine.

For each of the testing temperature, the sandwich test vehicles with OSP surface finish and ENIG surface finish were tested under four strain levels, as is shown in Table 4-8. The effect of temperature on the fatigue life of each combination of solder alloy and surface finish are systematically researched in the strain-controlled tests. Other

interested parameters, such as work per cycle and plastic strain range per cycle, were also compared under various temperatures. Coffin-Manson model and Morrow energy model were developed for SAC305 and SnPb solder alloy per surface finish and test temperature.

Table 4-8 Test matrix for study IV

Solder Alloy	Strain Level	OSP Surface Finish			ENIG Surface Finish		
		248K	298K	348K	248K	298K	348K
SAC305	L1	5	5	5	5	5	5
	L2	5	5	5	5	5	5
	L3	5	5	5	5	5	5
	L4	5	5	5	5	5	5
SnPb	L1	5	5	5	5	5	5
	L2	5	5	5	5	5	5
	L3	5	5	5	5	5	5
	L4	5	5	5	5	5	5

4.5 Microstructure Analysis

Test vehicles in each study were cross-sectioned before microscopic examination. Each sample was cold mounted using the holder clip in the plastic mold, filling with an epoxy system made from blended epoxy resin and hardener with the weight ratio of 6:1. The epoxy system was fully cured at room temperature for 24 hours and then pulled out from the mold for next procedures. The samples were grinded on the Pace Technologies NANO 1000T semi-automated polishing machine (Figure 4-21), using sandpapers following the sequence of 240, 320, 400, 600, 800, and 1200 grits. Before moving to the next grit size, the samples were inspected using microscope to ensure the quality of each step. The grinding direction was rotated by 90° for the next step to cover the cut

scratches incurred from the previous step. The expected grinded sample would give a clear cross-section view of about the middle of the solder joints and provide a reasonable roughness of the surface for polishing.

After grinding, four polishing stages were implemented including 3 μm, 1 μm, 0.05 μm alumina base particles, and 0.02 μm non-crystallizing colloidal silica suspension. Each polishing stage was carried out on the separate polishing pad for around 5 minutes. The ultrasonic cleaner was used in the last to vibrate the sample and remove residuals.

After polishing process, the Sophisticated ZEISS Axio Imager.M2m optical microscope, as is shown in Figure 4-22, together with an Axiocam 503 color microscope camera and ZENCore software were used to examine the failure mode of the samples.

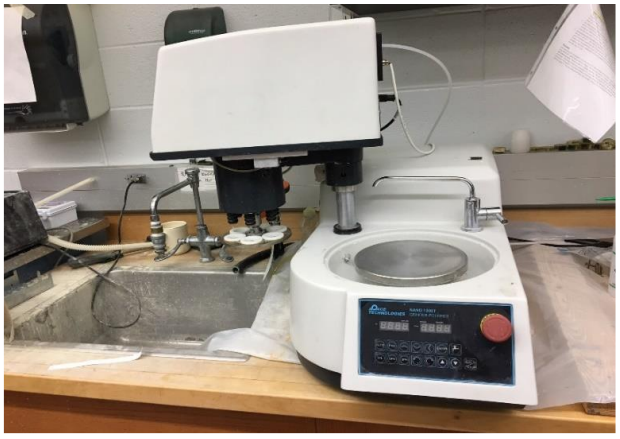

Figure 4-19 Pace Technologies NANO 1000T semi-automated polishing machine

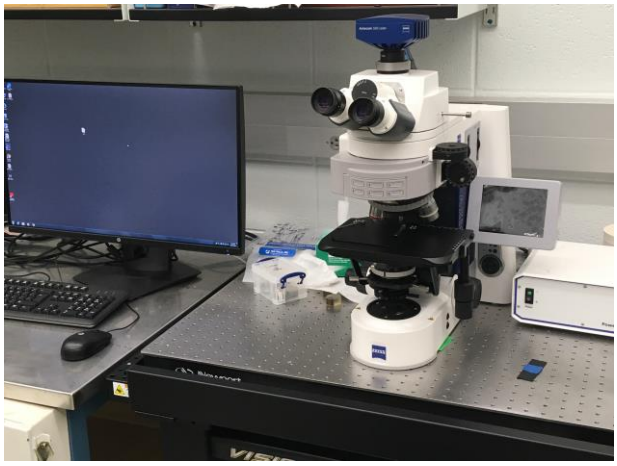

Figure 4-20 ZEISS Axio Imager.M2m optical microscope

Furthermore, the samples were gold sputter coated for SEM and EDS examination. The CRESSINGTON sputter coater (Figure 4-23) was utilized to coat the samples. Afterwards, SEM analysis (Figure 4-24) was conducted to examine more detailed microstructure of solder joints, which performs higher magnification than microscope. EDS analysis was utilized with SEM, which revealed the elemental composition of a particular section of the solder joint.

Figure 4-21 CRESSINGTON SPUTTER COATER

Figure 4-22 JEOL JSM-7000F SEM

Chapter 5 Shear and Fatigue Properties of Lead-Free Solder Joints: Modeling and Microstructure Analysis

5.1 Introduction

Fatigue failure of interconnected solder joints is a critical consideration for the reliability of an electronic product. A great deal of previous research has focused on the mechanical fatigue properties of large bulk samples through uniaxial tension-tension test [137], simple shear test [138], thermomechanical shear test [139], and multiaxial tension-torsion test [140]. There is however a general consensus that the mechanical properties of solder joints assembled in the electronic packages vary greatly from the large bulk samples considering the effect of IMC layer, surface finish, precipitate distribution, and size difference. This inconsistency draws forth the necessity to study the fatigue performance of individual solder joints.

The electronics manufacturing has experienced significant material transformation since the adoption of the Directives on Hazardous Materials and Waste Electrical and Electronic Products. Solder manufacturers and suppliers have developed a variety of lead-free solders to transition out of the use of lead and meet regulatory criteria. SAC-based solder alloys were primarily proposed to supersede typical eutectic Sn-Pb solder alloys because of their improved mechanical strength, thermal fatigue characteristics, and solderability. Further studies have found that solder alloys, including minor alloying metals like In, Sb, and Bi, are more reliable[71][72]. These elements were reported to prevent IMC coarsening precipitates and the growth of IMC layer development [73]. However, the undesired high re-flow temperature of the above-mentioned solder alloys has an adversely affects the packaging materials and assembly processes. This has prompted the development of a new generation of LTS solder alloys,

mostly based on SnBi, to enhance the integrity and reliability of microelectronic packages.

To minimize the coarsening impact of IMC precipitates and the development of the IMC layer, micro-alloying with components like as Ni, Bi, and Sb is commonly added to Sn-based solders [73][74][75][76][77]. The inclusion of these elements demonstrated enhanced mechanical properties in terms of creep, tensile, and fatigue [78][79][80], whereas excessive content might generate undesirable effects such as reduced elongation, brittle fracture, and poor creep properties [81][82][83]. SnBi-based solders have received considerable attention because of their low melting temperature of approximately 139°C, high creep resistance, and reasonable price [84][38]. According to Rajendran et al., the addition of ZnO nanoparticles to SnBi solder improved the wettability, tensile strength, and ductility, as well as provided a finer microstructure [85][86]. Wang et al. studied the impact of Bi substance on the shear characteristics of Sn-*x*Bi solder joints and indicated that when the Bi content increased, the fracture phase shifted from ductile to brittle [87][88]. The strain rate affects the shear characteristics of SnBi solders. The strain rate affects the shear characteristics of the SnBi solders. The shear strength increased as the strain rate increased, but decreased once the strain rate exceeds 3.33×10^{-2} s^{-1} [83].

The fatigue and shear properties of LTS joints have been reported in many studies[21][89][90], including both traditional SAC-based solders and new-emerged LTS solders. However, no study has made a comprehensive comparison between the widely used SAC solders and Sn-Bi solders in terms of shear and fatigue performance. In this study, the fatigue and shear behaviors of individual solder joints were examined using four solder alloys featuring ENIG surface finishes. The shear strength of each solder alloy was tested at three different strain rates. The fatigue life of solder alloys

was evaluated using load cycling at a constant strain rate with four stress amplitudes. Shear and fatigue testing were utilized to investigate the failure processes. The effect of surface on the fatigue and shear properties of Sn-Ag was also investigated.

5.2 IMC Morphology Characterization

During the re-flow process, the uppermost Au layer of the ENIG surface finish was solubilized into the solder alloy. As a result, the molten solder comes into contact with the Ni layer, acting as a barrier against Cu atom diffusion from the Cu pad. Figure 5-1 depicts the interfacial microstructures of all examined solder alloys. Ni was revealed to make a reaction with Sn to generate Ni_3Sn_4 layer at the interface together with the Cu pad in the Sn-Ag solder alloy [91], as shown in Figure 5-1(a). There was another scallop-like interfacial layer on top of the Ni_3Sn_4 layer, which EDS analysis identified as the Ni-Sn phase. In the β-Sn dendritic structure, Ag_3Sn particles were observed to form a network. Due to the precipitate hardening process, these particles would enhance the mechanical characteristics of the Sn-Ag solder alloy. Figure 5-1(b) shows a similar interfacial layer with a scallop-like morphology above the Ni layer in the SAC-Bi solder alloy. The composition of the IMC layer was validated to be $(Cu, Ni)_6Sn_5$ because of the inclusion of Cu in the solder alloy. This is in agreement with previous findings [71]. Furthermore, the Bi content refined the Ag_3Sn and Cu_6Sn_5 particles compared to the micrograph of the Sn–Ag solder alloy. Because of the presence of the Bi in solid solution, the β-Sn lattice was deformed, affecting the self-diffusion of Sn to the IMC layer. Consequently, Bi improved the mechanical behaviors of the solder alloys [53]. As demonstrated in Figure 5-1(c), the Sn42Bi solder alloy exhibited two distinct phases: Sn-rich and the Bi-rich. In addition, an IMC film between the Ni layer and bulk solder appeared as a tertiary phase of Sn-Ni. Fig. 5(d) shows a micrograph of Sn52Bi with a

similar microstructure, although the composition of the IMC layer seemed to be the Sn-Ni-Sb phase.

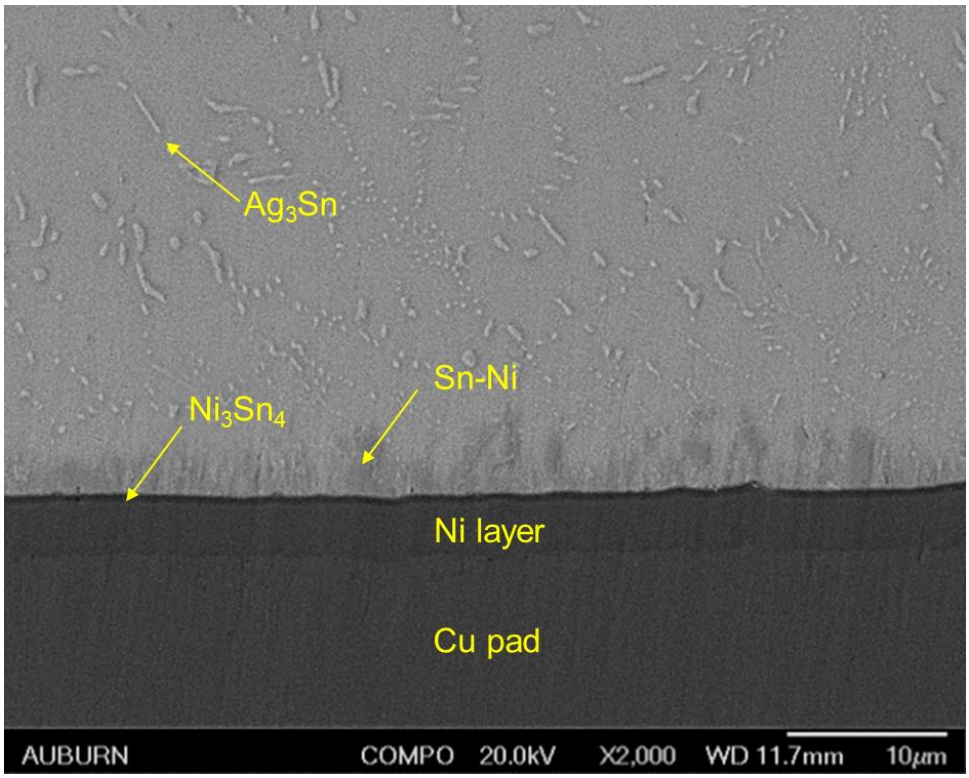

(a)

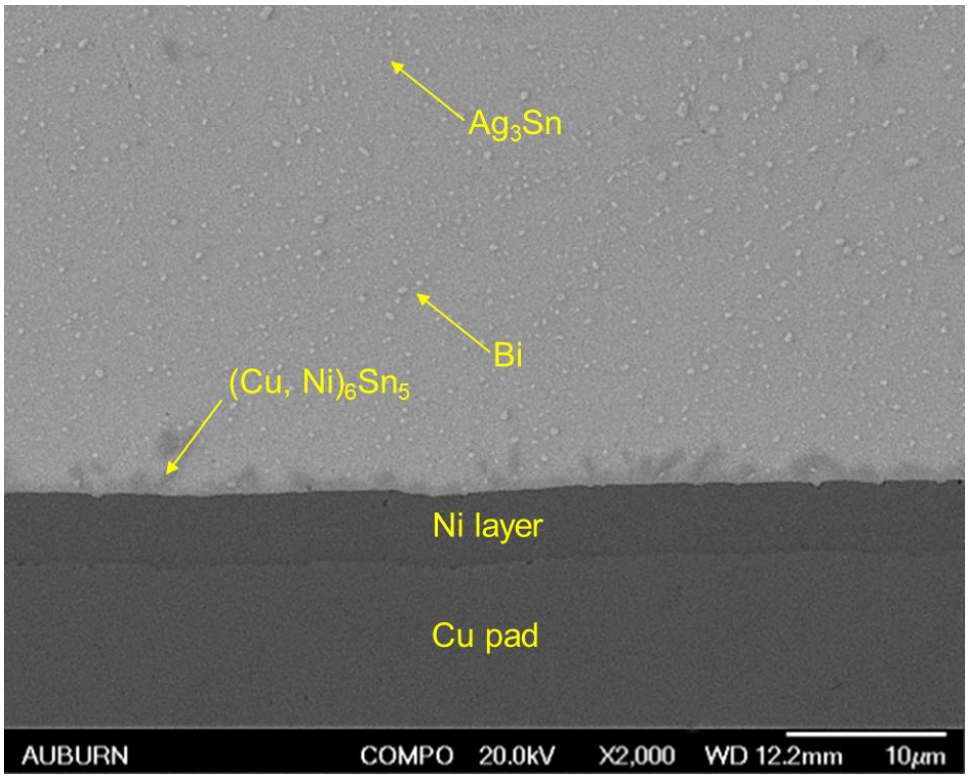

(b)

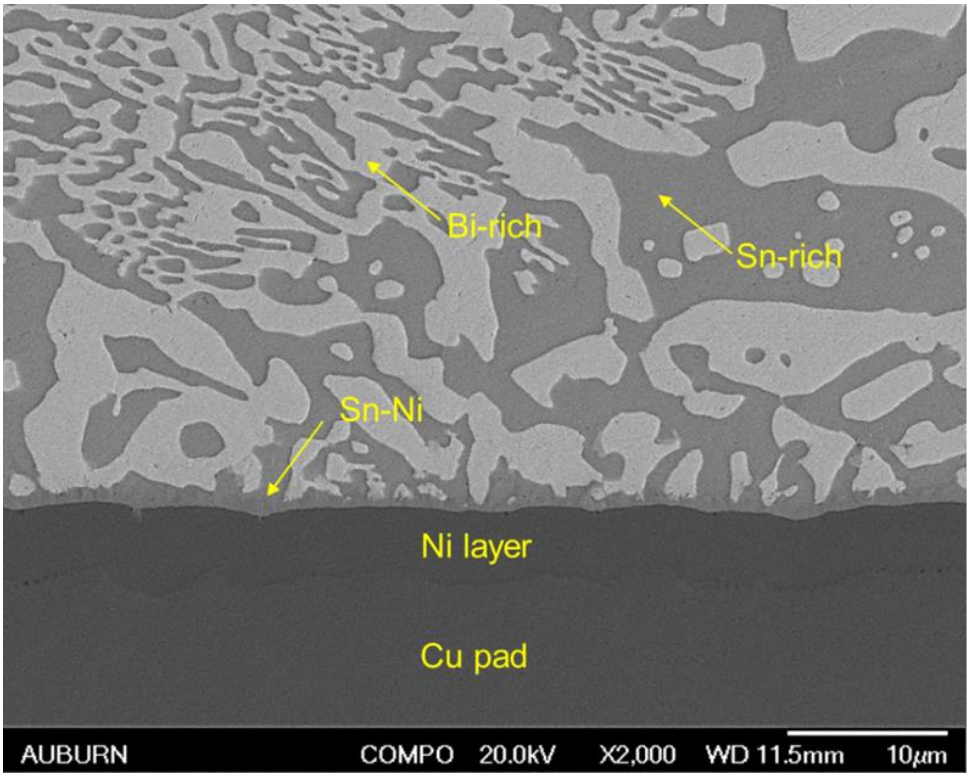

(c)

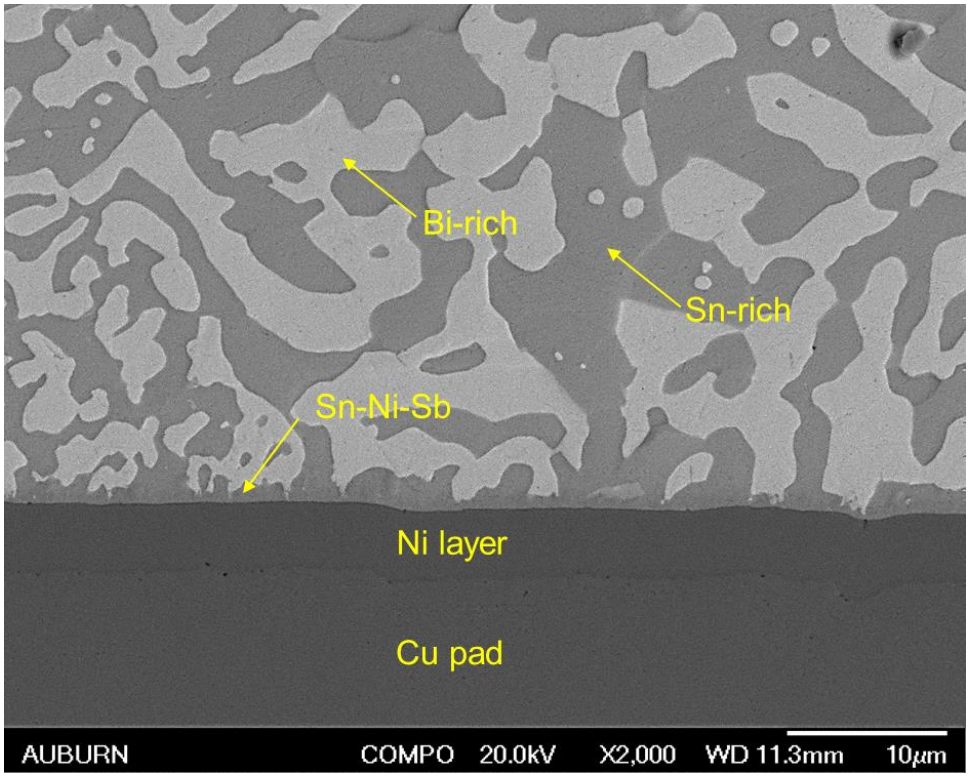

(d)

Figure 5-1 Micrograph of solder alloys: (a) Sn-Ag; (b) SAC-Bi; (c) Sn42Bi; and (d) Sn58Bi

5.3 Analysis of Shear Strength

Shear strength of the Sn-Ag solder alloys tested at different rates of shear strain is mapped in Figure 5-2. The blue dots depict the outcome of seven samples taken at different rates of shear strain numerically 0.01, 0.1, and 1 s^{-1}, while the red dots represent the average shear strength at each strain rate. As the rate of shear strain increases, the average shear strength increased in a non-linear manner, as displayed in Figure 5-2. In general, higher shear rates would shorten the creep time inside the solder alloy, resulting in higher shear strength. According to Chia et al. [92], the applied shear strain rate v is used to express the shear strength (τ_{max}) of a solder ball by

$$\tau_{max} = a * \ln(v) + b \qquad 5\text{-}1$$

where a and b are material constants.

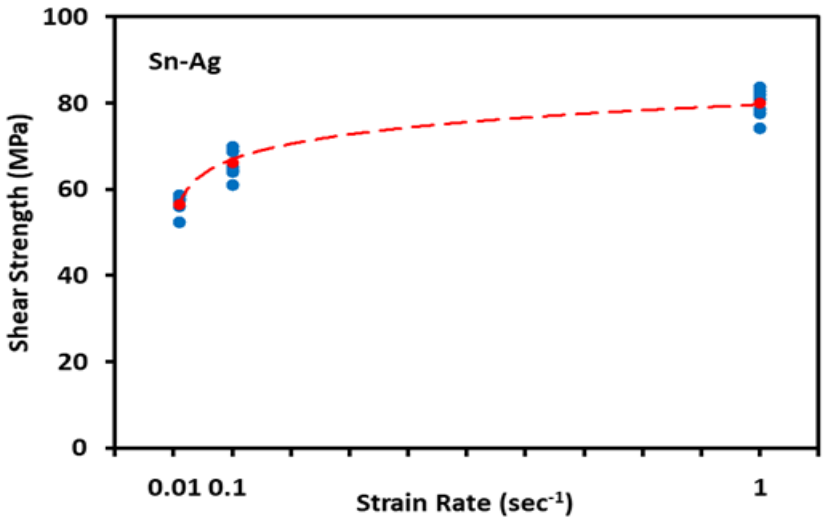

Figure 5-2 Shear strength of Sn-Ag solder alloys at different rates of shear strain

Figure 5-3 shows the average shear strength of the four solder alloys versus different rates of shear on a logarithmic scale. For all tested solder alloys, the dashed line represents the fitted linear equation (1). These curves were found to have excellent goodness of fit. For all of the tested solder alloys, shear strength increased as strain rates increased. At all shear strain rates, SAC-Bi exhibited the best shear strength, whereas

Sn-Ag exhibited the worst shear strength. Minor elements such as Bi, Sb, and In were found to remain in the Sn solid solution and cause crystalline lattice deformation. The solid solution hardening effect can enhance the mechanical characteristics of solder alloys by impeding the dislocation motion. This is consistent with the findings in Figure 5-2, where SAC-Bi outperformed Sn-Ag in terms of shear strength. Despite a slight offset between the trendlines of the two solders, the two LTS, Sn42Bi and Sn58Bi, performed similarly in the shear tests when compared to the two SAC solder alloys. For SAC-Bi, Sn42Bi, and Sn58Bi, the variance in the shear strength increased significantly as the shear strain rates increased. Meanwhile, there was no discernible difference in the variation between the three shear strain rates used for Sn-Ag. Table 5-1 summarizes constants a and b fitted using Equation 5-1 for the four solder alloys.

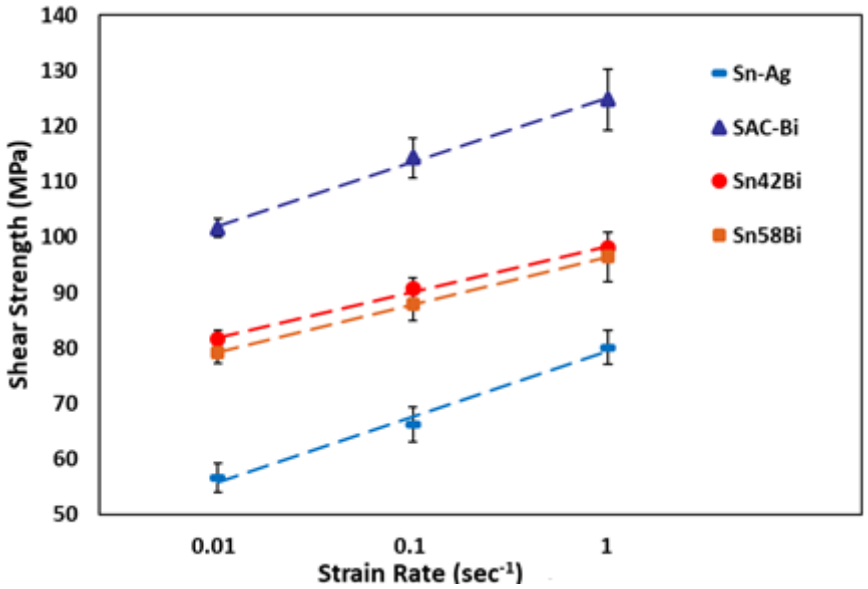

Figure 5-3 Average shear strength of the four solder alloys versus different rates of shear strain

Table 5-1 Summary of shear strength constants

Solder Materials	Constant "a"	Constant "b" (MPa)
Sn-Ag	5.10	79.38
SAC-Bi	5.02	125.13

Sn-58Bi	3.73	96.45
Sn-42Bi	3.57	98.37

Despite the quantitative study of shear properties by comparing shear strengths, a qualitative assessment was performed by identifying the failure mechanisms. The failure modes were divided into three types based on fracture initiation and propagation: ductile, brittle, and mixed failures. The ductile or brittle fracture of the solder alloy was determined based on the distinct shape of the stress-strain curve. In the state of ductile failure, there was a rapid increase in stress as the shear tester contacted the solder joint, causing plastic deformation of the solder joint, followed by a slower increase in stress due to the strain hardening effect, and finally, a gradual reduction in shear stress until the fracture is complete. In the case of brittle failure, there was also a steep increase in stress, after that a steep decrease when the solder joint and Cu pad damaged suddenly. Figure 5-4 shows the typical stress-strain curves for Sn-Bi and Sn-Ag solder alloys evaluated at the same strain rate of 1 s^{-1}. Ductile failures were identified in both the stress-strain curves. However, whereas SAC-Bi had almost double the shear strength of Sn-Ag, its shear strain causing fracture was only one-third that of Sn-Ag. On the other hand, SAC-Bi was less ductile than Sn-Ag. This aligns with prior findings.

The shear strain rate is a crucial tool in determining the failure mode All of the solder alloys were examined at three different rates of shear stain, and the stress-strain curves for each are displayed in Figure 5-5 (a-d). As previously stated, shear strength is enhanced when the shear strain rate is increased. The peak shear strength was highest at a rate of shear strain of 1 s^{-1}, followed by 0.1 s^{-1} and 0.01 s^{-1}. Simultaneously, higher shear strain rates are associated with a reduced shear strain to failure. This pattern was observed for all four tested solder alloys.

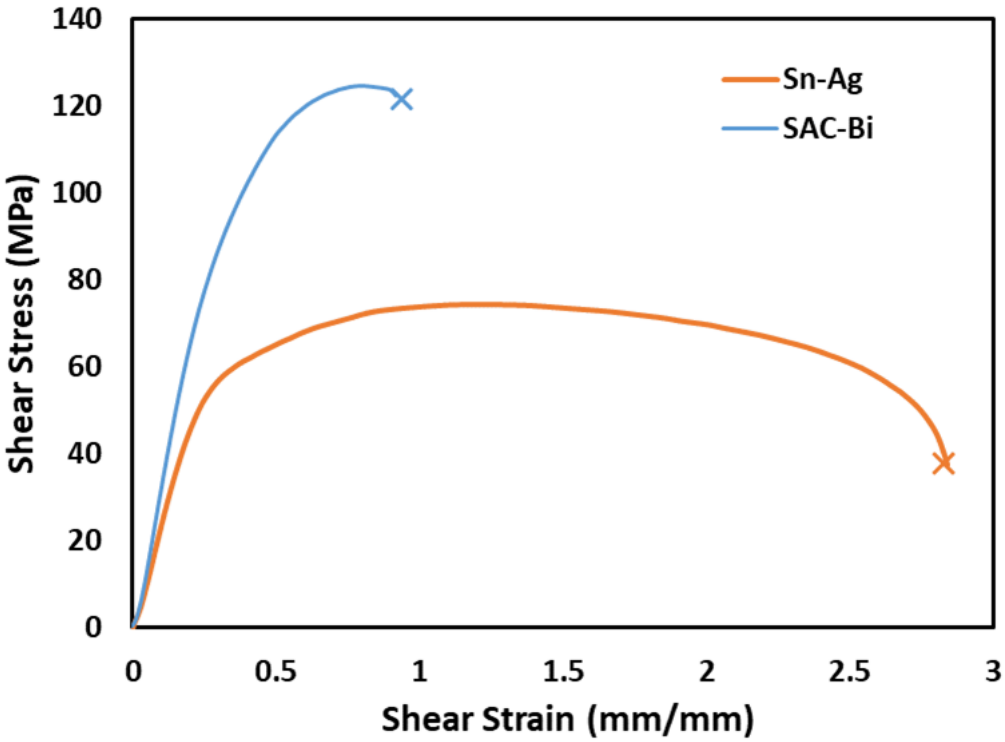

Figure 5-4 Typical stress-strain curves of SAC-Bi and Sn-Ag solders

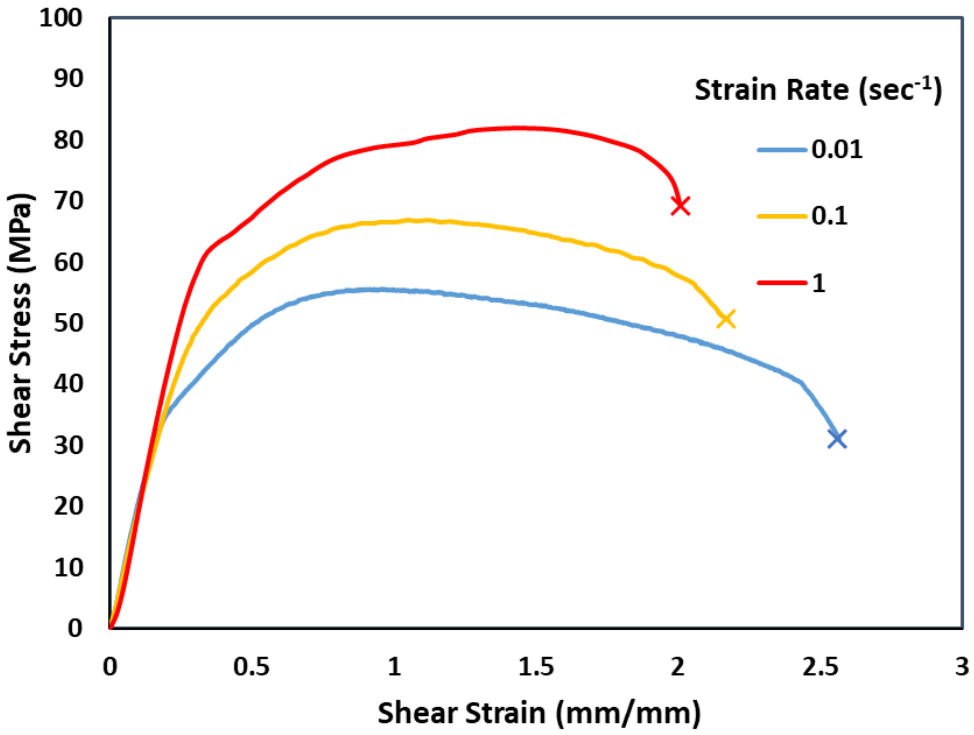

(a)

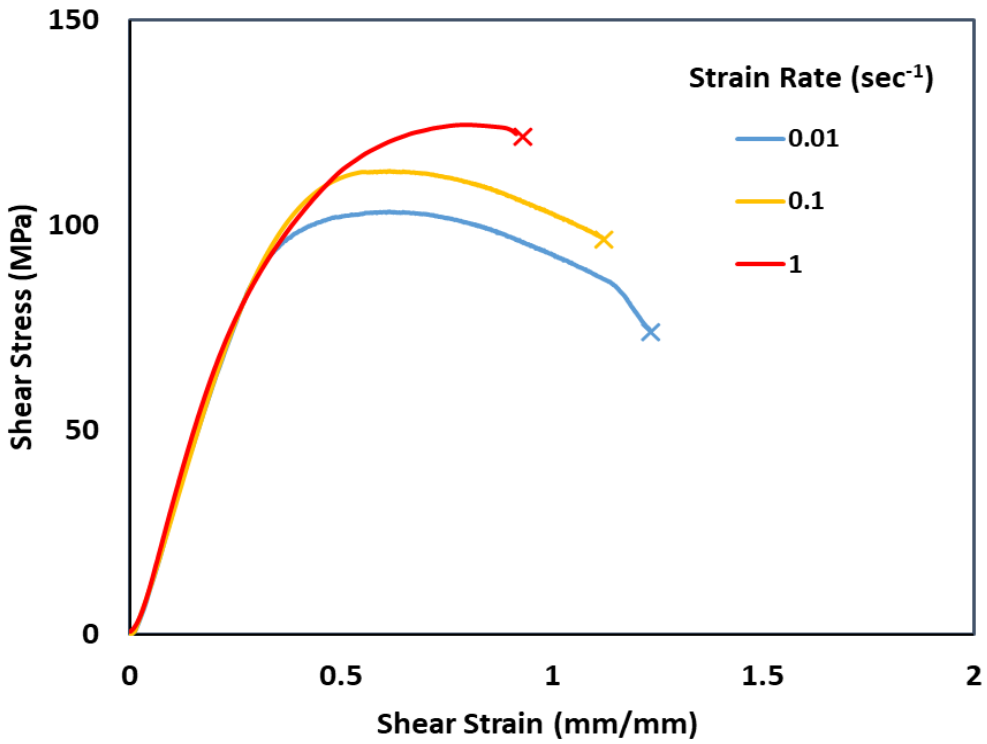
150
100
50
0
Shear Stress (MPa)
0
0.5
1
1.5
2
Shear Strain (mm/mm)
Strain Rate (sec-1)
0.01
0.1
1

(b)

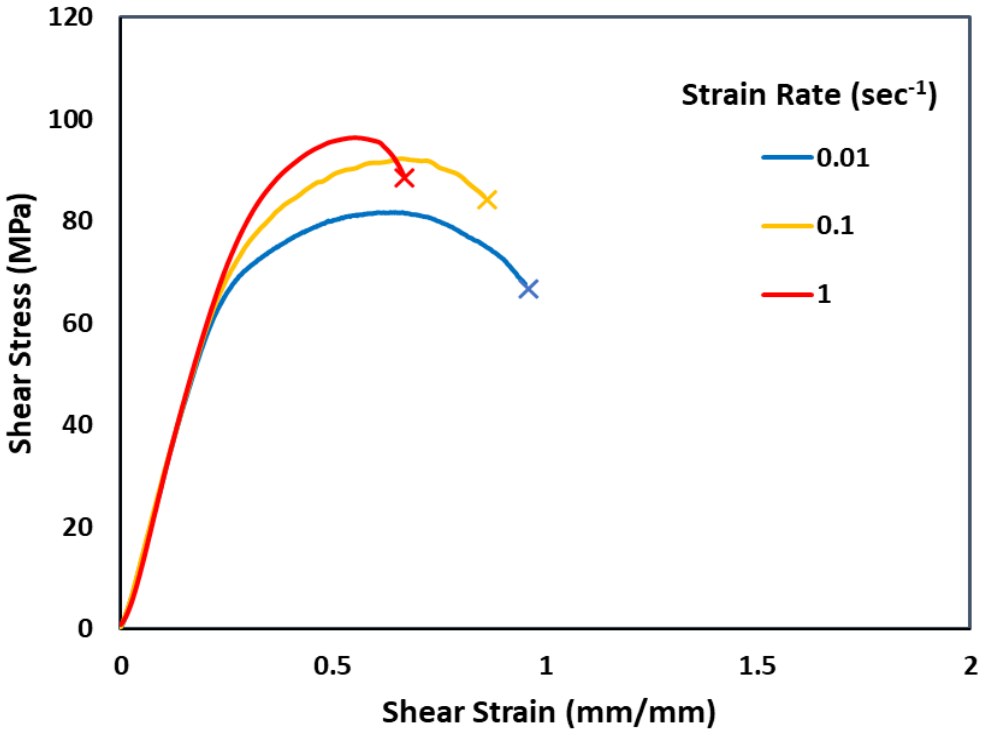
120
100
80
60
40
20
0
Shear Stress (MPa)
0
0.5
1
1.5
2
Shear Strain (mm/mm)
Strain Rate (sec-1)
0.01
0.1
1

(c)

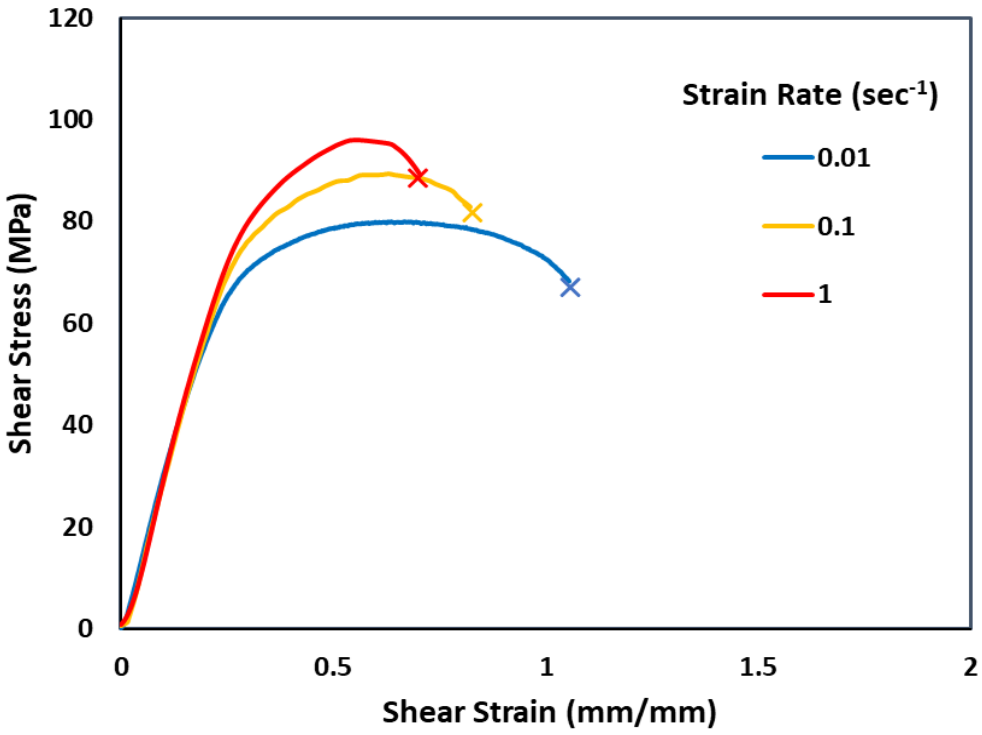

(d)

Figure 5-5 Stress-strain curves of tested alloys at several rates of shear strain: (a) Sn-Ag; (b) SAC-Bi; (c) Sn-42Bi; and (d) Sn58Bi

The stress-strain curves in SAC-Bi demonstrated a shift in failure mode from ductile to less ductile. A typical ductile fracture was observed at the low shear strain rate of 0.01 s^{-1}. As shear strain rates go up, the shear stress tended to decline rapidly immediately after reaching the peak value, according to stress-strain curve in Figure 5-5 (b). With Sn-Ag, Sn42Bi, and Sn58Bi, minor modifications in the form of the stress-strain curves were observed.

The flow stress of the solder significantly contributes to the failure mechanisms in the shear test [70]. When the shear probe deforms the solder connection, the viscoplasticity of the solder results in flow stress. The weakest values of the bulk flow stress, copper peel and interfacial strengths all contributed to the occurrence of fractures. When the bulk flow stress surpasses the copper peel strength, the pad cratering occurs. However,

ductile fracture when flow stress is less than copper peel and interfacial strength. In this case, the shear probe plows the bulk solder. Otherwise, brittle failure with clean separation along the IMC layer occurs if the flow stress is higher than the interfacial strength. A mixed failure mode could also occur as a result of various amounts of shear force being applied to different parts of the pad. Consequently, both ductile and brittle fractures were spotted in a single solder joint. The flow stress of the bulk solder during the test is determined by the movement speed of the shear probe, which plays a vital role in producing distinct failure modes by locating the start and spread of cracks. In all testing cases, the failure location was in the solder joint structure, and no failure was observed in the copper pad or board structure. Thus, the constants in Table 4 for Equation 1 are valid regardless of the change in the failure mode as long as the failure location is in the solder joint.

Figure 5-5 (a) displays the typical fractures of the Sn-Ag solder at low (left) and high (right) levels of rates of shear strain testing. In each case, a smooth shear plane was demonstrated, leaving a substantial amount of Sn-Ag solder covering the Cu pad. This indicates that the crack developed and propagated in the bulk solder. For the Sn-Ag solder, the shear strain rate had a negligible impact on failure mode.

Figure 5-5 (b) demonstrates the two distinct failure mechanisms of the SAC-Bi solder. The SAC-Bi solder had a flow stress that was less than the interfacial strength at a low shear strain rate of 0.01 s^{-1}. This prompts ductile fracture on the surface. However, the flow stress exceeded the interfacial strength at a high rate of shear strain of 1 s^{-1}, resulting in brittle failure.

The top views of the Sn-42Bi solder after shearing off the solder joints are shown in Figure 5-5 (c). The copper pad was completely covered with solder following the shear

test with a low shear strain rate, whereas part of the Ni layer was exposed on the top view with a high shear strain rate, indicating mixed-mode failure.

Figure 5-5 (d) displays how the shear strain rate affects Sn58 solder. The SEM images of Sn42Bi and Sn58Bi were extremely similar due to the large Bi content in both. As the shear strain rate increased, the flow stress increased to a point near the interfacial strength, resulting in a mixed-mode failure.

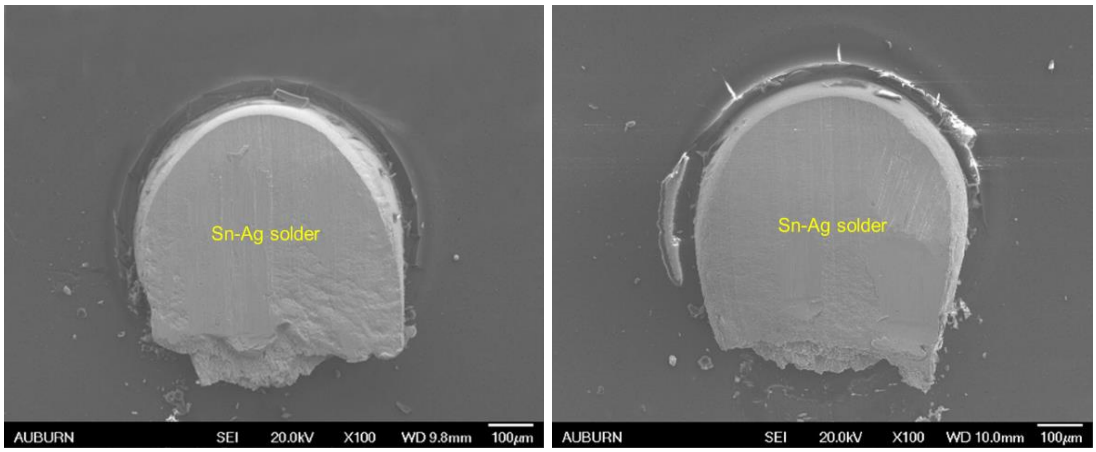

(a)

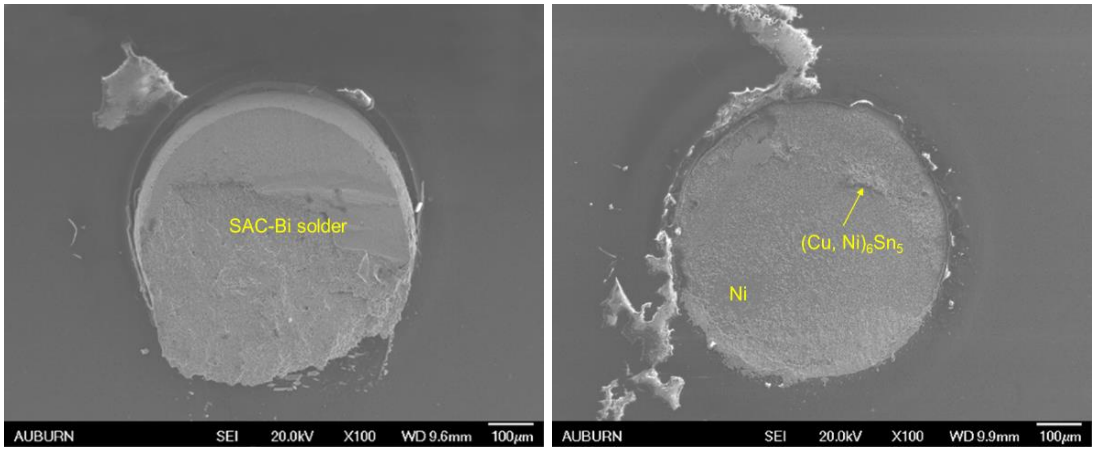

(b)

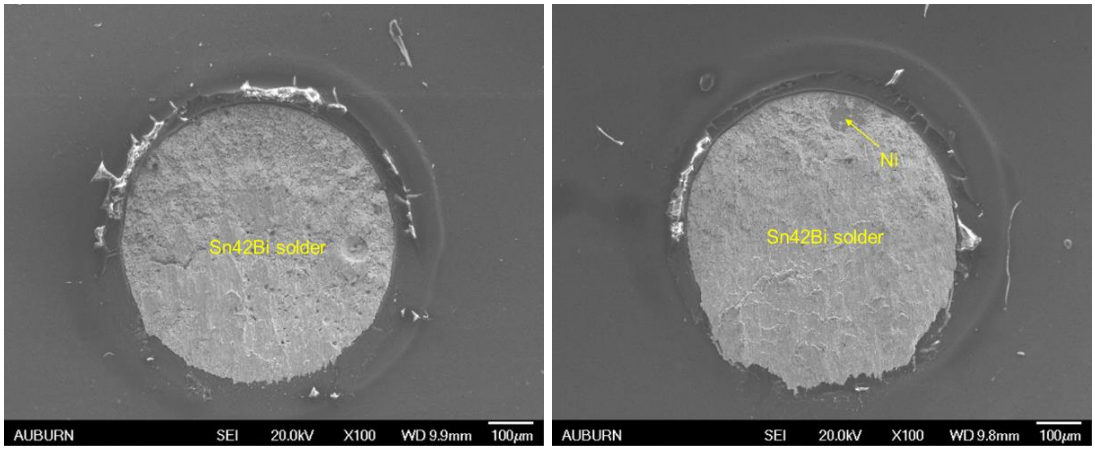

(c)

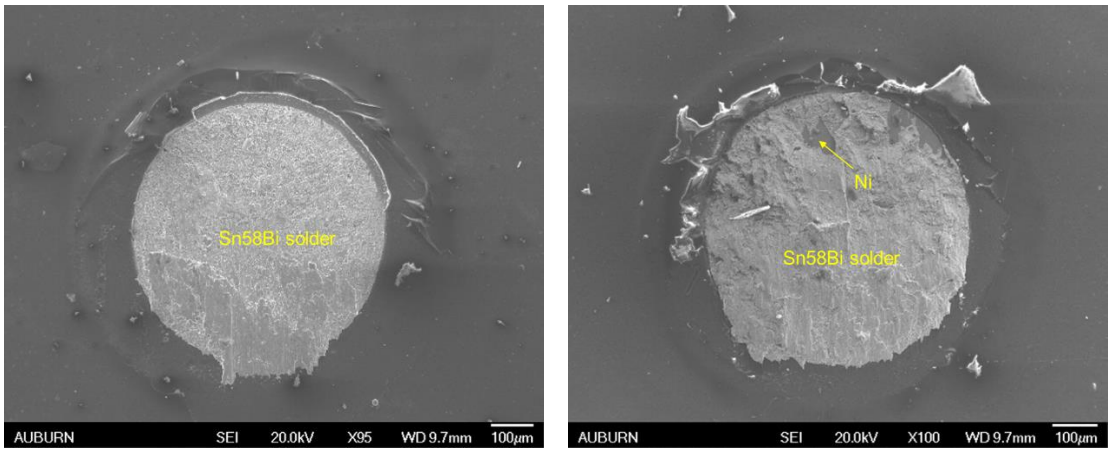

(d)

Figure 5-6 Top views at low and high rates of shear strain: (a) Sn-Ag; (b) SAC-Bi; (c) Sn-42Bi; and (d) Sn58Bi

5.4 Shear Fatigue Results

Shear stress and shear strain were measured in the same manner during shear fatigue experiments. Weibull distribution involving two parameters was employed to quantify the fatigue life of the test vehicles at each stress amplitude in the shear fatigue cyclic test. The Weibull distribution with two parameters is indicated as follows:

$$R(t) = e^{-\left(\frac{t}{\theta}\right)^{\beta}} \qquad 5\text{-}2$$

where *R(t)* denotes the level of reliability; β, θ are the shape and scale parameters, respectively. The slope of the regression line was represented by the shape indicator. The scale coefficient, also known as the characteristic life, specifies cycles number for which the probability of failure is 63.2 %. Figure 5-7 (a-d) illustrates the Weibull distribution of the four solder alloys under four different stress amplitudes, with each dot representing the cycle fatigue test results. Random Sn orientation and secondary precipitation account for the variation throughout the fatigue life with the same amplitude of applied stress.

Using an empirical power equation, the typical fatigue life derived from the Weibull distribution was embedded as a parameter of the stress amplitude *P*, as follows:

$$N = a * P^{-c} \qquad 5\text{-}3$$

where *N* is the fatigue data for a specific stress amplitude, *a* s the substance constant, while *c* is the stress exponent, which reflects the solder alloy's fatigue ductility. The solder alloy's ductility decreases as the *c* value goes up.

Figure 5-8 depicts the fatigue life behavior versus the magnitude of the stress for all the tested solder alloys on a logarithmic scale. Due to the increased induced inelastic work during the cyclic fatigue test, an increase in stress value resulted a reduction in fatigue life. At all the stress amplitudes, the SAC-Bi solder outperformed the other three solders, with Sn-Ag having the worst fatigue performance. This is in line with previous findings that solder alloys containing both high Ag and Bi contents have better fatigue life than those containing only high Ag or Bi contents [3]. Sn42Bi was shown to have deteriorated fatigue characteristics at low stress amplitudes, although it gained significant shear strength compared with Sn58Bi at all shear strain rates. We believe that when subjected to large stress amplitudes, it would provide better fatigue

performance. The trend line shows that the Sn42Bi solder has a more prolonged fatigue life than the Sn58Bi solder at higher amplitudes.

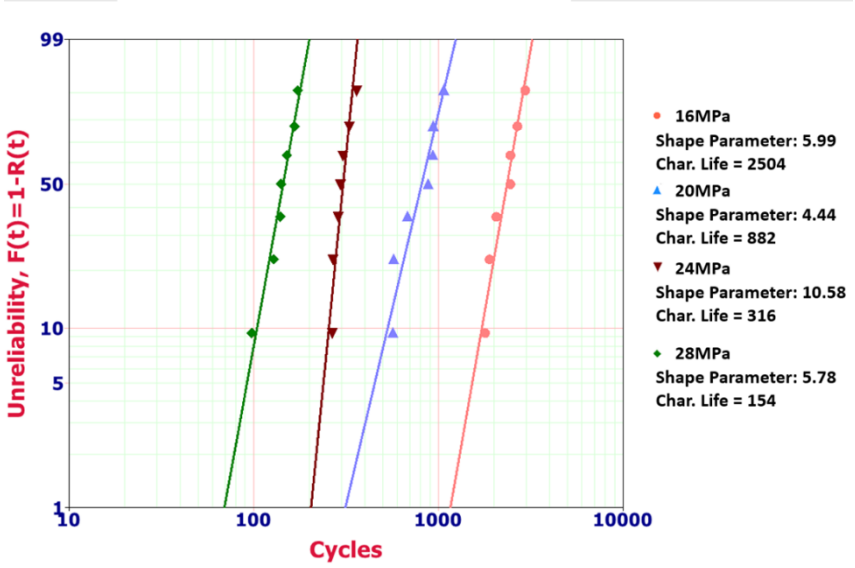

(a)

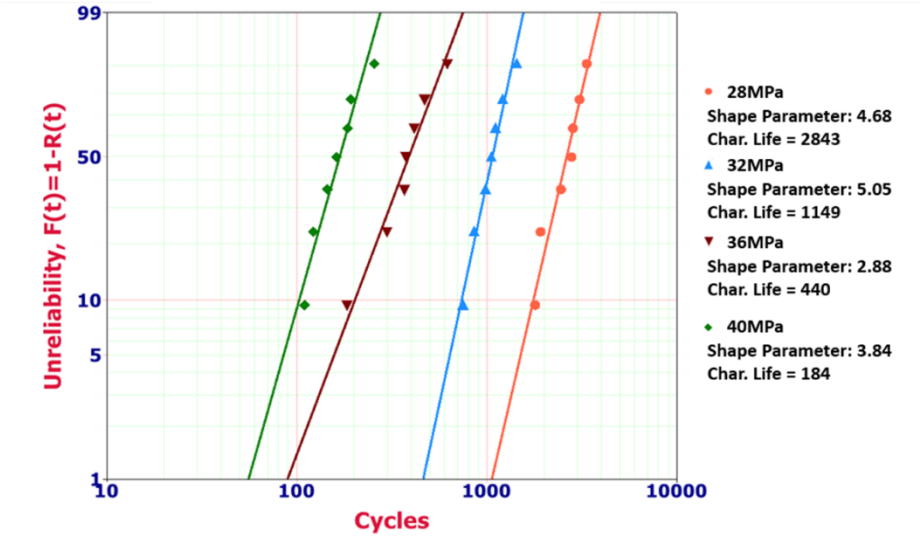

(b)

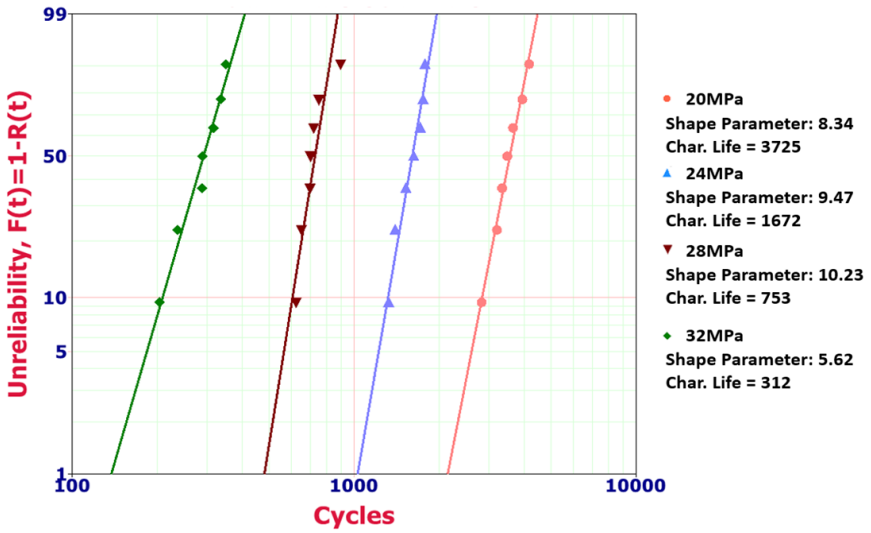

(c)

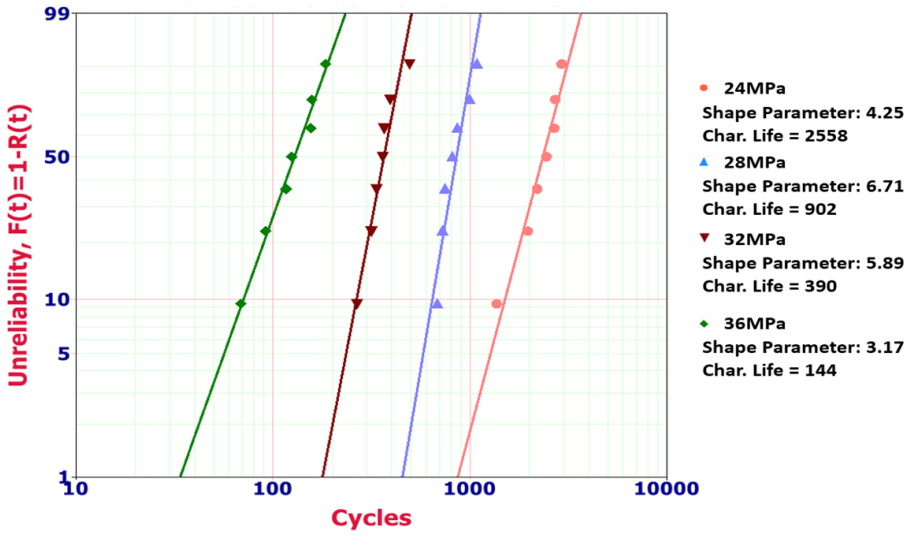

(d)

Figure 5-7 The fatigue life represented in Weibull plots of solder alloys for: (a) Sn-Ag; (b) SAC-Bi; (c) Sn-42Bi; and (d) Sn58Bi

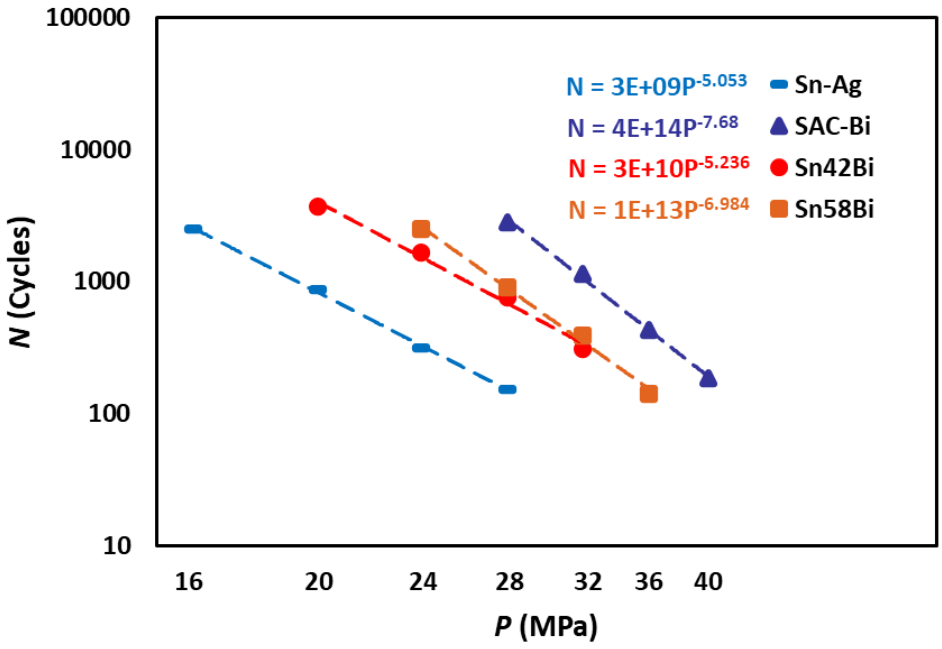

Figure 5-8 Solder alloy life characteristics as a function of stress amplitude

The behavior of solder joints under cyclic loading can be understood by monitoring the changes of hysteresis loops. Figure 5-9 shows a typical hysteresis loop for one individual Sn-Ag solder joint, which shares fatigue life that is the closest to calculated characteristic fatigue life, cycled in isothermal shear fatigue test. Indicated in Figure 5-9, two parameters can be determined for each cycle from the hysteresis loop - plastic strain range and inelastic work. Plastic strain range is the width of the hysteresis loop at 0 MPa, and inelastic work is the enclosed area within the hysteresis loop. With the help of programmed coding in MATLAB, the work per cycle and plastic strain range per cycle were estimated for each individual solder joint.

Figure 5.10 demonstrates the inelastic work per cycle as a function of cycles. The behavior of inelastic work per cycle can be identified as three main stages. Stage R1 shows a steep drop in the work per cycle for the first few cycles caused by the initial flatting and hardening. Stage R2 is a steady stage that accounts for about 90% of the fatigue life. Stage R3 accounts for the remaining of the fatigue life, where a sharp rise

of work per cycle is observed due to the initiation and propagation of crack in the solder joint.

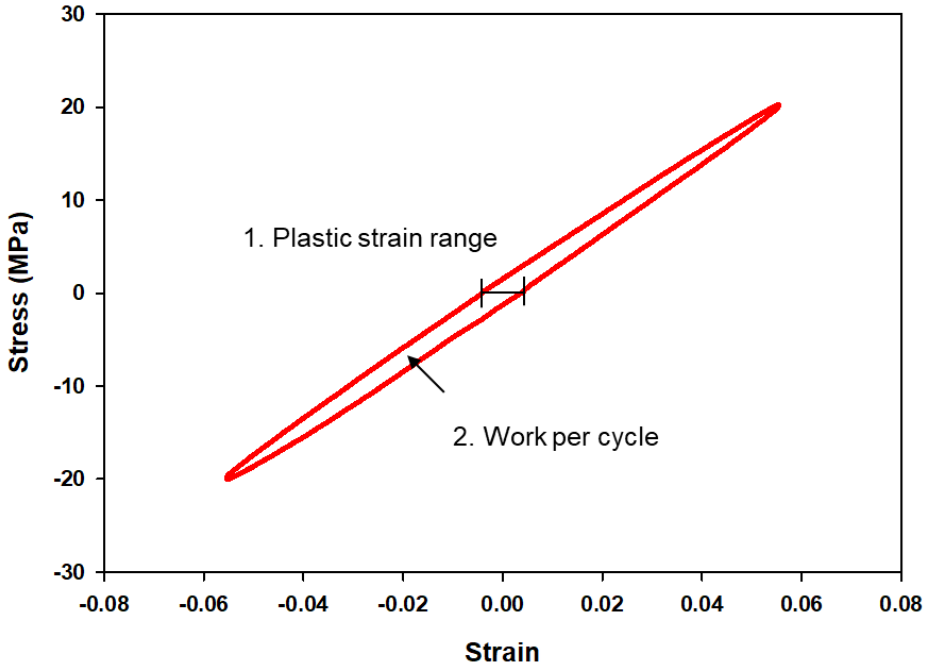

Figure 5-9 Hysteresis loop for a typical Sn-Ag solder joint cycled under 20 MPa

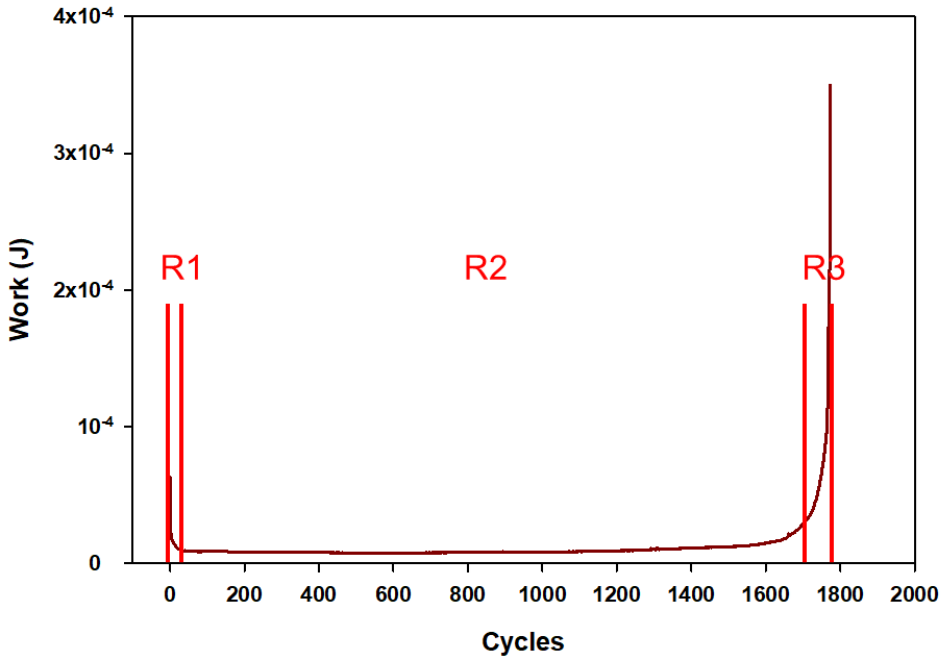

Figure 5-10 Inelastic work of Sn-Ag solder alloy under 16 MPa in stress control mode

Figure 5-11 shows the effect of stress amplitude on the behavior of inelastic work for Sn-Ag solder alloy. Four stress amplitudes ranging from 16 MPa to 28 MPa were tested in the same cycling environment. What can be clearly seen in this figure is the trending that larger stress amplitude tends to incur more work per cycle in all the three stages, thus less fatigue life.

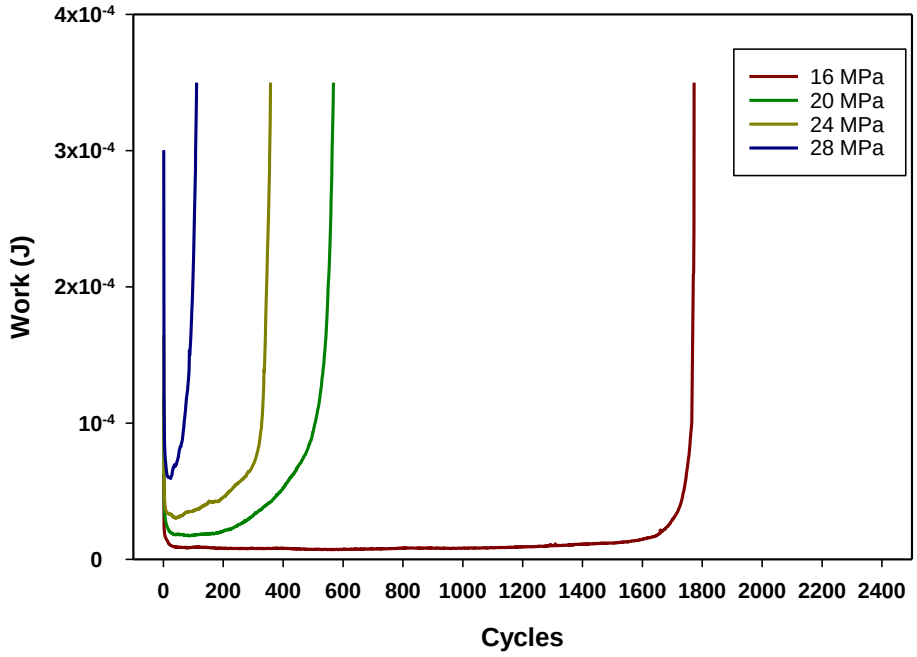

Figure 5-11 Inelastic work of M30 solder alloy under different stress amplitudes

Under various stress amplitudes, the average enclosed area of the steady-state hysteresis loops was employed to determine the inelastic work per cycle. The work per cycle for Sn42Bi is depicted in Figure 5-12 for the four stress amplitudes. As displayed in Figure 5-12, with increasing stress amplitude and more variations in work per cycle, more inelastic work per cycle was induced. The trend of the average work per cycle estimated from the seven specimens showed a non-linear fitting of the stress amplitudes. The typical fatigue life of solder alloys under varied stress amplitudes can be associated with the average work per cycle employing Morrow energy model as follows:

$$N = C^{1/m} * W^{-1/m} \qquad 5\text{-}4$$

where N (cycles) is the typical fatigue life, W (J) denotes the steady-state average work per cycle, C denotes the ductility coefficient of a material fatigue, and m denotes the exponent of a fatigue. Figure 5-13 depicts a log-log plot of the typical fatigue life vs the inelastic work per cycle for all tested solder alloys under different stress amplitudes. The fatigue data fit well with the stress amplitude obtained using the Morrow energy model, as illustrated in Figure 5-13. This also explains why the work per cycle data in Figure 5-12 were fitted exponentially. Table 5-2 lists the estimated the fatigue ductility coefficient C and fatigue exponent m for each of the four solder alloys.

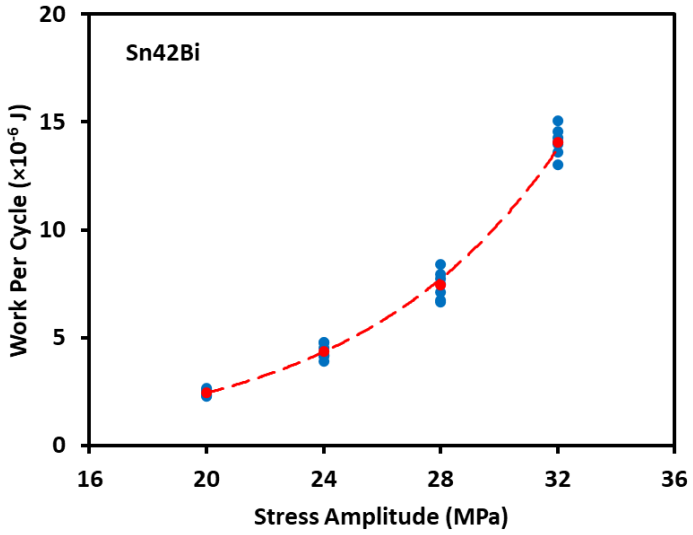

Figure 5-12 Work per cycle results for Sn42Bi

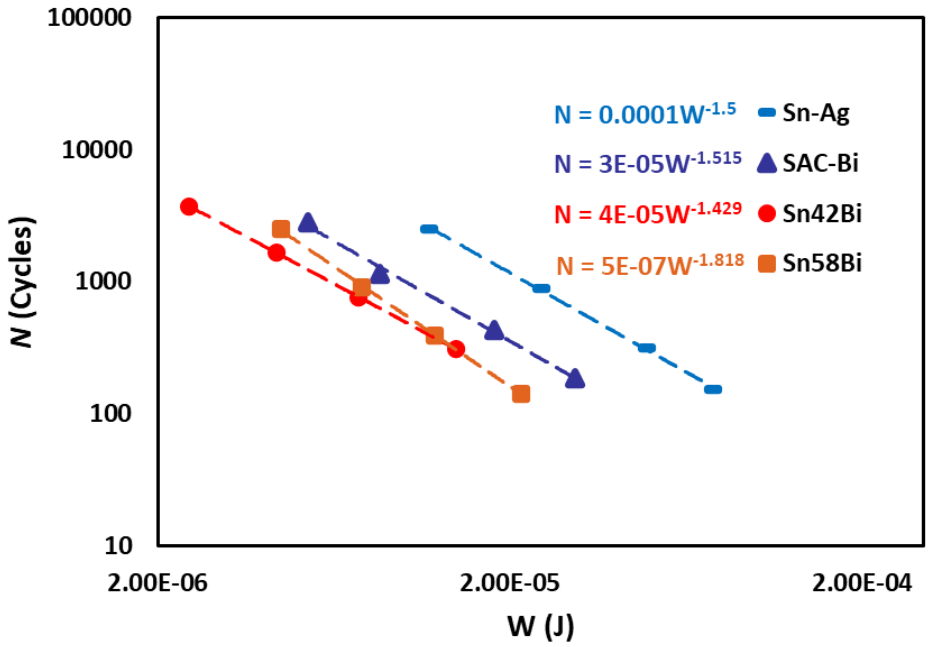

Figure 5-13 Morrow energy model fitting curves for solder alloys

Table 5-2 Summary of constants fitted in Morrow's energy model

Solder Alloy	Fatigue ductility, C	Fatigue exponent, m
Sn-Ag	2.15×10^{-3}	0.667
SAC-Bi	1.03×10^{-3}	0.660
Sn42Bi	8.36×10^{-4}	0.700
Sn58Bi	3.42×10^{-4}	0.550

Figure 5-14 shows the evolution of plastic strain range per cycle for a typical Sn-Ag solder alloy example cycled under 16 MPa stress amplitude. The evolution process mainly undergoes three stages. In stage P1, plastic strain drops drastically owing to initial hardening. After that, the plastic strain keeps steady in stage P2, and then increases exponentially until complete failure in Stage P3 caused by crack initiation and propagation. Figure 5-15 illustrates the comparison of the plastic strain range of Sn-Ag solder joints cycled under different stress amplitudes. Interpreting the figure comes the evident conclusion that with higher stress amplitudes, the plastic strain range per cycle in steady stage P2 demonstrates larger numbers. At the same time, severe stress amplitudes would lead to less fatigue life, as expected.

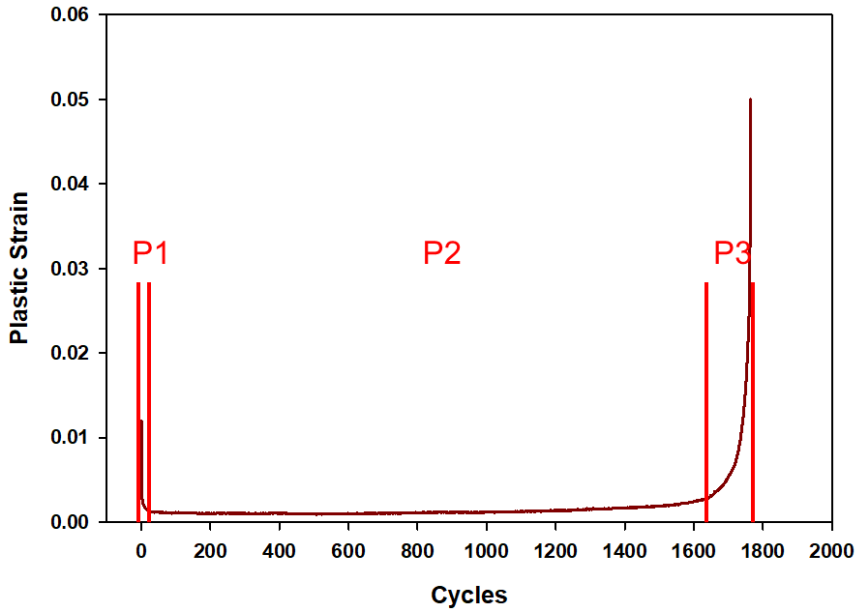

Figure 5-14 Plastic strain range of Sn-Ag solder alloy under 16 MPa

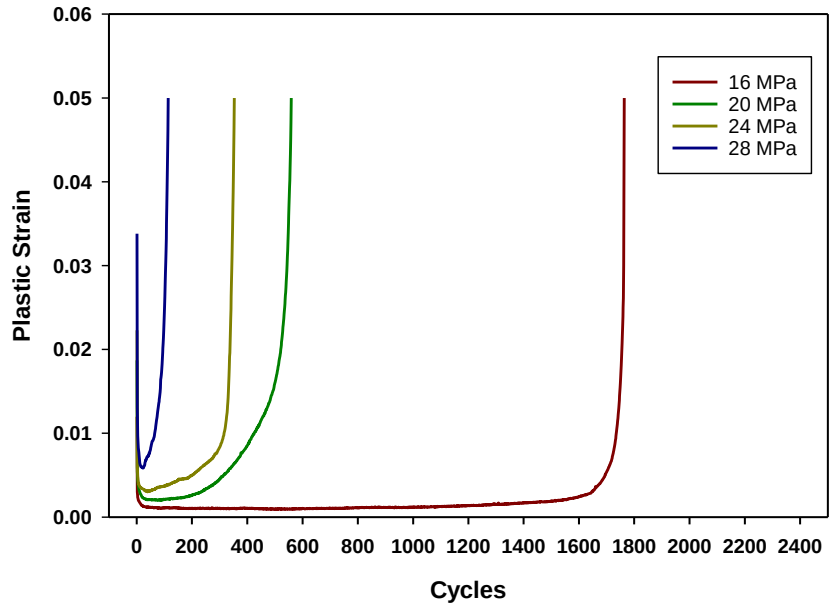

Figure 5-15 Plastic strain range of Sn-Ag solder alloy under different stress amplitudes

Similarly, the plastic strain range per cycle was determined employing steady-state hysteresis loops. The plastic strain range of the steady hysteresis loops determined for each Sn42Bi specimen is presented in Figure 5-16. A higher range of plastic strain per cycle was observed when the stress amplitude was increased. From 20MPa to 28MPa,

there was a considerable increase in the data variation for the plastic strain range, which remained at the same level when jumping to 30MPa. The Coffin-Manson model can explain the exponentially growing plastic strain range with stress amplitude as follows:

$$N = \delta^{1/\alpha} * \Delta\varepsilon_p{}^{-1/\alpha} \qquad 5\text{-}5$$

where N (cycles) donates the typical fatigue life, $\Delta\varepsilon_p$ (mm/mm) donates the average range of plastic strain per cycle, δ is the material coefficient of fatigue ductility, and α donates the fatigue exponent. Figure 5-17 shows the characteristic fatigue life as a function of the range of a plastic strain on a logarithmic scale. The Coffin-Manson equations with a high R-square are represented by dashed lines. Table 5-3 presents the Coffin-Manson model constants for all the tested solder alloys.

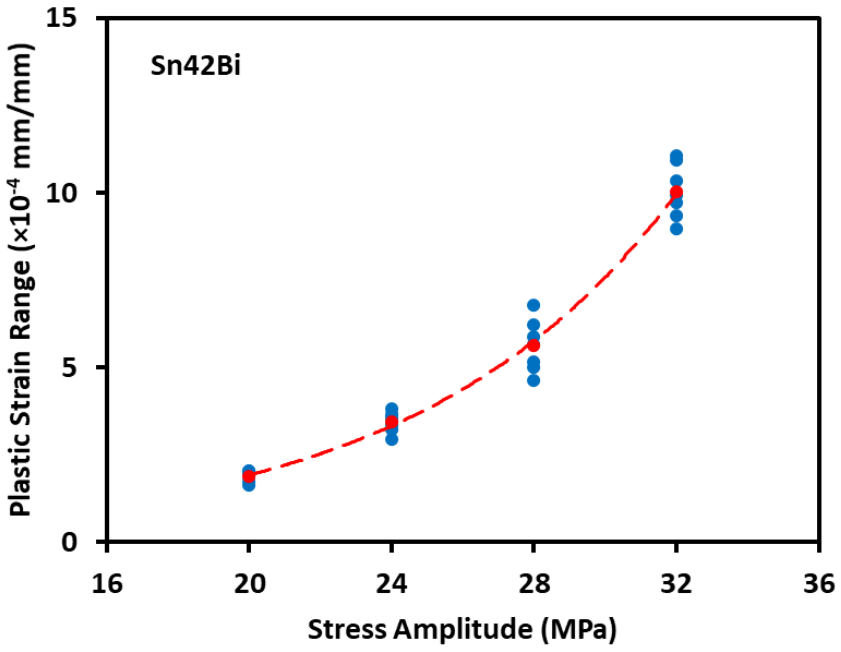

Figure 5-16 Plastic strain results for Sn42Bi

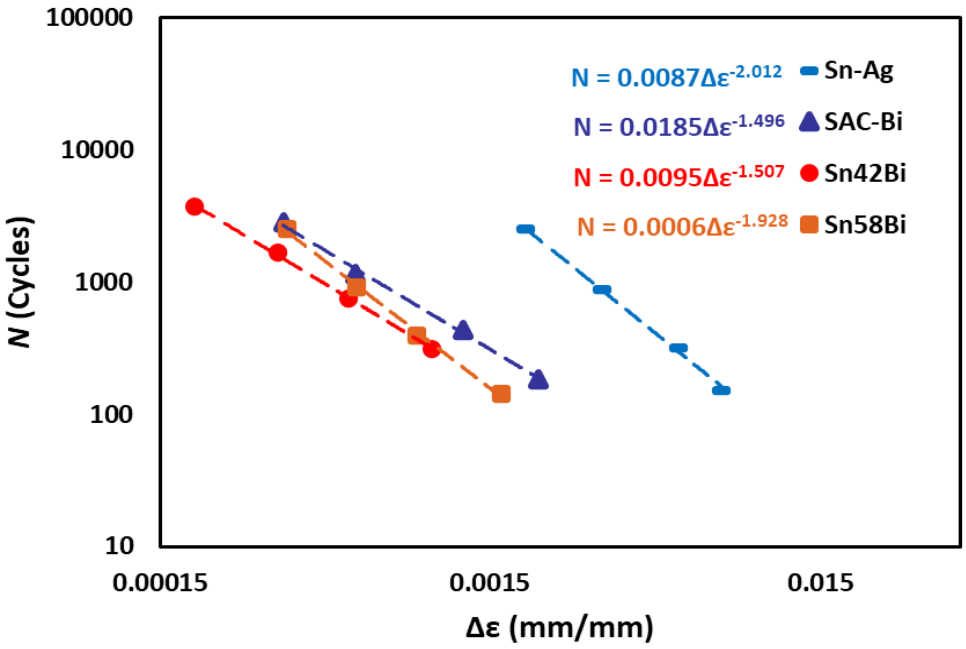

Figure 5-17 Fitted curves of Coffin-Manson model for solder alloys

Table 5-3 Summary of constants fitted in Coffin-Manson model

Solder Alloy	Fatigue ductility, θ	Fatigue exponent, α
Sn-Ag	9.46×10^{-2}	0.497
SAC-Bi	6.95×10^{-2}	0.668
Sn42Bi	4.55×10^{-2}	0.664
Sn58Bi	2.13×10^{-2}	0.519

The top views of the failed solder joints following shear fatigue testing are shown in Figure 5-18 (a-d). It is worth mentioning that in the fatigue test, the Sn-Ag solder displayed a typical mixed failure mode, however in the shear strength test, it demonstrated a ductile failure mode. In the fatigue test, SAC-Bi exhibited the same brittle failure behavior. Although the two LTS had the same mixed failure mode, the exposed Ni layer area was noticeably different.

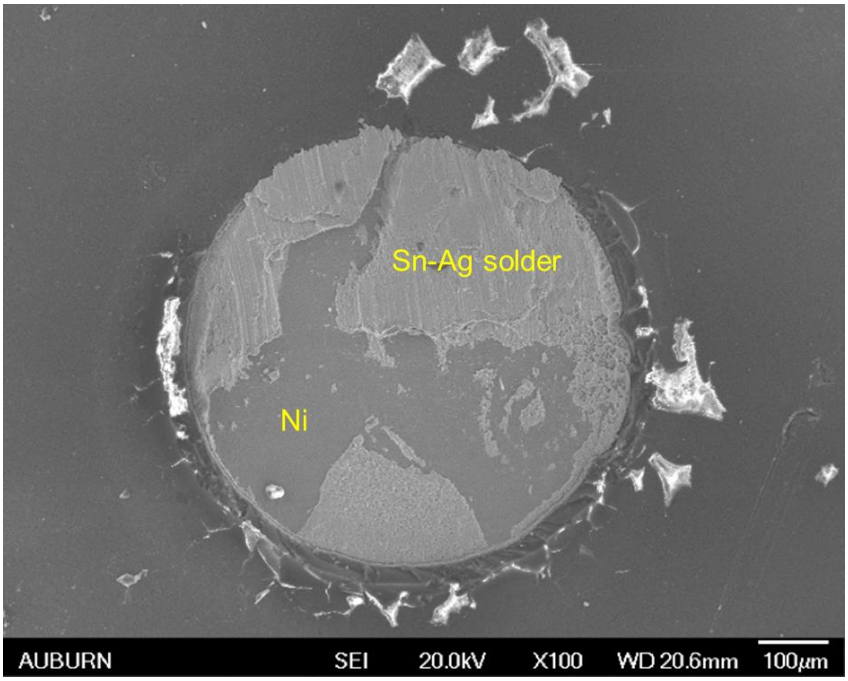
Sn-Ag solder
Ni
AUBURN SEI 20.0kV X100 WD 20.6mm 100μm

(a)

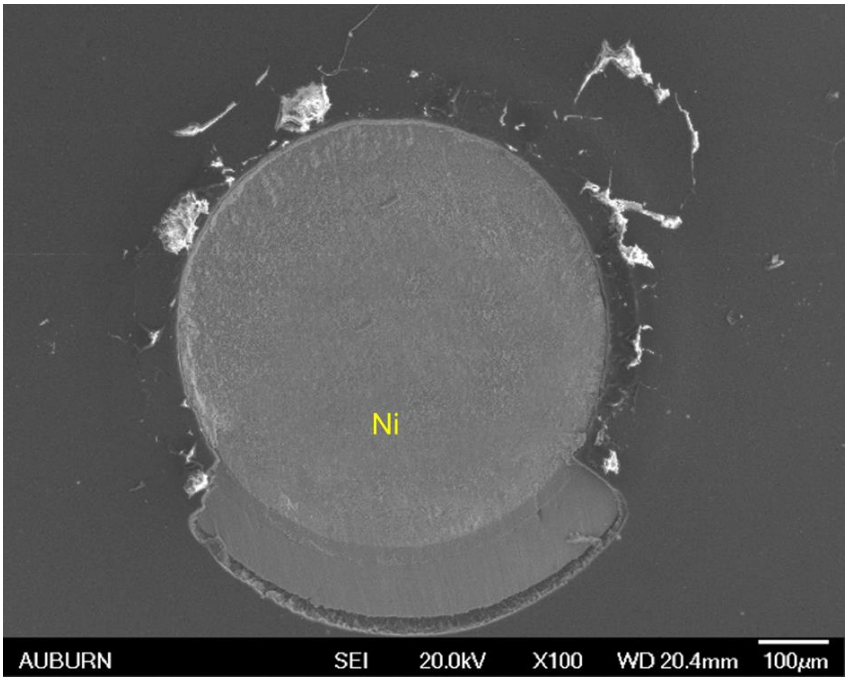
Ni
AUBURN SEI 20.0kV X100 WD 20.4mm 100μm

(b)

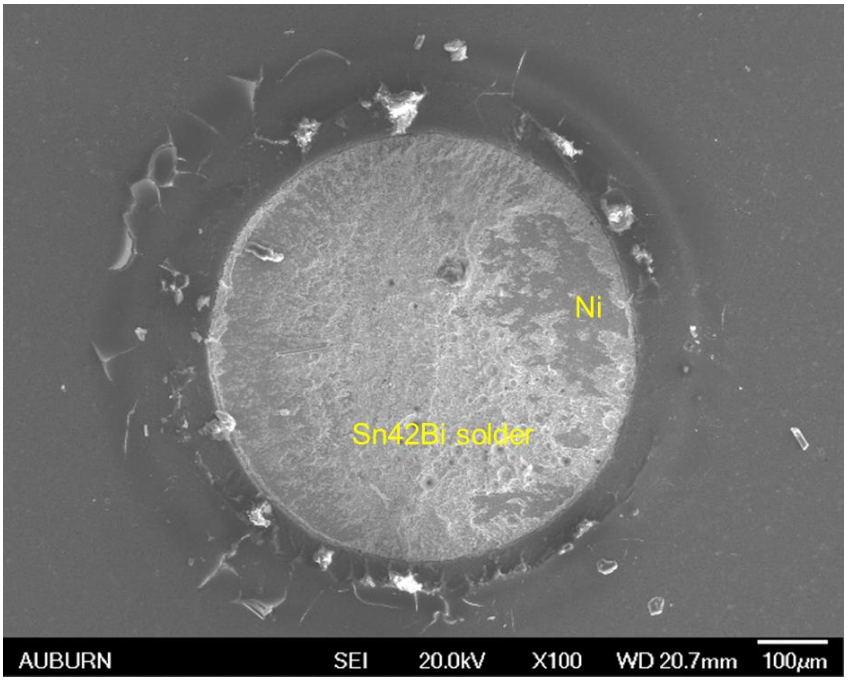

(c)

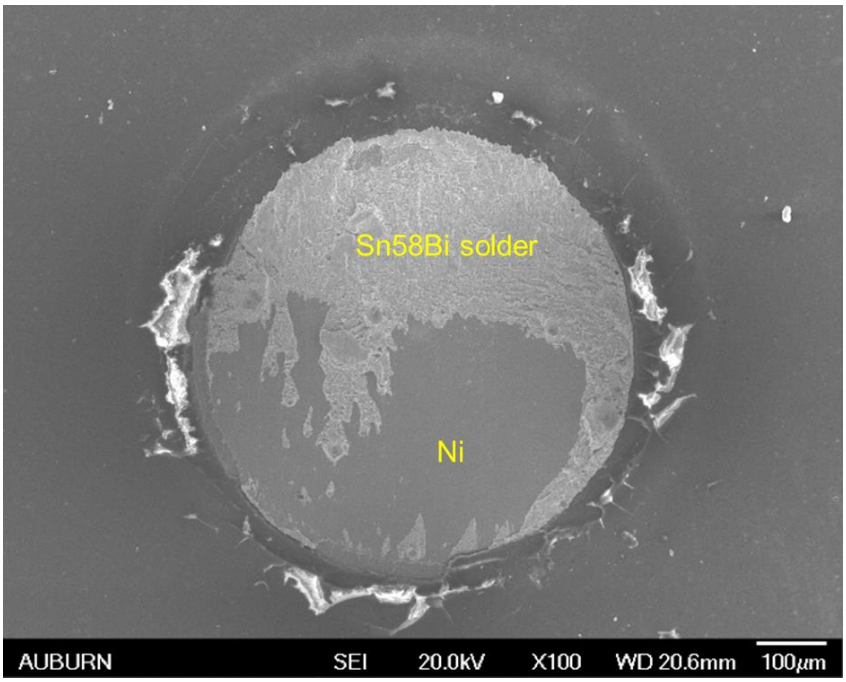

(d)

Figure 5-18 Top views of failed solder joints for: (a) Sn-Ag; (b) SAC-Bi; (c) Sn-42Bi; and (d) Sn58Bi

5.5 Effect of Surface Finish

The fatigue life of Sn-Ag solder alloy with OSP surface finish was investigated in the same experimental setup and testing environment, as stated in the test plan. Figure 5-

19 shows the fatigue life of Sn-Ag solder alloy with OSP surface finish in Weibull plot. Four stress amplitudes were applied to corelate fatigue life with stress amplitude for Sn-Ag solder alloy in a power equation, as is shown in Figure 5-20. The ductility exponent, *c*, of Sn-Ag solder alloy with ENIG surface finish is larger than the solder alloy with OSP surface finish, which indicates that ENIG surface finish would result in enhanced embrittlement characteristic. However, the fatigue life of Sn-Ag solder alloy with OSP surface finish demonstrates preferably fatigue performance than ENIG surface finish under all the stress amplitude.

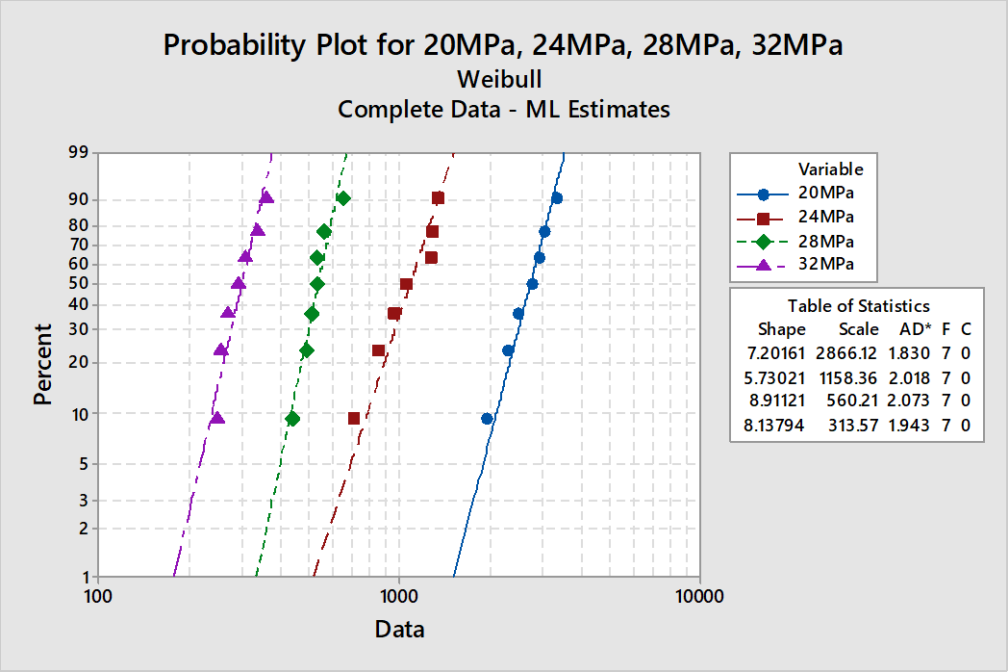

Figure 5-19 Weibull plot of Sn-Ag solder joint with OSP surface finish

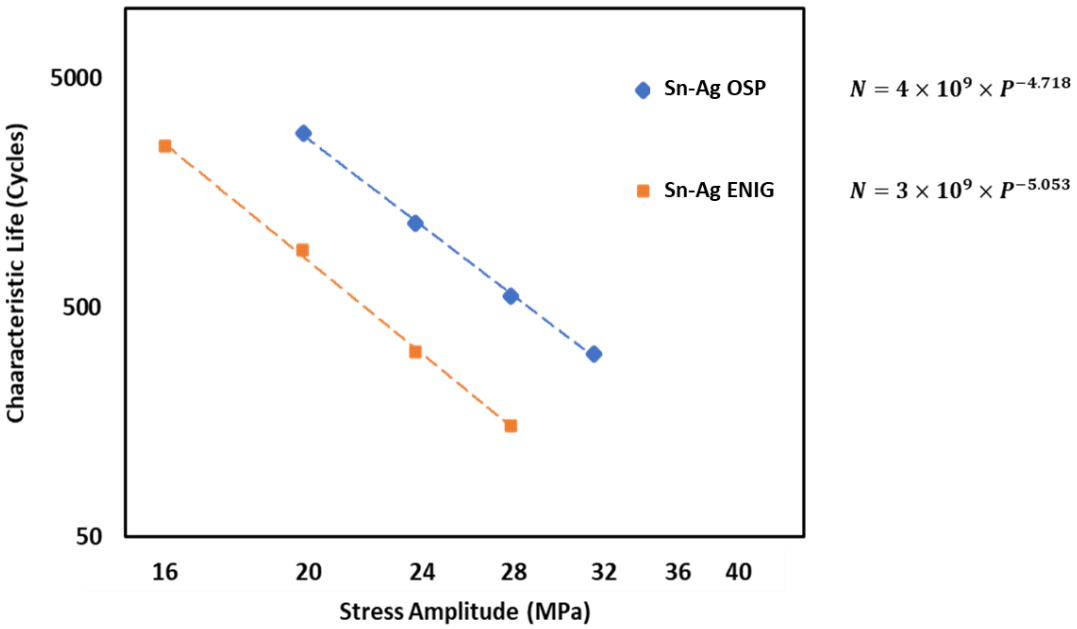

Figure 5-20 Characteristic life of Sn-Ag solder alloy as a function of stress amplitude

Figure 5-21 and Figure 5-22 show the fitted curves of Morrow energy model and Coffin-Manson model for Sn-Ag solder alloy with the interested two surface finishes. Table 5-4 and Table 5-5 summarize the comparison constants from the two models.

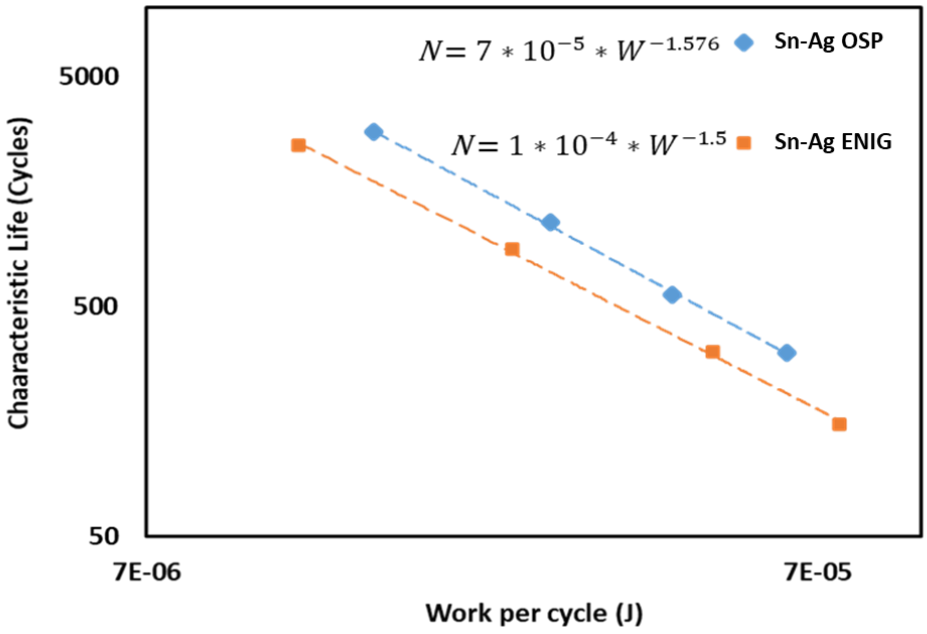

Figure 5-21 Fitted curves of Morrow energy model for M30 solder alloys

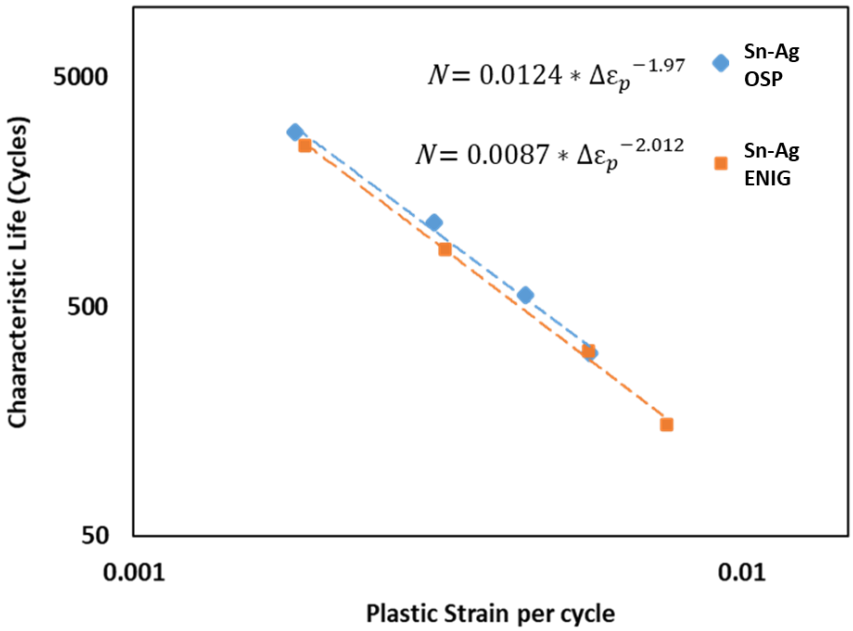

Figure 5-22 Fitted curves of Coffin-Manson model for M30 solder alloys

Table 5-4 Summary of Morrow energy model coefficients of M30

Solder Alloy		**m**	**C**
Sn-Ag	ENIG	0.667	2.15×10^{-3}
Sn-Ag	OSP	0.635	2.31×10^{-3}

Table 5-5 Summary of Coffin-Manson model coefficients of M30

Solder Alloy		**m**	**C**
Sn-Ag	ENIG	0.497	9.46×10^{-2}
Sn-Ag	OSP	0.508	0.108

Figure 5-23 shows the IMC morphology of Sn-Ag solder alloy with OSP surface finish. Compared with the morphology of ENIG surface finish, Ni layer was not presented in this case. The Cu pad reacted with Sn, forming another Cu_6Sn_5 layer. Figure 5-24

demonstrates a typical failed Sn-Ag solder joint with OSP surface finish. A clear ductile failure mode is presented with bulk solder covered on the copper pad.

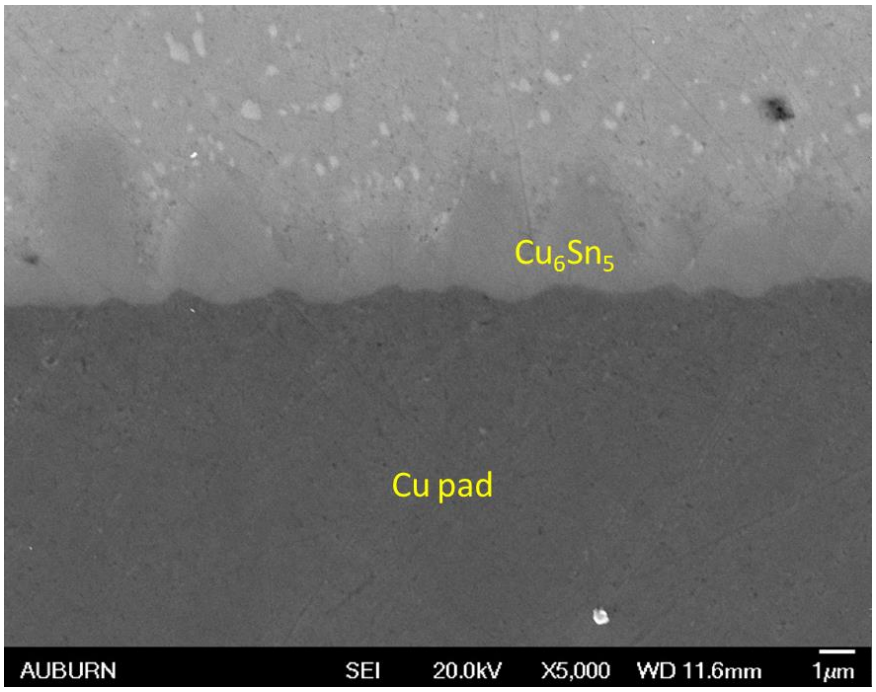

Figure 5-23 Micrograph of Sn-Ag solder alloy with OSP surface finish

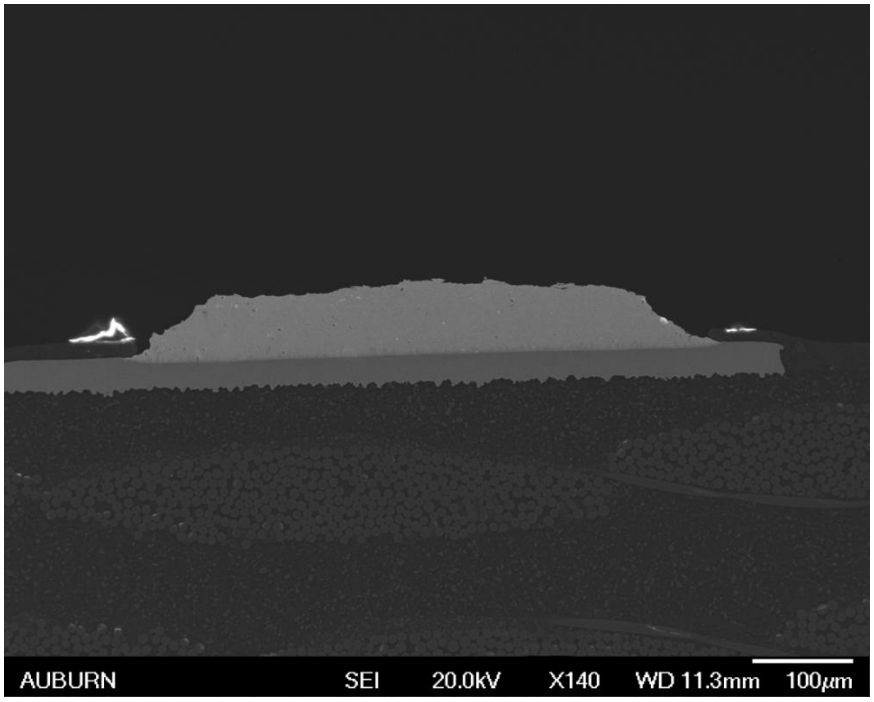

Figure 5-24 Cross-section view of failed Sn-Ag solder alloy with OSP surface finish

5.6 Conclusion

The shear and fatigue properties of several solder alloys with an ENIG surface finish, like Sn-Ag, SAC-Bi, Sn42Bi, and Sn58Bi, were examined in this study. The effects of shear strain rate (0.01, 0.1, and 1 s^{-1}) on shear strength and the influence of stress amplitude on shear fatigue were explored. The effect of surface finish on Sn-Ag solder alloy was discussed. The SEM and EDS were used to determine the microstructure and failure mechanisms of each solder alloy. The following is a summary of the study results:

1. For all tested solder alloys, the shear strength and variation increased as the shear strain rate goes up.
2. Due to the increased flow stress, the high shear strain rate changed the failure mode of SAC-Bi, Sn42Bi, and Sn58Bi. The shear strain rate was shown to be less sensitive to Sn-Ag.
3. As the stress amplitude increased, more damage to the solder joints was induced every cycle, reducing the typical fatigue life.
4. SAC-Bi outperformed all the tested solder alloys in the shear strength and shear fatigue tests, whereas Sn-Ag exhibited the lowest results.
5. The Morrow energy and Coffin-Manson models were found to be suitable for all the tested solder alloys.
6. The Sn-Ag solder alloy with the OSP surface finish demonstrated better interfacial toughness than that with the ENIG surface finish.

5.7 Contribution

The quality and reliability of solder connections in electronics packaging can be assessed by investigating their shear and fatigue performance. The robustness of the attachment of the solder ball to the package is estimated using a destructive method in shear and fatigue tests. The failure mode analysis and the fundamental understanding of the testing process are necessary in determining the reliability of solder joints accurately.

This study compared the failure mode and shear strength of different solder joints at various shear strain rates. This provided insights into accessing the reliability of solder joints. In terms of fatigue test, it is worth noting that isothermal cycling tests were conducted in this study, which undergone significant differentiated failure mechanism compared to thermal cycling. As a result, one cannot simply extrapolate the life of realistic components experiencing temperature changing environments by the presented life prediction models and the corresponding parameters. For example, the OSP surface finish was found to provided better fatigue life than the ENIG surface finish in this study. However, the ENIG surface finish usually outperforms the OSP surface finish in thermal cycling test mainly because of the different failure mechanisms, the much lower deformation rate, and the creep effect during dwell times. The Ni layer of the ENIG surface finish also inhibits the growth of IMC layer during thermal cycling test, which further improves the reliability of solder joints featured the ENIG surface finish.

To realize the extrapolation, the true parameters, such as plastic strain, inelastic work, and stress, of the realistic component must first be obtained from the finite element model. These data can then be fitted in the above-mentioned Coffin-Manson and Morrow energy models for more reliable predictions.

Chapter 6 Assessing the SAC305 Solder Joint Fatigue in BGA Assembly Using Strain-Controlled and Stress-Controlled Approaches

6.1 Introduction

The high-temperature variations in electronic packages, particularly during the operation of high power-density devices or in the presence of harsh environmental conditions, are the primary causes of fatigue failure of solder joints in practical service life [93,94]. The weakest interconnected solder joints fail because of thermal stress caused by an imbalance in the coefficient of thermal expansion of various component materials [95–97]. Because there is a considerable distance to the neutral point and a more significant percentage of thermo-mechanical stress, corner joints in BGA components often exhibit early failure [98]. The existing literature on the fatigue characteristics of solder alloys with either rectangular or circular cross-sections employed bulk specimen testing [60,99–101]. However, because real solder joints have various microstructures, differences in their mechanical and fatigue characteristics have been reported. In contrast, rapid solidification during the reflow process occurs because the reduced solder joint volume can result in a finer grain size in the as-cast microstructure [28,102–104]. In addition, the surface finish considerably affects the composition and growth of the IMC layer, significantly affecting its reliability [105]. This further influenced the crack propagation and produced several failure types [22].

Several factors affect the fatigue life of the solder alloys. The decreased strain rate was observed to diminish the fatigue life of solder joints due to the higher work being performed in each cycle in stress-controlled and strain-controlled testing [27,106]. If the strain rate is low, the fracture starts at the interphase borders; however, if the strain rate is high, the crack expands in the Sn-dendrites [27,107]. A lower fatigue life results from the increased damage accumulation in each cycle when the stress amplitude or total strain range is higher [80,108]. Additionally, it was observed that different stress amplitudes in the cyclic fatigue test dislocated the cell structures and dramatically diminished the fatigue resistance, which led to a breakdown of Miner's rule [109]. Using a strain-controlled test to examine the impact of temperature on the fatigue characteristics of Sn-Ag solder, Kanchanomai and Mutoh [24] found that the fatigue ductility coefficients are temperature-dependent. They highlighted that the primary deformation process could be a pipe-diffusion-controlled dislocation climb. In stress-controlled experiments, OSP and ImAg surface finishes were shown to exhibit better fatigue performance than ENIG surface finishes for various doped solder alloys, according to Su and Jian [105]. Moreover, the fatigue characteristics of certain solder joints were enhanced by adding Ag and Bi to the solder alloys [110]. According to Kariya and Otsuka [111], adding Bi, Cu, In, and Zn to Sn-3.5Ag solder increases the tensile strength of dog-bone specimens and reduces their ductility, which reduces the fatigue life in strain-controlled testing. According to published studies [22,27,105–107,112,113], micro-alloying elements including, Cu, Bi, In, Ni, and Sb, may increase solder junction fatigue resistance because of the solid solution hardening process of the β-Sn lattice. It has been reported that the dislocation pinning effect of Ag3Sn particles contributes to enhanced thermal fatigue performance with increasing Ag content

[78,114,115]. However, the severe thermal cycling profile revealed a decreased sensitivity of the typical fatigue life to Ag content [116,117].

Numerous studies have used various fatigue criteria to characterize the failure of strain-controlled techniques. The ASTM standard [118] recommends a maximum load drop of 50% for bulk samples to indicate fatigue failure. Kanchanomai et al. [24,27,108] defined the fatigue life as a 25% drop in the maximum load, which marked the beginning of the load drop acceleration. However, to define fatigue failure, a maximum load drops of 90% was used for individual solder joints [67]. According to Lee et al. [68], the definition of applicable failure for a solder joint is significantly dependent on its composition. Using a fatigue test to assess the resistance of BGA solder joints, Park et al. [23,28] observed that failure occurred at around a 50% maximum load drop.

Although some studies have focused on more realistic individual solder joints [67,68,79,119,120] and BGA solder joints [23,28,121], researchers have thoroughly investigated the fatigue behavior of solder alloys using large bulk samples. Numerous relevant aspects have been investigated in many influential factors, including strain rate (frequency), surface finish, stress amplitude, strain level, aging, and temperature. Fatigue ductility and fatigue exponent parameters in Coffin-Manson model and Morrow energy model were estimated in many studies [105][89][122], where their values were found dependent on specimen shape and size, cycling frequency, solder microstructure, definition of failure, and assemble configuration. To the best of the authors' knowledge, no study has been conducted on BGA solder joints utilizing a stress-controlled approach. Instead, strain-controlled methods have been used in limited work, primarily because of the ease of controlling the strain during the fatigue test rather than stress. Consequently, strain-controlled and stress-controlled tests have not yet been compared. In strain-controlled testing, the ambiguity of the failure

criteria must also be addressed. In this study, the fatigue behavior of BGA solder joints was examined using SAC305 solder alloys. Both stress-controlled and strain-controlled profiles were used for comparison. A new approach for defining fatigue failure in strain-controlled tests was proposed. In addition, the influence of the surface finish was examined.

6.2 Stress-controlled test

In stress-controlled tests, the absolute values of the maximum and minimum loads were identical. A typical stress-strain hysteresis loop for the SAC305 test vehicle with an OSP surface finish subjected to a stress level of 20 MPa is shown in Figure 6-1. The inelastic work of the cycle is defined as the enclosed area within the hysteresis loop. The breadth of the hysteresis loop at 0 MPa was used to determine the plastic strain range. MATLAB was implemented to compute both parameters. Figure 6-2 depicts the progression of the stress-strain hysteresis for SAC305 at the same stress level of 20 MPa. A slight change in the hysteresis loop was observed for the first 2,000 cycles. Then, the enlarged hysteresis loop at cycle 4,000 with more inelastic work and a larger plastic-strain range. The hysteresis loop further extends, as indicated by the 5,000 cycles.

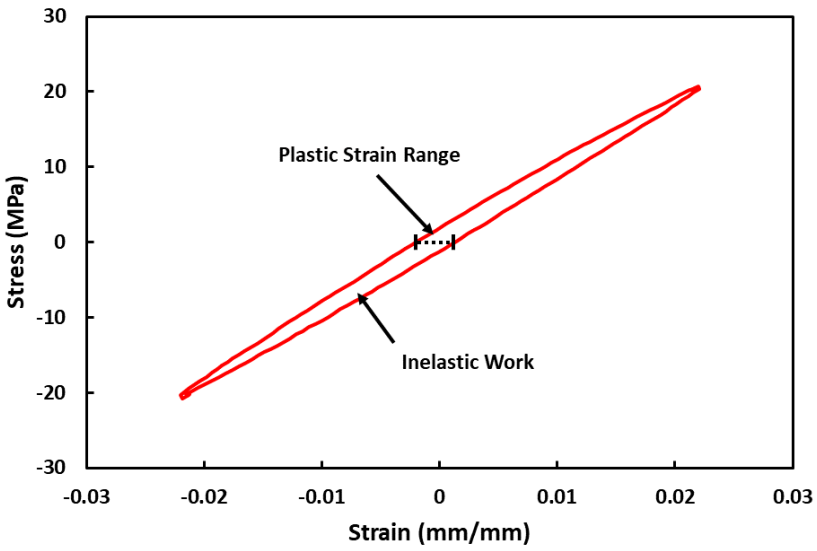

Figure 6-1 Typical hysteresis loop of SAC305 with OSP surface finish

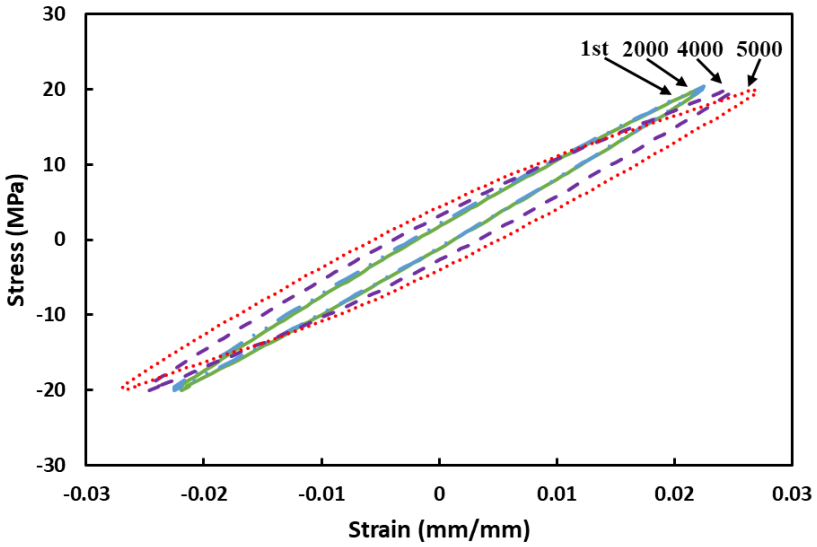

Figure 6-2 Evolution of hysteresis loop for SAC305 with OSP surface finish at 20MPa

The evolution of inelastic work per cycle in the stress-controlled mode is better visualized in Figure 6-3, which is typically classified into two regions: a steady region that accounts for most of the life; and an exponentially increased phase caused by the initiation and propagation of significant cracks. The fatigue life was estimated at the end of region 2. Three zones have been identified by Ming et al. [89]. In contrast, the inelastic work per cycle development for individual solder joints also initially included

an additional rapid reduction due to early hardening. The first region was mainly attributed to the flattening of the solder joint in the contact area. The first region was not observed for the BGA solder joints because the substrates were glued onto the fixtures instead of being probed using shear. Consequently, this investigation identified only two zones. Figure 6-4 illustrates the work development per cycle under stress values of 20 MPa, 24 MPa, 28 MPa, and 32 MPa. The inelastic work per cycle of the steady region was larger for higher stress levels, indicating that more damage occurred in each cycle. In addition, higher stress levels decreased fatigue life.

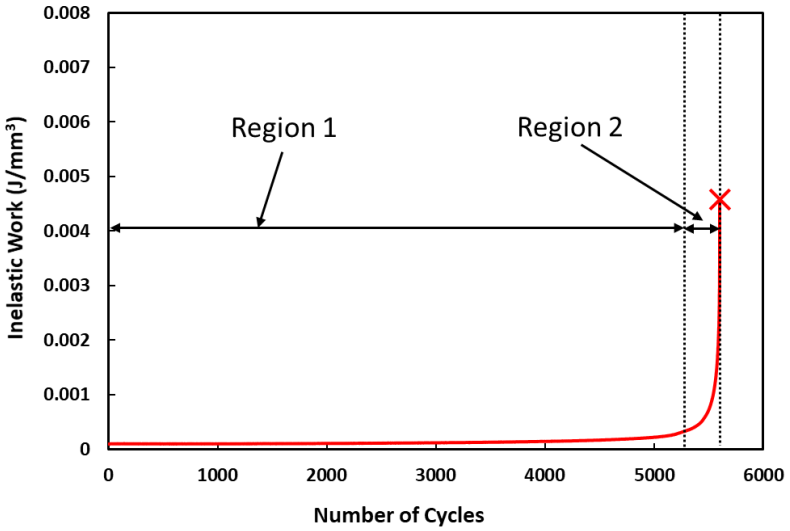

Figure 6-3 Evolution of inelastic work per cycle for SAC305 with OSP surface finish at 20MPa

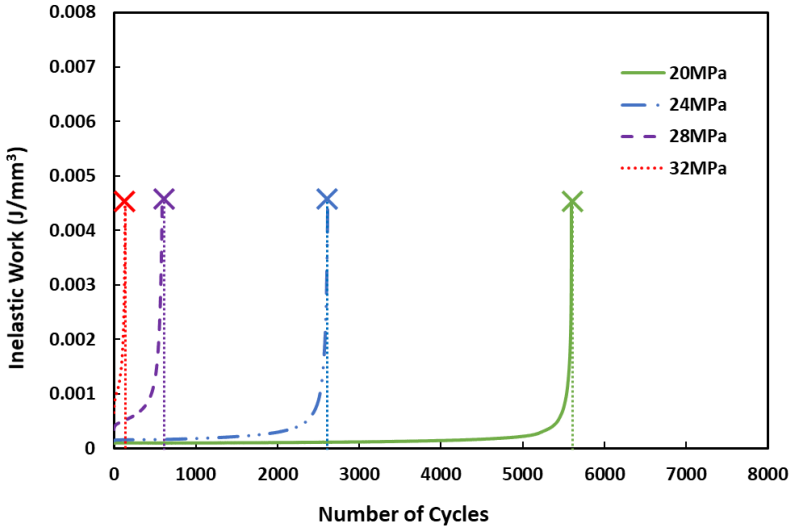

Figure 6-4 Inelastic work to number of cycles of SAC305 OSP solder joints in stress-controlled test

Figure 6-5 shows the evolution of the plastic strain range over the fatigue life of SAC305 with the OSP surface finish cycled under a 20MPa stress level. Similarly, the curve depicts two zones. The steady-state region continues until ultimate failure, which is indicated by a significant increase in the plastic strain in region 2. Figure 6-6 compares the evolution of the plastic strain range under four different stress levels. Higher stress levels resulted in increased plastic strain in the steady state. Consequently, more damage was acquired in every cycle, resulting in a shorter fatigue life.

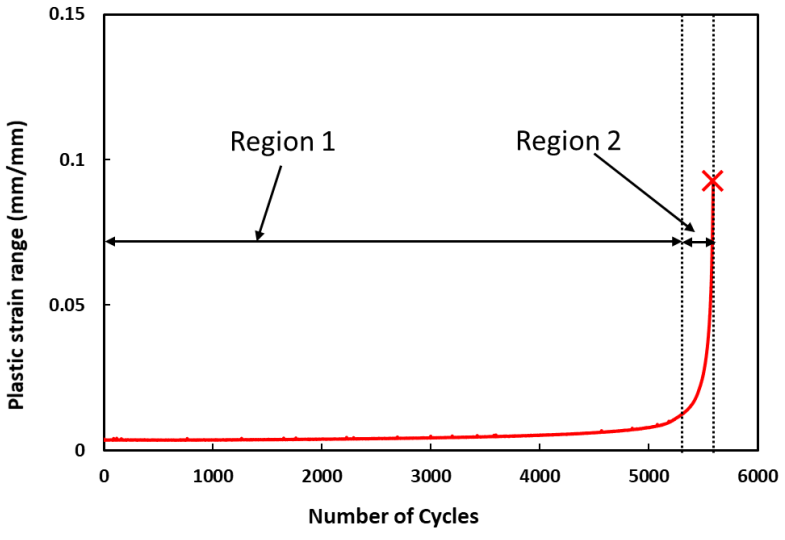

Figure 6-5 Evolution of plastic strain per cycle for SAC305 with OSP surface finish at 20MPa

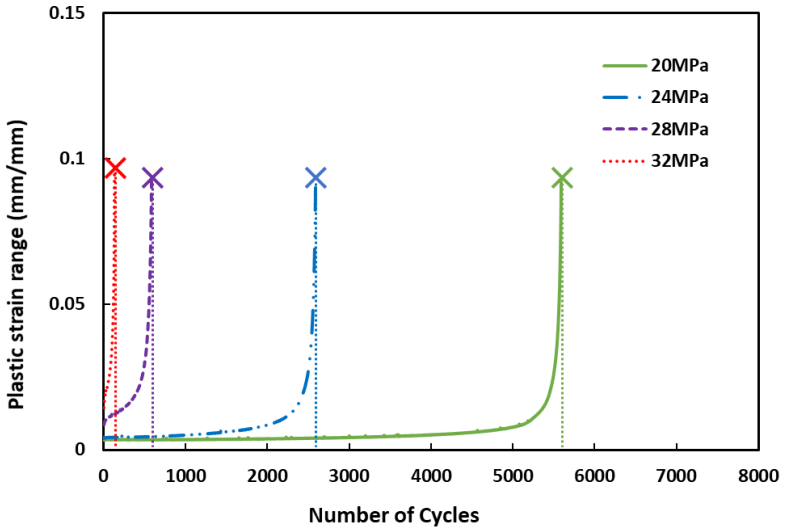

Figure 6-6 Plastic strain to number of cycles of SAC305 OSP solder joints in stress-controlled test

As previously stated, in the stress-controlled test, the fatigue life of the BGA solder joints is defined as the cycle by the end of region 2. A two-parameter Weibull distribution was used to compute the test vehicles' characteristic fatigue life. Figure 6-7 shows the fitted fatigue life of SAC305 with the OSP surface finish at stress levels of 20, 24, 28, and 32 MPa. The five data points reflect the fatigue life of the five testing specimens at each stress level. The middle regression line indicates that these data points match well with the Weibull distribution. The 95% confidence range of the Weibull distribution, depicted by the two curved lines, included all the fatigue data. The slope of the regression line is represented by the shape parameter. The characteristic fatigue life, which is a scale parameter, provides the cycle number at which failure occurs with a 63.2% probability.

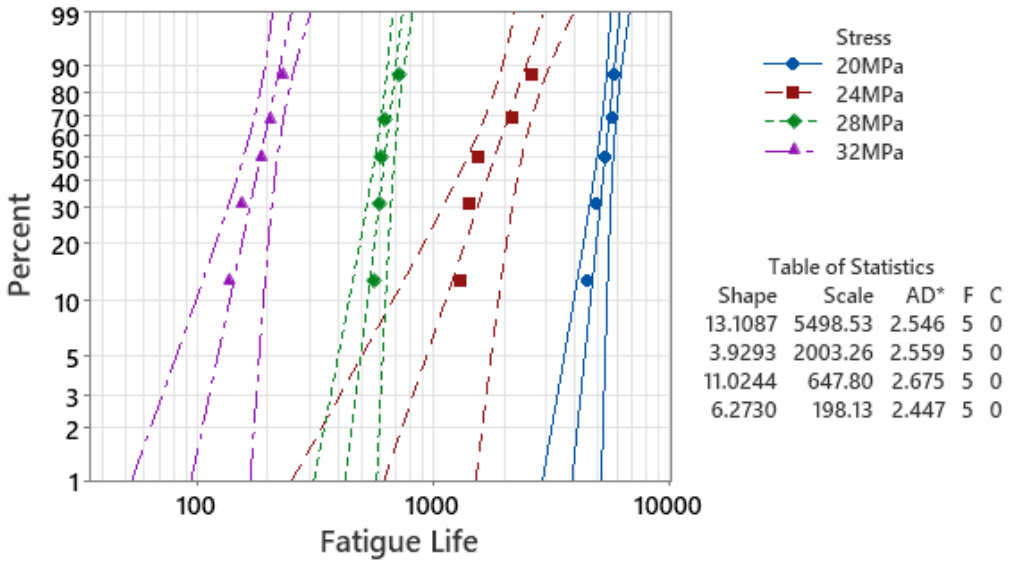

Figure 6-7 The fatigue life of SAC305 OSP represented in Weibull plots in stress-controlled test

An empirical power equation was used to include the typical fatigue life obtained from the Weibull distribution in the stress amplitude *P*, as follows:

$$N = A * P^{-c} \qquad 6\text{-}1$$

where *N* is the fatigue data for a specific stress amplitude, *A* is the substance constant, and *c* is the stress exponent, representing the fatigue ductility of the solder alloy. With increasing *c*, the ductility of the solder alloy decreased. Figure 6-8 displays the fatigue life behavior vs. stress level for SAC305 with the OSP surface finished on a logarithmic scale. A high R^2 value indicates excellent goodness of fit. A higher stress level led to a reduced fatigue life because of the increased inelastic work per cycle in region 1.

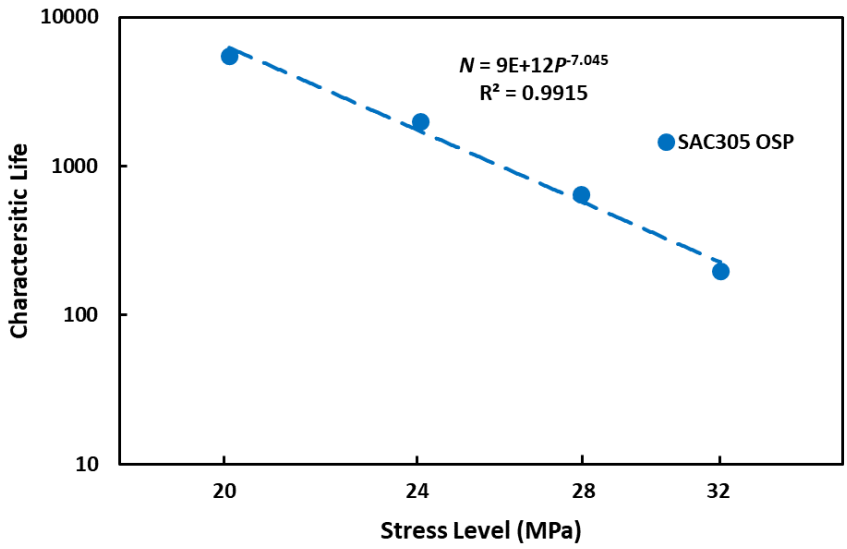

Figure 6-8 SAC305 OSP solder alloy life characteristics as a function of stress level

6.3 Strain-controlled test

The absolute values of the maximum and minimum displacements in strain-controlled testing were the same. The stress-strain relationship is quite close to that one shown in Figure 6-1. Figure 6-9 depicts the evolution of the hysteresis loops during cycling. During the first 1,000 cycles, the hysteresis loop changed slightly. As the cycle fatigue test progressed, the maximum stress continually decreased, indicating an increasing plastic strain. On the other hand, the enclosed region of the hysteresis loop underwent a growing and decreasing phase. That is, the inelastic work increased to a maximum and then decreased. Subsequently, the progression of inelastic work per cycle is shown.

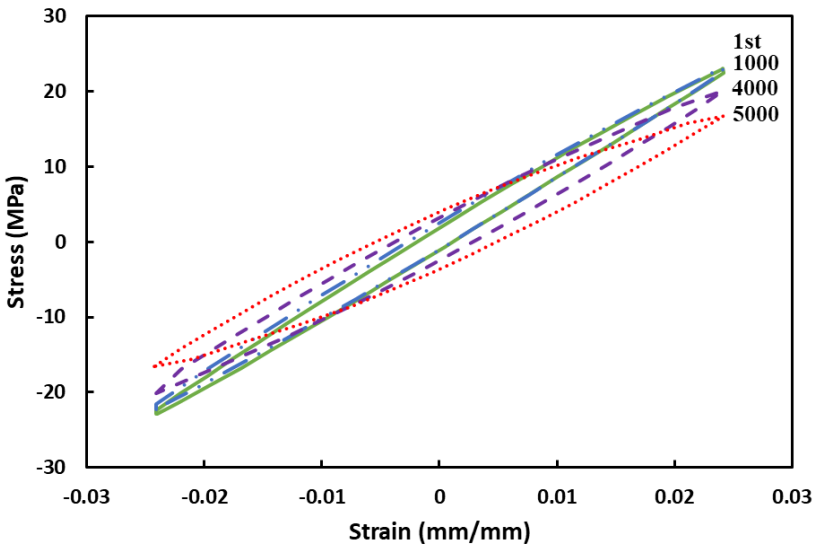

Figure 6-9 Evolution of hysteresis loop for SAC305 with OSP surface finish at total strain 2.4%

Figure 6-10 depicts the variations in the maximum load with the cycle number at different strain levels. The initial maximum load at cycle one increased with the controlled strain level. Under controlled strain levels of 2.4%, 3.0%, 3.6%, and 4.2%, the initial maximum loads were 50.5, 57.3, 69.9, and 73.9N, respectively. The increase in the initial load was related to the shear deformation of the solder materials. It is also worth mentioning that complete fracture was not observed for all the solder joints after the cyclic fatigue test. Instead, the solder joints could provide similar small stresses without breaking in the test vehicle. Partial connections were still observed between the solder joints and the substrates.

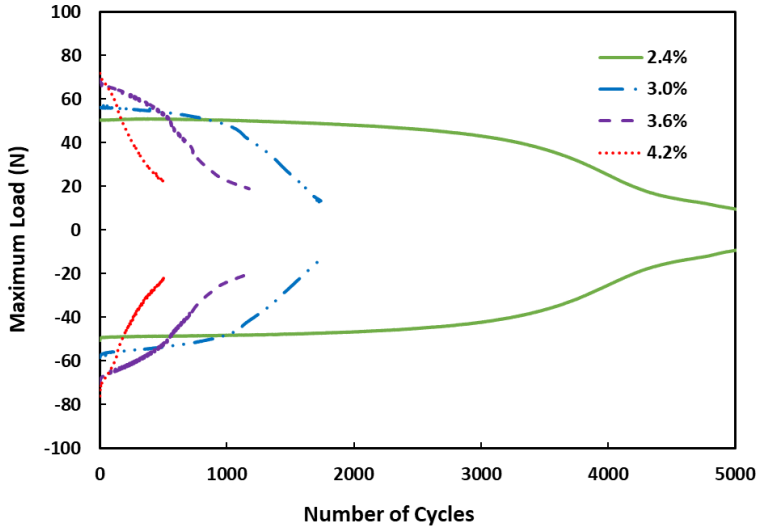

Figure 6-10 Variation of maximum load of hysteresis loop under various strain levels for SAC305 OSP

The maximum load drop is often used to define the fatigue failure in tests with strain control. However, in previous studies [27][67][23][24], a wide range of maximum load drops, from 20% to 90%, has been proposed for failure definitions. The ASTM standard [118] recommends a 50% decrease in the maximum load to define the failure in strain-controlled fatigue tests. During the cycle test, Park and Lee [23] examined the resistance of the BGA solder joints. They found that a sudden increase in resistance occurred arbitrarily at a load drop of 50%, with a significant deviation. This is because the solder joints with the most damage were primarily responsible for the resistance of the BGA test vehicle. In contrast, solder joints with the average damage are responsible for load reduction. Thus far, a precise definition of the fatigue life of solder joints is required to develop prediction models and conduct inter-laboratory comparisons. In the strain-controlled test described by Solomon [123], the author proposed a load drop parameter to show the fracture onset and propagation, defined by:

$$\emptyset = 1 - \left(\frac{\Delta P}{\Delta P_m}\right) \qquad 6\text{-}2$$

where ΔP is the load range in one cycle and ΔP_m is the maximum load range allowed during the test. Figure 6-11 shows the load drop parameters for several SAC305 solder joints with OSP surface finish cycles. Previous studies [89][65][124][119] on individual solder joints have shown three typical stages that lead to failure: an initial rapid increase in the load drop parameter, a slow and steady phase with a constant increase rate of the load drop parameter afterward, and a quick increase in the load drop parameter in the final stages. For the BGA solder joints, the first stage disappeared from the minimized flattening effect with nine solder joints. This finding is in agreement with the outcomes reported by Park and Lee [23]. As shown, the second stage evolved clearly under a controlled strain level of 2.4%, whereas it shortened significantly under increased strain levels. The fatigue life of the OSP surface finish is shown by a load drop parameter of 0.5, as 4012, 1452, 749, and 289 cycles.

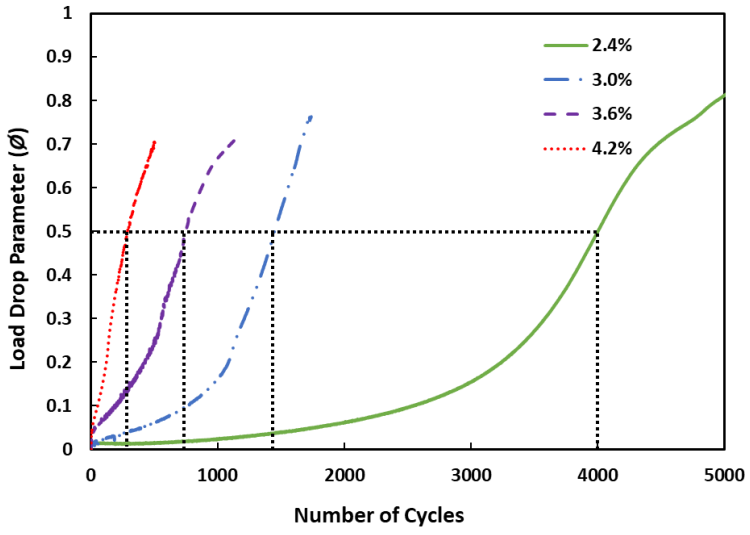

Figure 6-11 Load drop parameter to number of cycles of SAC305 OSP solder joints

The rate of inelastic work per cycle during the cyclic fatigue test was examined to further understand the behavior of the fatigue mechanism. The inelastic work per cycle

as a function of cycle number is shown in Figure 6-12. A larger strain level was related to higher initial inelastic work, higher peak inelastic work, and shorter fatigue life. The inelastic work per cycle increased at a certain strain level until it reached its peak value, as indicated by the solid line. This implies that energy is stored in solder joints. Subsequently, there was a decrease in the inelastic work per cycle. For the OSP surface finish, the highest values of inelastic work were observed at 3840, 1316, 554, and 155 cycles. It is interesting to note how the cycles with peak inelastic work are very close but always less than those with a load drop parameter of 0.5. Under the estimated 2.4% strain level, the two methods exhibited a 4.3% deviation. The divergence becomes dramatically with larger controlled displacements, i.e., about 46.4% deviation at a 4.2% strain level. Some researchers [68][108] have proposed the onset of an accelerated increase in load drop parameters as a failure criterion, resulting in lower load drop parameters for determining failure. The divergence between the two techniques was estimated to be 9.9 % and 2.5 % under the 2.4% strain level and 4.2% strain level, respectively, with load drop parameters of 0.3. In general, defining fatigue life is subjective. The solder substance and strain determine the load drop parameter for failure. Therefore, the fatigue life was calculated by estimating the cycles to obtain the peak inelastic work to overcome this issue. The preliminary speculation is that while the strain-controlled test continues, the damage is formed and accumulates in the solder joints, resulting in microcracks. The formation and propagation of these microcracks increase the inelastic work each cycle. However, the microcracks gradually connect and join together to generate cracks. This caused a decrease in the inelastic work per cycle after the peak value. The primary crack would propagate and develop until it fractured completely.

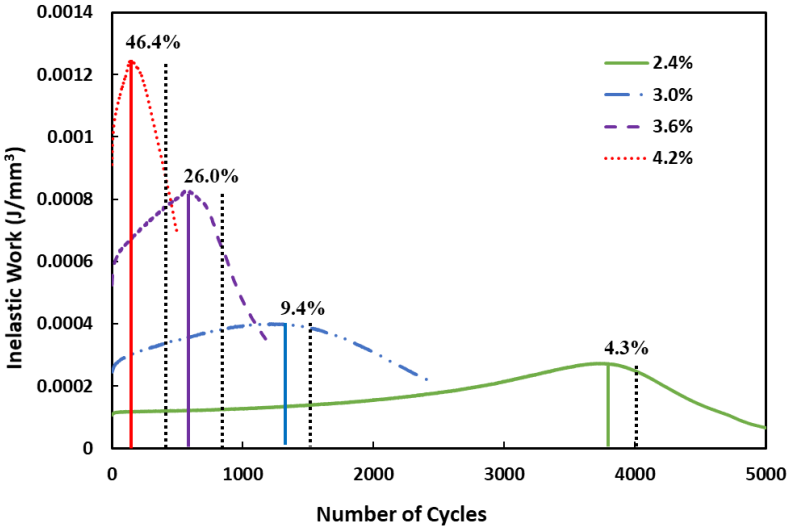

Figure 6-12 Inelastic work to number of cycles of SAC305 solder joints in strain-controlled test

Figure 6-13 depicts the plastic strain range versus the number of cycles at different strain levels. The plastic strain initially experienced a steady stage at 2.4% strain, then climbed at accelerated speed until complete fracture. The initial plastic strain increased dramatically at a higher strain level. Meanwhile, a significant drop in the steady-state was observed. Almost no steady phase was observed at the 5.5% strain level, and the plastic strain increased rapidly.

The cycle with the peak inelastic work was utilized to quantify the fatigue life of the test vehicles using the Weibull distribution. Figure 6-14 shows the fitted fatigue life of SAC305 with the OSP surface finish under four-strain levels. On a logarithmic scale, Figure 6-15 displays the fatigue life behavior of SAC305 against the strain level. The increased strain level lowered the fatigue life owing to the higher amount of inelastic work generated during the cyclic fatigue test.

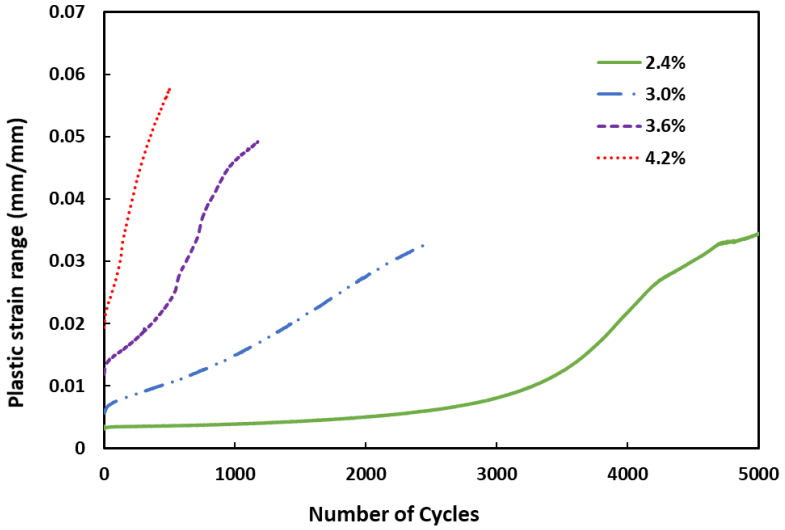

Figure 6-13 Plastic strain range to number of cycles of SAC305 solder joints in strain-controlled test

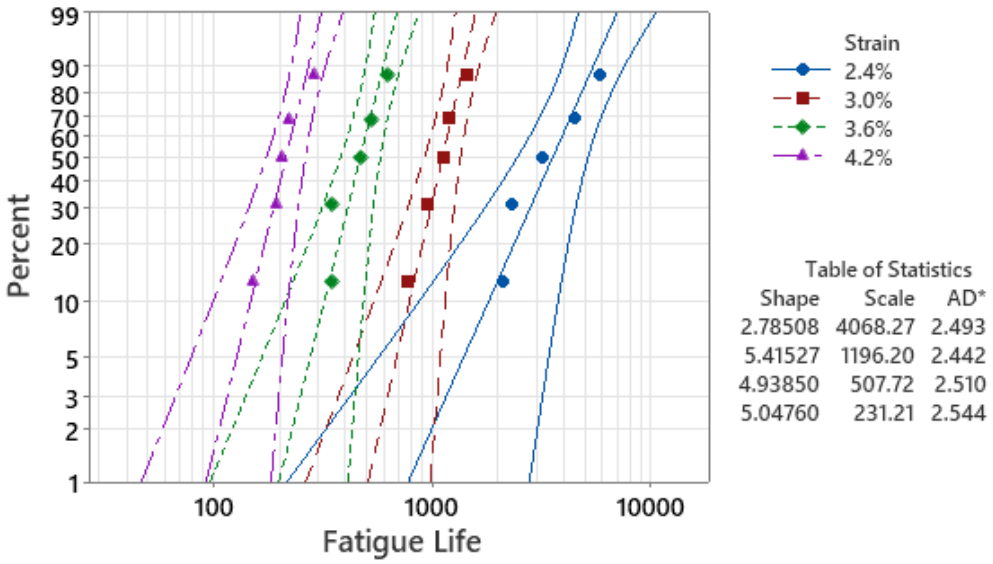

Figure 6-14 The fatigue life of SAC305 OSP represented in Weibull plots in strain-controlled test

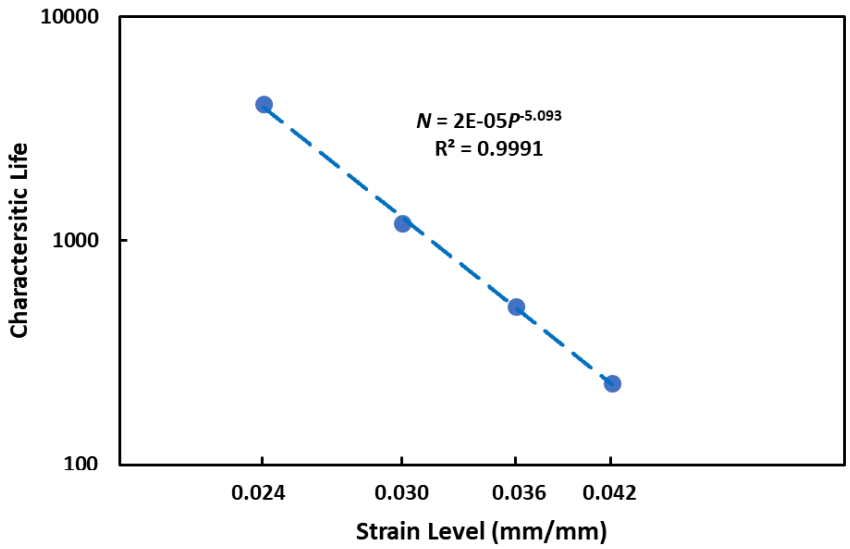

Figure 6-15 SAC305 OSP solder alloy life characteristics as a function of stress level

6.4 Effect of surface finish

The surface finish used affects the fatigue performance of the SAC solder alloys. Figure 6-16 depicts the interfacial microstructures of SC305 with the OSP and ENIG surface finishes. Regardless of the surface finish, Sn and Ag in the SAC305 solder alloy form Ag_3Sn particles. They were distributed as networks in the β-Sn dendritic structure. Sn and Ag interact with Cu, predominantly from the Cu pad and partly from the solder alloy, to generate a scallop-like Cu_6Sn_5 IMC layer with a thickness of 2~3μm using the OSP surface finish. With the ENIG surface finish, the Ni layer serves as a barrier to prevent Cu atoms from diffusing from the Cu pad. However, the small amount of Cu in the SAC305 solder alloy promoted the formation of another $(Ni, Cu)_6Sn_5$ IMC layer with a thickness estimated around 1μm. The thickness of the $(Ni, Cu)_6Sn_5$ IMC layer is substantially smaller than that of the Cu_6Sn_5 IMC layer. Figure 6-17 shows the corresponding interfacial microstructures after failure. The ductile failure mechanism was recognized as the fracture propagating along the bulk solder for the OSP surface

finish. Regarding the ENIG surface finish, the fracture also propagated into the bulk solder, but was extremely close to the IMC layer, resulting in near-IMC failure [105].

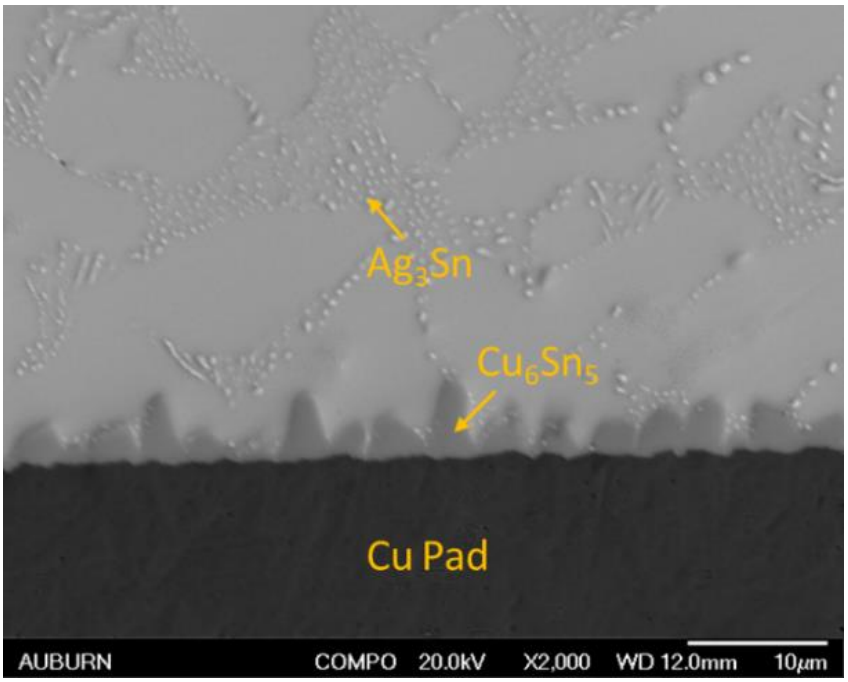

(a)

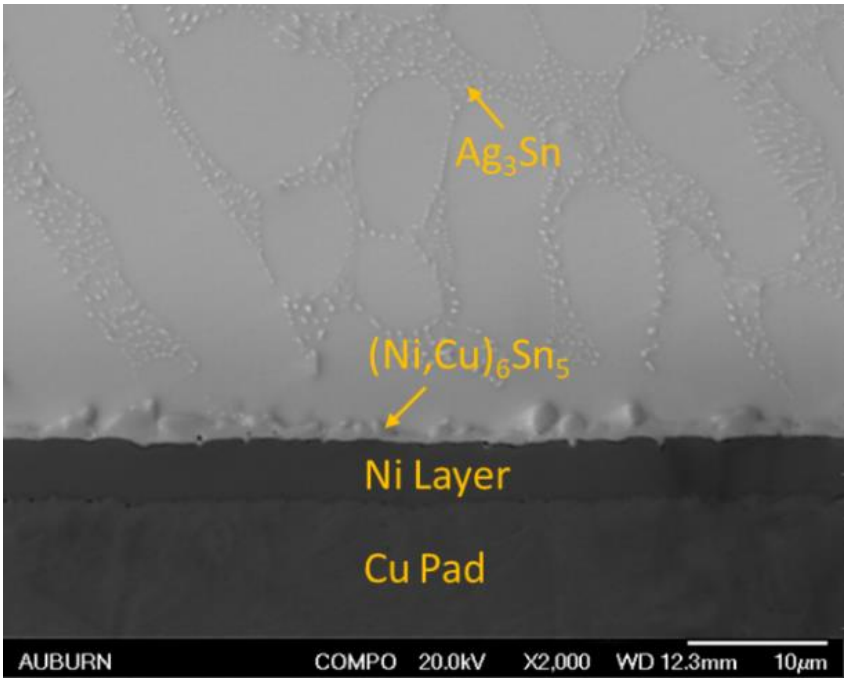

(b)

Figure 6-16 Interfacial micrographs of SAC305 solder alloy before failure: (a) OSP surface finish; (b) ENIG surface finish

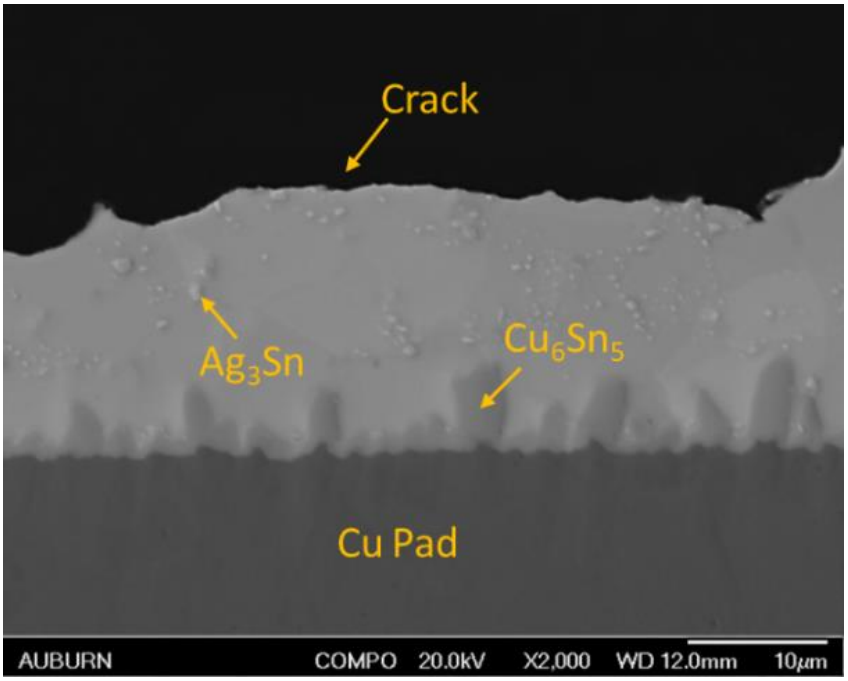

(a)

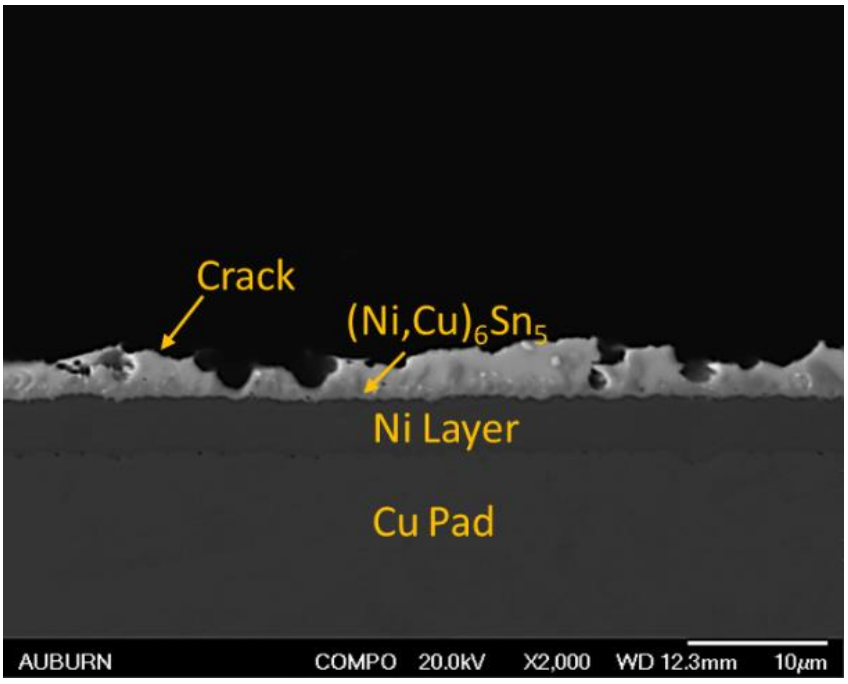

(b)

Figure 6-17 Interfacial micrographs of SAC305 solder alloy after failure: (a) OSP surface finish; (b) ENIG surface finish

Figure 6-18 shows the Weibull plots for SAC305 with the ENIG surface finish in the stress-controlled and strain-controlled tests. Figure 6-19 displays the fatigue life behavior versus the stress level for SAC305 with two surface finishes on a logarithmic

scale. A high R^2 value indicates the excellent goodness of fit. The OSP surface finish outperformed the ENIG surface finish in fatigue tests at a high-stress level of 32MPa. However, at a low-stress level of 20MPa, the fatigue life of the OSP and ENIG surface finishes were similar. In other words, if less stress is applied, the ENIG surface finish is expected to have a higher fatigue life than the OSP surface finish. At all strain levels, the OSP surface finish outperformed the ENIG surface finish, as shown in Figure 6-20.

Using the Morrow energy model, the characteristic fatigue life can also be correlated with the inelastic work per cycle, as follows:

$$N = C^{1/m} * W^{-1/m} \qquad 6\text{-}3$$

where N is the typical fatigue life, W is the inelastic work per cycle, C is the ductility coefficient of material fatigue, and m is the exponent of fatigue. It is worth noting that the initial inelastic work is utilized for W in the strain-controlled method. In contrast, the average work per cycle in the steady region is determined for W by using the stress-controlled method. Figure 6-21 depicts a log-log plot of the fatigue life vs. the inelastic work per cycle for SAC305 using different testing methods. Using the Morrow energy model, the fatigue results matched well with the inelastic work. Table 6-1 lists the fatigue ductility coefficient C and fatigue exponent m estimated for the SAC305 solder alloy under various testing conditions.

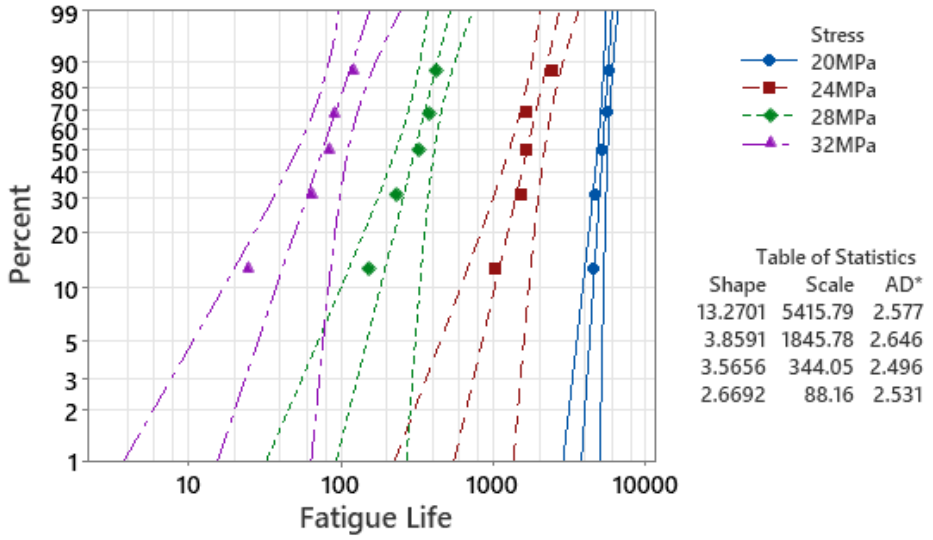

(a)

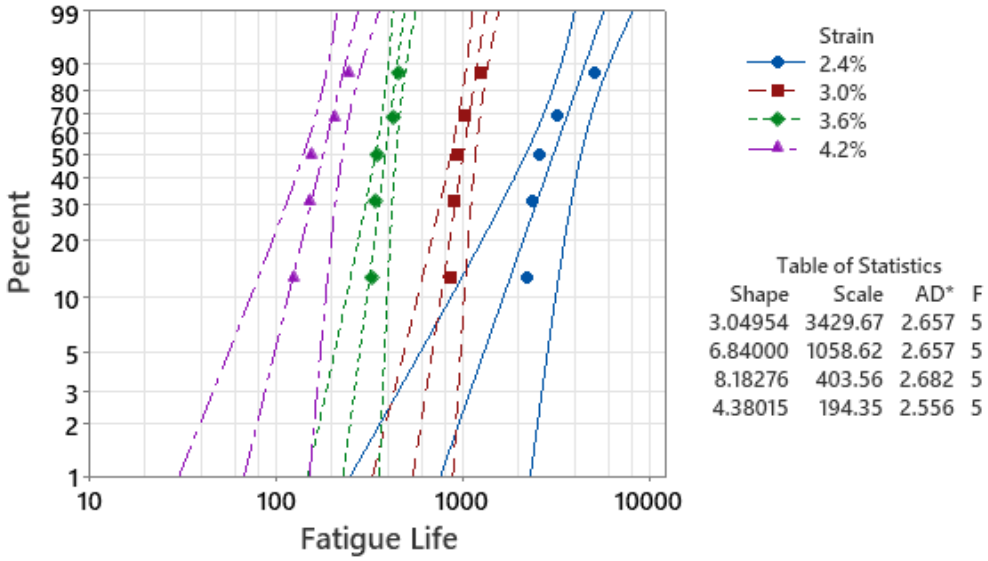

(b)

Figure 6-18The fatigue life of SAC305 ENIG represented in Weibull plots in: (a) stress-controlled test; (b) strain-controlled test

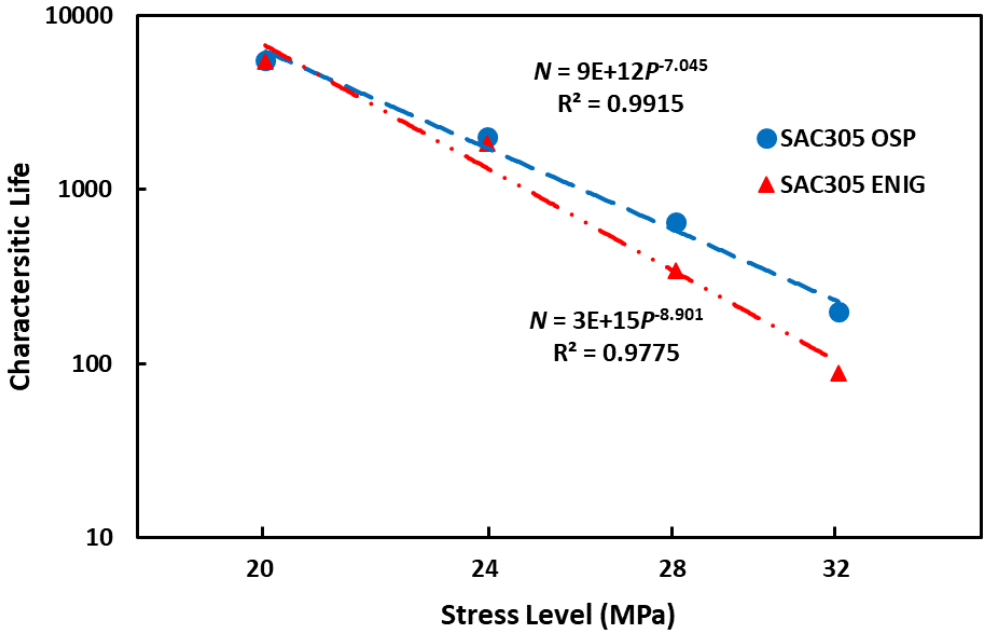

Figure 6-19 Solder alloy life characteristics as a function of stress level

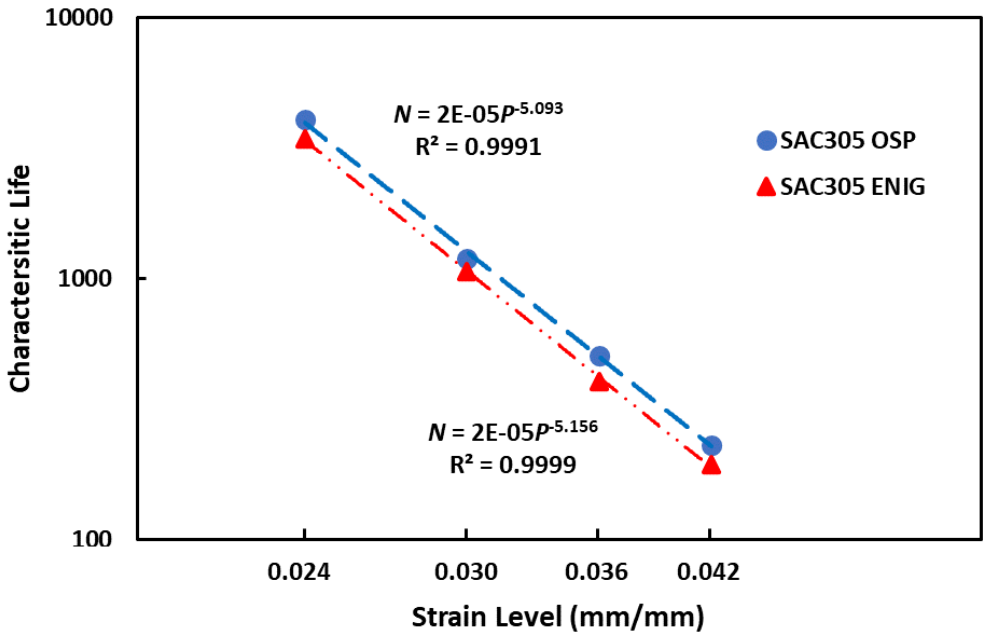

Figure 6-20 Solder alloy life characteristics as a function of strain level

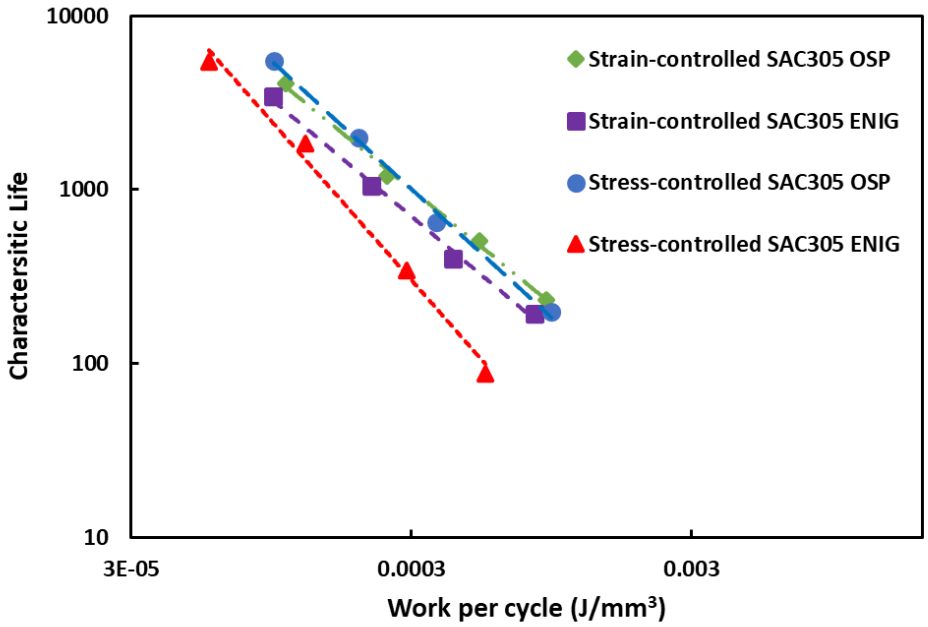

Figure 6-21 Morrow energy model fitting curves for SAC305 solder alloy

Table 6-1 Summary of constants fitted in Morrow's energy model

Method	Surface finish	Fatigue ductility, C	Fatigue exponent, m
Strain-controlled	OSP	0.057	0.760
	ENIG	0.039	0.742
Stress-controlled	OSP	0.032	0.678
	ENIG	0.007	0.547

Similarly, the plastic strain range per cycle was determined by employing initial plastic strain for the strain-controlled test and steady-state plastic strain for the stress-controlled test. The Coffin-Manson model can explain the exponentially growing plastic strain range with stress amplitude as follows:

$$N = \delta^{1/\alpha} * \Delta\varepsilon_p{}^{-1/\alpha} \qquad 6\text{-}4$$

where N donates the typical fatigue life, $\Delta\varepsilon_p$ donates the average range of plastic strain per cycle, δ is the material coefficient of fatigue ductility, and α donates the fatigue exponent. Figure 6-22 shows the characteristic fatigue life as a function of the range of

a plastic strain on a logarithmic scale. Table 6-2 presents the Coffin-Manson model constants for all the tested solder alloys.

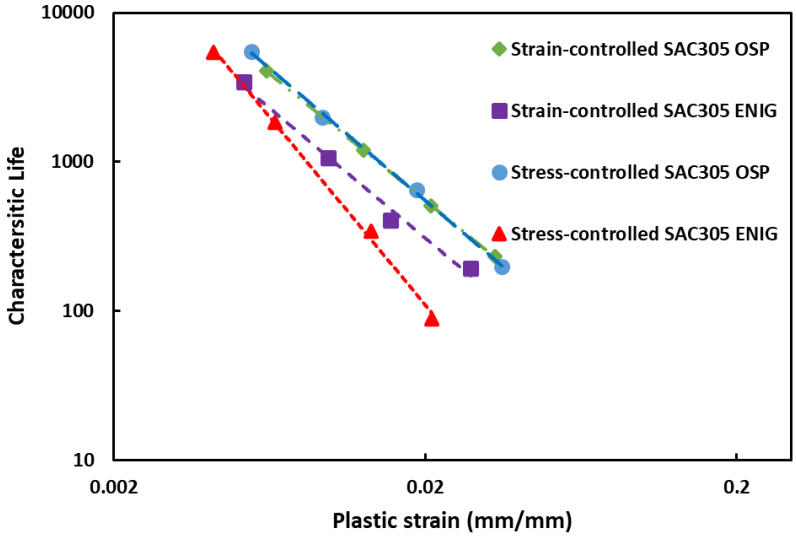

Figure 6-22 Fitted curves of Coffin-Manson model for SAC305 solder alloy

Table 6-2 Summary of constants fitted in Coffin-Manson model

Method	Surface finish	Fatigue ductility, θ	Fatigue exponent, α
Strain-controlled	OSP	0.815	0.587
	ENIG	0.535	0.573
Stress-controlled	OSP	0.699	0.563
	ENIG	0.129	0.396

6.5 Conclusion

This study examined the fatigue properties of SAC305 solder alloy with OSP and ENIG surface finishes using strain-controlled and stress-controlled methods. The evolution of hysteresis loops, inelastic work, and plastic strain were explored. A novel method was proposed to define the fatigue failure in the strain-controlled test. The study findings are summarized below:

1. The characteristic fatigue life decreased as the strain or stress level increased because the solder joint experienced more damage every cycle.
2. In both the stress-controlled and strain-controlled tests, the OSP surface finish outperformed the ENIG surface finish for SAC305. However, the ENIG surface finish is expected to perform better at even lower stress levels.
3. SAC305 with OSP surface finish was associated with ductile failure mode, while the ENIG surface finish demonstrated near-IMC failure mode. The near-IMC failure mode indicates the weaker strength of IMC layer. At higher stress level, the weaker IMC layer accelerates the fatigue failure.
4. The cycle used to obtain a peak inelastic work in a strain-controlled test was more appropriate for determining fatigue life.
5. In both stress-controlled and strain-controlled tests, the Morrow energy and Coffin-Manson models match well with fatigue data. The fatigue ductility and fatigue exponent parameters estimated for the more realistic solder joints in BGA assembly were different from that for bulk samples and individual solder joints.
6. The strain-controlled test yielded a higher fatigue ductility coefficient than the stress-controlled test. For the OSP surface finish, the difference is minimal, but for the ENIG surface finish, it is considerable.

6.7 Contribution

The fatigue properties of SAC305 solder joints in BGA assembly were assessed using stress-controlled and strain-controlled approaches at the room temperature. The damage accumulated in solder joints in BGA assembly using stress-controlled test was found

akin to that in individual solder joints except for the initial hardening effect. In strain-controlled tests, this study proposed a more appropriate definition to address the ambiguity of failure criteria. Different models, including the empirical model, Coffin-Manson model, and Morrow energy model, were suitable for fitting the fatigue data. Among them, the empirical model indicated that the OSP surface finish performed better than the ENIG surface finish. This is explained by the differentiated failure modes (near-IMC failure and ductile failure) associated with the two surface finishes. The near-IMC failure mode implied a weaker interfacial connection on the Ni layer compared to that on Cu pad. This conclusion only holds true for isothermal cycling conditions. When it comes to thermal cycling, the Ni layer acts as a barrier to restrain the growing of IMC layer during the process, thus the improved reliability. In addition, the failure mechanism in thermal cycling and isothermal cycling varies. Extrapolating the real service data from the proposed models might be misleading without a solid understanding of the testing procedure and failure mechanisms. The proper implementation of these models starts with a finite element model to obtain the true stress/strain, plastic strain range, or work dissipation of components with their specific configurations and working environment. Predictions can then be made using these true inputs.

Chapter 7 Fatigue Performance and Microstructure of Lead-Free Solder Joints in BGA Assembly

7.1 Introduction

Lead-based solders were previously employed in electronic products due to their exceptional mechanical, chemical, thermal, and physical qualities [125]. However, the electronic industry has begun to avoid it due to its environmental and health concerns. Sn-Cu-Ag (SAC) alloy is one of the most preferred replacements for lead-based solders, due to its superior mechanical qualities, low melting temperature, and low cost [126][127]. Recent studies have shown that doping improves solder alloy reliability [128][129][22]. Dopants such as Ni, Sb, and Bi are commonly used [130][113]. In comparison to SAC305, solder alloys with higher Bi content had better ultimate shear strength [131]. It has been observed that Sn-3.0Ag-0.5Cu-3.0Bi and Sn-3.0Ag-0.5Cu-1.0Bi have better resistance to crack growth, as a result of the strengthening effect of the Bismuth constituent [132]. Bismuth in SAC solder at a concentration of around 1% can lower the melting temperature, minimize Cu consumption, and limit the growth rate of the IMC layer [133]. A study also discovered that combining Bi and Ni improves drop impact reliability and thermal fatigue life [134]. According to a few studies, Bi can also improve the tensile strength of solders while decreasing their elongation [135] and improving the wettability of SAC alloy [136].

Solder joints typically experience cyclic loading, such as thermal cycling or mechanical cycling [61][18]. The most common failure mode for mechanical cycling is a transgranular failure, in which the crack propagates into the bulk solder [18][106][65]. Chowdhury et al. [137] examined how the microstructure of a solder joint changes as

a result of mechanical cyclic loading. They found that the microcracks initiated at the β-Sn dendrites' subgrain boundary and grew longer with cycling. Then, the microcracks connected and tangled with each other leading to the formation of bigger transgranular cracks [138]. The crack propagation path varies depending on the strain range level, according to Andersson et al. [17]. At high strain ranges, cracks propagate through the bulk of solder joints, whereas at lower strain ranges, cracks propagate through the interface between the solder joints and the pads.

The effects of variables including strain rate, changing amplitudes, and aging time on the mechanical characteristics and fatigue life of lead-free solder junctions have been studied in several researches [119][139][115]. It has been discovered that a lower strain rate may cause more damage accumulation per cycle and reduce the fatigue life of solder joints. Cycling samples with a low strain rate at the harsh amplitude and a high strain rate at the mild amplitude would result in most work per cycle and thus the fastest failure. In addition, as the aging time increases, it results in larger plastic strain and inelastic work per cycle; this accelerates the time to failure.

The effect of surface finishes on the thermal cycling reliability and shear strength of solder joints has been studied [140][141][142]. In general, the Ni/Au surface finish [electroless nickel immersion gold (ENIG)] has shown better reliability in thermal cycling with aging since the Ni layer is used as a diffusion barrier to control the growth of the IMC in thermal environments. However, the Ni/Au surface finish is associated with a brittle fracture in high-speed shear testing. The fracture is propagated along with the interface of the solder joint and the nickel layer, causing a relatively low shear strength [143][144][145].

The majority of the fatigue properties studies [146][24] were conducted using large bulk samples, for example, dog bone shape samples, while Su et al. examined individual

solder joints, which is a more reliable way to predict the fatigue of solder joints [22][147]. However, the situation for solder joints in BGA components is more complex, and the component's fatigue life is different from the fatigue life of individual solder joints, on one hand, the solder joints in one component would affect each other, on the other hand, failure of any solder joint would fail the whole component. Limited literature has investigated shear fatigue performance of solder joints in BGA assembly [79][80][28][23], where strain-controlled method was implemented. Furthermore, no study has utilized stress-controlled method for BGA solder joints, and none has focused on investigating the effect of surface finish on the reliability of doped solder joint. In this study, the fatigue performance of SAC305, SAC-R, SAC-Q, and SAC-I BGA solder joints was examined and compared with both OSP and ENIG surface finishes. Both stress-controlled method and strain-controlled method were implemented. The microstructure and failure mechanism of each solder alloy with OSP and ENIG surface finish was characterized using SEM/DES.

7.2 Fatigue Life Analysis

The variation of fatigue properties among solder joints has been shown in several studies [20][53][54]. The primary causes of this variability are differences in the distribution of secondary precipitates and the orientation of the anisotropic Sn grains. Each of the nine interconnected solder joints on the BGA test vehicles examined in this work has a distinct microstructure. Also, during the shear fatigue test, these solder joints have an impact on each other. The fatigue life of a BGA test vehicle is greatly reduced by the failure of any solder joint. The failure distribution in this case is the minimum extreme value distribution, which can be obtained from Weibull analysis. The failure definitions of BGA test vehicles in both stress-and strain-controlled mode have been

explained in my previous paper. A two-parameter Weibull distribution was used to characterize the fatigue life of each set of BGA solder joints. The two-parameter Weibull distribution is expressed as:

$$R(t) = e^{-\left(\frac{t}{\theta}\right)^{\beta}} \qquad 7\text{-}1$$

where *R(t)* is the reliability, θ is the scale parameter, and β is the shape parameter. The shape parameter represents the slope of the regression line. The scale parameter, which is also known as the characteristic life, defines the number of cycles with a 63.2% probability of failure. Figures 7-1 to Figure 7-4 show the fitted Weibull distribution for SAC305, SAC-R, SAC-Q, and SAC-I solder alloys in stress-controlled method and in strain-controlled method, respectively. Previous studies [22][113][105] have demonstrated an excellent goodness of fit between characteristic fatigue life and applied stress/strain levels using an empirical power equation. On a logarithmic scale, the equation exhibits as a straight line. The characteristic fatigue life of each solder alloy in this work was examined at a low level and a high level, which could be used to illustrate the trend of the fatigue performance. Figure 7-5 and Figure 7-6 plot the characteristic life of the four solder alloys in stress-controlled tests and strain-controlled tests at different stress/strain levels.

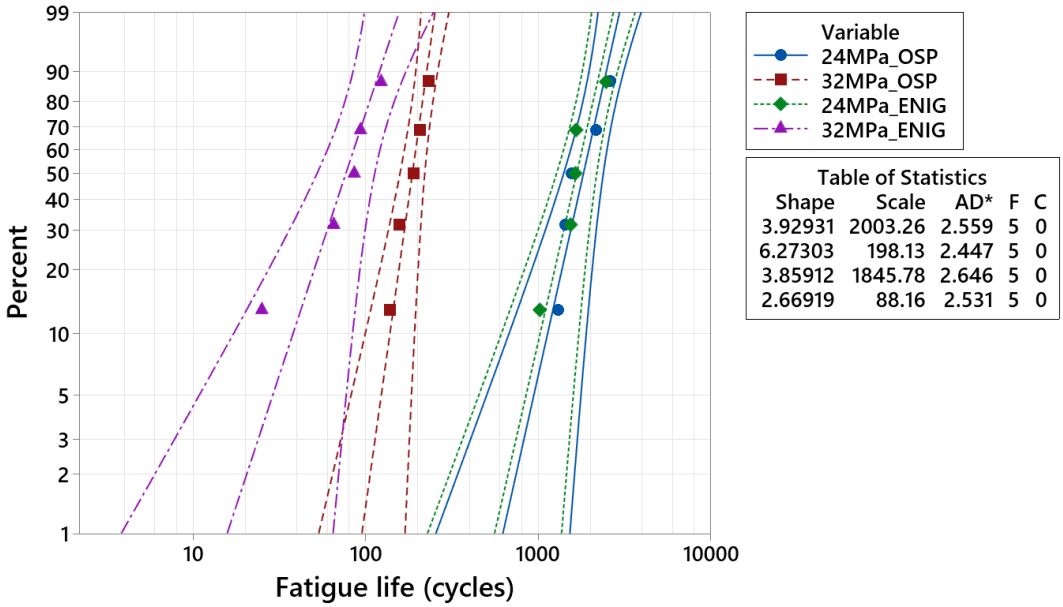

(a)

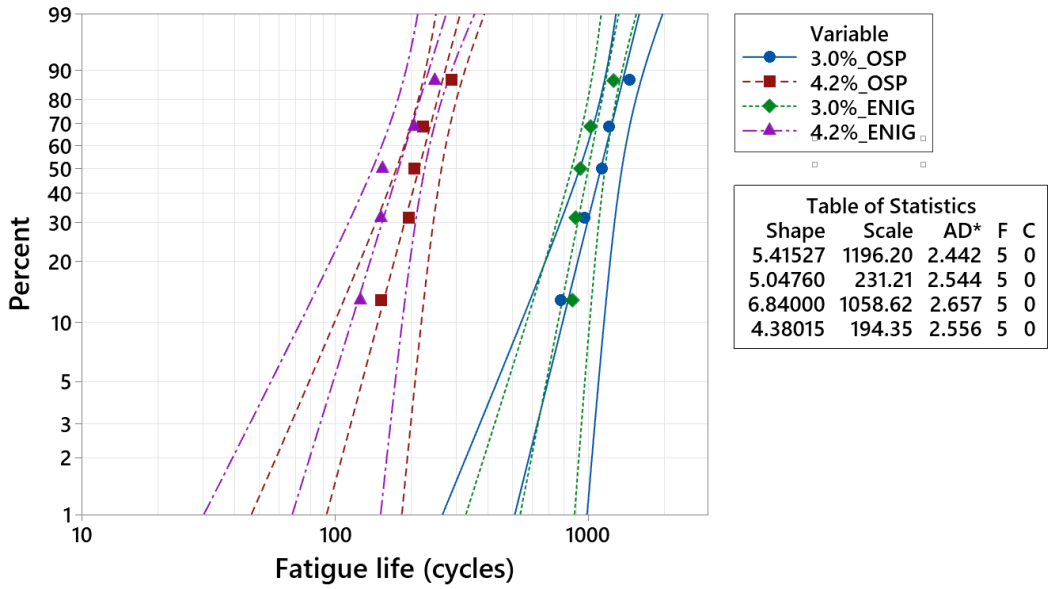

(b)

Figure 7-1 Weibull plots of the fatigue life of SAC305 solder alloy in (a) stress-controlled test, (b) strain-controlled test

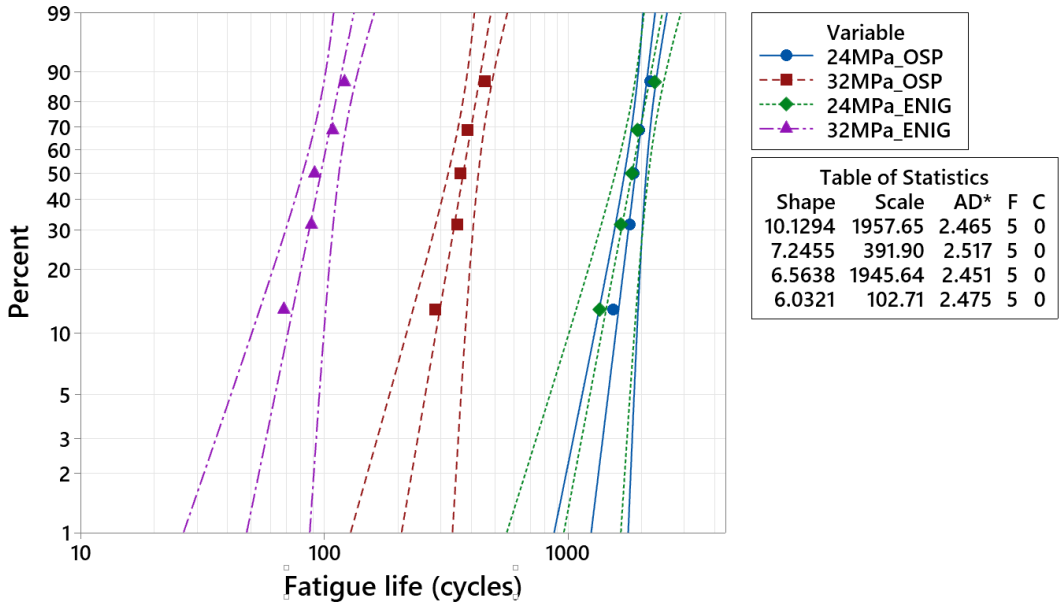

(a)

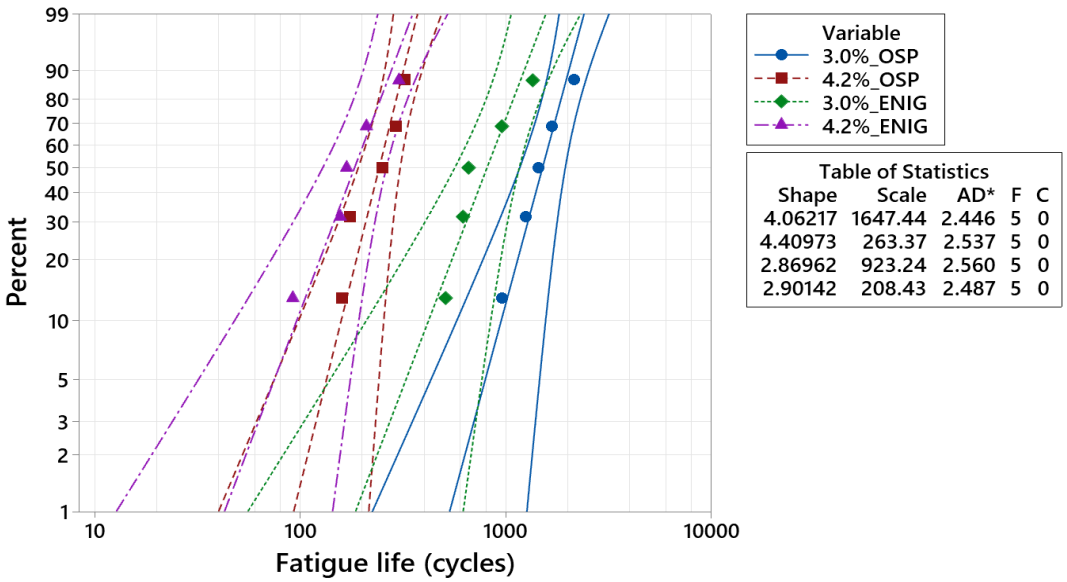

(b)

Figure 7-2 Weibull plots of the fatigue life of SAC-R solder alloy in (a) stress-controlled test, (b) strain-controlled test

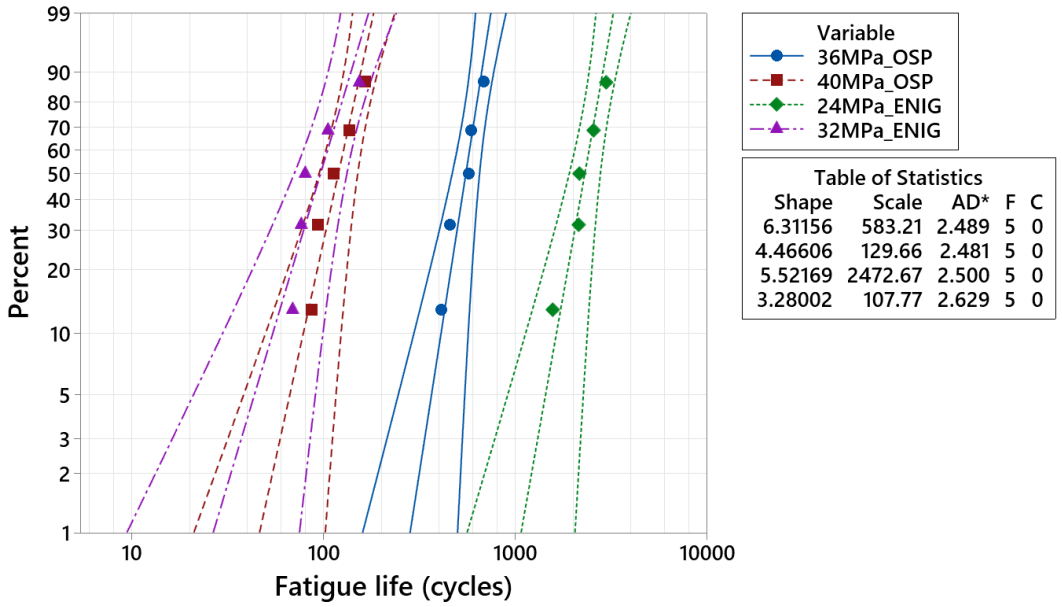

(a)

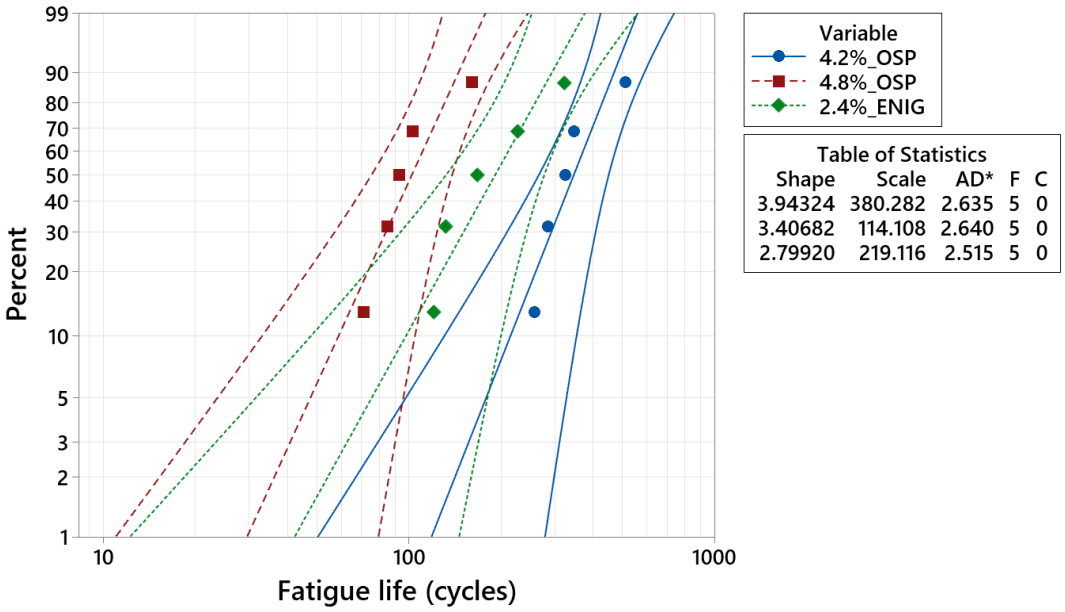

(b)

Figure 7-3 Weibull plots of the fatigue life of SAC-Q solder alloy in (a) stress-controlled test, (b) strain-controlled test

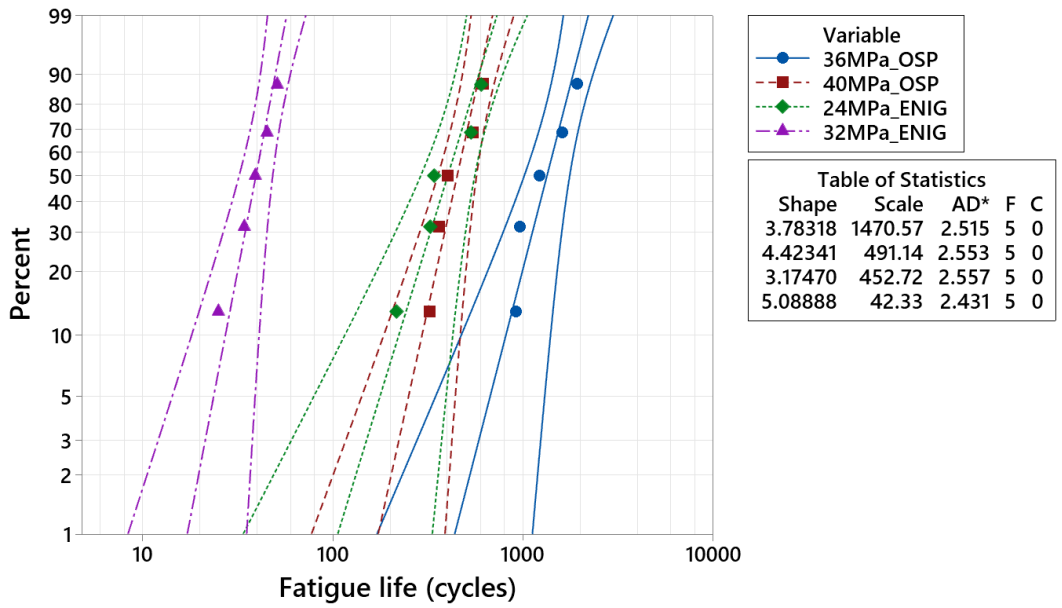

(a)

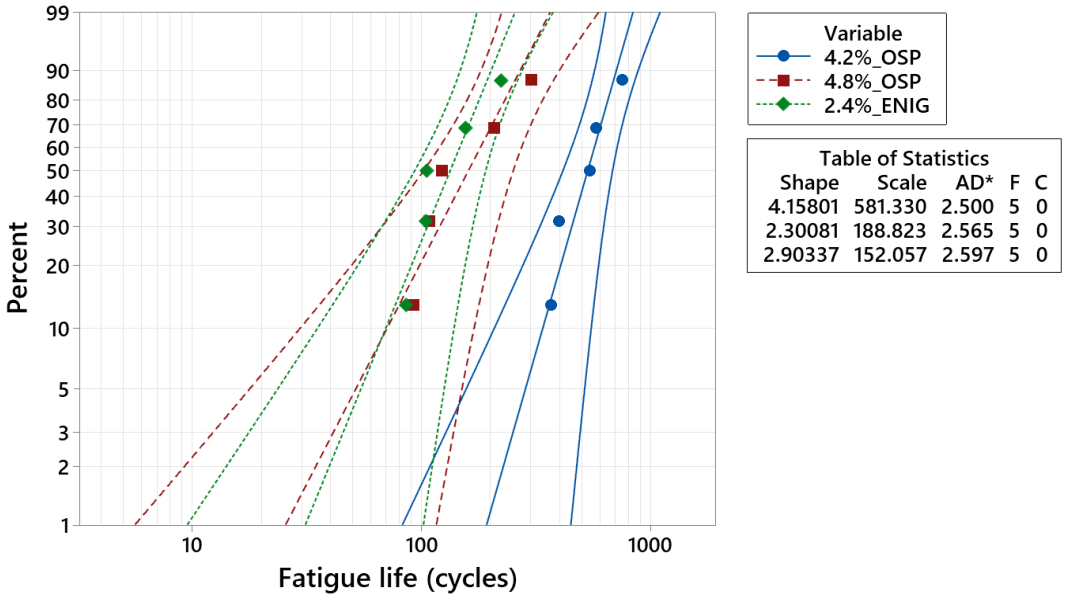

(b)

Figure 7-4 Weibull plots of the fatigue life of SAC-I solder alloy in (a) stress-controlled test, (b) strain-controlled test

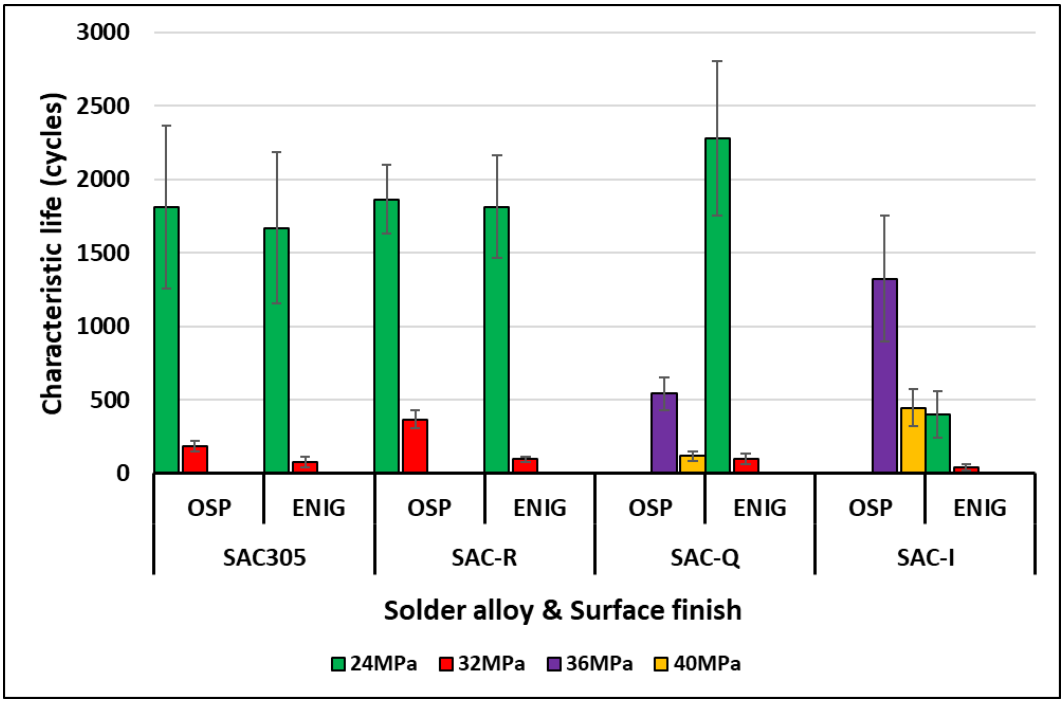

Figure 7-5 Characteristic life (cycle) of solder alloys in stress-controlled test

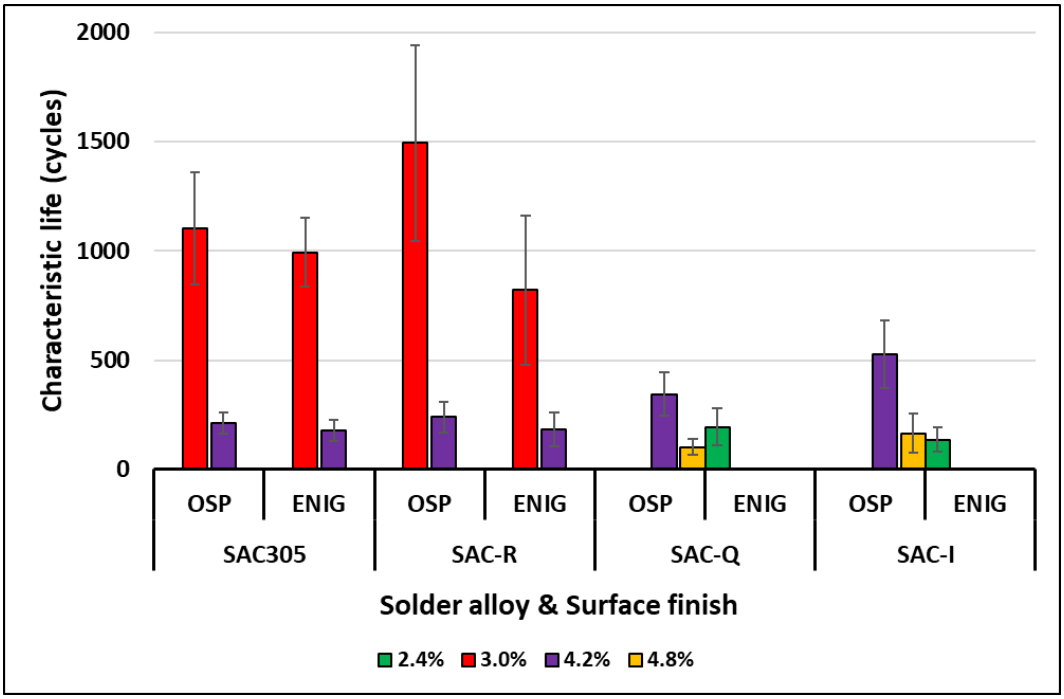

Figure 7-6 Characteristic life (cycle) of solder alloys in strain-controlled test

In a stress-controlled test, the higher stress level leads to more damage accumulated in each cycle resulting in a shorter fatigue life. This conclusion holds true for all the tested solder alloys, regardless of surface finish. With the same OSP surface finish, SAC-Q and SAC-I tend to perform better than SAC305 and SAC-R since the two SAC-Bi

solder alloys provided good fatigue life even at higher stress amplitudes. When it comes to ENIG surface finish, SAC-Q, SAC305, and SAC-R exhibit no significant difference in terms of fatigue life, although SAC-Q performs better than the other two alloys. SAC-I demonstrates the worst fatigue performance, owing to its embrittlement characteristic. This is in line with the observations in previous research using individual solder joints [105]. It is also interesting to see that SAC305 solder joints with the OSP surface finish tends to have a better performance than the ENIG surface finish, especially at higher stress levels. This suggests a more robust connection between the solder joints and the copper pad with the adoption of OSP surface finish. It is not surprising to see that the fatigue life of SAC-R was close to that of SAC305, attributing to the addition of 2.4% Bi and the absence of 3% Ag. Both of Bi and Ag have showed a positive impact on solder joint reliability. Nonetheless, the fatigue life of SAC-R was found greater than SAC-305 at a high stress level irrespective of the surface finish.

In strain-controlled test, a higher strain level would also result in more cyclic damage during the fatigue test, leading to a shorter fatigue life. The fatigue performance of SAC305 with OSP was again found to be better than ENIG surface finish at both low and high strain levels. SAC-R performs similarly to SAC305, despite the slight offset between the two. This coincides with the observation in stress-controlled test. As far as SAC-Q and SAC-I solder alloys are concerned, they also exhibited greater fatigue life than SAC305 and SAC-R at strain level of 4.2% with OSP surface finish. Similarly, SAC-I demonstrates better fatigue resistance than SAC-Q. However, the harmful embrittlement nature of SAC-Bi solder joints with ENIG surface finish resulted in a lower fatigue life. In a strain-controlled test, it was discovered that this effect was amplified. SAC-Q and SAC-I showed their extraordinary sensitivity to the change of strain level as a result of their brittle failure mode. The plastic deformation applicable

was less in this failure mode, resulting in rapid jump of fatigue life from hundreds of cycles to even more than 10,000 cycles if reducing the strain level. Despite this, SAC-Q outperformed SAC-I with ENIG surface finish at the strain level of 2.4%.

7.3 Microstructure Analysis

As previously stated, the mechanical and fatigue characteristics of solder joints are strongly influenced by their microstructure. The as-cast microstructures of the SAC305, SAC-R, SAC-Q, and SAC-I solder bulks are displayed in Figure 7-7. A typical SAC305 solder joint consists of two phases: the β-Sn phase and eutectic phase. In the bulk solder, both Ag and Cu reacted with Sn to form Ag_3Sn and Cu_6Sn_5 IMC particles dispersed inside the β-Sn matrix. These particles act as impediments to dislocation movement, providing improved mechanical and fatigue characteristics through the precipitation hardening process. The morphology and distribution of the Ag_3Sn phase in solder joints also influence their reliability. Keller et al. [148][76][149] found that Ag_3Sn precipitates with finer microstructures and lower aspect ratios exhibit more robust mechanical characteristics. This finding was derived after studying solder joints containing the same Ag quantity but various distributions. Other micro-alloying elements, including Bi, Sb, and Ni, can dissolve into the Sn crystalline lattice by replacing the Sn atoms in their lattice locations, forming a substitutional solid solution. Local lattice distortions also impede dislocation mobility and prevent plastic deformation. The solid solution hardening process improves the strength of solder alloys. The SAC-R solder alloy includes 2.46 wt.% Bi, which exceeds the solubility limit of Bi in the Sn matrix at room temperature, which is 2.3 wt.%. The excess Bi separated to form Bi precipitates, illustrated in Figure 7-7 (b) as a brilliant white zone. The addition of Bi to the SAC-R solder joints compensates for the absence of Ag_3Sn

precipitates, bringing its mechanical and fatigue characteristics closer to those of SAC305. The microstructure of SAC-Q and SAC-I in Figure 7-7 (c) and (d) respectively showed more Bi particles in the solder bulks than SAC-R due to their higher Bi content, which is 3.3 wt.% and 3.0 wt.%, respectively. Furthermore, the inclusion of Bi was found to improve the needle-like Ag_3Sn and plate-like Cu_6Sn_5 [150], which increased the reliability. Although SAC-I has less Bi than SAC-Q, it has more Ag and Cu. The addition of Sb and Ni to SAC-I also improves its dependability. The asterisk symbols in Figure 7-7 represent typical precipitates identified using EDS spectrum analysis, as depicted in Figure 7-8. In the SAC305 bulk solder, the Ag_3Sn precipitates formed a network in the β-Sn dendrites. However, an Ag_3Sn morphology resembling needles was observed in SAC-Q and SAC-I. The same precipitate composition was observed in the EDS spectra of the SAC-R and SAC-Q solder alloys, both of which were characterized as Cu_6Sn_5 particles. Furthermore, Ni was detected in the Cu-Sn rich phase in spectrum 4, which is not surprising for the composition of the SAC-I solder. The new Sn-Cu-Ni phase is identified as Cu_6Sn_5.

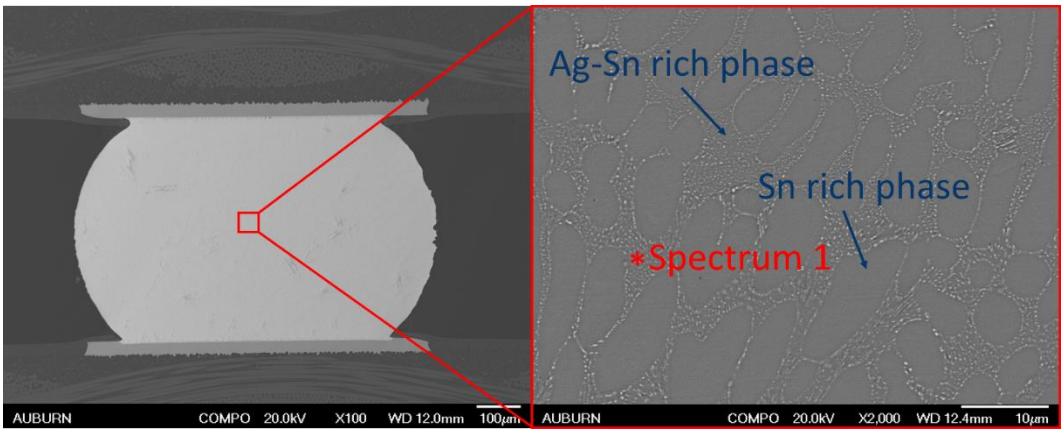

(a)

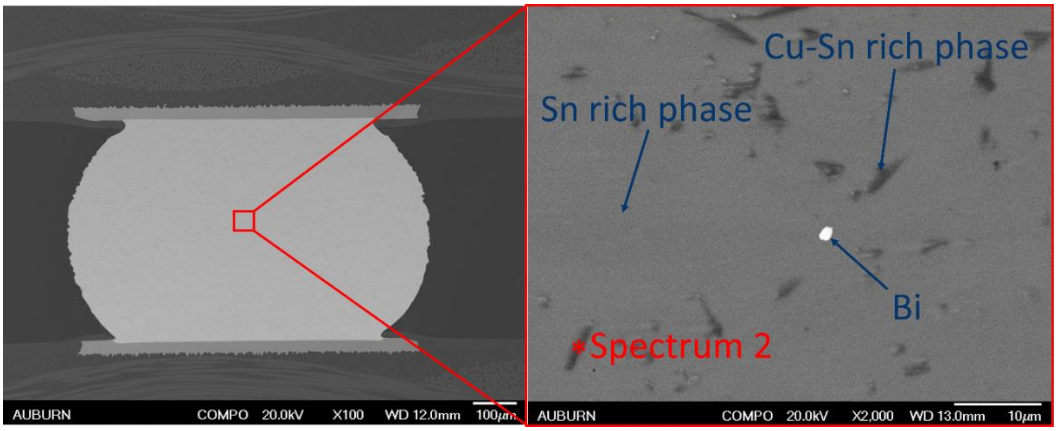

(b)

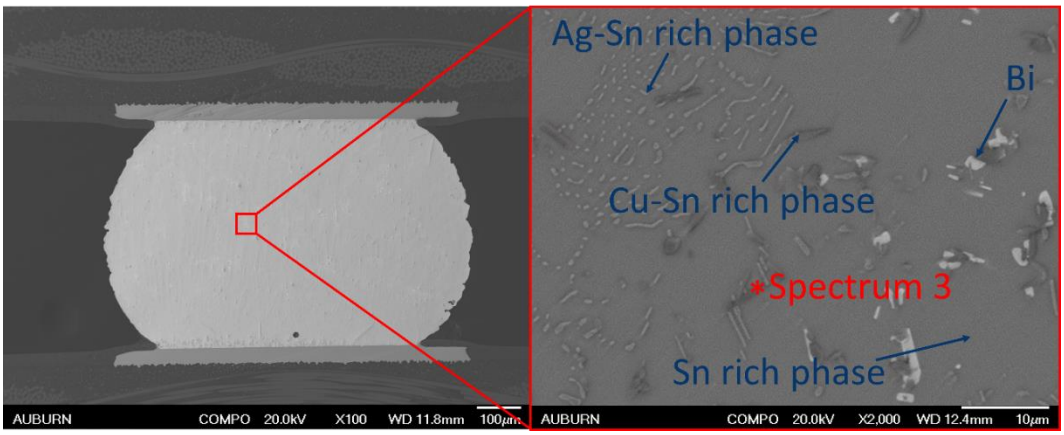

(c)

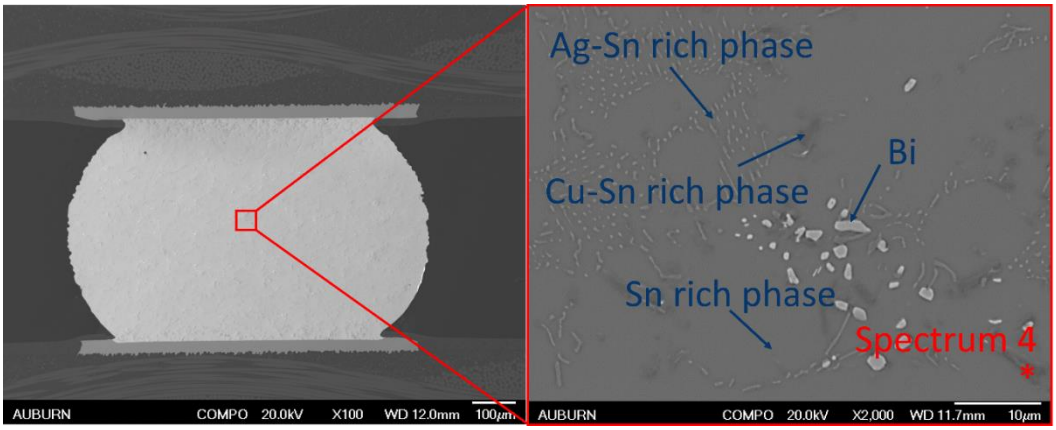

(d)

Figure 7-7 SEM microstructure of (a) SAC305, (b) SAC-R, (c) SAC-Q, and (d) SAC-I

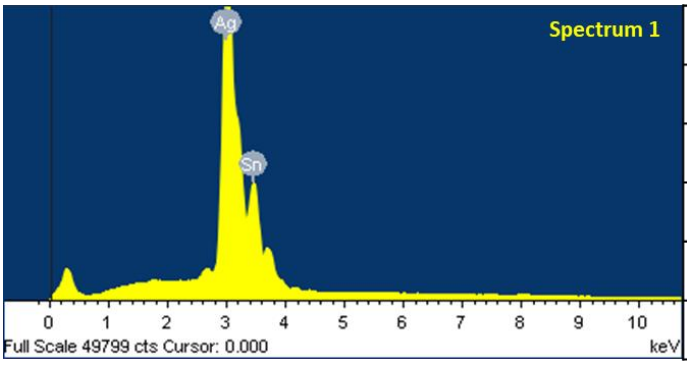

Element	Weight%	Atomic%
Ag L	71.59	73.50
Sn L	28.41	26.50
Totals	100.00	

(a) SAC305 (spectrum 1 location)

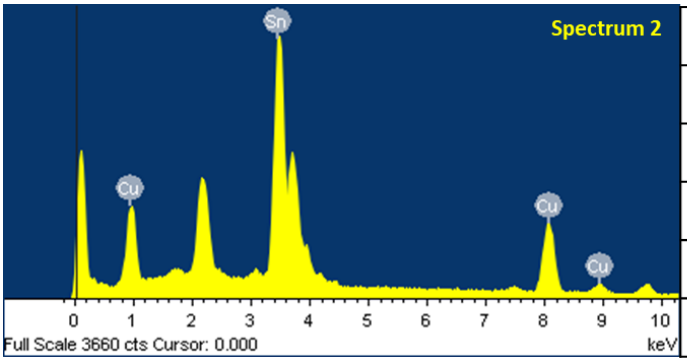

Element	Weight%	Atomic%
Cu K	30.38	44.91
Sn L	69.62	55.09
Totals	100.00	

(b) SAC-R (spectrum 2 location)

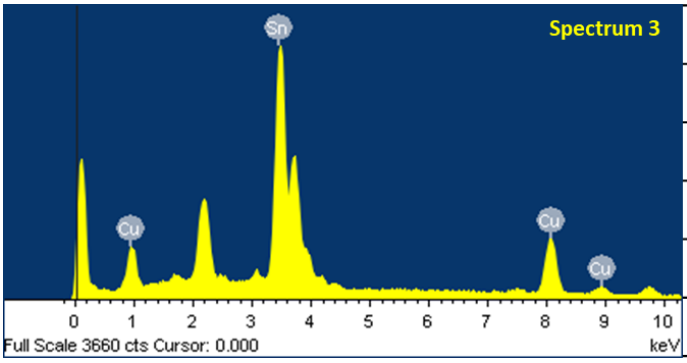

Element	Weight%	Atomic%
Cu K	26.44	40.17
Sn L	73.56	59.83
Totals	100.00	

(c) SAC-Q (spectrum 3 location)

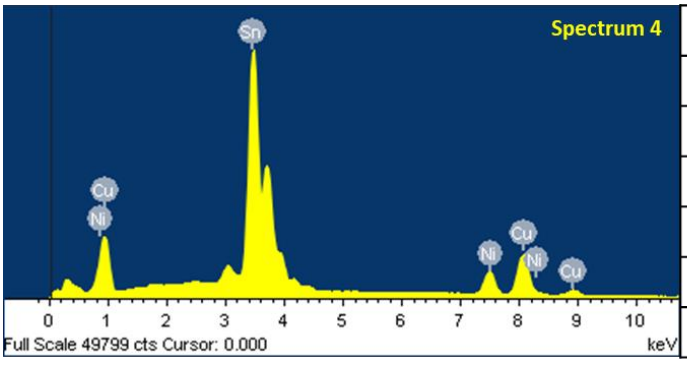

Element	Weight%	Atomic%
Ni K	8.95	14.34
Cu K	19.58	29.00
Sn L	71.47	56.66
Totals	100.00	

(d) SAC-I (spectrum 4 location)

Figure 7-8 Energy dispersive X-ray (EDS) spectrum analysis of (a) SAC305 (spectrum 1 location), (b) SAC-R (spectrum 2 location), (c) SAC-Q (spectrum 3 location), and (d) SAC-I (spectrum 4 location).

The surface finish guarantees the solderability and protects the Cu pad from oxidation and corrosion. The OSP surface finish interacted with the flux during the reflow process and decomposed, leaving the Cu pad and molten solder in direct contact. This enables the formation of an interfacial layer between the copper pad and the solder joint. The ENIG surface finish consisted mainly of a two-layers of Ni-Au metallic coating. At the reflow temperature, the topmost layer of Au dissolves into the molten solder. The Ni layer acts as a barrier between the Cu pad and the solder joint. The cross-sectional morphologies of the interfacial IMC layers in SAC305, SAC-R, SAC-Q, and SAC-I solder joints are depicted in Figure 7-9. In Figure 7-10, the compositions of some typical IMC layers were determined using EDS spectrum analysis. The OSP and ENIG surface finishes revealed significantly different IMC layers compositions. As shown in Figure 7-9 (a), the Sn in the SAC305 solder interacts with the Cu provided primarily by the Cu pad and, to a minor extent, by the solder to generate a scalloped Cu_6Sn_5 IMC layer. Another thin Cu_3Sn IMC layer was also observed between the Cu_6Sn_5 layer and Cu pad immediately after reflow. However, the Cu_3Sn IMC layer grows by consuming the Cu_6Sn_5 IMC layer ($9Cu + Cu_6Sn_5 \rightarrow 5Cu_3Sn$). This diffusion process between the Cu6Sn IMC layer and the Cu pad is accelerated by external influences such as temperature, aging, stress, current, and magnetic field. However, no IMC layers were observed in this study. The Ni layer inhibits the interdiffusion rate between Cu atoms from the Cu pad and Sn atoms in the bulk solder with the ENIG surface finish, delaying the formation of Cu-Sn compounds. Meanwhile, because Cu and Ni have comparable

atomic sizes and are both face-centered cubic lattice structures, a new Cu-Ni-Sn phase can be formed without incurring lattice distortion. Ho et al. [151] observed that the Cu content of the solder affected the nature and morphology of the IMC layer. A low Cu content (< 0.3 wt%) led to the formation of a single $(Cu, Ni)_3Sn_4$ IMC layer at the interface, whereas increasing the Cu content promoted the formation of a second $(Cu, Ni)_6Sn_5$ IMC layer. Figure 7-9 (b) depicts a thin and continuous $(Cu, Ni)_3Sn_4$ IMC layer adjacent to the Ni layer and the comparatively large discontinuous IMC layer. These two IMCs were based on Cu_6Sn_5 and Ni_3Sn crystal structures [152]. The addition of Ni stabilizes the Cu_6Sn_5 phase by preventing the allotropic phase transformation from hexagonal η-Cu_6Sn_5 to monoclinic η-Cu_6Sn_5 [153].

Figure 7-9 (c) shows the IMC interfaces of the SAC-R solder joints. SAC-R had a smoother and thinner Cu_6Sn_5 IMC layer than SAC305, as shown in Figure 7-9 (c). According to Yang et al. [154], Ag influences grain orientation and forms additional Cu_6Sn_5 grain boundaries at the interface, resulting in a thicker IMC interfacial layer. Furthermore, the solid solution of Bi produces lattice distortions in the Sn-rich phase, reducing the self-diffusion of Sn atoms. This also slowed the growth of the Cu6Sn5 IMC layer. Regarding the ENIG surface finish, only a hexagonal $(Cu, Ni)_6Sn_5$ IMC layer was observed on the Ni layer, as shown in Figure 7-9 (d). The absence of a $(Cu, Ni)_3Sn_4$ IMC layer was due to the comparatively high Cu content of the SAC-R solder. The impact of the Cu content is explained using the Cu-Ni-Cn isotherm [155].

Figures 7-9 (e) and (f) demonstrate the cross-sectional morphologies of the interfacial IMC layers of the SAC-Q solder joints with OSP and ENIG surface finishes, respectively. The interfacial IMC layers were identified as a single layer of Cu_6Sn_5 with an OSP surface finish, as displayed in Figure 7-9 (e), and a dual layer of $(Cu, Ni)_3Sn_4$ and $(Cu, Ni)_6Sn_5$ with ENIG surface finish, as depicted in Figure 7-9 (f). The smoother

Cu_6Sn_5 IMC layer outperformed the scalloped Cu_6Sn_5 in SAC305 solder joints in terms of strength. When the Ni layer acted as a barrier, large facet-like $(Cu, Ni)_6Sn_5$ IMC precipitates were observed on top of the thin $(Cu, Ni)_3Sn_4$ IMC layer. Furthermore, SAC-Q solder alloys generate large amount of Ag_3Sn plates, which can adversely affect the plastic deformation properties and induce plastic-strain localization at the boundary between the Ag_3Sn plates and the β-Sn phase [156].

The composition of the IMC layers differs slightly from those of the aforementioned IMC layers as a result of the addition of Ni to the SAC-I solder alloy. Figure 7-9 (g) shows a new type of $(Cu, Ni)_6Sn_5$ IMC layer. The Cu-Ni-Sn IMC layer was formed when Ni atoms in the SAC-I solder reacted with Cu and Sn atoms. The EDS spectra identified much less Ni in this situation than in the $(Cu, Ni)_6Sn_5$ IMC layer on top of the Ni layer. Figure 7-9 (h) illustrates the interfacial morphology of SAC-I with ENIG surface finish. As shown, a small $(Cu, Ni)_6Sn_5$ IMC layer was formed on top of the $(Cu, Ni)_3Sn_4$ IMC layer. The observation was consistent with the findings of Yao et al. [157]. Both layers exhibited increased Ni concentrations. Large Ag_3Sn plates with any of the two surface finishes are observed again. Furthermore, Bi precipitates were detected, which could further improve reliability by precipitation hardening.

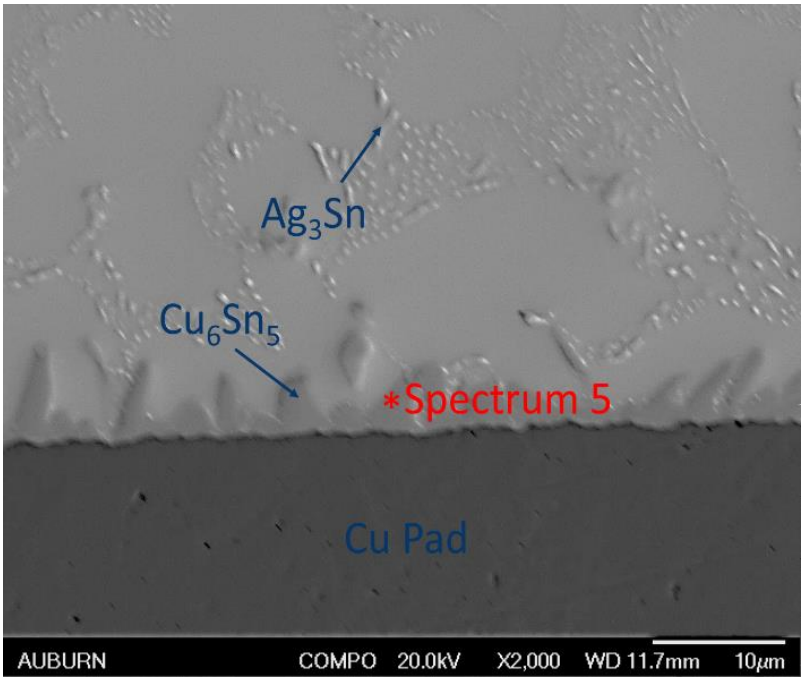
Ag3Sn
Cu6Sn5
*Spectrum 5
Cu Pad
AUBURN COMPO 20.0kV X2,000 WD 11.7mm 10μm

(a)

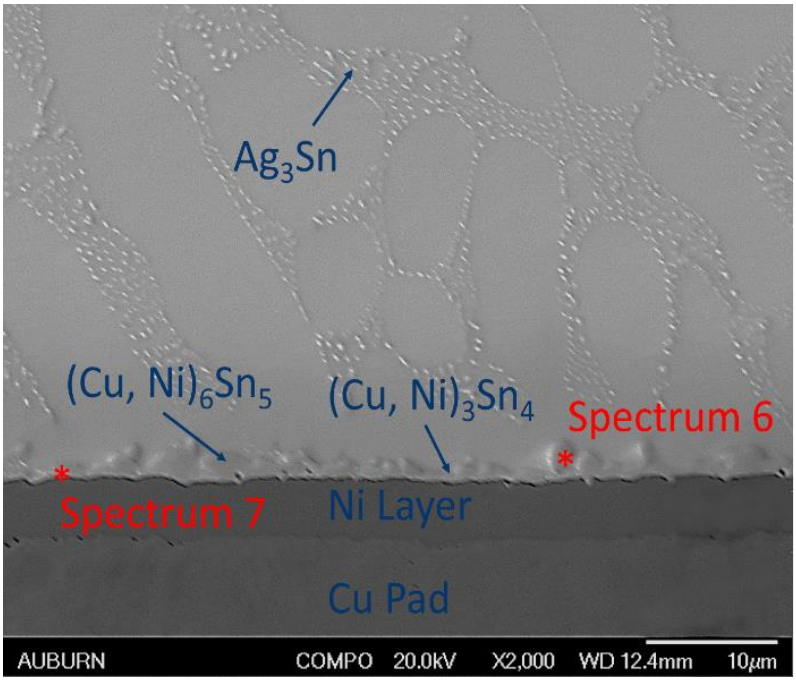
Ag3Sn
(Cu, Ni)6Sn5
(Cu, Ni)3Sn4
Spectrum 6
*
*
Spectrum 7
Ni Layer
Cu Pad
AUBURN COMPO 20.0kV X2,000 WD 12.4mm 10μm

(b)

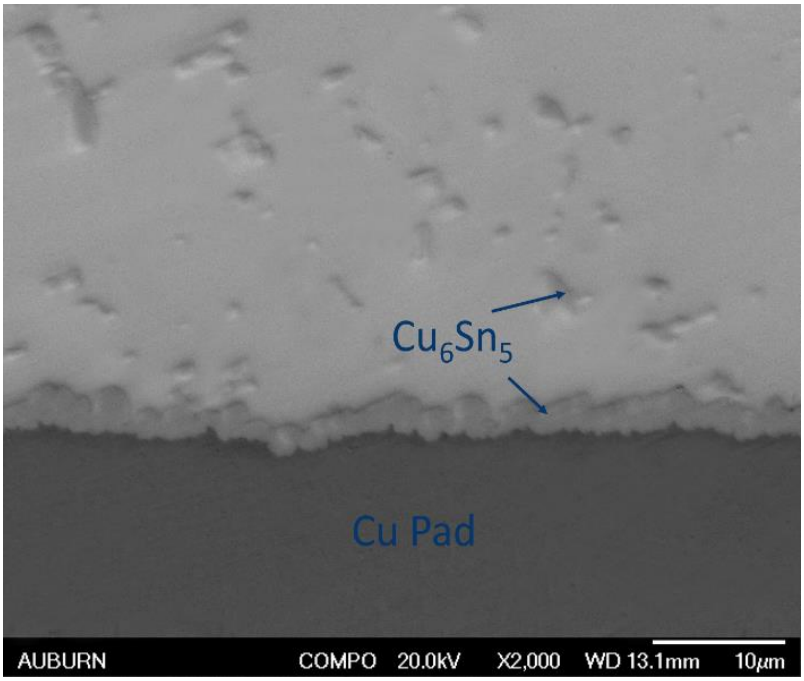
Cu_6Sn_5
Cu Pad
AUBURN COMPO 20.0kV X2,000 WD 13.1mm 10μm

(c)

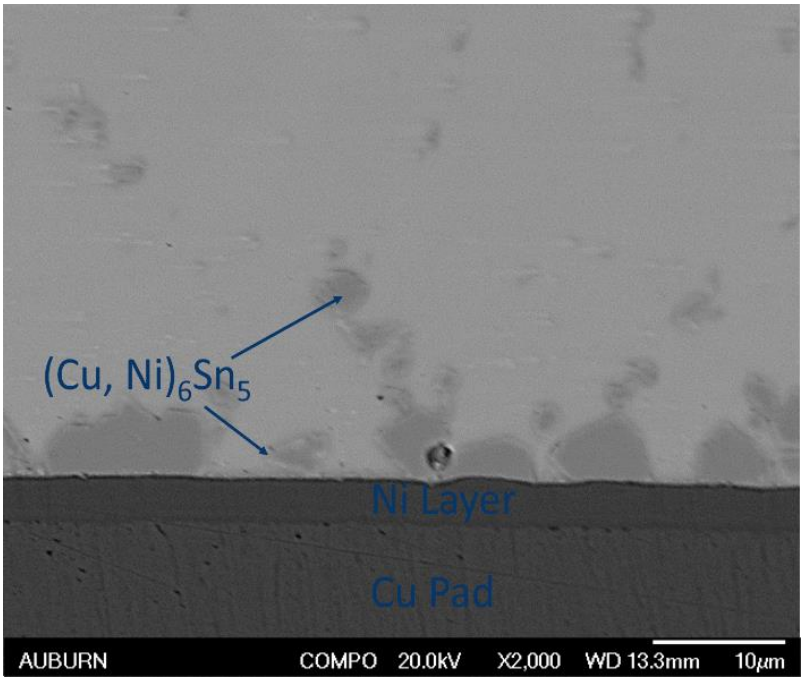
$(Cu, Ni)_6Sn_5$
Ni Layer
Cu Pad
AUBURN COMPO 20.0kV X2,000 WD 13.3mm 10μm

(d)

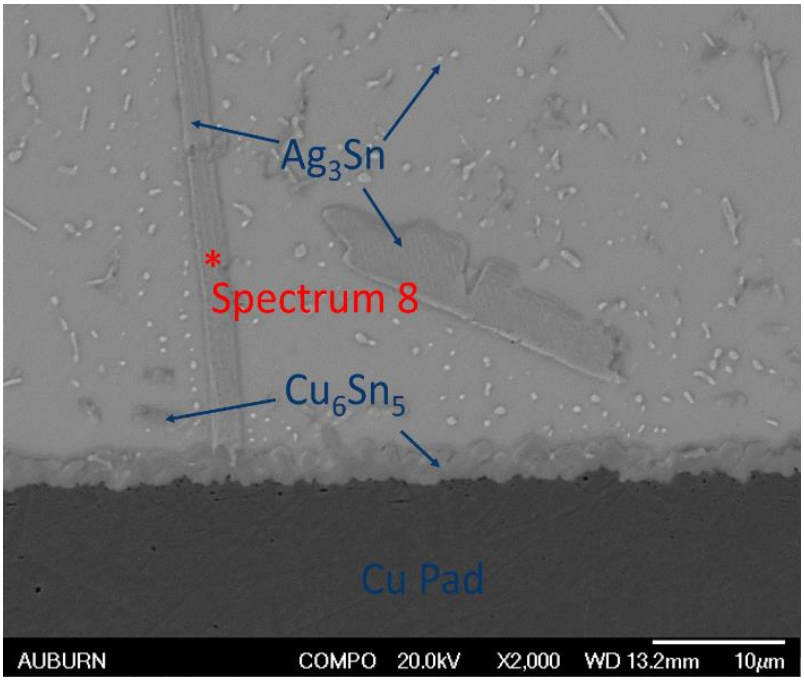
Ag_3Sn
*
Spectrum 8
Cu_6Sn_5
Cu Pad
AUBURN
COMPO 20.0kV X2,000 WD 13.2mm 10μm

(e)

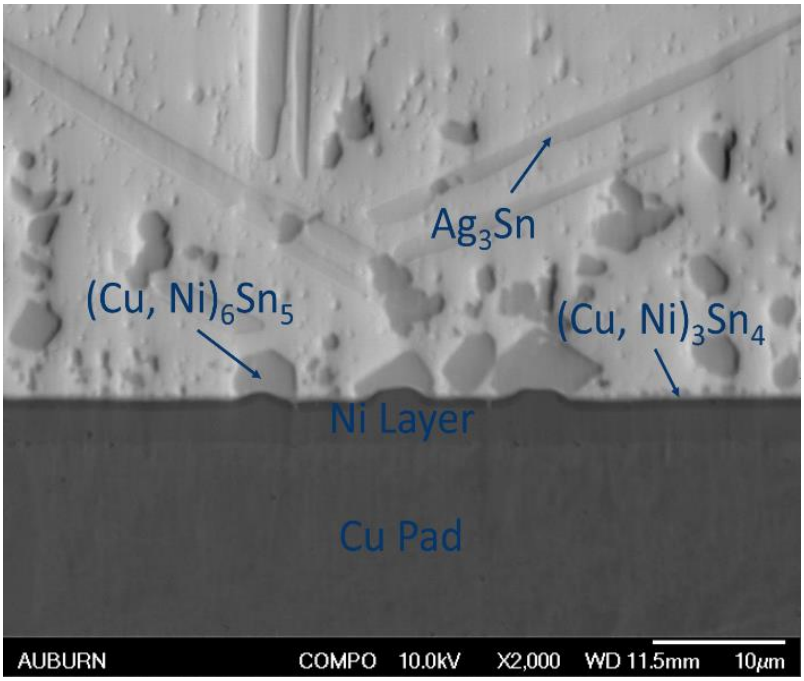
Ag_3Sn
$(Cu, Ni)_6Sn_5$
$(Cu, Ni)_3Sn_4$
Ni Layer
Cu Pad
AUBURN
COMPO 10.0kV X2,000 WD 11.5mm 10μm

(f)

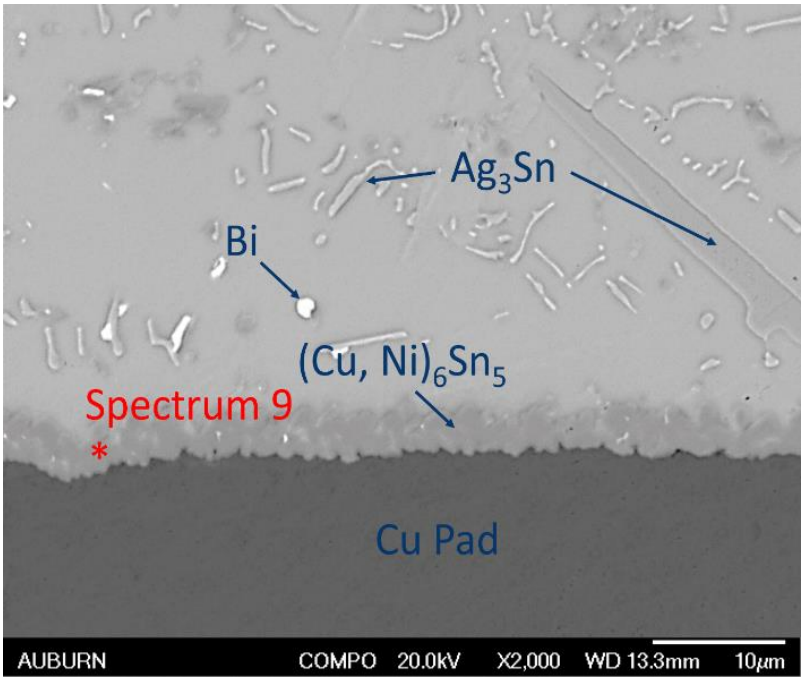

(g)

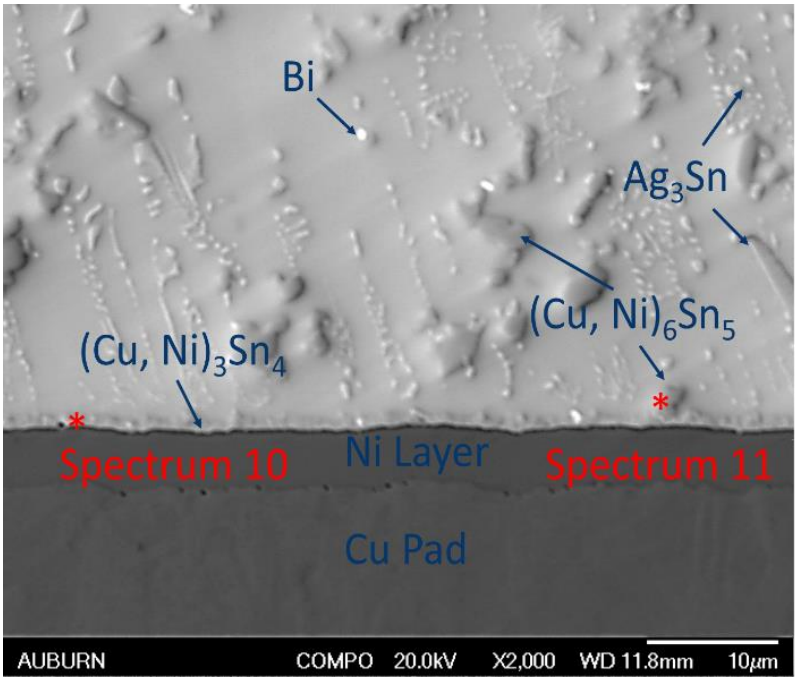

(h)

Figure 7-9 IMC morphology of (a) SAC305 with OSP surface finish, (b) SAC305 with ENIG surface finish, (c) SAC-R with OSP surface finish, (d) SAC-R with ENIG surface finish, (e) SAC-Q with OSP surface finish, (f) SAC-Q with ENIG surface finish, (g) SAC-I with OSP surface finish, and (h) SAC-I with ENIG surface finish

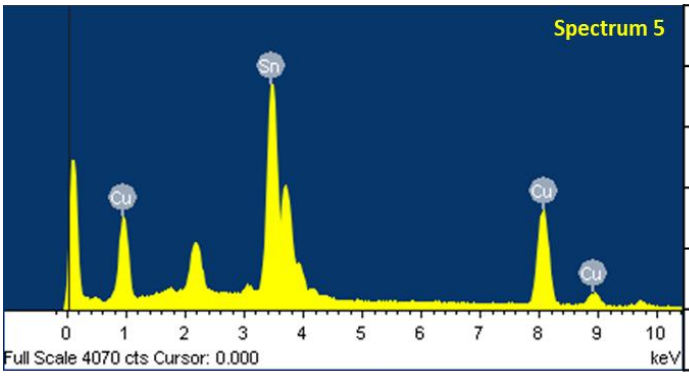

Element	Weight%	Atomic%
Cu K	41.14	56.63
Sn L	58.86	43.37
Totals	100.00	

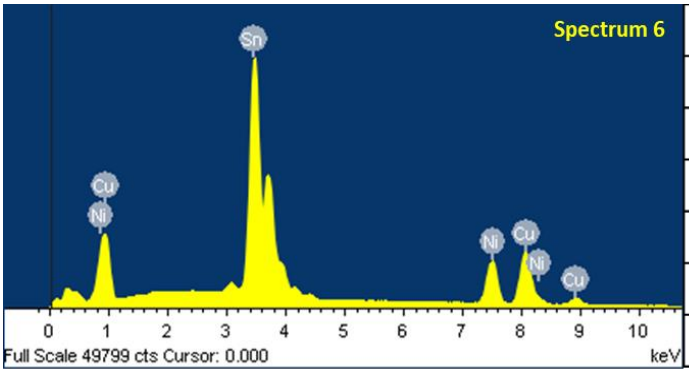

Element	Weight%	Atomic%
Ni K	14.57	21.97
Cu K	22.04	30.73
Sn L	63.39	47.30
Totals	100.00	

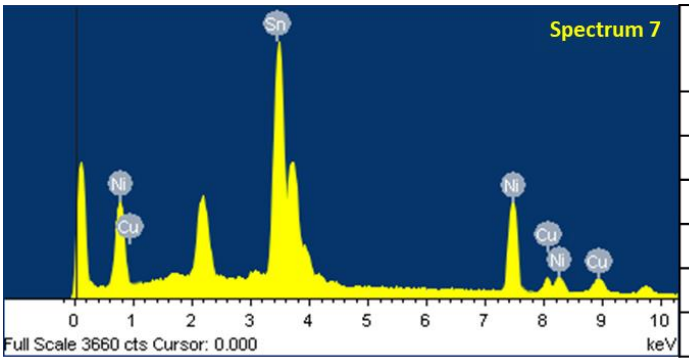

Element	Weight%	Atomic%
Ni K	23.57	36.88
Cu K	5.94	8.58
Sn L	70.50	54.54
Totals	100	

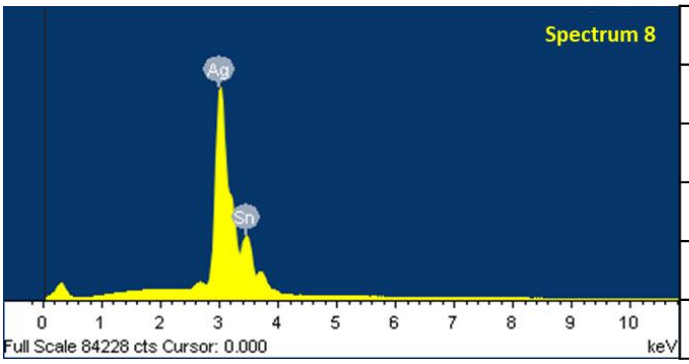

Element	Weight%	Atomic%
Ag L	72.92	74.76
Sn L	27.08	25.24
Totals	100.00	

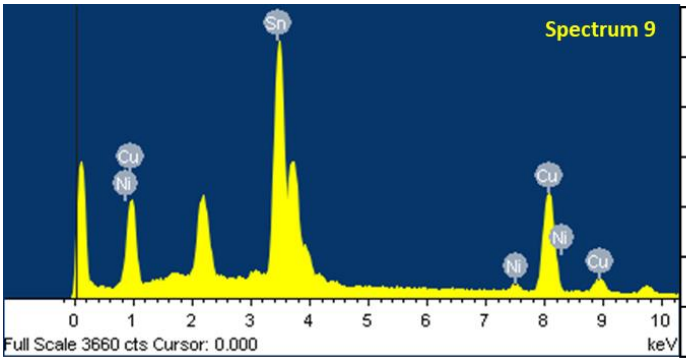

Element	Weight%	Atomic%
Ni K	1.62	2.41
Cu K	39.16	53.93
Sn L	59.23	43.67
Totals	100.00	

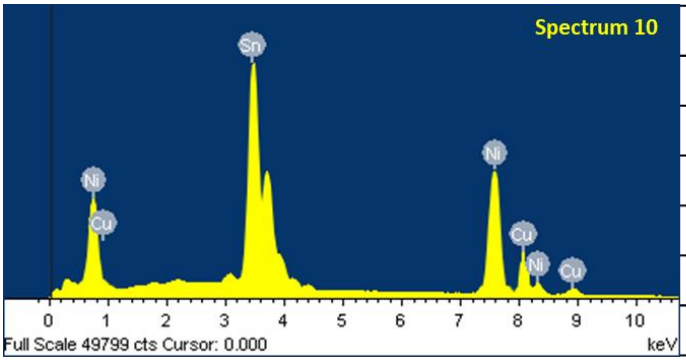

Element	Weight%	Atomic%
Ni K	26.81	41.41
Cu K	4.09	5.83
Sn L	69.10	52.76
Totals	100	

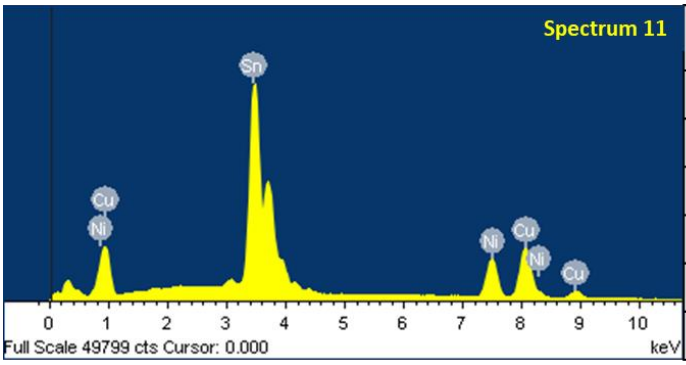

Element	Weight%	Atomic%
Ni K	14.36	21.43
Cu K	23.90	32.98
Sn L	61.74	45.59
Totals	100.00	

Figure 7-10 Energy dispersive X-ray (EDS) spectrum analysis spectrum 5, 6, 7, 8, 9, 10, and 11 locations

Figure 7-11 displays the thickness of the various interfacial IMC layers in the SAC305, SAC-R, SAC-Q, and SAC-I solder joints. A Cu_6Sn_5 IMC layer was formed with the same OSP surface finish in the SAC305, SAC-R, and SAC-Q solder joints, whereas another $(Cu, Ni)_6Sn_5$ IMC layer was observed in the SAC-I solder joints. The Ni in the $(Cu, Ni)_6Sn_5$ IMC layer originates the SAC-I bulk solder. There was no significant difference in the IMC thickness between SAC305 and SAC-R with the OSP surface

finish, while SAC-Q and SAC-I generated a thicker IMC layer. Bi in SAC-Q and SAC-It would also inhibit the growth rate of IMC layer when exposed to external factors such as stress, current, or temperature, thus providing better fatigue resistance [158][159]. The growth of the $(Cu, Ni)_6Sn_5$ phase dominated the $(Cu, Ni)_3Sn_4$ phase in SAC305 and SAC-Q, while more $(Cu, Ni)_3Sn_4$ phase was found in SAC-I. Because of the high Cu concentration, no $(Cu, Ni)_3Sn_4$ phase was observed in the SAC-R solder joint. In general, the Ni layer of the ENIG surface finish impeded the diffusion of Cu from Cu pad, resulting a thinner IMC layer. However, it is well worthy note that the variability of IMC layer was significantly increased since the presence of hexagonal $(Cu, Ni)_6Sn_5$ phase. A thinner IMC layer does not necessarily provide better reliability for solder joints.

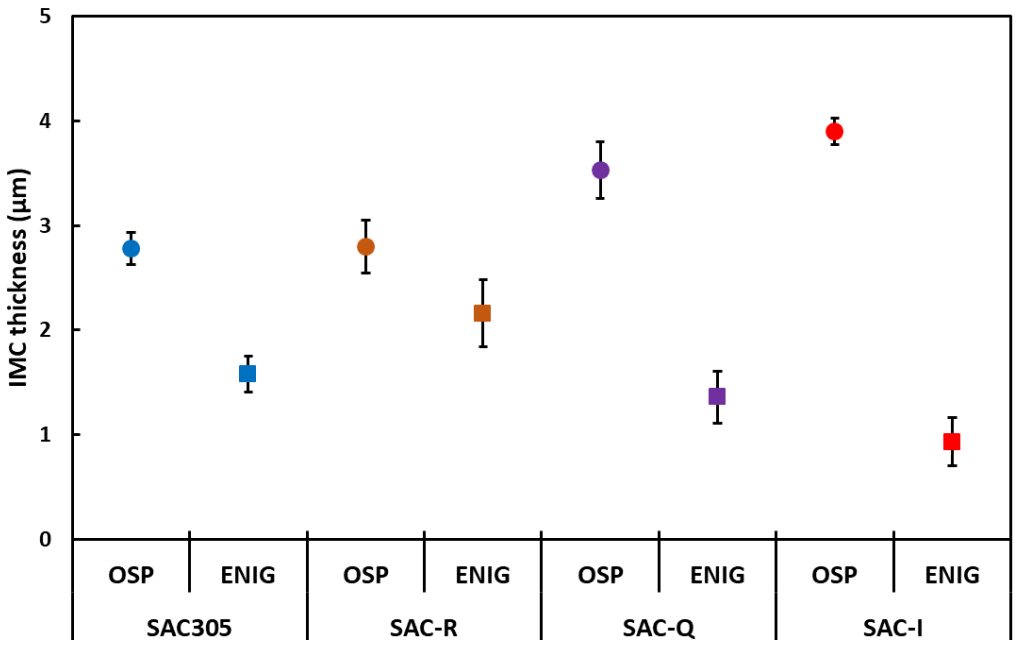

Figure 7-11 Thickness of interfacial IMC layer in SAC305, SAC-R, SAC-Q, and SAC-I solder joint

Both the stress-controlled and strain-controlled methods revealed the same solder joint failure mechanisms. Figure 7-12 depicts the fracture surfaces of the SAC305, SAC-R, SAC-Q, and SAC-I solder joints after fatigue failure. The flow stress theory explains the failure mechanisms of solder joints [70]. During the shear fatigue test, the

deformation of the viscoplastic solder joint induced flow stress. The flow stress competes with the copper peel and interfacial strength to initiate fractures. Pad cratering occurs when the flow stress exceeds the copper peel strength. Otherwise, when the interfacial strength is stronger than the flow stress, fractures can develop at the solder wedge and propagate intergranular into the solder matrix, indicating a ductile failure mechanism. However, crack initiation and propagation can occur either at the IMC/pad interface or near the IMC/solder interface, where the interfacial strength is lowest. The former is referred to as brittle failure, whereas the latter is referred to as a near-IMC failure. Ductile failure was observed for SAC305 (Figure 7-12 (a)) and SAC-R (Figure 7-12 (c)) with the OSP surface finish because a significant amount of bulk solder was on the Cu pad, indicating fracture growth in the bulk solder. SAC305 (Figure 7-12 (b)) and SAC-R (Figure 7-12 (d)) exhibited near-IMC cracks with an ENIG surface finish, where a partial $(Cu, Ni)_6Sn_5$ IMC layer was visible around the bulk solder. The growth of the $(Cu, Ni)_6Sn_5$ IMC layer degrades the mechanical characteristics of solder joints and causes the failure mode to shift from ductile to brittle [44]. Near-IMC failure was also observed for SAC-Q (Figure 7-12 (e)) and SAC-I (Figure 7-12 (g)) with an OSP surface finish. A distinct separation developed between the bulk solder and IMC layer, leaving the exposure of Cu_6Sn_5 and $(Cu, Ni)_6Sn_5$ on the Cu pad. The two solder alloys exhibited a very distinct brittle failure mechanism with an ENIG surface finish, resulting in a smoother fracture surface. The smooth surface was recognized as the Ni layer, indicating the separation of IMC and Ni layers on the Cu pad.

(a)

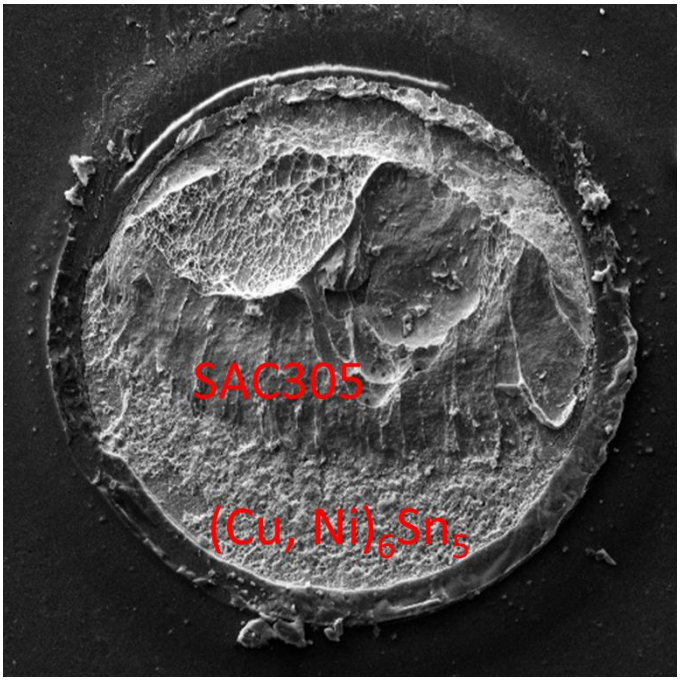

(b)

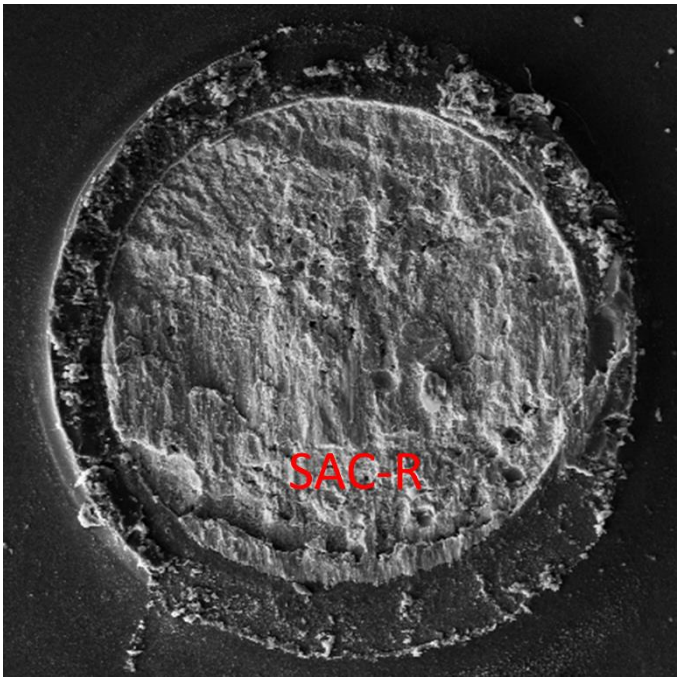

(c)

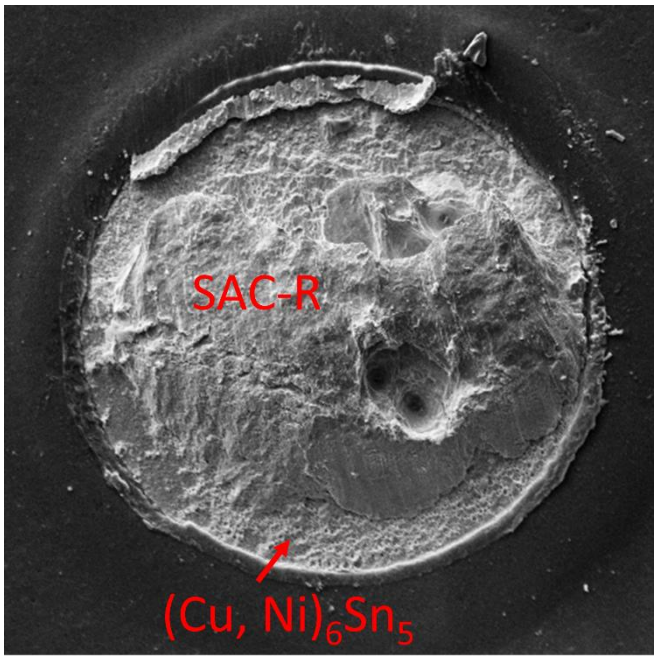

(d)

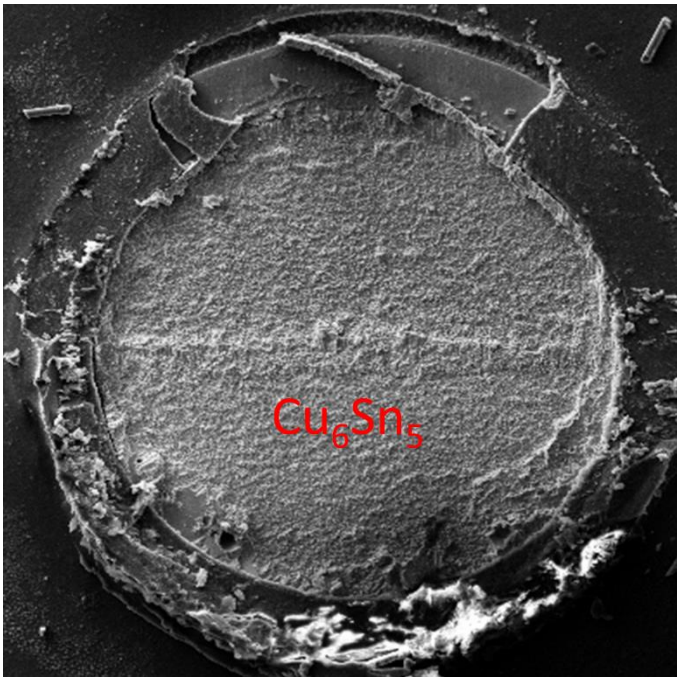

(e)

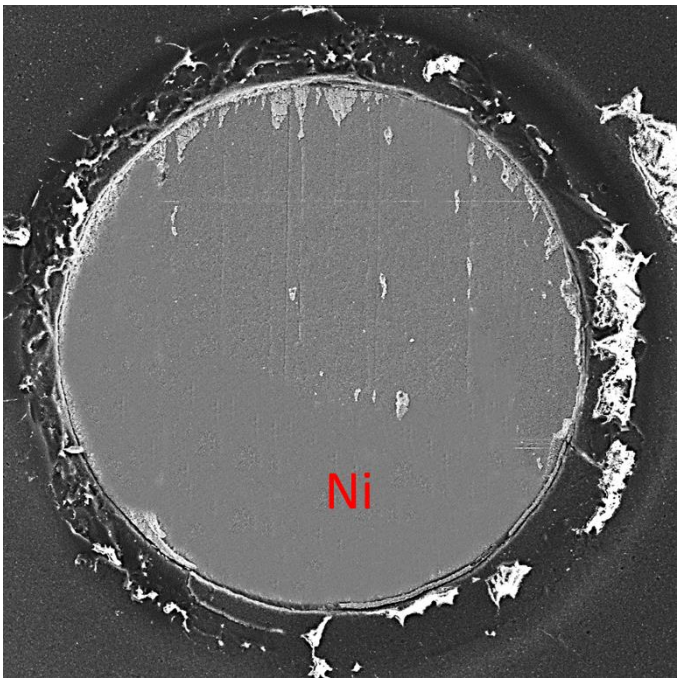

(f)

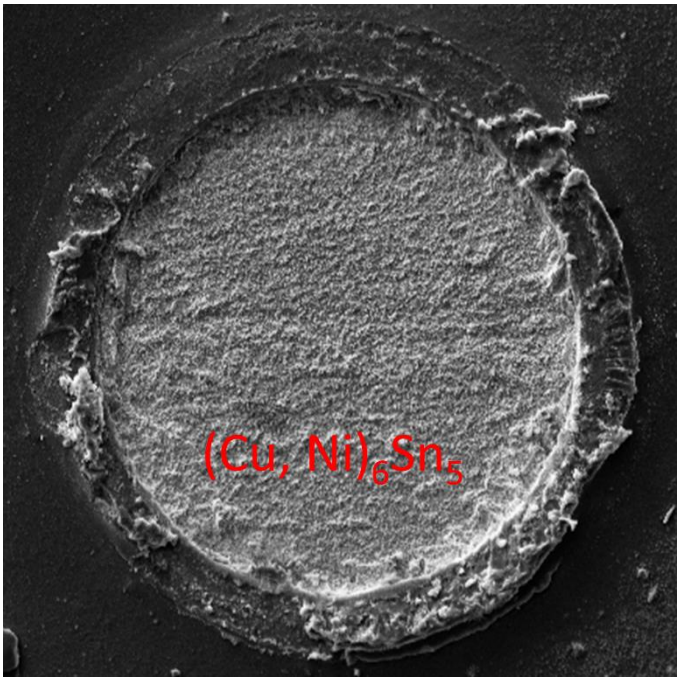

(g)

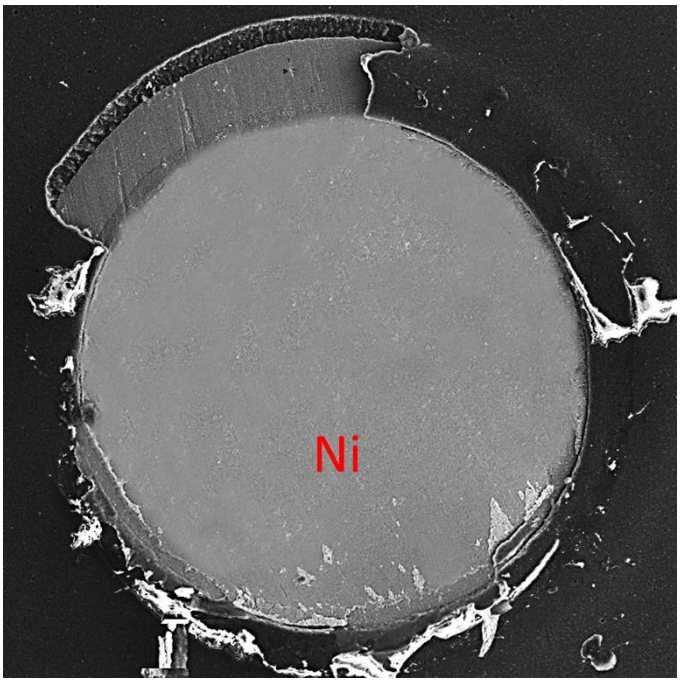

(h)

Figure 7-12 Top views of failed solder joints for (a) SAC305 with OSP surface finish, (b) SAC305 with ENIG surface finish, (c) SAC-R with OSP surface finish, (d) SAC-R with ENIG surface finish, (e) SAC-Q with OSP surface finish, (f) SAC-Q with ENIG surface finish, (g) SAC-I with OSP surface finish, and (h) SAC-I with ENIG surface finish

7.4 Conclusion

This study examined the fatigue properties of SAC305, SAC-R, SAC-Q, and SAC-I solder alloys with OSP and ENIG surface finishes using strain-controlled and stress-controlled methods. The fatigue performance of these solder alloys was compared. The SEM and EDS were used to determine the microstructure and failure mechanisms of each solder alloy. The findings of this study are summarized as follows:

1. A higher stress/strain level leads to more damage accumulation in each cycle, resulting in a shorter fatigue life.
2. The OSP surface finish outperformed the ENIG surface finish, regardless of the testing methods and solder alloys.
3. Solder alloys with higher Ag and Bi contents demonstrate better fatigue resistance associated with the OSP surface finish.
4. Brittle failure was observed in SAC-Q and SAC-I with an ENIG surface finish. They are more susceptible to changes in strain and stress, particularly strain.
5. The interfacial IMC layer of SAC305 with the OSP surface finish was scallop-like Cu_6Sn_5, whereas smoother layers were observed in the SAC-R, SAC-Q, and SAC-I solder joints.
6. Each IMC interface exhibited a facet-like $(Cu, Ni)_6Sn_5$ IMC layer with ENIG surface finish. Except for SAC-R, a thin $(Cu, Ni)_3Sn_4$ layer was also formed. This ascribes to the higher Cu concentration in SAC-R.

7.5 Contribution

The fatigue performance of SAC305, SAC-R, SAC-Q, and SAC-I solder joints in BGA assembly were compared using stress-controlled and strain-controlled tests at the room

temperature. This study examined the fatigue life as the cycle to obtain peak inelastic work in strain-controlled test. The results indicated the substitutability of the more economic SAC-R to SAC305 since their similarities in terms of fatigue life, regardless of the surface finish and testing method. SAC-Q and SAC-I solder alloys showed more fatigue resistance than SAC305 and SAC-R with the OSP surface finish mainly because of the superior mechanical properties of the solder spheres. As such, the interfacial strength became the bottleneck and crack was observed to propagate near the IMC layer. However, with the ENIG surface finish, the two solder alloys developed even weaker IMC layers. Another brittle failure mode was observed in this case, shown as the clear and smooth separation between the Ni layer and the IMC layer. Since the difference in failure mode, SAC-Q and SAC-I are more sensitive to the change of strain and stress, particularly strain.

The comparison of fatigue life and the identification of failure mode in this study revealed that the OSP surface finish could potentially provide stronger interfacial IMC bonding than the ENIG surface finish. One should take careful considerations if extrapolating this conclusion in real service life. The present conclusions were drawn from isothermal cycling test. It might give valuable insights for the development of more reliable solder alloys. However, it doesn’t mean that the OSP surface finish is always better than the ENIG surface finish. For example, usually the ENIG surface finish outperforms the OSP surface finish in thermal cycling tests.

Chapter 8 Effect of Temperature on the Fatigue Behavior of Solder Joints in BGA Assembly

8.1 Introduction

Various materials, including metal, ceramic, and polymers, are used to construct electronic packaging. Each material has its own thermal and mechanical qualities, which collectively affect the failure mechanisms and overall reliability of an electronic assembly [160][161]. Interconnections in this system act as mechanical support and electrical conduction between components and substrates are typically subjected to rather high plastic strain. In a thermal cycling environment, the plastic strain is caused by the mismatch of the Coefficient of Thermal Expansion (CTE) between the component and substrate [107][162][163].

Extensive research has been carried out to examine the behaviors of interconnections during thermal cycling testing [164][165], Thermal Shock [166][167], and Low Cycle Fatigue (LCF) [99][113], and several models have been established to forecast the interconnections' reliability in thermal cycling. The interconnections may also be subjected to a long-term isothermal cycling state, such as vibration [168][169].

Many mechanical property studies were conducted on bulk samples, with the implicit assumption that relationships developed for bulk samples can be directly applied to solder joints in realistic applications, regardless of sample size or other impact factors such as intermetallic compound or surface finish [147]. During the PCB design and fabrication process, a layer of solder mask ink must be applied to the PCB's surface [170]. A solder mask is a thin layer of polymer that is put to the copper traces of a PCB to prevent oxidation and avoid "bridging" from solder pads that are closely spaced. The

solder mask aperture for solder mask defined (SMD) pads is smaller than the copper pad, which reduces the size of the copper pad on which components are soldered. Due to the fact that solder masks can only cover a portion of the copper traces, copper pads on PCB remain unprotected and exposed to the air, which may also contribute to a reliability issue [171]. To shield the remaining copper pads from additional corrosion and oxidation prior to assembly, a protective surface finish is applied [141]. In addition, surface finishes serve as a basis for connecting electronic components, thereby facilitating the assembly process, and promoting more durable solder joints for long-term functionality. Each surface finish has its own distinct characteristics and processing obstacles, such as Hot Air Solder Level (HASL) [172], Organic Solderability Preservative (OSP) [173], Immersion Silver (ImAg) [174], Electroless Nickel, and Immersion Gold (ENIG) [175].

Su et al. [21] investigated how different "micro-alloyed" SnAgCu-based solder materials' shear properties were affected by the surface finish. It was revealed that, when compared to other solder alloy-surface finish combinations, the combination of high Silver (Ag) and Bismuth (Bi) content solder alloy and ENIG surface finish is more prone to brittle failure. Moreover, for all shear strain rates, OSP and ImAg surface finishes outperform ENIG surface finishes in terms of shear strength. Another research results [105] appear consistent with the above findingsm which indicated that OSP and ImAg surface finishes exceeded ENIG surface finishes in terms of fatigue resistance in solder joints. The best fatigue resistance was found to be in CycloMax, whereas the worst was found to be in SAC-X-Plus, which had an ENIG surface finish. This study identified the ductile, brittle, and near-IMC failure modes.

In addition to surface finish and composition of the solder alloy; temperature is one of the variables that affect the shear strength and mechanism of failure of solder joints. It

was discovered that the mechanical properties of solder material changed noticeably with temperature [176][177]. At 25 degrees Celsius, Xiao et al. [178] performed tensile tests on solder alloys, and at higher temperatures and it was found that the tensile strength of Sn-Pb and Sn-3.9Ag-0.6Cu solder alloys decreased by 25% after being aged at room temperature. In addition, lower frequency and higher temperature have a negative impact on low cycle fatigue endurance for lead-free solders made of 95.5Sn, 3.8Ag, and 0.7Cu as reported by Pang [99]. The fracture morphology gives brief details on the types of modes resulting from different temperatures. Zhu et.al [25] found a transgranular mode is visible in the fracture morphology at 348 K and mixed intergranular and transgranular mode at 398 K. The fatigue life of solder joints under high temperatures can also be assessed using the Coffin-Manson model and the Morrow energy-based model. Temperature affects both the fatigue ductility exponent and the fatigue ductility coefficient in the two models. In addition, the two parameters were found to fit linearly [26] and polynomially [13] as a function of testing temperature.

Tin-Lead alloys are still often utilized in defense-related applications as a soldering material mainly because of its predictability. However, many studies have revealed the superiority of SAC-based solder alloys over SnPb solder alloys [29][179]. Considering this situation, Department of Defense (DoD) has recently launched the ‘Solder Reliability and Assurance Project’ to ensure the safe transition from SnPb alloys to Lead-Free solder alloys for the crucial defense-related electronic applications. Until now, some research has studied the effect of temperature on the fatigue properties of solder alloys, but using bulk samples [13][24], while limited work employed individual solder joints [25][26]. Most of the studies focused on the effects of frequency and strain level on the fatigue behavior of solder alloys [23][27][28]. No literature has compared the fatigue properties between SAC305 and SnPb solder joints considering the effect

of surface finish and testing temperature. There is indeed a need to conduct a comprehensive study to investigate the fatigue properties of SAC305 and SnPb solder joints in BGA assembly. An empirical model is required to predict their fatigue performance given the strain level and testing temperature. In this study, SAC305 and SnPb solder joints with the OSP and ENIG surface finishes in BGA assembly were tested at the temperatures of 248K, 298K, and 348K using the strain-controlled profile. Various strain levels were selected to investigate the fatigue properties of the test vehicles at different temperatures. An empirical model was proposed to predict the fatigue life given the strain level and testing temperature.

8.2 Microstructure and IMC Morphology

The microstructure of the solder joints influences the robustness of the interconnection between the component and substrate for electronic packaging. Flow stress was applied to distort the viscoplastic solder joint in the isothermal shear fatigue test [70], which resulted in accumulated damage in the bulk solder. The brittle IMC layer between the bulk solder and substrate is another potential path for initiating cracks. In terms of the fatigue resistance to initiate and propagate fractures, the bulk solder competes with the interfacial IMC layer. Thus, it is critical to explore the microstructure of the bulk solder and the morphology of IMC layers within solder joints in BGA assemblies. According to previous studies, a wide range of variables, including solder volume [156][180][181][182], surface finish [174][21][183], aging time [174][184], aging temperature [182][185], and alloying additives [186][187][22], affect the microstructure and IMC morphology. The solder volume and reflow profile strongly influence the size of the bulk solder phases, which are controlled by solidification conditions [156][180]. However, because the Cu concentrations increase more quickly in smaller solder joints

than in larger ones, the decrease in solder volume favors the formation of a giant scallop-like Cu_6Sn_5 [181]. The availability of Cu atoms in bulk solder is also limited by the solder volume, which changes the composition of the IMC layer [182] with the ENIG surface finish. The surface finish selection significantly affected the composition and morphology of the IMC layer. Figure 8-1depicts the as-reflowed microstructures of the SAC305 and SnPb solder joints. A typical SAC305 microstructure comprises the β-Sn and eutectic phases. Ag and Cu interacted with Sn to form Ag_3Sn and Cu6Sn5 IMC particles distributed throughout the β-Sn matrix. The Ag_3Sn particles in the β-Sn dendritic structure tend to form a network. Through the precipitation hardening process, these particles impede the movement of dislocations, thereby strengthening solder alloys. In contrast, the SnPb solder joint displayed a combination of Sn-rich and Pb-rich phases. Figure 8-2 demonstrates the cross-sectional morphologies of the interfacial IMC layers in the SAC305 and SnPb solder joints. With the OSP surface finish, the same Cu_6Sn_5 IMC layers were formed, whereas the ENIG surface finish revealed the $(Cu, Ni)_6Sn_5$ and Ni_3Sn_4 IMC layers. Before soldering, the OSP surface finished protecting the Cu pad, but it decomposed during the reflow process. As such, the Cu pad interacted with the molten solder to form an interfacial layer between the Cu pad and bulk solder. As a result, the Cu pad interacted with the molten solder to create an interfacial layer between the Cu pad and the bulk solder. In the SAC305 solder joints, the thickness of the Cu_6Sn_5 IMC layer was 2.78 μm, whereas the SnPb solder joints had a thinner and smoother IMC layer of 2.24 μm. This is due to the extra Cu concentration (0.5 wt.%) in the SAC305 solder joint, which promotes the creation of a scallop-like Cu_6Sn_5 IMC layer. The ENIG surface finish was a double-layer metallic coating, with the Ni layer in the center functioning as a barrier to the Cu pad and the Au layer on top to protect the Ni layer during storage. On average, the thickness of the uppermost Au

layer ranges between 0.05 μm and 0.1 μm. At the reflow temperature, it dissolves in the molten solder. Owing to the decreased reaction rate of Ni-Sn (interfacial reaction issues for lead-free electronic solders, reference), a thinner $(Cu, Ni)_6Sn_5$ IMC layer of 1.58 μm was developed in the SAC305 solder joint. Simultaneously, a tertiary phase of Ni_3Sn_4 occurs in the SnPb solder joints.

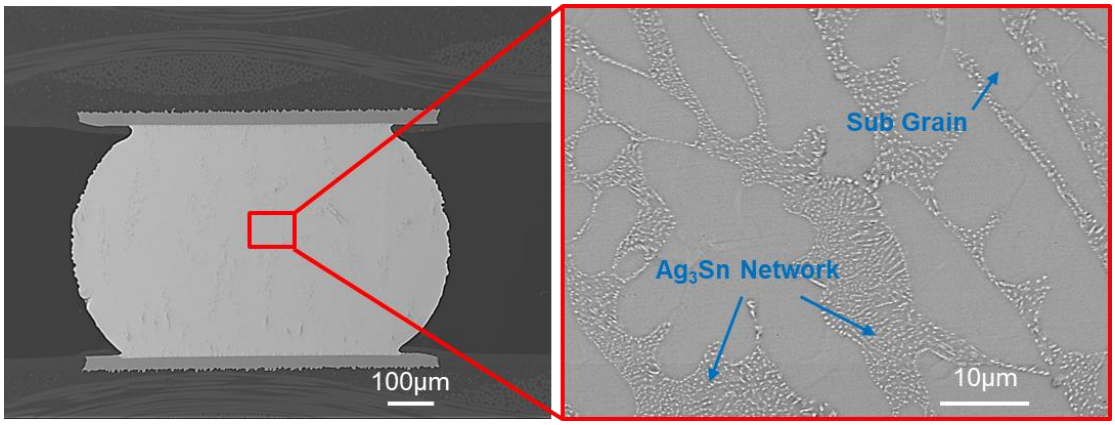

(a)

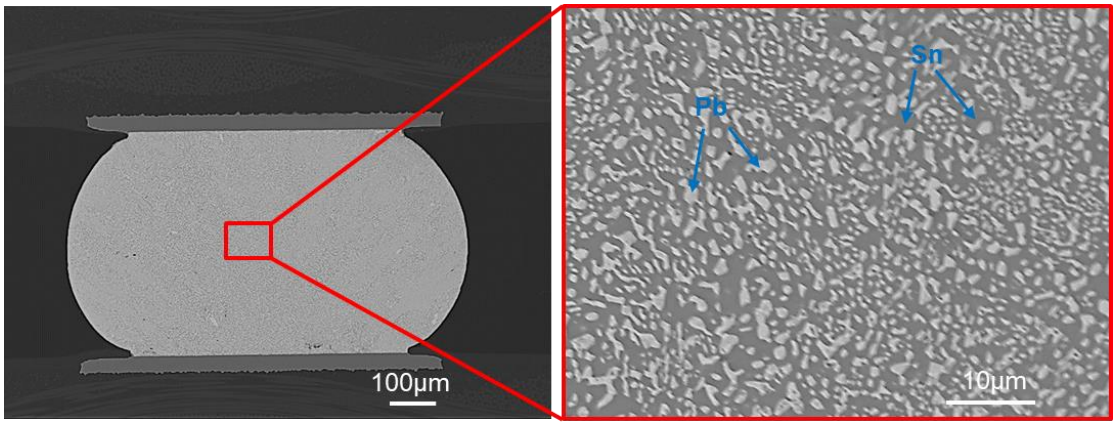

(b)

Figure 8-1 Microstructure of bulk solder (a) SAC305, (b)SnPb

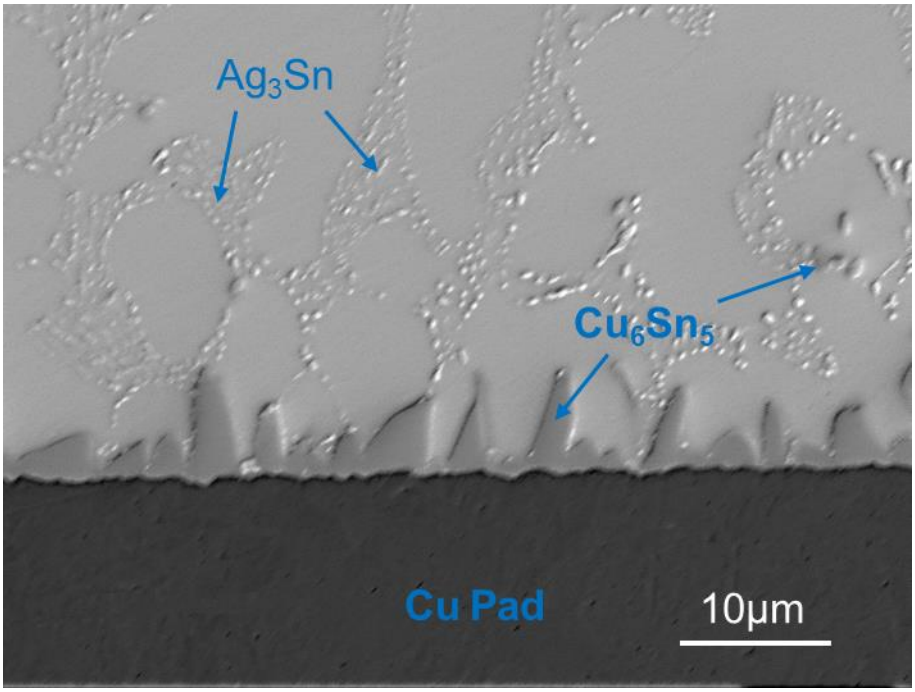

(a)

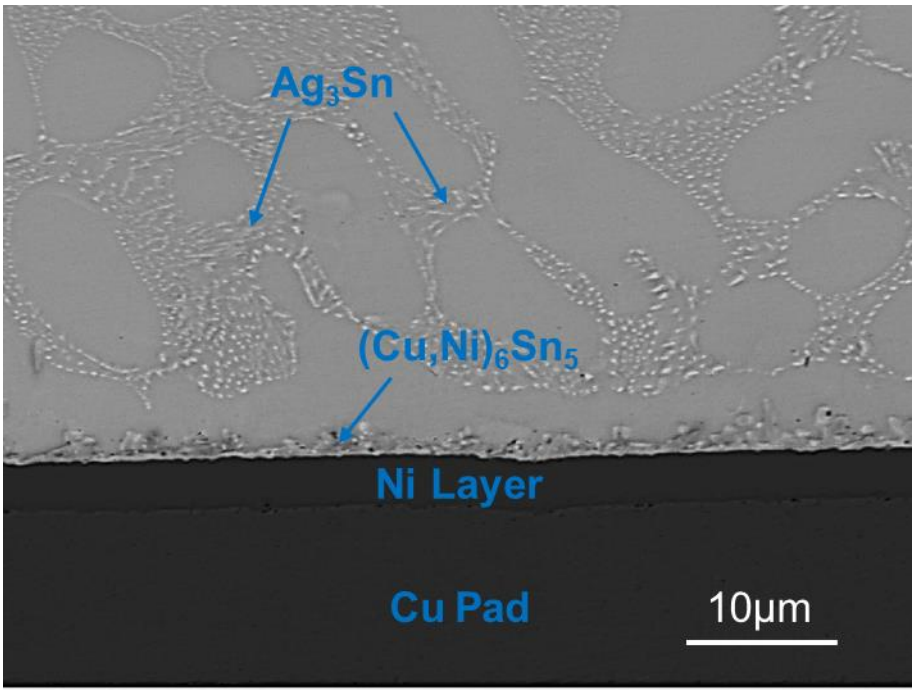

(b)

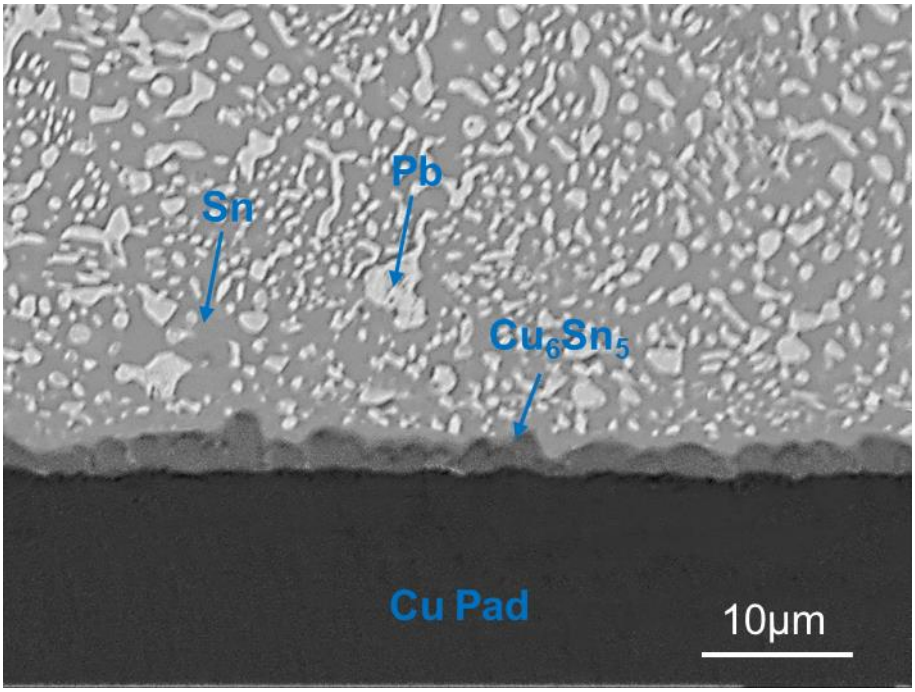

(c)

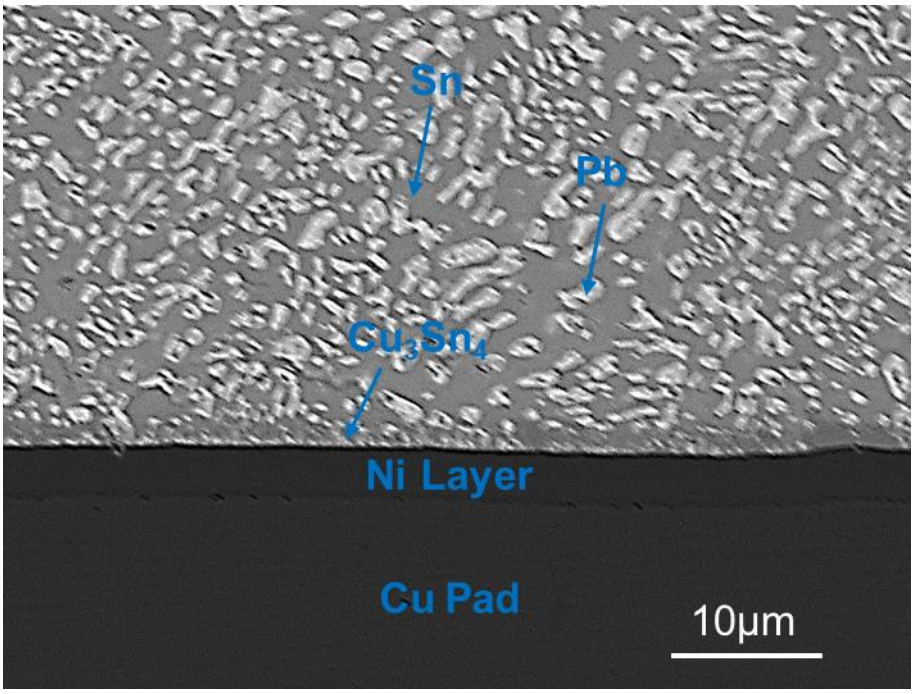

(d)

Figure 8-2 IMC morphologies of (a)SAC305 OSP, (b)SAC305 ENIG, (c)SnPb OSP, and (d) SnPb ENIG

8.3 Evolution of Hysteresis Loop

In strain-controlled testing, the absolute values of the maximum and lowest displacements were the same. The strain was calculated by dividing the displacement by the gauge length, while the stress was derived by dividing the load by the entire pad-opening area. Figure 8-3 depicts the initial hysteresis loops for the different test vehicles with the OSP and ENIG surface finishes cycled at 10% total strain at 248 K, 298 K, and 348 K temperatures. The enclosed region inside the hysteresis loop represents the inelastic work in each cycle. A hysteresis loop width of 0 MPa was used to calculate the plastic-strain range. As demonstrated, increasing the testing temperature decreased the peak stress value while increasing the inelastic work and plastic strain range. The peak stress was reduced slightly when the testing temperature was elevated from 248 K to 298 K, but significantly when the testing temperature was increased to 348 K. Enlargement of the width and size of the hysteresis loops followed the same pattern. The result is consistent, independent of the strain level, solder alloy, and surface finish.

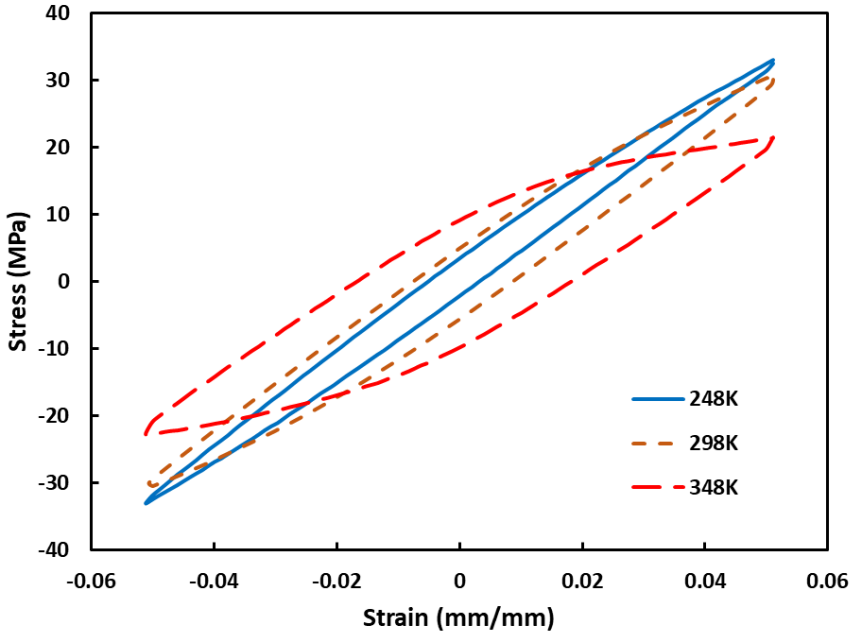

(a)

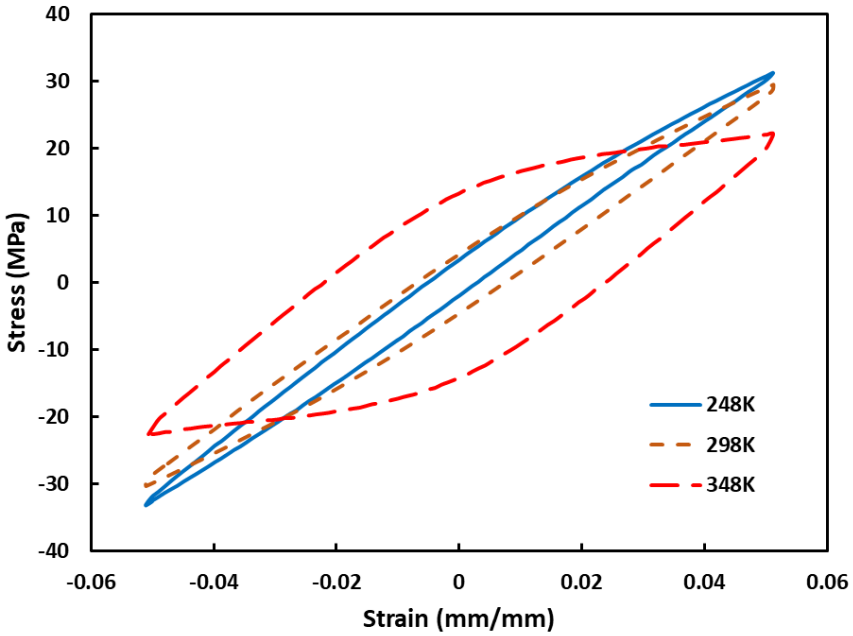
40
30
20
10
0
-10
-20
-30
-40
Stress (MPa)
-0.06
-0.04
-0.02
0
0.02
0.04
0.06
Strain (mm/mm)
248K
298K
348K

(b)

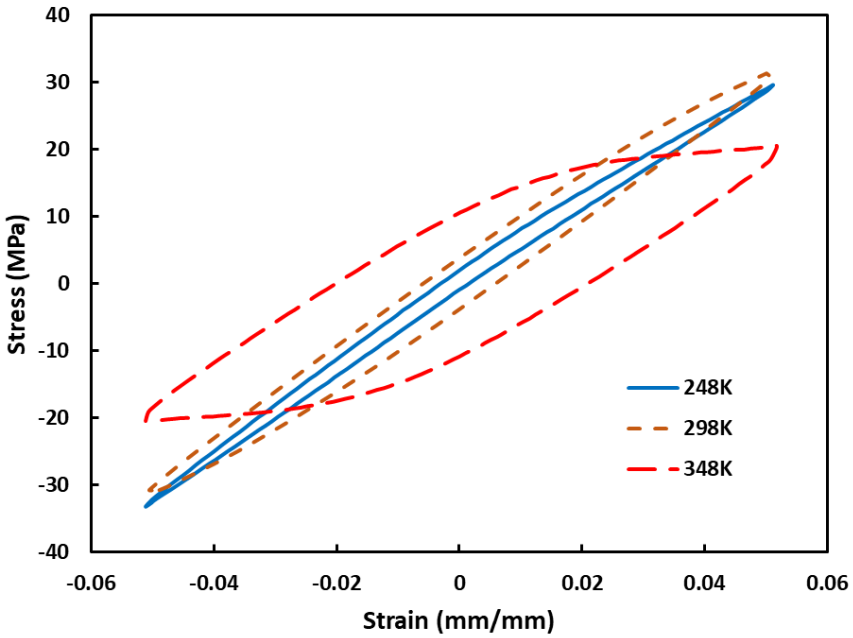
40
30
20
10
0
-10
-20
-30
-40
Stress (MPa)
-0.06
-0.04
-0.02
0
0.02
0.04
0.06
Strain (mm/mm)
248K
298K
348K

(c)

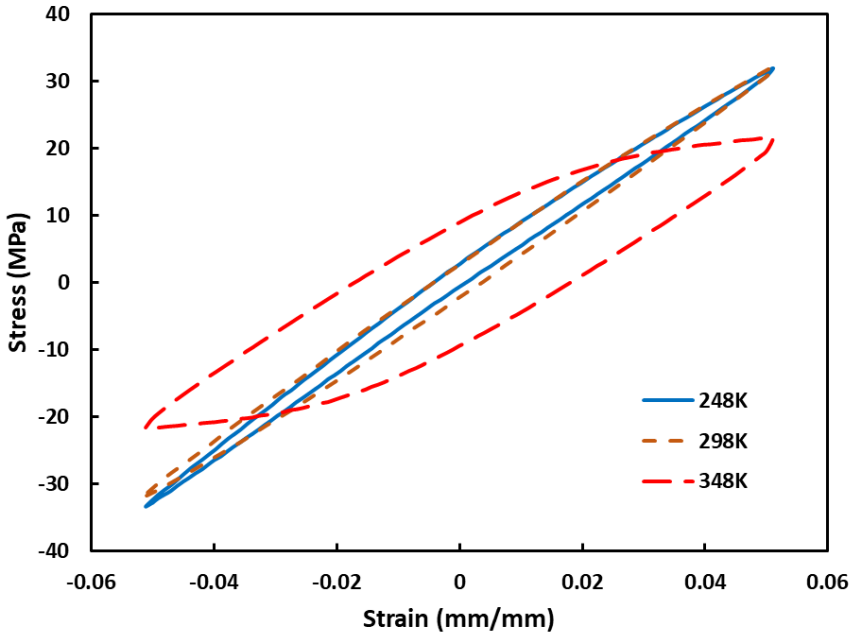

(d)

Figure 8-3 Effect of temperature on the first hysteresis loop with ΔεT = 10% for (a)SAC305 OSP, (b)SAC305 ENIG, (c)SnPb OSP, and (d) SnPb ENIG

Figure 8-4 shows the evolution of the stress-strain hysteresis for SAC305 with the OSP surface finish at 10% total strain at 298 K. During the first 100 cycles, the hysteresis loop changed only slightly. The maximum stress constantly decrease as the cyclic fatigue test progresses, as does the loop breadth. However, the size of the hysteresis loop goes through a growth and reduction phase. The inelastic work increased to a maximum and then decreased. The development of inelastic work per cycle during the cyclic fatigue test was computed using MATLAB to analyze the behavior of the fatigue mechanism. Figure 8-5 shows the inelastic work per cycle as a function of the cycle numbers. The inelastic work per cycle first increases until it reaches its maximum value, as represented by the red line. This implies that solder joints store energy. Subsequently, there was a drop in the inelastic work per cycle. According to the preliminary speculation, damage is generated and accumulates in the solder joints during the strain-controlled test, resulting in microcracks. In each cycle, the formation and propagation

of microcracks increased the inelastic work. However, microcracks progressively connect and join to form cracks. This resulted in a decline in the inelastic work per cycle following the peak value. The main crack expanded and propagated until it fractured completely.

Figure 8-6 demonstrates the variations in the maximum load with the cycle number for SAC305 and SnPb, considering the surface finish and testing temperature. As previously described in the hysteresis loop analysis, a lower testing temperature results in a higher initial maximum load. In each of the four situations shown in Figure 8-6, the maximum load of the solder joints at 248 K experienced a steady stage that accounted for most of the fatigue life, followed by a rapid decrease in the maximum load. The maximum load continually decreased at a low rate of 298 K. Subsequently, the reduction rate began to accelerate until the fracture completion. The fatigue life of the specimens tested at 298 K was shorter than those of the specimens tested at 248 K. An elevated temperature of 348 K accelerates the fatigue process. The maximum load was reduced instantly and swiftly to create a crack fracture, resulting in the shortest fatigue life. It is worth noting that, following the cyclic fatigue test, not all solder joints showed total breakage. Instead, the solder joints in the test vehicle could provide minor stresses without breaking. Consequently, the curves indicate a positive value when fatigue testing is completed. The black X markings in the images represent the cycles to attain the highest value of inelastic work or fatigue life. This fatigue life assessment occurred before the 50% maximum load drop, which was established as a failure criterion in the ASTM standard [118]. In several studies [108][68], the beginning of the accelerated increase in the load drop rate was identified as a complete failure dependent on the solder alloy and the strain level. The definition of failure used in previous studies is often subjective. The configuration, joint size, and surface finish solder joints in the

BGA assembly should all be considered. Thus, it is not unexpected that this method yielded an estimate of fatigue life just before the 50% maximum load decrease but before the start of the accelerated load drop. The proposed method for identifying failure based on peak inelastic work avoids ambiguities in a strain-controlled test.

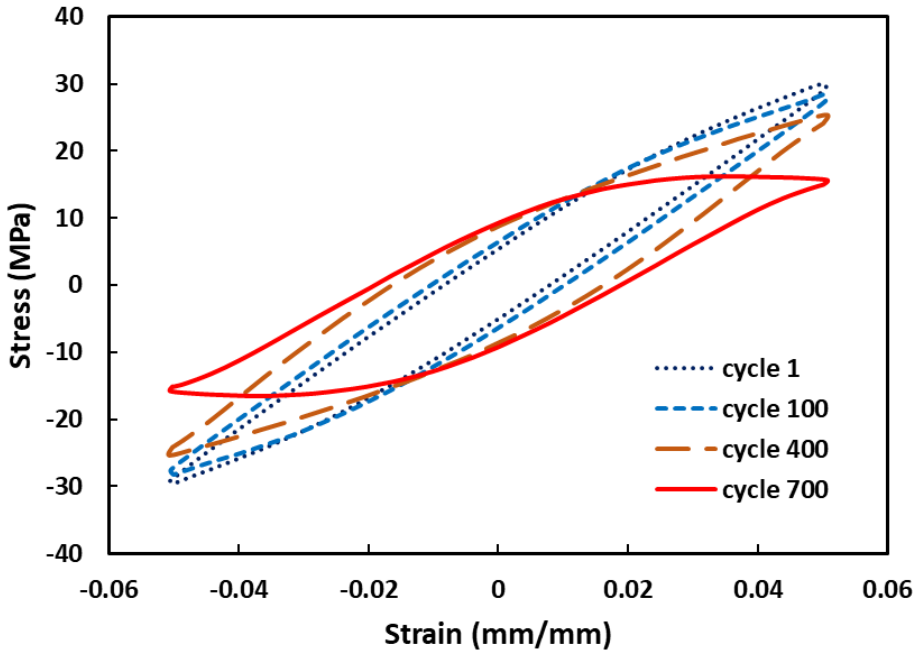

Figure 8-4 Evolution of hysteresis loop for SAC305 with OSP surface finish (ΔεT = 10%)

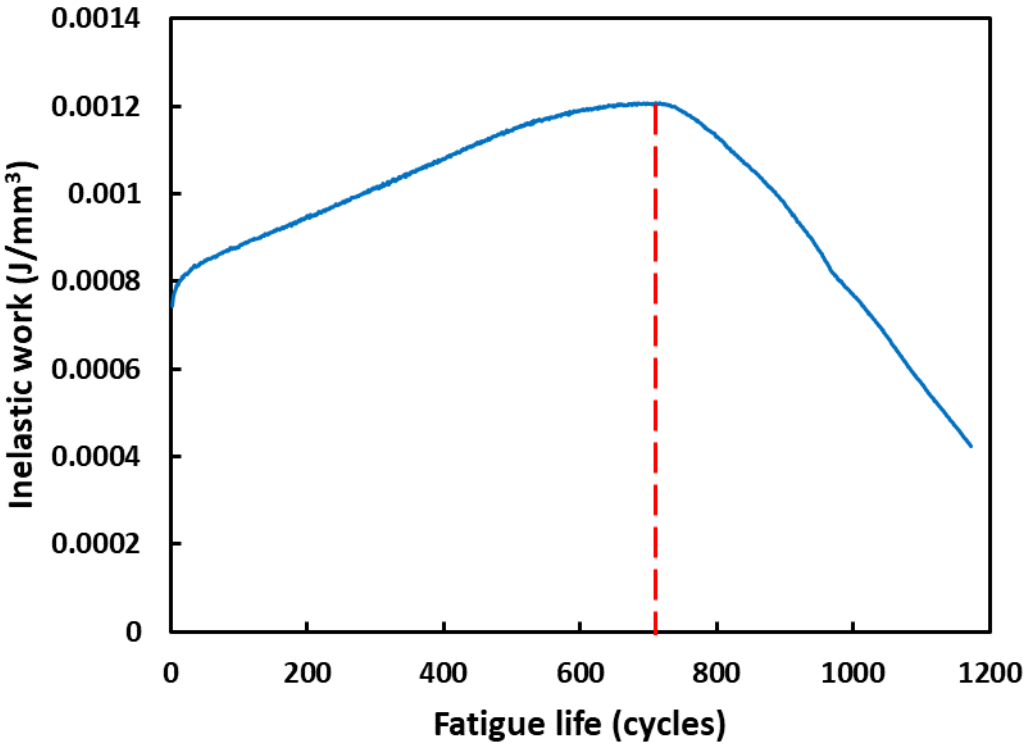

Figure 8-5 Evolution of inelastic work per cycle for SAC305 with OSP surface finish ($\Delta\varepsilon_T$ = 10%)

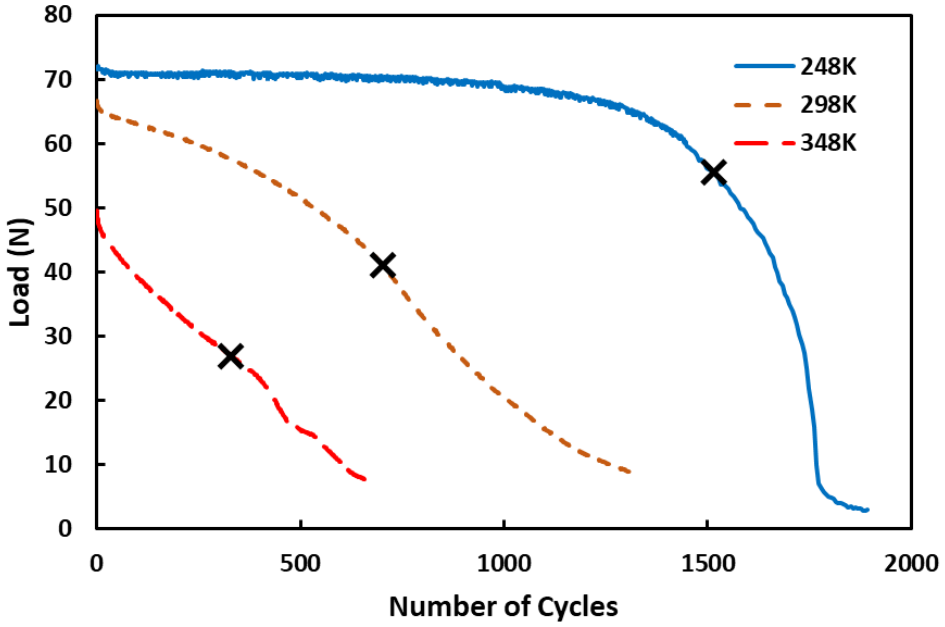

(a)

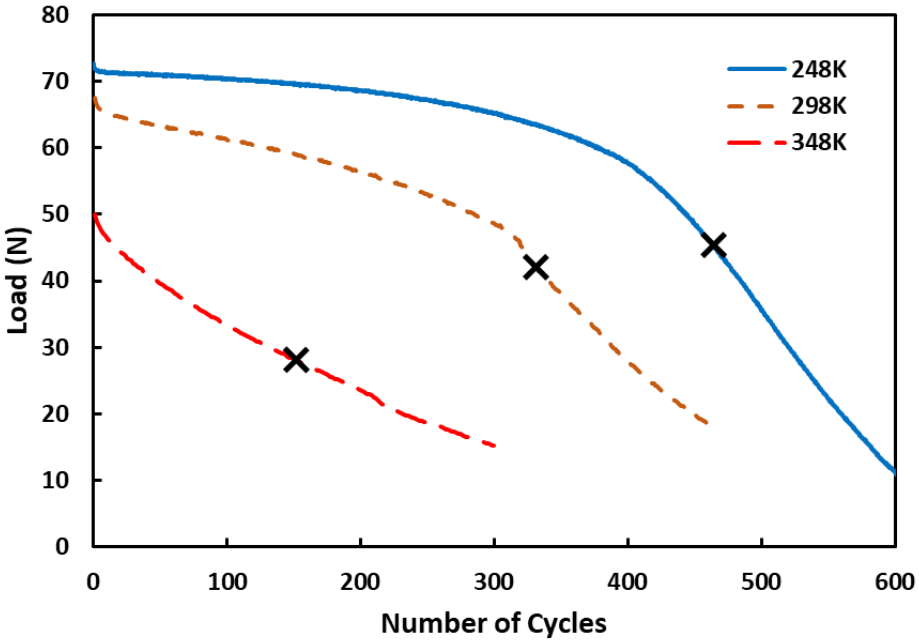
Load (N)
Number of Cycles
248K
298K
348K
0
10
20
30
40
50
60
70
80
0
100
200
300
400
500
600

(b)

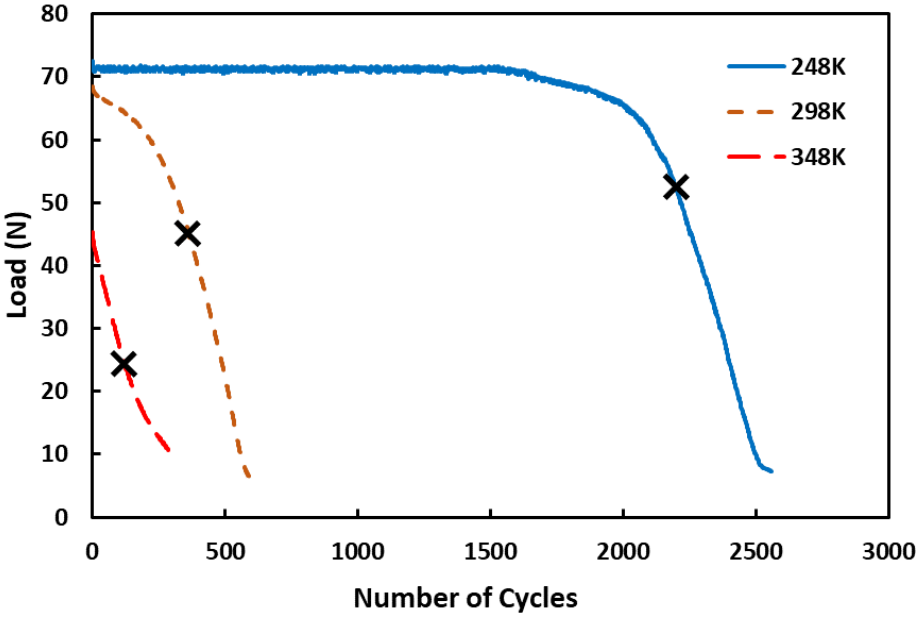
Load (N)
Number of Cycles
248K
298K
348K
0
10
20
30
40
50
60
70
80
0
500
1000
1500
2000
2500
3000

(c)

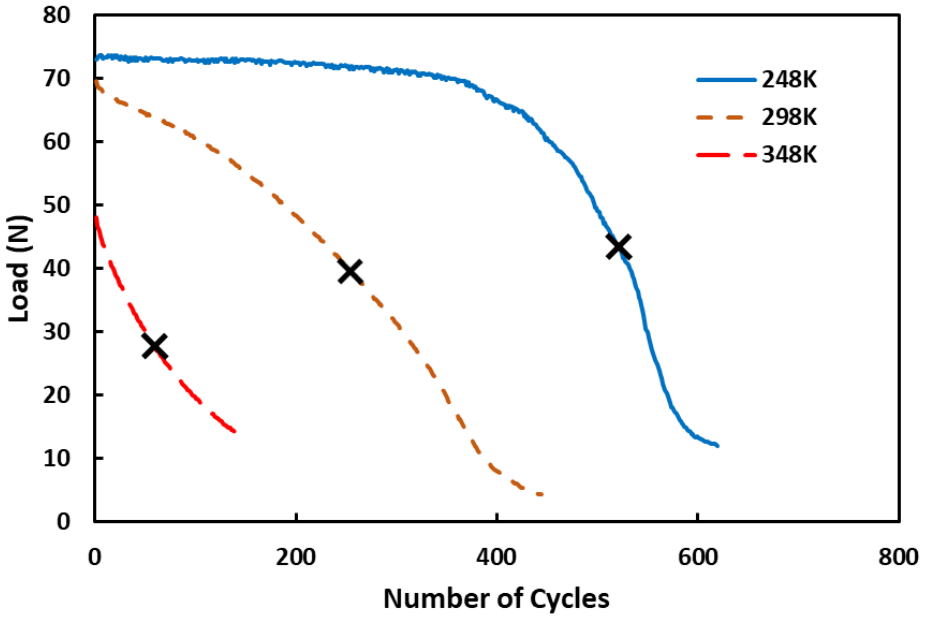

(d)

Figure 8-6 Variation of maximum load of hysteresis loop under various temperatures for (a)SAC305 OSP, (b)SAC305 ENIG, (c)SnPb OSP, and (d)SnPb ENIG ($\Delta\varepsilon_T$ = 10%)

8.4 Fatigue Life Analysis

As previously stated, the cycle with the peak inelastic work was used to estimate the fatigue life of the test vehicles using a two-parameter Weibull distribution. Figure 8-7 shows the fatigue life of each test vehicle under different total strains at the specific testing temperature. Figure 8-8 depicts the fatigue life of the test vehicles under typical conditions. Figure 8-8 (a) shows the fitted fatigue life of SAC305 with the OSP surface finish at 298 K for various strain values of 6.0%, 8.0%, 10.0%, and 12.0%. The five data points for each testing condition indicate the fatigue life of the five testing specimens at each strain level. The middle regression line shows that these data points effectively fit the Weibull distribution. The two curved lines represent the 95% confidence interval of the Weibull distribution, which include all fatigue data. The

shape parameter denotes the slope of the regression line. The typical fatigue life in terms of a scale parameter provides the cycle number at which failure occurs, with a 63.2% probability. The effects of the testing temperature and solder combination on the predicted fatigue life are shown in Figs. 12 (b) and 12(c), respectively. In Fig. 12(b), SAC305 solder joints with the OSP surface finish were evaluated with the same $\Delta\varepsilon_T$ (10%), and Fig. 12(c) examines various solder combinations at the same temperature (298 K) and $\Delta\varepsilon_T$ (10%).

The typical fatigue life derived from the Weibull distribution at strain level ε_T, is included in the empirical power equation as follows:

$$N_{63} = A(\Delta\varepsilon_T/2)^{-c} \qquad 8\text{-}1$$

Where N_{63} is the fatigue data for a given strain level, c is the strain exponent, representing the fatigue ductility of the solder alloy, and A is the substance constant. The ductility of the solder alloy decreases as c increases. Figure 8-9 depicts the fatigue life behavior at various temperatures vs. strain levels for various solder combinations on a logarithmic scale. High R^2 values imply that the goodness of fit was high. As shown, increasing the strain level resulted in a shorter fatigue life owing to the increased inelastic work per cycle. These results were consistent with the findings of Park et al. [23][26]. Furthermore, increasing the testing temperature reduces the solder fatigue resistance at all strain levels [13][24]. This can be attributed to the increased inelastic work per cycle. Figure 8-3 has shown the enlarged size of hysteresis loop during the first cycle at the higher test temperatures. This is because of the increase in the inelastic work per cycle. The enlarged size of the hysteresis loop during the first cycle at higher test temperatures is displayed in Figure 8-3. This finding continued to be accurate as the cycle test progressed, resulting in shorter fatigue life. Furthermore, independent of solder alloys or surface finishes, increasing the test temperature tended to diminish the

ductility of the solder alloys. Kanchanomai et al. [24][188] reported similar observations.

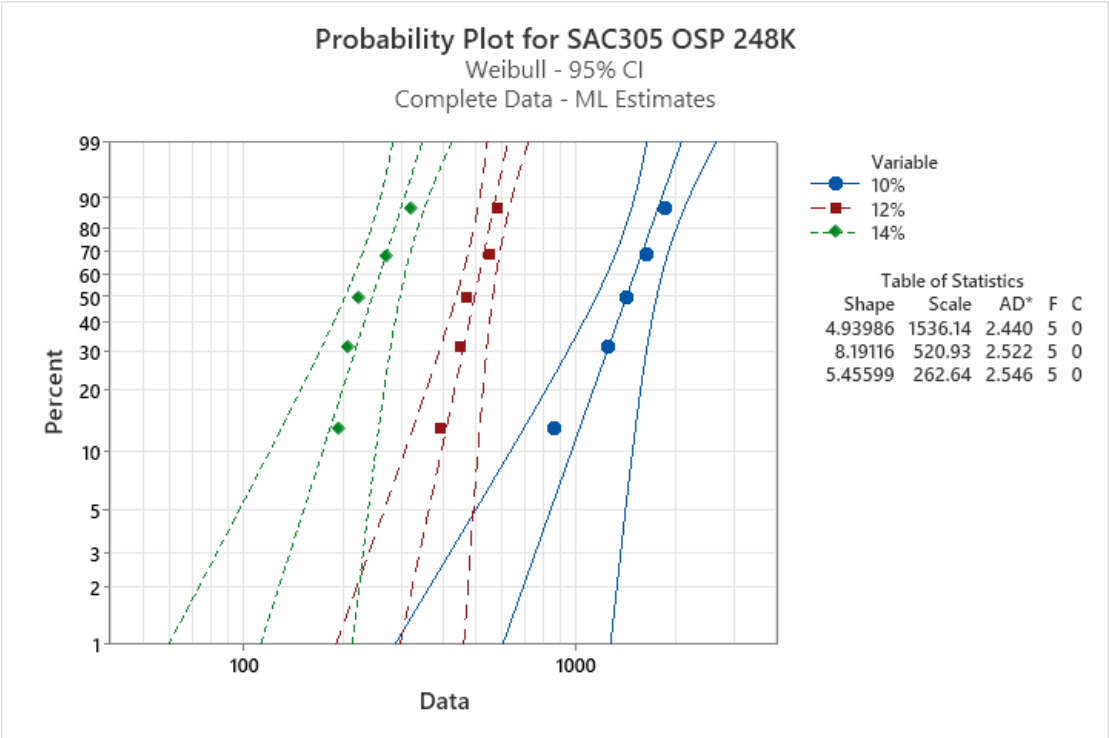

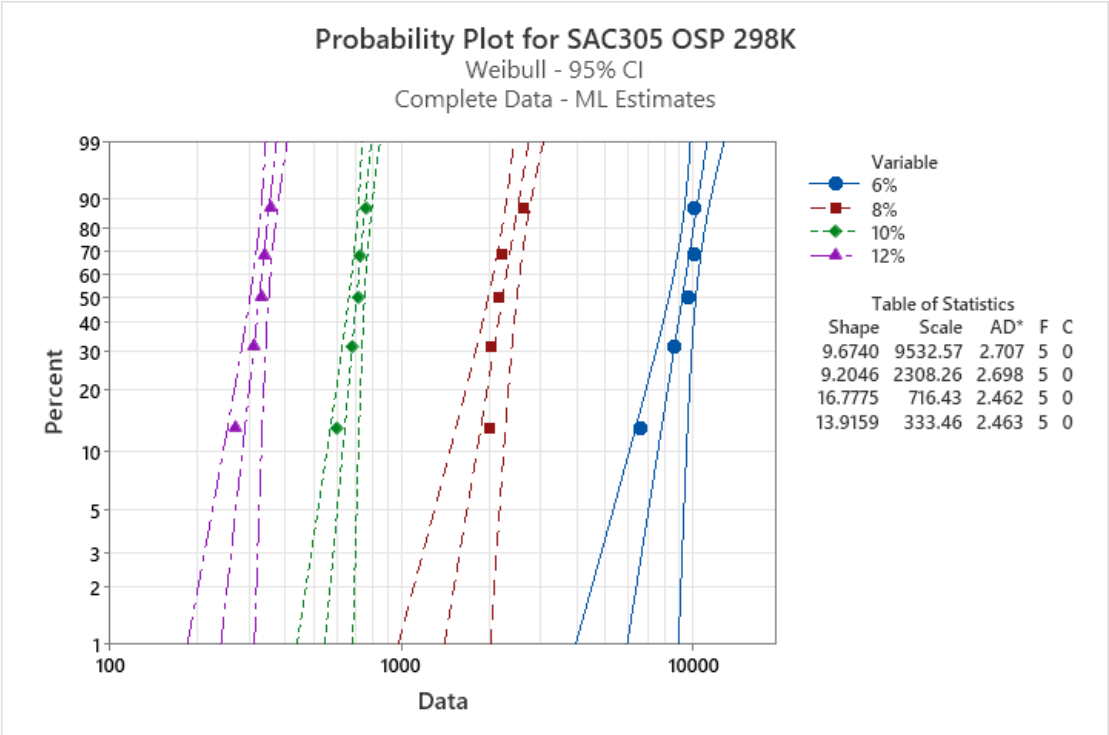

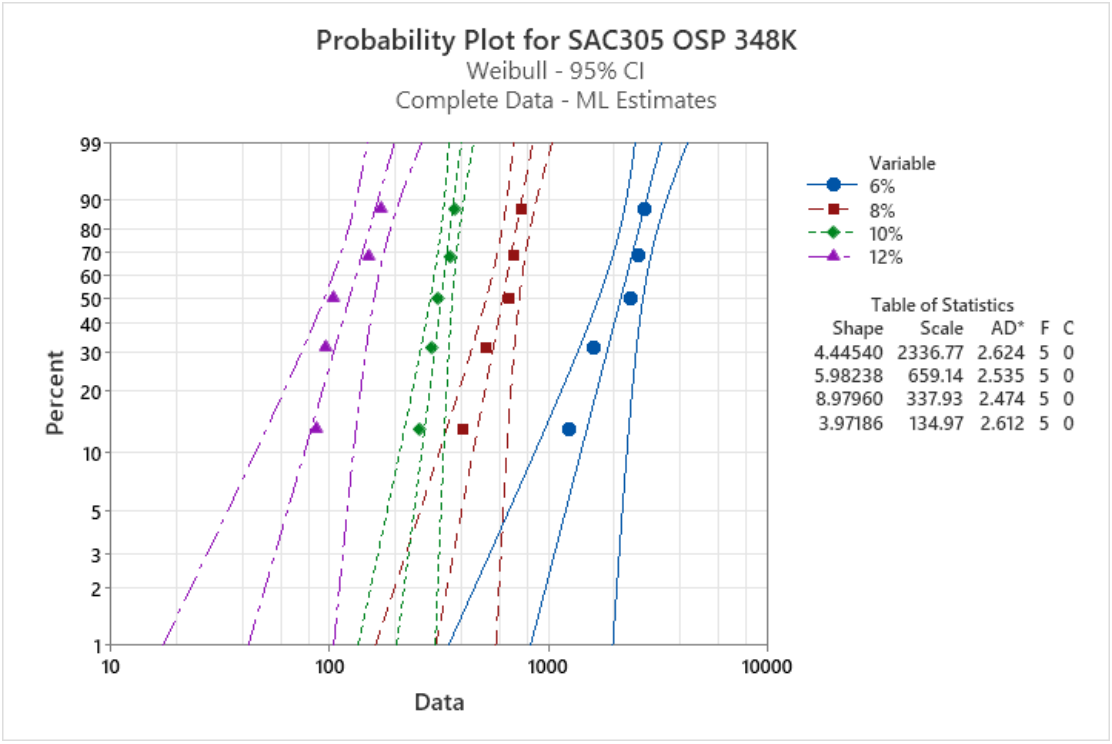
Probability Plot for SAC305 OSP 348K
Weibull - 95% CI
Complete Data - ML Estimates
Percent
Data
Variable
6%
8%
10%
12%
Table of Statistics
Shape Scale AD* F C
4.44540 2336.77 2.624 5 0
5.98238 659.14 2.535 5 0
8.97960 337.93 2.474 5 0
3.97186 134.97 2.612 5 0

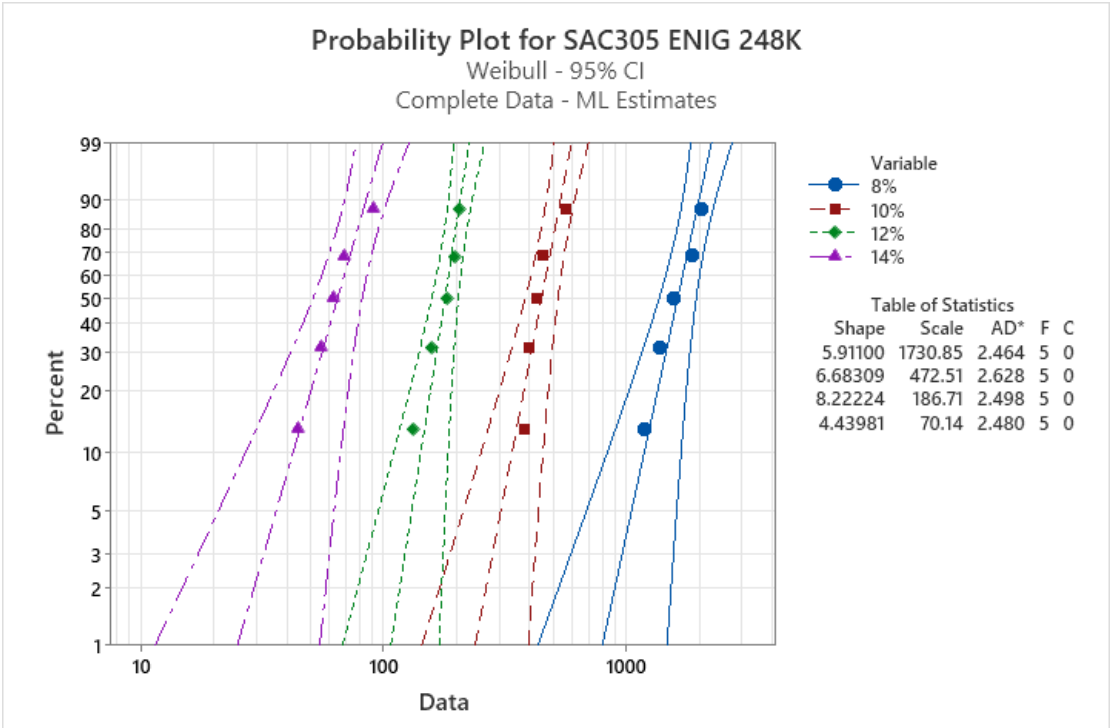
Probability Plot for SAC305 ENIG 248K
Weibull - 95% CI
Complete Data - ML Estimates
Percent
Data
Variable
8%
10%
12%
14%
Table of Statistics
Shape Scale AD* F C
5.91100 1730.85 2.464 5 0
6.68309 472.51 2.628 5 0
8.22224 186.71 2.498 5 0
4.43981 70.14 2.480 5 0

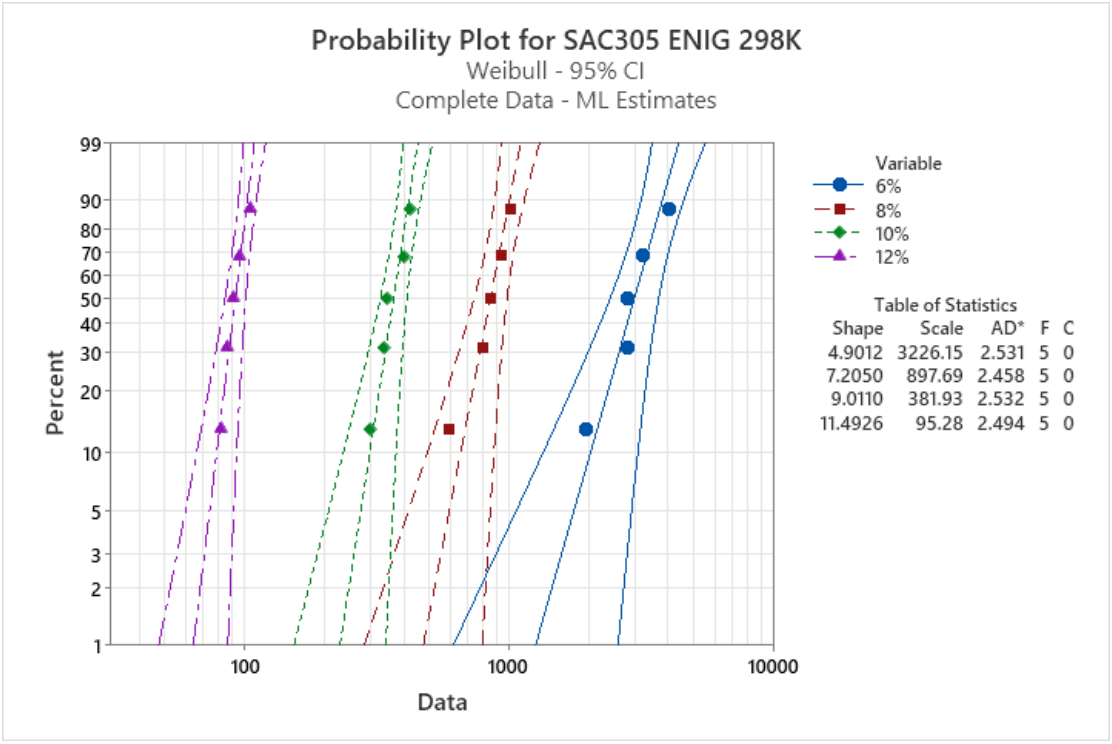
Probability Plot for SAC305 ENIG 298K
Weibull - 95% CI
Complete Data - ML Estimates
Percent
Data
Variable
6%
8%
10%
12%
Table of Statistics
Shape Scale AD* F C
4.9012 3226.15 2.531 5 0
7.2050 897.69 2.458 5 0
9.0110 381.93 2.532 5 0
11.4926 95.28 2.494 5 0

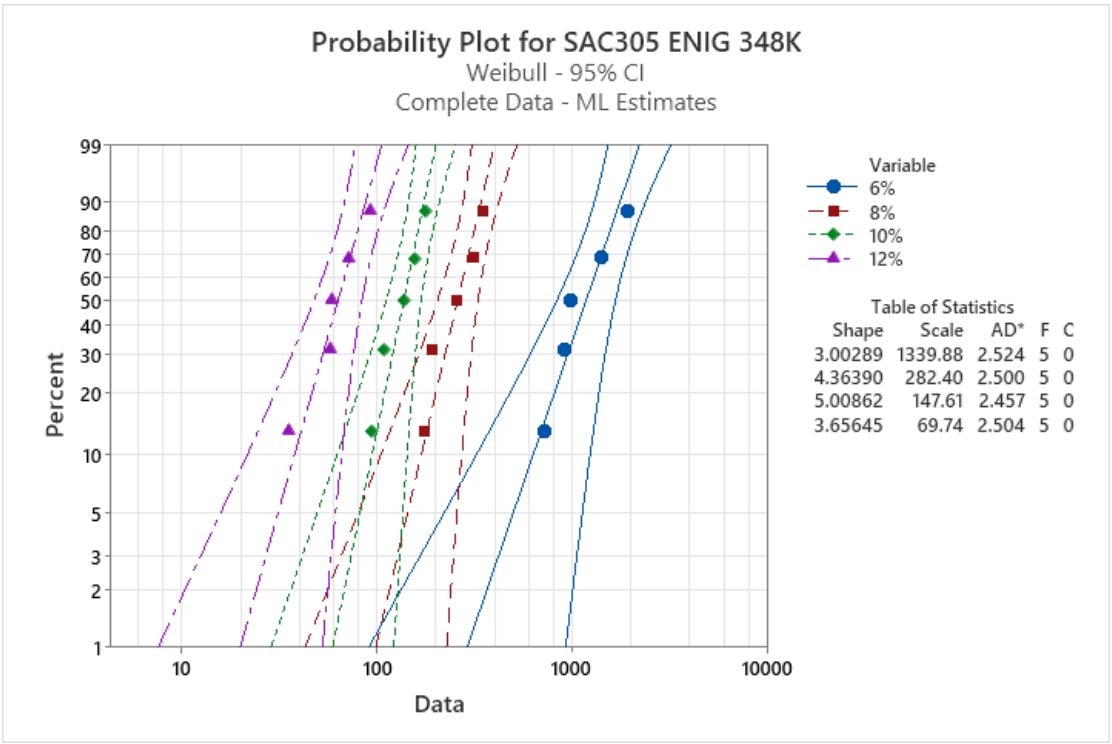
Probability Plot for SAC305 ENIG 348K
Weibull - 95% CI
Complete Data - ML Estimates
Percent
Data
Variable
6%
8%
10%
12%
Table of Statistics
Shape Scale AD* F C
3.00289 1339.88 2.524 5 0
4.36390 282.40 2.500 5 0
5.00862 147.61 2.457 5 0
3.65645 69.74 2.504 5 0

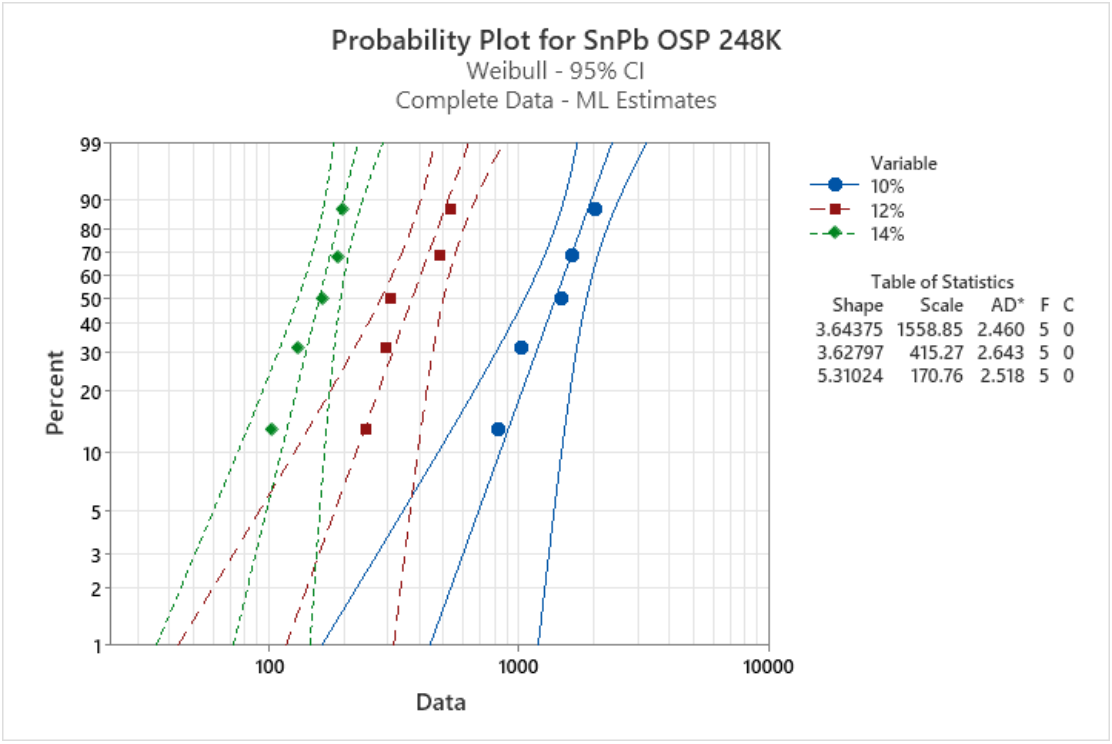
Probability Plot for SnPb OSP 248K
Weibull - 95% CI
Complete Data - ML Estimates
Percent
Data
Variable
10%
12%
14%
Table of Statistics
Shape Scale AD* F C
3.64375 1558.85 2.460 5 0
3.62797 415.27 2.643 5 0
5.31024 170.76 2.518 5 0

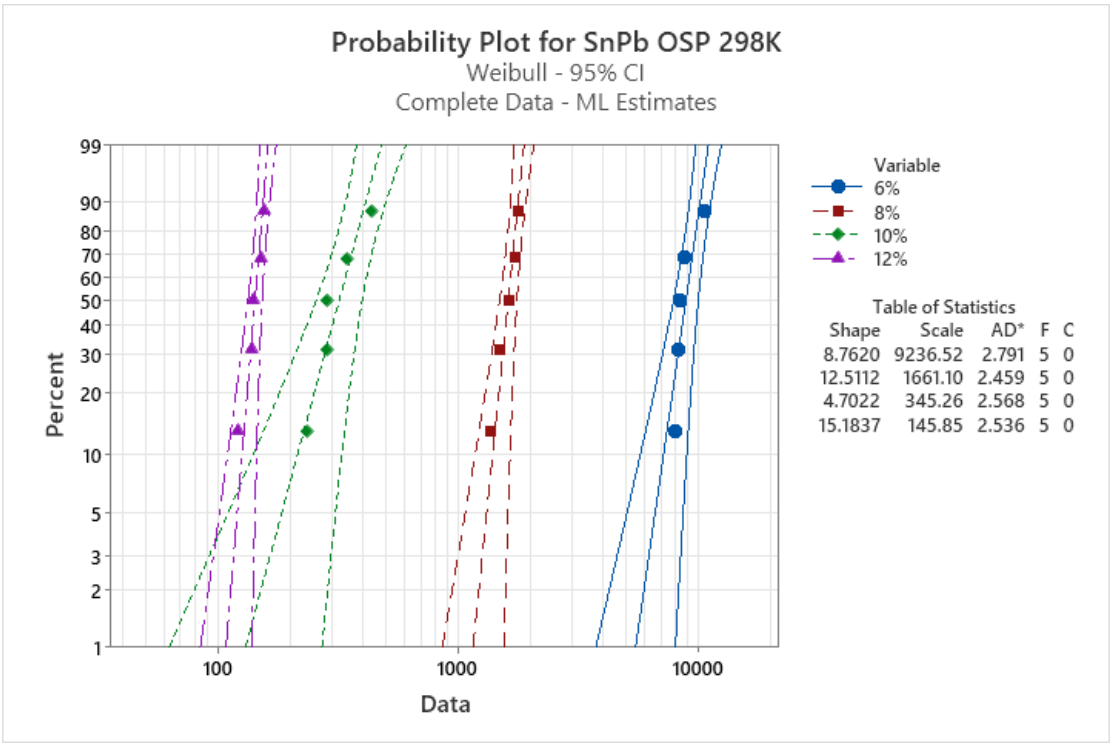
Probability Plot for SnPb OSP 298K
Weibull - 95% CI
Complete Data - ML Estimates
Percent
Data
Variable
6%
8%
10%
12%
Table of Statistics
Shape Scale AD* F C
8.7620 9236.52 2.791 5 0
12.5112 1661.10 2.459 5 0
4.7022 345.26 2.568 5 0
15.1837 145.85 2.536 5 0

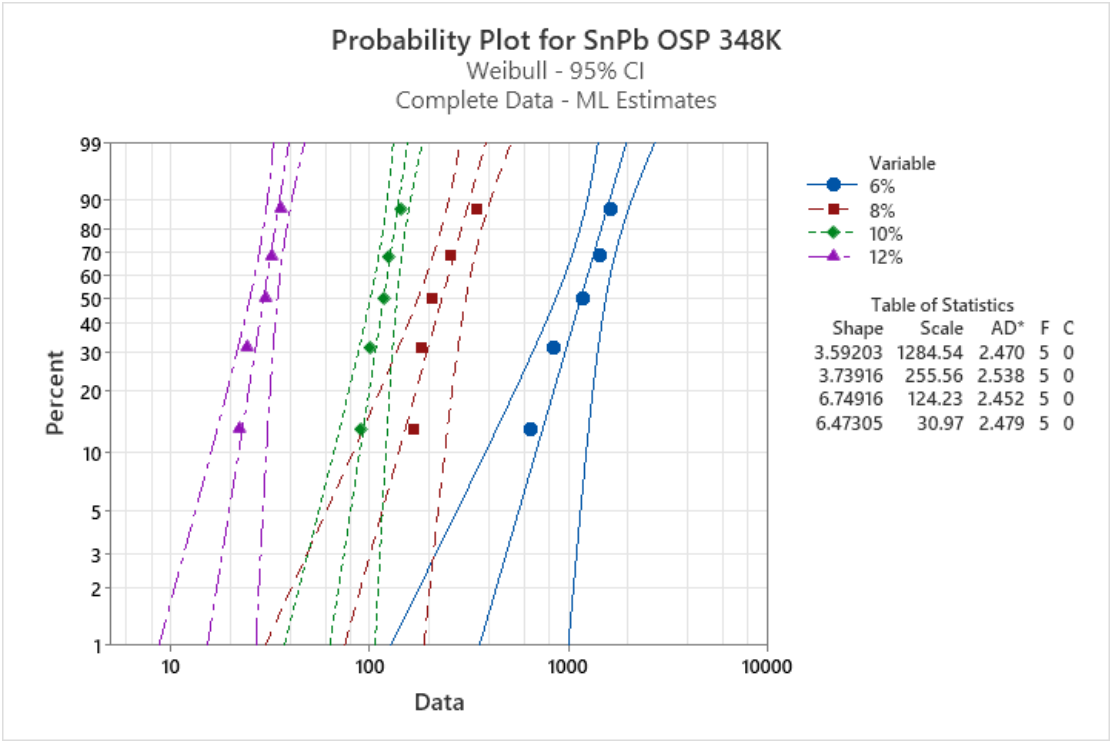
Probability Plot for SnPb OSP 348K
Weibull - 95% CI
Complete Data - ML Estimates
Percent
Data
Variable
6%
8%
10%
12%
Table of Statistics
Shape Scale AD* F C
3.59203 1284.54 2.470 5 0
3.73916 255.56 2.538 5 0
6.74916 124.23 2.452 5 0
6.47305 30.97 2.479 5 0

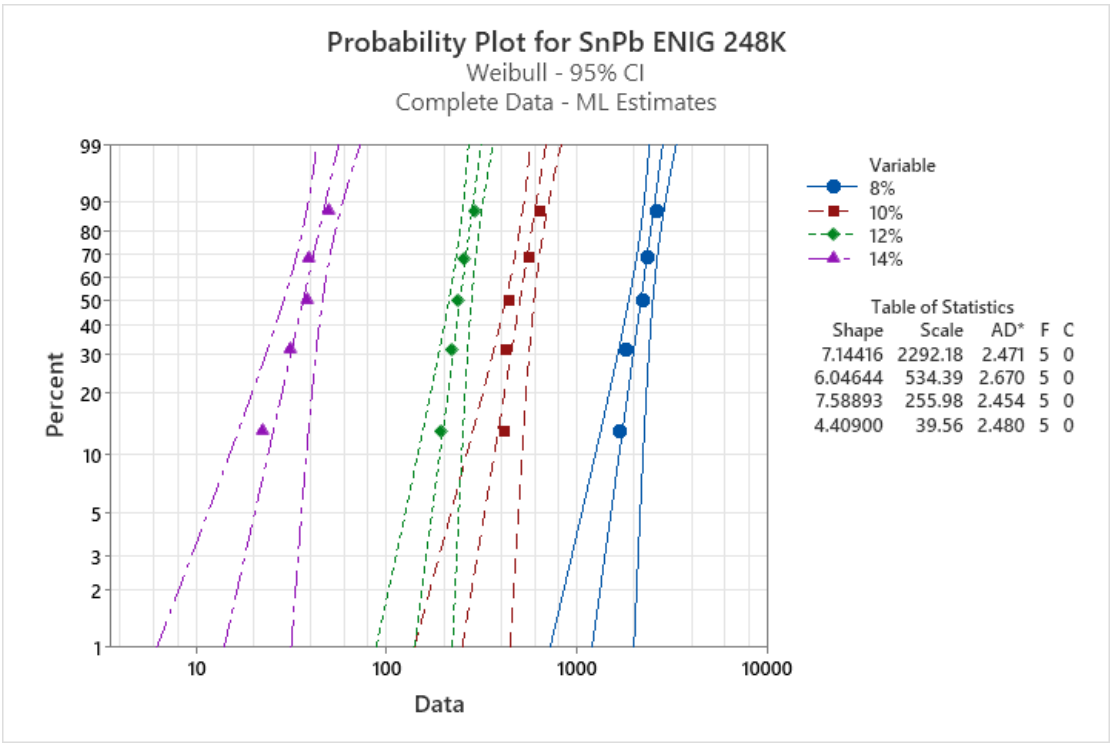
Probability Plot for SnPb ENIG 248K
Weibull - 95% CI
Complete Data - ML Estimates
Percent
Data
Variable
8%
10%
12%
14%
Table of Statistics
Shape Scale AD* F C
7.14416 2292.18 2.471 5 0
6.04644 534.39 2.670 5 0
7.58893 255.98 2.454 5 0
4.40900 39.56 2.480 5 0

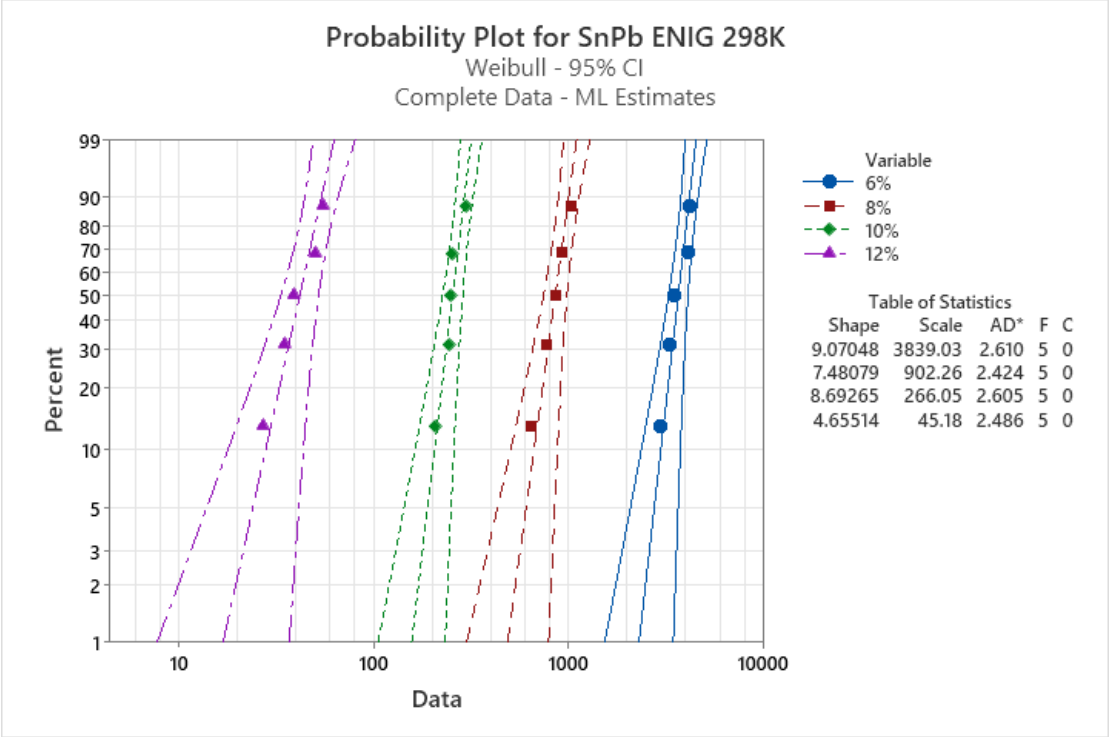

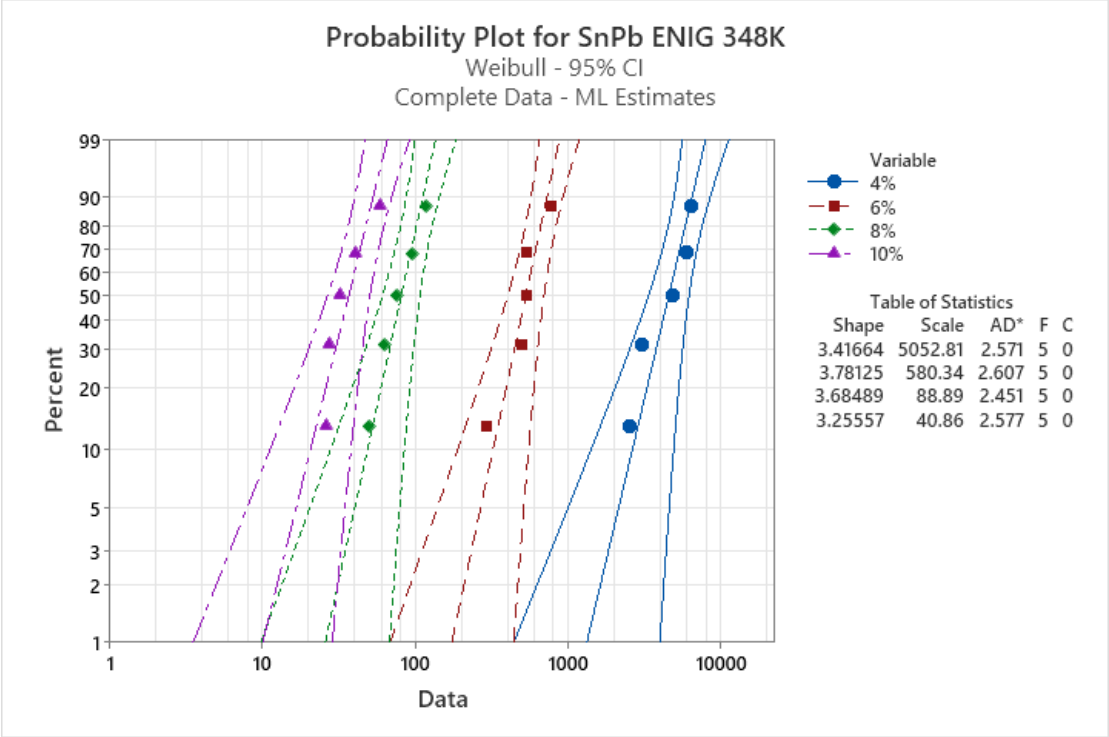

Figure 8-7 Fatigue life of solder alloys under different total strains at the specific testing temperature

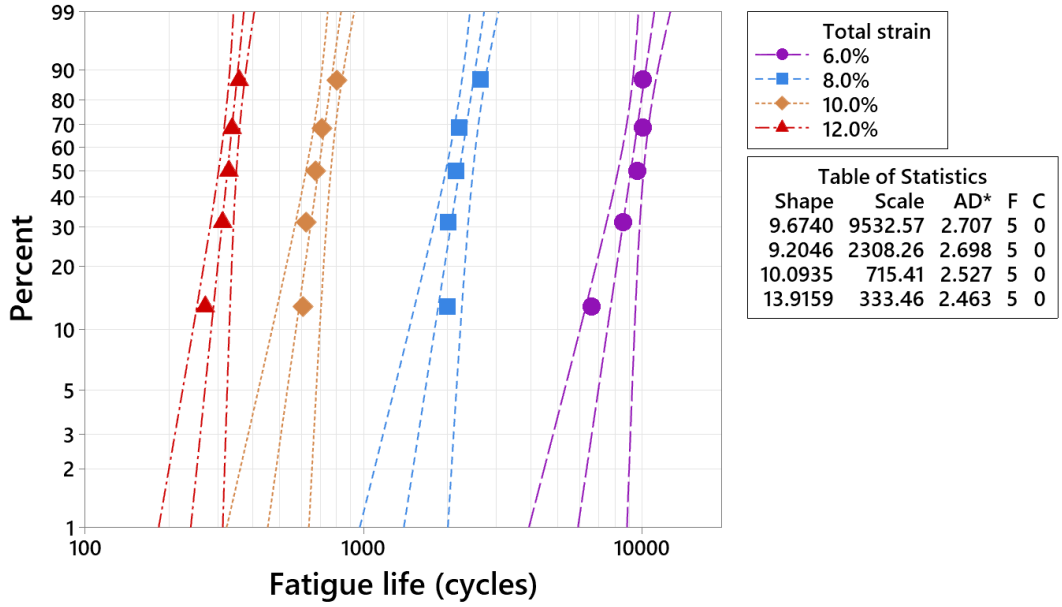
Percent
99
90
80
70
60
50
40
30
20
10
5
3
2
1
100
1000
10000
Fatigue life (cycles)
Total strain
6.0%
8.0%
10.0%
12.0%
Table of Statistics
Shape Scale AD* F C
9.6740 9532.57 2.707 5 0
9.2046 2308.26 2.698 5 0
10.0935 715.41 2.527 5 0
13.9159 333.46 2.463 5 0

(a)

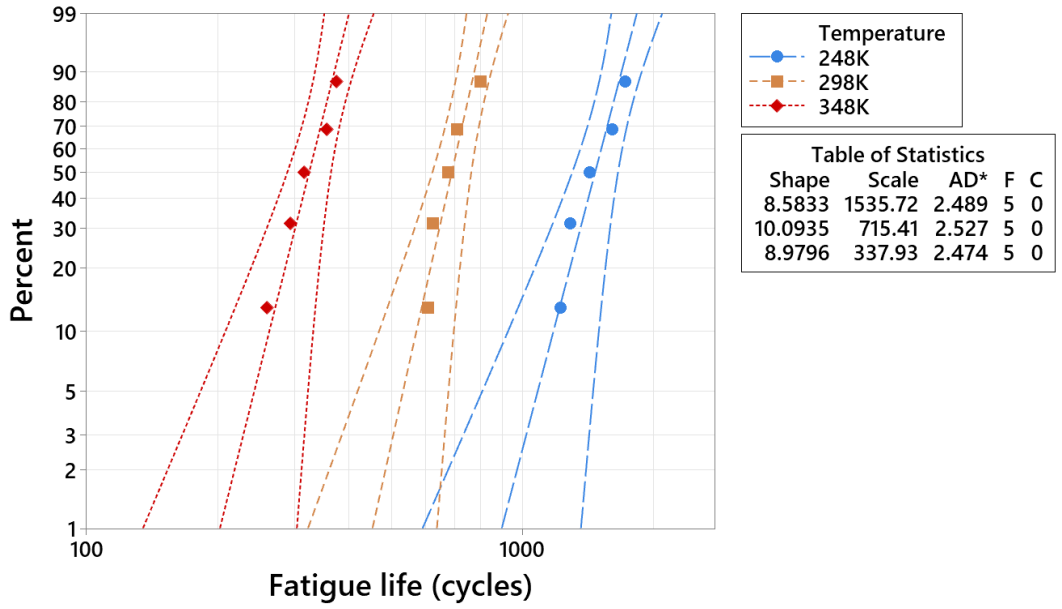
Percent
99
90
80
70
60
50
40
30
20
10
5
3
2
1
100
1000
Fatigue life (cycles)
Temperature
248K
298K
348K
Table of Statistics
Shape Scale AD* F C
8.5833 1535.72 2.489 5 0
10.0935 715.41 2.527 5 0
8.9796 337.93 2.474 5 0

(b)

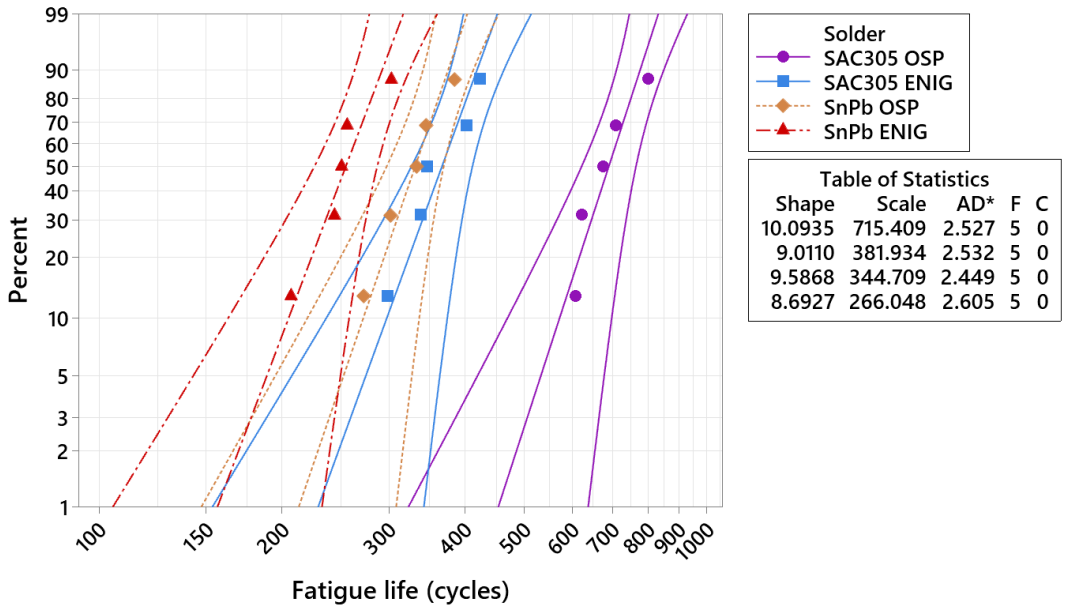

(c)

Figure 8-8 The fatigue life represented in Weibull plots: (a) SAC305 with OSP surface finish at 298K; (b) SAC305 with OSP surface finish at $\Delta\varepsilon_T$ = 10%; and (c) solder alloys tested at 298K and $\Delta\varepsilon_T$ = 10%.

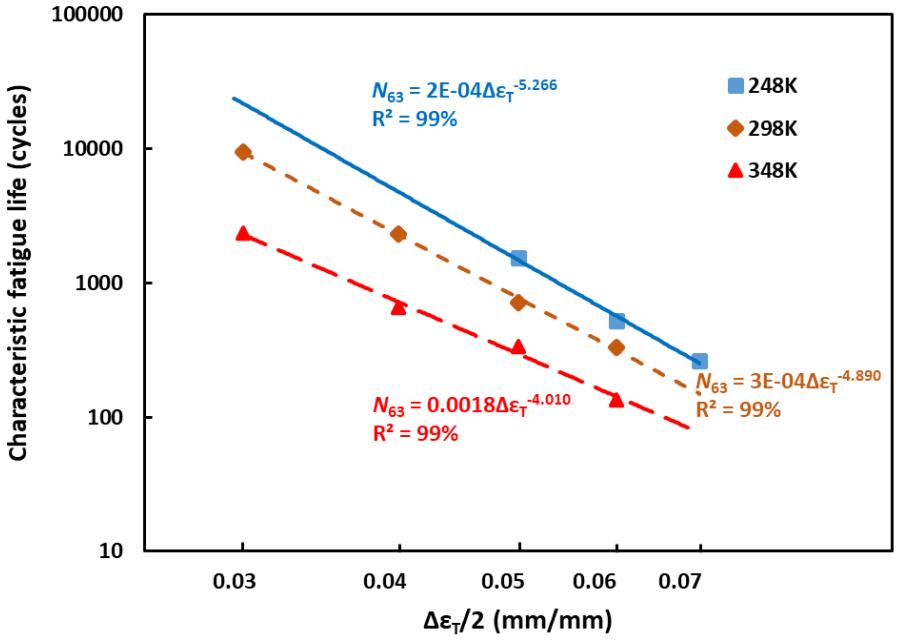

(a)

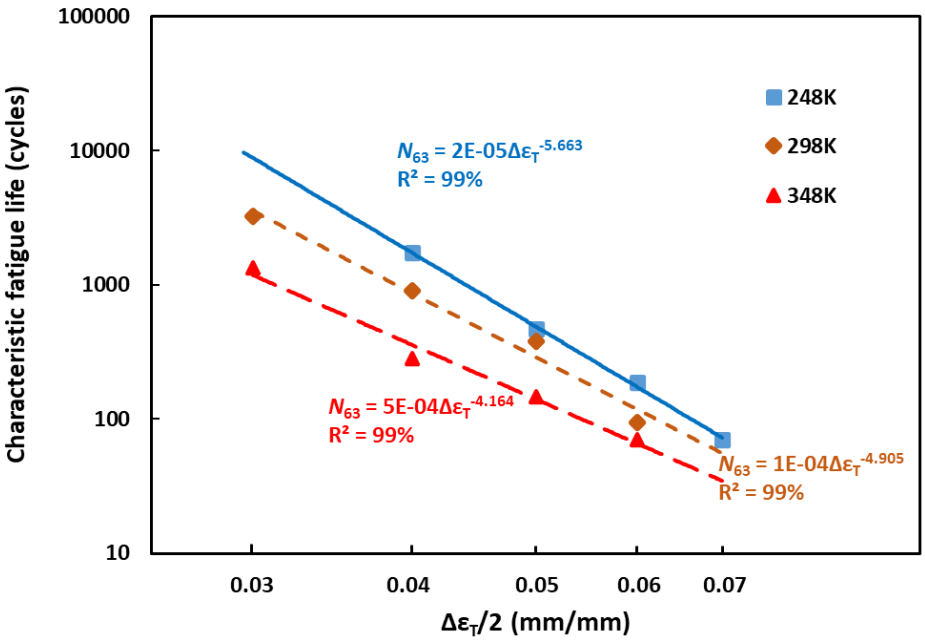
100000
10000
1000
100
10
Characteristic fatigue life (cycles)
248K
298K
348K
N_{63} = 2E-05$\Delta\varepsilon_T^{-5.663}$
R² = 99%
N_{63} = 5E-04$\Delta\varepsilon_T^{-4.164}$
R² = 99%
N_{63} = 1E-04$\Delta\varepsilon_T^{-4.905}$
R² = 99%
0.03
0.04
0.05
0.06
0.07
$\Delta\varepsilon_T$/2 (mm/mm)

(b)

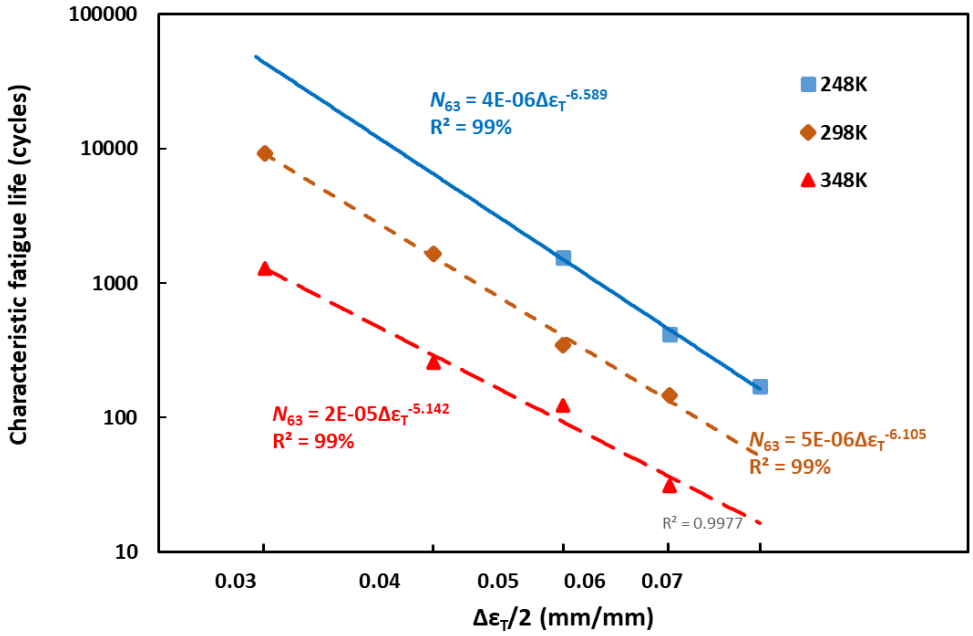
100000
10000
1000
100
10
Characteristic fatigue life (cycles)
248K
298K
348K
N_{63} = 4E-06$\Delta\varepsilon_T^{-6.589}$
R² = 99%
N_{63} = 2E-05$\Delta\varepsilon_T^{-5.142}$
R² = 99%
N_{63} = 5E-06$\Delta\varepsilon_T^{-6.105}$
R² = 99%
R² = 0.9977
0.03
0.04
0.05
0.06
0.07
$\Delta\varepsilon_T$/2 (mm/mm)

(c)

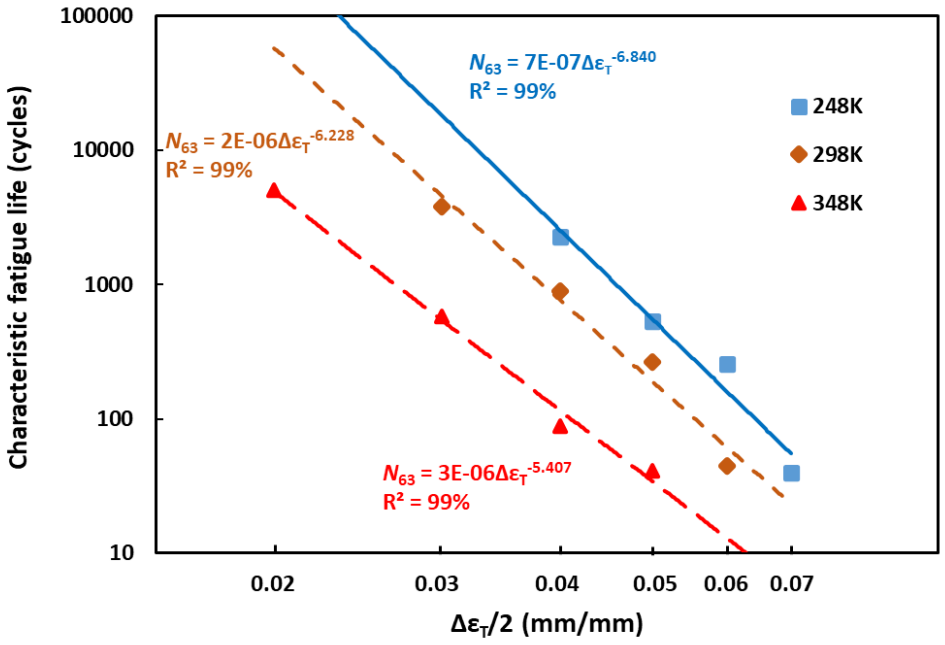

(d)

Figure 8-9 Solder alloy life characteristics as a function of strain level at 248K, 298K, and 348K for (a) SAC305 OSP, (b) SAC305 ENIG, (c) SnPb OSP, and (d) SnPb ENIG

Figure 8-10 shows fatigue life of the four combinations tested at 248K, 298K, and 348K. At the low temperature of 248K, SAC305 and SnPb tend to behave in a similar way with the same surface finish. However, SAC305 outperformed SnPb at high strain levels but performed less fatigue life at low strain levels. At the room temperature of 298K, SAC305 showed the better fatigue life than SnPb with the same surface finish. At the elevated temperature of 348K, even more superiority of SAC305 was observed at all strain levels. It is also worth noting that the OSP surface finish provided better fatigue performance than the ENIG surface finish for both SAC305 and SnPb solder alloys. This could be explained by the stronger IMC interface of OSP surface finish. The failure mode analysis also supports this opinion.

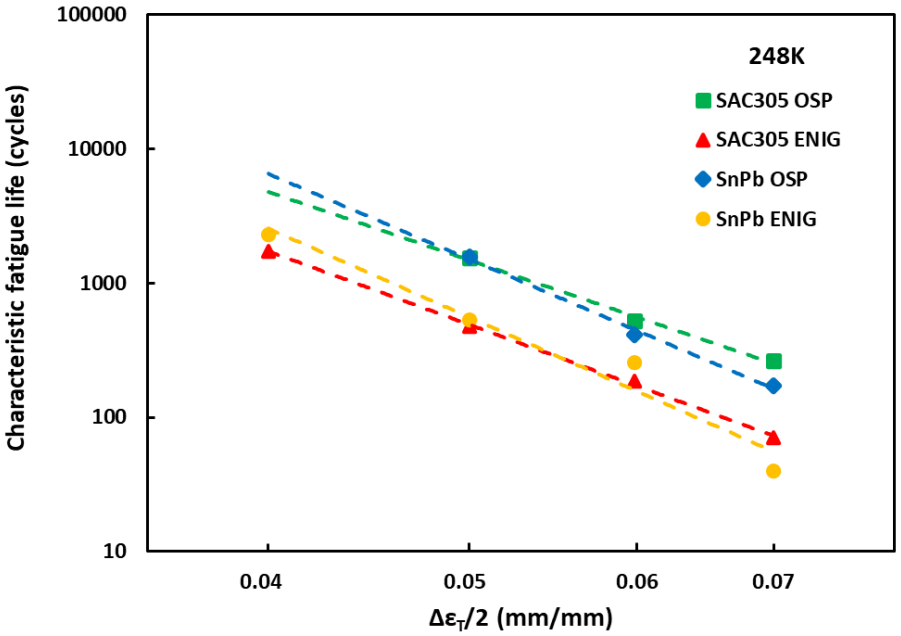
100000
10000
1000
100
10
Characteristic fatigue life (cycles)
248K
SAC305 OSP
SAC305 ENIG
SnPb OSP
SnPb ENIG
0.04
0.05
0.06
0.07
Δε_T/2 (mm/mm)

(a)

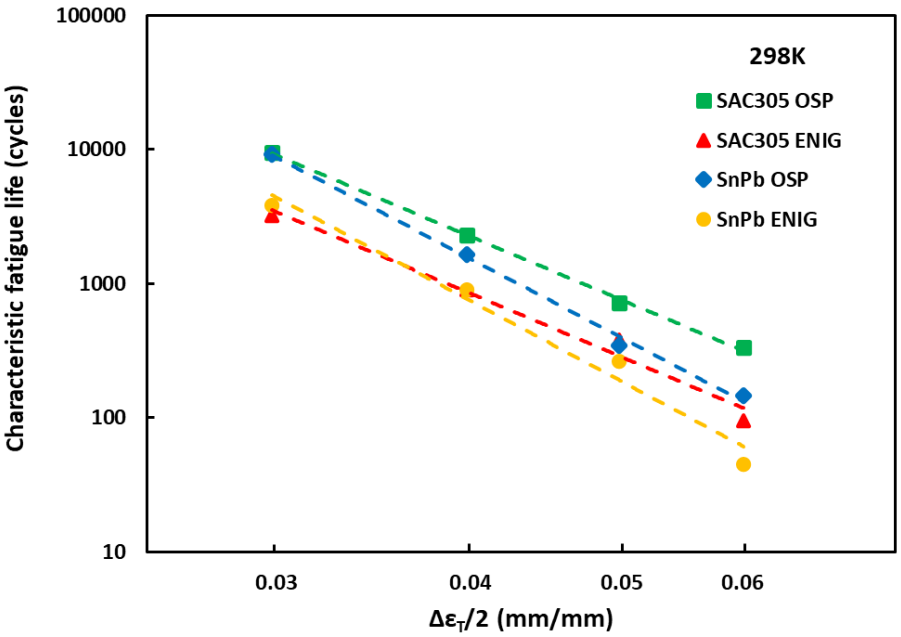
100000
10000
1000
100
10
Characteristic fatigue life (cycles)
298K
SAC305 OSP
SAC305 ENIG
SnPb OSP
SnPb ENIG
0.03
0.04
0.05
0.06
Δε_T/2 (mm/mm)

(b)

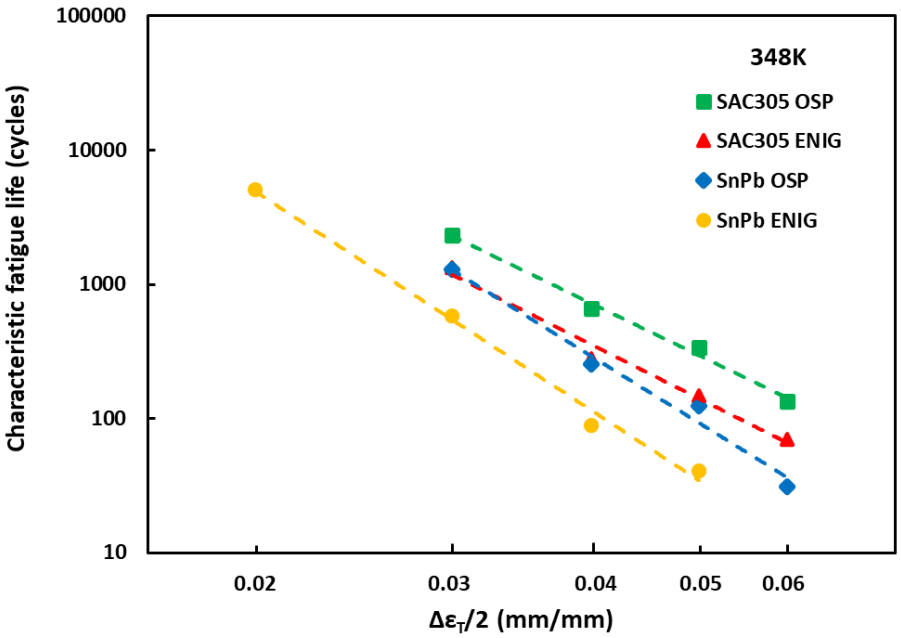

(c)

Figure 8-10 Fatigue life of solder alloys at the temperature of (a) 248K, (b) 298K, and (c) 348K

The two fitted parameters, *A* and *c*, of Equation 8-1 in Figure 8-9 were plotted in Figure 8-11. The substance constant *A* increased exponentially as the test temperature increased. However, the strain exponent decreased linearly. The effects of varying the operating temperature conditions on material reliability were described using the Arrhenius equation. Consequently, the Arrhenius equation indicated in Equation 8-2 explains how the testing temperature affects the strain-life equation structure, where *A* and *T* are the process rate and testing temperature, respectively, and k_1 and k_2 are the equation constants [31].

$$A = k_1 e^{\frac{-k_2}{T}} \qquad 8\text{-}2$$

The strain exponent *c* can also be expressed as a function of temperature *T*:

$$c = k_3 + k_4 T \qquad 8\text{-}3$$

Where k_3 and k_4 denote linear constants, and *k3* defines the slope of the fitted line in Figure 8-11 (b). The typical model adequacy values, with the least R-squared value for

all equations being 92%, are exhibited in Figure 8-11. The calculated constants (k_1, k_2, k_3, and k_4) for the four combinations are listed in Table 8-1. The fatigue life of a solder alloy (N_{63}) can be expressed as a function of temperature (T) and strain level ($\Delta\varepsilon_T/2$) using a combination of Eqs. 8-1, 8-2, and 8-3, as shown in Equation 8-4. The satisfactory goodness of fit for the Equation 8-4 was obtained, with an R-squared value of 96%.

$$N_{63} = k_1 e^{\frac{-k_2}{T}} (\Delta\varepsilon_T/2)^{-(k_3+k_4T)} \qquad 8\text{-}3$$

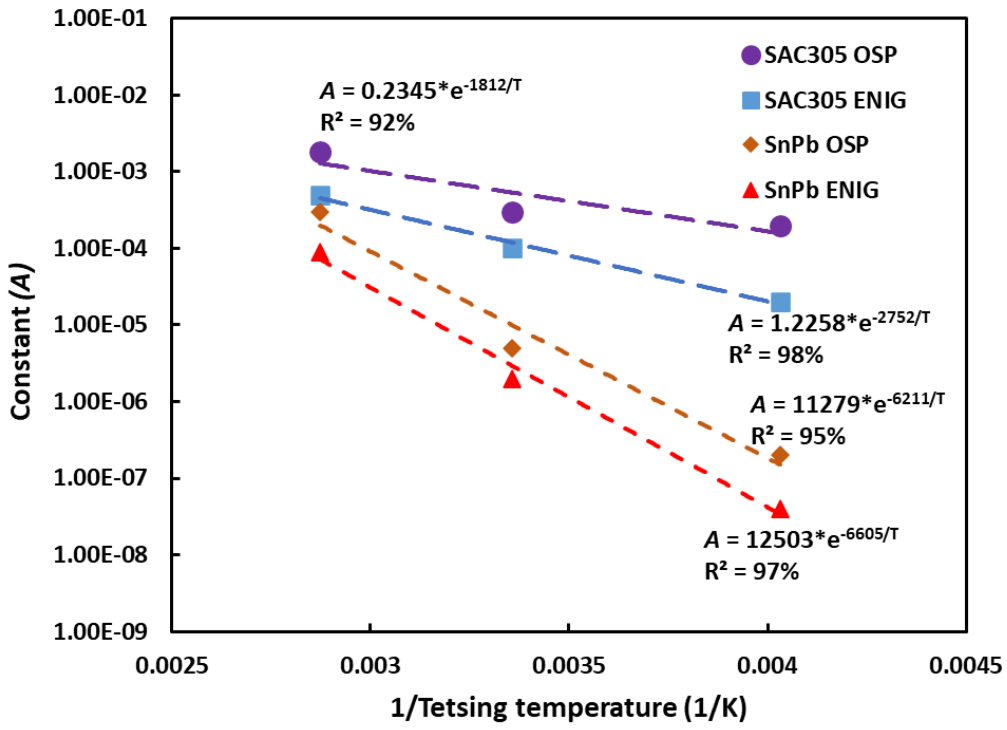

(a)

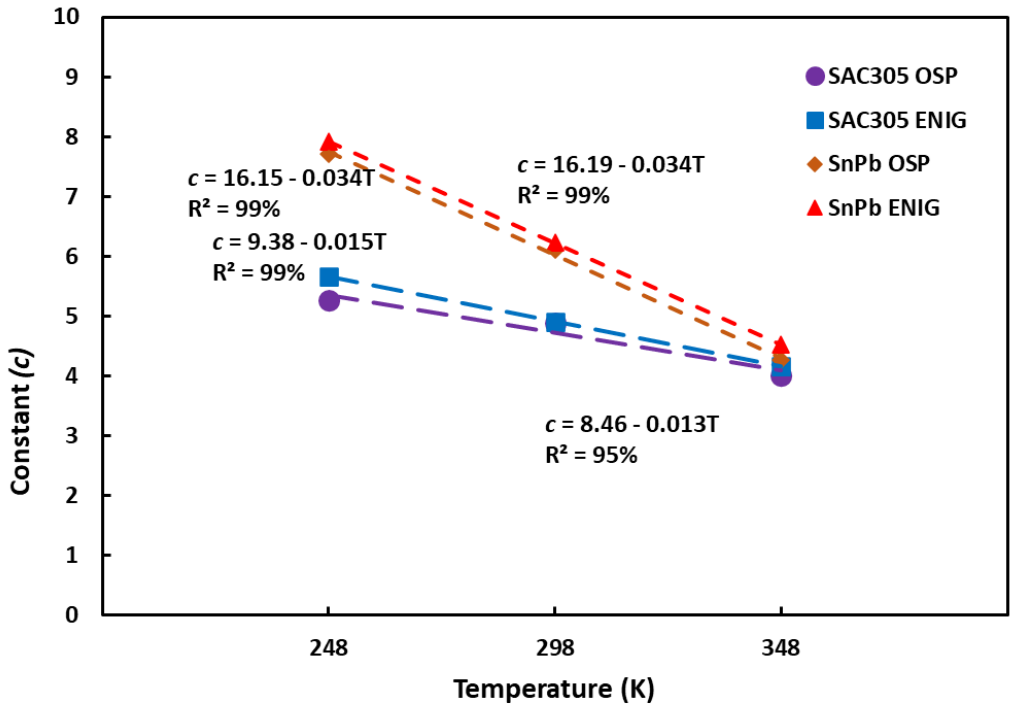

(b)

Figure 8-11 Parameters of the empirical model as a function of temperature: (a) substance constant P and (b) strain exponent c

Table 8-1 Summary of constants fitted in the empirical equation

	SAC305 OSP	SAC305 ENIG	SnPb OSP	SnPb ENIG
k_1	0.2345	1.2258	11279	12503
k_2	1812	2752	6211	6605
k_3	8.46	9.38	16.15	16.19
k_4	-0.0126	-0.0150	-0.0344	-0.0339

Figure 8-12 displays the fracture surfaces of the SAC305 and SnPb solder joints following fatigue failure. Because the accelerated isothermal fatigue tests were conducted over a short period, a minimal difference was found between cycling at temperatures of 248, 298, and 348 K. Consequently, no local recrystallization was observed in this study, as described in the literature [53]. Multiple surface cracks were predominantly initiated along the boundary steps of Sn dendrites in an intergranular

manner and subsequently joined together to develop microcracks in the Sn-Ag bulk solder. Flow stress was induced to deform the viscoplastic solder joints during the cyclic shear fatigue tests. Flow stress causes microcracks in the bulk solder or near the IMC layer. Flow stress causes microcracks in the bulk solder or near the IMC layer. Both SAC305 and SnPb displayed a ductile failure mechanism with the OSP surface finish, where the fracture propagated along the bulk solder, leaving a significant portion of the bulk solder on the Cu pad. However, the ENIG surface finish resulted in another near-IMC failure mode for the SAC305 and SnPb. Fractures can originate and propagate near the IMC interface in this failure scenario, exposing a distinct partial separation between the Ni and IMC layers. This implies that the ENIG surface finish formed a weaker IMC interface than the OSP surface finish. The multiple failure mechanisms also explain why the ENIG surface performed poorly in the strain-controlled tests.

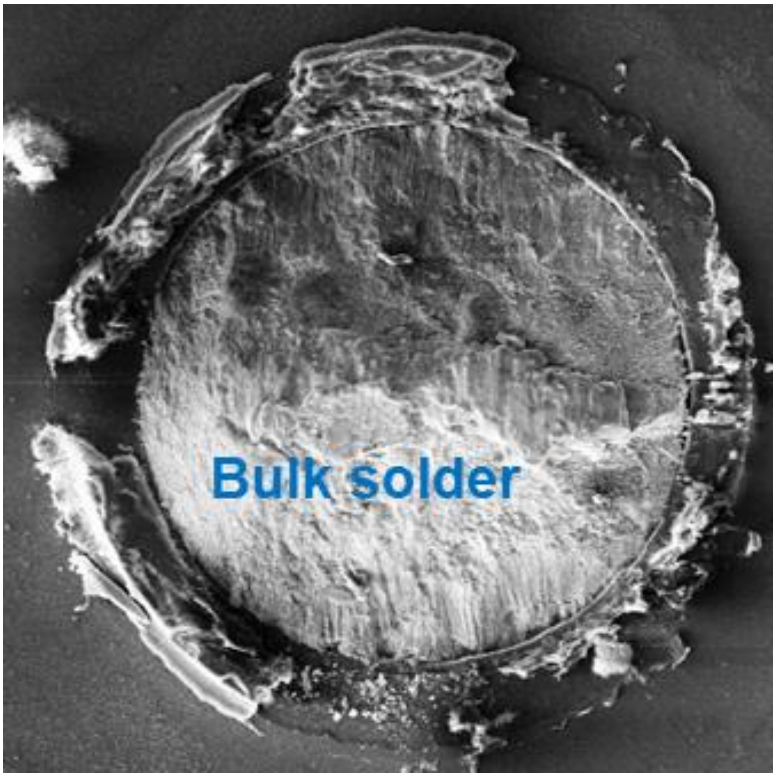

(a)

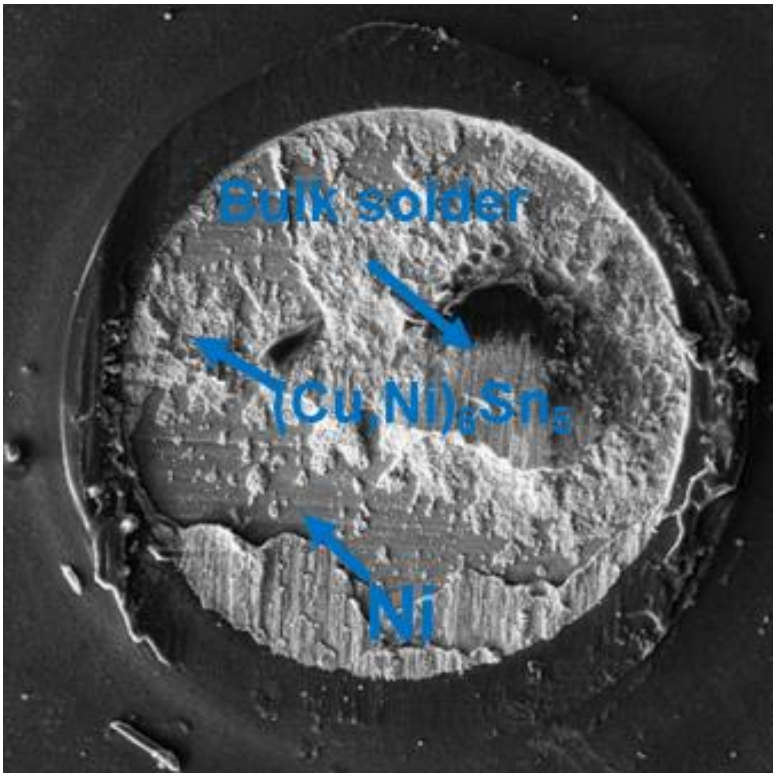

(b)

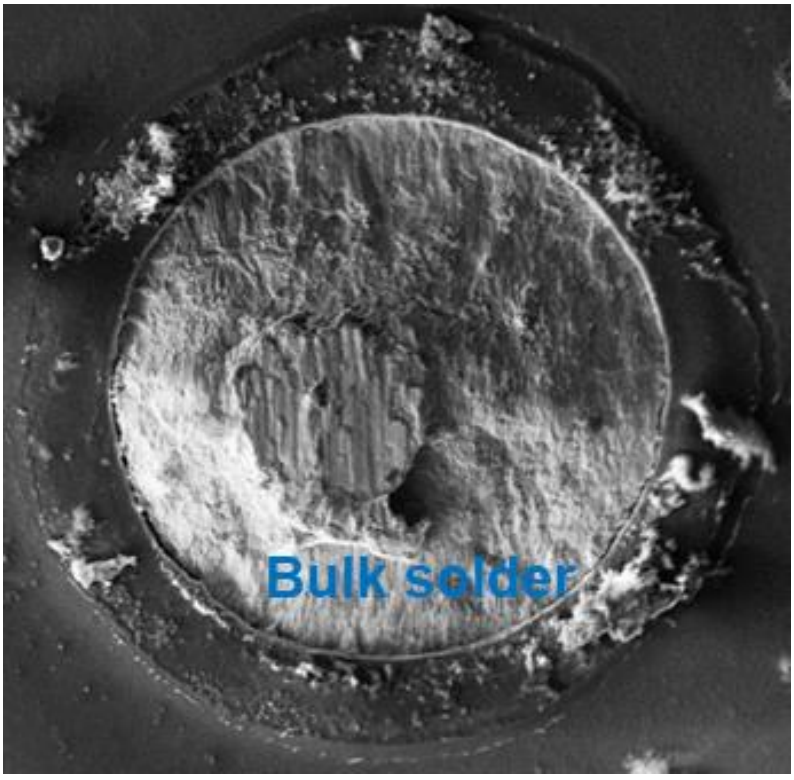

(c)

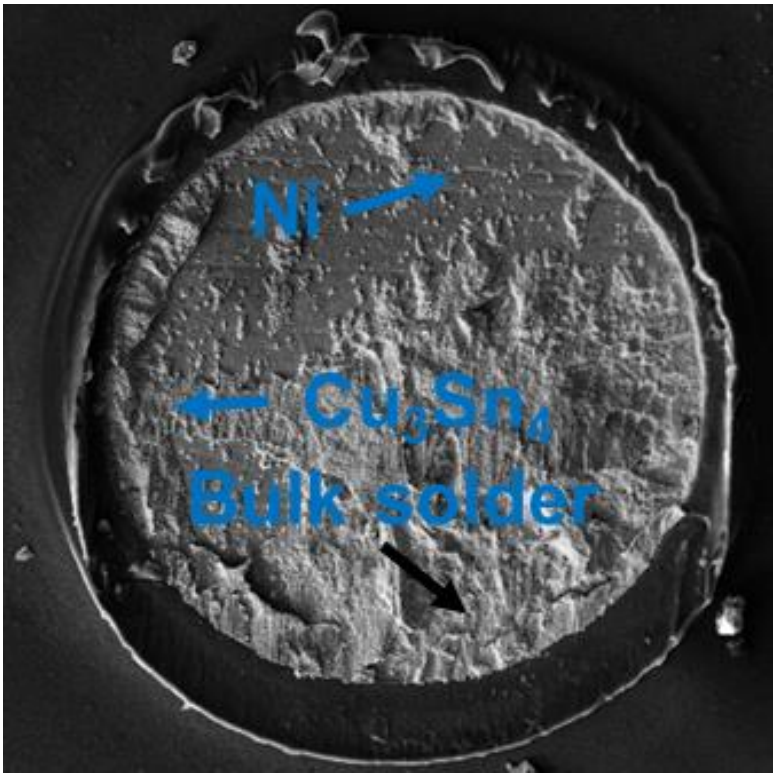

(d)

Figure 8-12 Top views of failed solder joints for (a) SAC305 with OSP surface finish, (b) SAC305 with ENIG surface finish, (c) SnPb with OSP surface finish, and (d) SnPb with ENIG surface finish

8.5 Conclusion

This study examined the fatigue properties of SAC305 and SnPb solder alloys at the testing temperature of 248K, 298K, and 348K using strain-controlled method. The evolution of hysteresis loops, inelastic work, and maximum load were explored. The microstructure and failure mode were characterized for both OSP and ENIG surface finishes. An empirical model was proposed to predict the fatigue life of SAC305 and SnPb solder alloys given the strain level and testing temperature. The study findings are summarized below:

1. The characteristic fatigue life decreased as the increase of strain level or testing temperature because the solder joint experienced more damage every cycle.

2. The higher testing temperature leads to the larger plastic strain range, the more inelastic work, and decreased peak stress for solder joints in BGA assembly. The temperature of 348K tends to amplify this effect.

3. Both SAC305 and SnPb solder alloys with OSP surface finish were associated with the ductile failure mode, while the ENIG surface finish demonstrated the near-IMC failure mode. This results the better fatigue performance of OSP surface finish than ENIG surface finish regardless of strain level or testing temperature.

4. The cycle used to obtain a peak inelastic work in a strain-controlled test was more appropriate for determining fatigue life.

5. The empirical model given in Equation 8-1 can be used to describe the effects of strain level on the fatigue behavior of SAC305 and SnPb solder joints at the temperature of 248K, 298K, and 348K. The substance constant A and strain exponent c are not constant but dependent on temperature. A modified empirical model given in Equation 8-4 was proposed to correlate fatigue life, strain level, and testing temperature.

6. The OSP surface finish demonstrated a better fatigue performance than the ENIG surface finish for SAC305 and SnPb at all the tested temperatures. SAC305 with OSP surface finish showed the best fatigue performance among all the combinations.

7. SAC305 solder alloy tends to provide enhanced fatigue performance at extreme environments (e.g., higher strain level or higher testing temperatures).

8.6 Contribution

The fatigue properties of SAC305 and SnPb solder alloys featured the OSP and ENIG surface finishes at various testing temperatures were examined in this study. The testing temperature plays a crucial role in determining the fatigue life of solder alloys. This can be explained by the reduction of ductility as the increase of testing temperature. Meanwhile, the lower peak stress and the larger size of hysteresis loop were observed. The reduced ductility resulted in the lower peak stress. However, more plastic strain range and inelastic work were accumulated per cycle since the higher testing temperature promoted the thermally activated process. This study focused on isothermal cycling tests at different temperatures, which varies from thermal cycling tests. The accelerated life tests were conducted within a short period of time. As a result, local recrystallization was not observed in this case. Since the different failure mechanisms of solder joints in isothermal cycling and thermal cycling tests, the proposed empirical model is not suitable to extrapolate into thermal cycling field. Despite this, the fatigue life of SAC305 and SnPb solder joints can be accurately estimated through this empirical model. This work serves as the evidence for the safe transition from tin-lead solders to lead-free solders.

Chapter 9 Conclusion and Future Work

9.1 Results and Conclusions

The reliability of electronic packages is determined by the fatigue life of individual solder joints. Factors such as solder material, surface finish, geometry, and shear strain rate could significantly affect the mechanical and fatigue properties of solder joints. This dissertation investigated both individual solder joints and solder joints in BGA assembly. Specifically, the shear and fatigue performance of Sn-Ag, SAC-Bi and two LTS were investigated using individual solder joints; the fatigue life of four solder alloys (SAC305, SAC-Q, SAC-R, and SAC-I) in both strain-controlled test and stress-controlled test were examined and compared using sandwich test vehicles; the effect of testing temperature and surface finish for SAC305 and SnPb was comprehensively studied as well. The fatigue performance of test vehicles was evaluated through the characteristic fatigue life, evolution of hysteresis loop, inelastic work, plastic strain range, and failure mode. Imaging tools such as Optical microscopy and SEM/DES were utilized to identify the IMC layer, compound participates, and crack propagation. Coffin-Manson model and Morrow energy model were developed, and the corresponding parameters were extracted. Conclusions of this dissertation are summarized as follow:

1. The shear strength of Sn-Ag, SAC-Bi, Sn58Bi, and Sn42Bi was obtained with different shear strain rates. The shear strength and variation increased as the shear strain rate goes up. Due to the increased flow stress, the high shear strain rate changed the failure mode of SAC-Bi, Sn42Bi, and Sn58Bi. The shear strain rate was shown to be less sensitive to Sn-Ag.

2. SAC-Bi outperformed all the tested solder alloys in the shear strength and shear fatigue tests, whereas Sn-Ag exhibited the lowest results. The Sn-Ag solder alloy with the OSP surface finish demonstrated better interfacial toughness than that with the ENIG surface finish.

3. As the stress/strain level increased, more damage to the solder joints was induced every cycle, reducing the typical fatigue life.

4. In strain-controlled test, inelastic work per cycle increased until reaching the peak value during the cyclic test. We assume a major crack occurred at the peak value, which resulted in the following decrease of work per cycle as the propagation and growing of cracks.

5. In the stress-controlled test, no initial hardening of the sandwich test vehicle was observed. The fatigue mechanism is similar to that of individual solder joints.

6. OSP surface finish demonstrated a larger fatigue life than ENIG surface finish at all strain levels and stress levels regardless of solder alloys.

7. SAC305 with OSP surface finish was associated with ductile failure mode, while the ENIG surface finish demonstrated near-IMC failure mode. The near-IMC failure mode indicates the weaker strength of IMC layer. At higher stress level, the weaker IMC layer accelerates the fatigue failure.

8. In both stress-controlled and strain-controlled tests, the Morrow energy and Coffin-Manson models match well with fatigue data. The fatigue ductility and fatigue exponent parameters estimated for the more realistic solder joints in BGA assembly were different from that for bulk samples and individual solder joints.

9. Solder alloys with higher Ag and Bi contents demonstrate better fatigue resistance associated with the OSP surface finish.
10. Brittle failure was observed in SAC-Q and SAC-I with an ENIG surface finish. They are more susceptible to changes in strain and stress, particularly strain.
11. The interfacial IMC layer of SAC305 with the OSP surface finish was scallop-like Cu_6Sn_5, whereas smoother layers were observed in the SAC-R, SAC-Q, and SAC-I solder joints.
12. Each IMC interface exhibited a facet-like $(Cu, Ni)_6Sn_5$ IMC layer with ENIG surface finish. Except for SAC-R, a thin $(Cu, Ni)_3Sn_4$ layer was also formed. This ascribes to the higher Cu concentration in SAC-R.
13. The characteristic fatigue life decreased as the increase of strain level or testing temperature because the solder joint experienced more damage every cycle.
14. The higher testing temperature leads to the larger plastic strain range, the more inelastic work, and decreased peak stress for solder joints in BGA assembly. The temperature of 348K tends to amplify this effect.
15. A modified empirical model was proposed to correlate fatigue life, strain level, and testing temperature for SAC305 and SnPb solder alloys with OSP and ENIG surface finishes.
16. The OSP surface finish demonstrated a better fatigue performance than the ENIG surface finish for SAC305 and SnPb at all the tested temperatures. SAC305 with OSP surface finish showed the best fatigue performance among all the combinations.
17. SAC305 solder alloy tends to provide enhanced fatigue performance at extreme environments (e.g., higher strain level or higher testing temperatures).

9.2 Future Work

The individual solder joints so far were investigated at room temperature, the shear properties of solder joints need to be further studied at various testing temperature to have a comprehensive understanding of shear properties of lead-free solder alloys.

This dissertation only focused on two surface finishes (OSP and ENIG). Another widely used ImAg surface finish need to be studied to make comparison.

So far only SAC305 and SnPb solders were tested at 248K and 348K. LTS and other SAC-based solders need to be investigated to study the effect of testing temperature. In addition, a wider temperature range is needed to better understand its effect and for modeling purpose. The modified Coffin-Manson model and Morrow energy model might fit these data combining Arrhenius equation.

Chapter 10 References

[1] J. H. Lau, "Electronics manufacturing with lead-free," *Halogen-free & Conductive-adhesive materials*, vol. 17, 2003.

[2] *Global Electronic Packaging Market: Growth Trends, Forecast (2020-2025)*. www.mordorintelligence.com/industry-reports/electronic-packaging-market.

[3] Prasad, R., 1997, Surface mount technology: principles and practice., Springer Science & Business Media.

[4] IPC, 2007, From Vacuum Tubes to Nanotubes: An Amazing Half Century. The Emergence of Electronic Circuit Technology 1957-2007., IPC - Association Connecting Electronics Industries.

[5] Hwang, J. S., 2004, Implementing lead-free electronics., McGraw-Hill.

[6] Saleh, J.h., and K. Marais. “Highlights from the Early (and Pre-) History of Reliability Engineering.” *Reliability Engineering & System Safety*, vol. 91, no. 2, 2006, pp. 249–256.

[7] M. Thurston, Practical Reliability of Electronic Equipment and Products, New York: Marcel Dekker Inc., 2003.

[8] M. Matin, W. Vellinga, and M. Geers, "Thermomechanical fatigue damage evolution in SAC solder joints," Materials Science and Engineering: A, vol. 445, pp. 73-85, 2007.

[9] Nelson, Wayne. “Accelerated Life Testing - Step-Stress Models and Data Analyses.” *IEEE Transactions on Reliability*, R-29, no. 2, 1980, pp. 103–108.

[10] Spencer, Floyd W. “Statistical Methods in Accelerated Life Testing.” *Technometrics*, vol. 33, no. 3, 1991, pp. 360–362.

[11] Bhattacharyya, G. K., and Zanzawi Soejoeti. “A Tampered Failure Rate Model for Step-Stress Accelerated Life Test.” *Communications in Statistics - Theory and Methods,* vol. 18, no. 5, 1989, pp. 1627–1643.

[12] Shi, X. Q., Pang, H. L. J., Zhou, W., and Wang, Z. P., 2001, “Low Cycle Fatigue Analysis of Temperature and Frequency Effects in Eutectic Solder Alloy,” *Int. J. Fatigue*, 22, pp. 217–228.

[13] Solomon, H. D., and Tolksdorf, E. D., 1995, “Energy Approach to the Fatigue of 60/40 Solder: Part I-Influence of Temperature and Cycle Frequency,” *ASME J. Electron. Packag.*, 118, pp. 130–135.

[14] Palmer, M. A., Redmond, P. E., and Messler Jr., R. W., 2000, “Thermomechanical Fatigue Testing and Analysis of Solder Alloys,” *ASME J. Electron. Packag*., 122, pp. 48–54.

[15] Cortez, R., Cutiongco, E. C., Fine, M. E., and Jeannotte, D. A., 1992, “Correlation of Uniaxial Tensio-Tension, Torsion, and Multiaxial Tension-Torsion Fatigue Failure in a 63Sn-37Pb Solder Alloy,” *Proc 42nd Electronic Components and Technology Conf.*, pp. 354–359.

[16] M. Wickham, J. Nottay, and C. Hunt, *A review of mechanical test method standards for lead-free solders:* National Physical Laboratory, 2001.

[17] C. Andersson, Z. Lai, J. Liu, H. Jiang, and Y. Yu, "Comparison of isothermal mechanical fatigue properties of lead-free solder joints and bulk solders," *Materials Science and Engineering:* A, vol. 394, pp. 20-27, 2005.

[18] Y. Jaradat, A. Qasaimeh, M. Obaidat, and P. Borgesen, "Assessment of solder joint fatigue life under realistic service conditions," *Journal of electronic materials*, vol. 43, pp. 4472-4484, 2014.

[19] Park T S, Lee S B. Low cycle fatigue testing of ball grid array solder joints under mixed-mode loading conditions[J]. 2005.

[20] Kanchanomai, C, and Y Mutoh. “Effect of Temperature on Isothermal Low Cycle Fatigue Properties of Sn–Ag Eutectic Solder.” *Materials Science and Engineering: A*, vol. 381, no. 1-2, 2004, pp. 113–120.

[21] Hamasha, Sa'd, et al. “Long-Term Isothermally Aged Concerns for SAC Lead-Free Solder in Harsh Environment Applications.” *2018 Pan Pacific Microelectronics Symposium (Pan Pacific)*, 2018

[22] Su, S., Akkara, F. J., Thaper, R., Alkhazali, A., Hamasha, M., & Hamasha, S. (2019). A state-of-the-art review of fatigue life prediction models for solder joint. *Journal of Electronic Packaging*, 141(4).

[23] Su, S., Jian, M., Akkara, F. J., Hamasha, S. D., Suhling, J., & Lall, P. (2018, October). Fatigue and shear properties of high reliable solder joints for harsh applications. *In SMTA International.*

[24] Su, S., & Hamasha, K. (2019). Effect of surface finish on the shear properties of SnAgCu-based solder alloys. *IEEE Transactions on Components, Packaging and Manufacturing Technology*, *9(8)*, 1473-ff1485.

[25] Su, S., Jian, M., Wei, X., Akkara, F. J., Suhling, J., & Lall, P. (2019, May). Effect of Surface Finish on the Fatigue Behavior of Bi-based Solder Joints. *In 2019 18th IEEE Intersociety Conference on Thermal and Thermomechanical Phenomena in Electronic Systems (ITherm) (pp. 1155-1159). IEEE.*

[26] James W. Dally, Pradeep Lall, Jeffrey C. Suhling. Mechanical Design of Electronic Systems. College House Enterprises LLC,2008.

[27] J. H. Lau and Y.-H. Pao, *Solder joint reliability of BGA, CSP, flip chip, and fine pitch SMT assemblies*: McGraw-Hill Professional Publishing, 1997.

[28] J. H. Lau, *Ball grid array technology*: McGraw-Hill Professional, 1995.

[29] G. Zweig, "Guest View: BGAs: Inspect the Process, Not the Product," *Circuits Assembly*, vol. 5, p. 92, 1994.

[30] Lau, John H. "Recent Advances and New Trends in Flip Chip Technology." *Journal of Electronic Packaging 138.3 (2016)*

[31] Elshabini, Aicha, Gangqiang Wang, and Fred Barlow. "Future Trends in Electronic Packaging." *Smart Structures and Materials 2006: Smart Electronics, MEMS, BioMEMS, and Nanotechnology*

[32] Wolter, Klaus-JÃ¼rgen. "System Integration by Advanced Electronics Packaging." *Bio and Nano Packaging Techniques for Electron Devices* (2012): 31-48.

[33] Tong, Xingcun Colin. "Advanced Materials for Thermal Management of Electronic Packaging." *Springer Series in Advanced Microelectronics* (2011): 11-20

[34] D.A. Benson, R. T. Mitchell, M. R. Tuck, D. R. Adkins, D. Shen, D. W. Palmer, “Micro-Machined Heat Pipes in Silicon MCM Substrates”, *Microelectronics and Photonics Sandia National Laboratories.*

[35] Dally, J. W., Lall, P., and Suhling, J. C., 2008, Mechanical Design of Electronic Systems.

[36] Sona, M., and Prabhu, K. N., 2013, “Review on microstructure evolution in Sn-Ag-Cu solders and its effect on mechanical integrity of solder joints,” *J. Mater. Sci. Mater. Electron.*, 24(9), pp. 3149–3169.

[37] J. DeVore, “Fatigue resistance of solder”, *NEPCON Proceedings*, February 1982, pp. 409- 414

[38] Zhang, Q. K., H. F. Zou, and Z. F. Zhang. "Tensile and fatigue behaviors of aged Cu/Sn-4Ag solder joints." *Journal of electronic materials 38.6 (2009)*: 852-859.

[39] Henderson, Donald W., et al. "The microstructure of Sn in near-eutectic Sn–Ag–Cu alloy solder joints and its role in thermomechanical fatigue." *Journal of Materials Research* 19.6 (2004): 1608-1612.

[40] Terashima, Shinichi, et al. "Recrystallization of Sn grains due to thermal strain in Sn-1.2 Ag-0.5 Cu-0.05 Ni solder." *Materials Transactions* 45.4 (2004): 1383-1390.

[41] Terashima, Shinichi, Yoshiharu Kariya, and Masamoto Tanaka. "Improvement on thermal fatigue properties of Sn-1.2 Ag-0.5 Cu flip chip interconnects by nickel addition." *Materials Transactions* 45.3 (2004): 673-680.

[42] Akkara, Francy, et al. "Effect of surface finish and high bi solder alloy on component reliability in thermal cycling." *2018 IEEE 68th Electronic Components and Technology Conference (ECTC)*. IEEE, 2018.

[43] Sundelin, Janne J., Sami T. Nurmi, and Toivo K. Lepistö. "Recrystallization behaviour of SnAgCu solder joints." *Materials Science and Engineering: A* 474.1-2 (2008): 201-207.

[44] X. Liu, J. Shang, J. Hao, A. Hu, L. Gao and M. Li, "Impact of tensile strength on thermal fatigue properties and failure modes of Sn-Ag-Cu-Ni solder joints," 2017 18th International Conference on Electronic Packaging Technology (ICEPT), Harbin, 2017, pp. 984-987.

[45] R. Zhang et al., "Tin-bismuth plating for component finishes," 2011 IEEE 61st Electronic Components and Technology Conference (ECTC), Lake Buena Vista, FL, 2011, pp. 2060- 2066

[46] Z. Shen, K. Fang, R. Wayne Johnson and M. C. Hamilton, "Characterization of Bi–Ag–X Solder for High Temperature SiC Die Attach," in *IEEE Transactions on Components, Packaging and Manufacturing Technology*, vol. 4, no. 11, pp. 1778-1784, Nov. 2014

[47] Liu Yang, Sun Fenglian, Zhang Hongwu and Wang Yang, "Influence of Ag, Cu and additive Bi elements on the thermal property of low-Ag SAC solder alloys," *Proceedings of 2011 6th International Forum on Strategic Technology*, Harbin, Heilongjiang, 2011, pp. 72-75.

[48] S. Ahmed, M. Basit, J. C. Suhling and P. Lall, "Effects of aging on SAC-Bi solder materials," *2016 15th IEEE Intersociety Conference on Thermal and Thermomechanical Phenomena in Electronic Systems (ITherm)*, Las Vegas, NV, 2016, pp. 746- 754

[49] Akkara, Francy John, et al. "Effect of solder sphere alloys and surface finishes on the reliability of lead-free solder joints in accelerated thermal cycling." *2018 17th IEEE Intersociety Conference on Thermal and Thermomechanical Phenomena in Electronic Systems (ITherm)*. IEEE, 2018.

[50] Akkara, Francy, et al. "Effect of surface finish and high bi solder alloy on component reliability in thermal cycling." *2018 IEEE 68th Electronic Components and Technology Conference (ECTC)*. IEEE, 2018.

[51] Chung, Soonwan, and Jae B. Kwak. "Comparative Study on Reliability and Advanced Numerical Analysis of BGA Subjected to Product-Level Drop Impact Test for Portable Electronics." *Electronics* 9.9 (2020): 1515.

[52] Shnawah, Dhafer Abdulameer, Mohd Faizul Mohd Sabri, and Irfan Anjum Badruddin. "A review on thermal cycling and drop impact reliability of SAC solder joint in portable electronic products." *Microelectronics reliability* 52.1 (2012): 90-99.

[53] Xie, H. X., & Chawla, N. (2013). Enhancing the ductility of Sn-Ag-Cu lead-free solder joints by addition of compliant intermetallics. *Journal of electronic materials*, *42*(3), 527-536.

[54] K. Suganuma, T. Sakai, K.-S. Kim, Y. Takagi, J. Sugimoto, and M. Ueshima, "Thermal and mechanical stability of soldering QFP with Sn-Bi-Ag lead-free alloy," IEEE Transactions on Electronics Packaging Manufacturing, vol. 25, no. 4, pp. 257–261, 2002.

[55] O. Mokhtari and H. Nishikawa, "Correlation between microstructure and mechanical properties of Sn-Bi-X solders," Materials Science and Engineering A, vol. 651, pp. 831–839, 2016.

[56] S. Sakuyama, T. Akamatsu, K. Uenishi, and T. Sato, "Effects of a third element on microstructure and mechanical properties of eutectic Sn-Bi solder," Transactions of the Japan Institute of Electronics Packaging, vol. 2, no. 1, pp. 98–103, 2009.

[57] Dusek, Milos, Chukwudi Okoro, and Christopher Hunt. "Establishing the Stress/Strain Behaviour of Solder Alloys under Multiple Constant Strain Cycles with Isothermal Conditions." *2006 1st Electronic Systemintegration Technology Conference*. Vol. 2. IEEE, 2006.

[58] Jaradat, Younis, et al. "Assessment of solder joint fatigue life under realistic service conditions." *Journal of electronic materials* 43.12 (2014): 4472-4484.

[59] Borgesen, Peter, et al. "Solder joint reliability under realistic service conditions." *Microelectronics Reliability* 53.9-11 (2013): 1587-1591.

[60] Su, Sinan, and Khozima Hamasha. "Effect of surface finish on the shear properties of SnAgCu-based solder alloys." *IEEE Transactions on Components, Packaging and Manufacturing Technology* 9.8 (2019): 1473-1485.

[61] Akkara, Francy John, et al. "Effect of Aging on Component Reliability in Harsh Thermal Cycling." *2019 18th IEEE Intersociety Conference on Thermal and Thermomechanical Phenomena in Electronic Systems (ITherm)*. IEEE, 2019.

[62] Su, Sinan, et al. "Effect of Surface Finish on the Fatigue Behavior of Bi-based Solder Joints." *2019 18th IEEE Intersociety Conference on Thermal and Thermomechanical Phenomena in Electronic Systems (ITherm)*. IEEE, 2019.

[63] Obaidat, M., et al. "Effects of varying amplitudes on the fatigue life of lead free solder joints." *2013 IEEE 63rd Electronic Components and Technology Conference*. IEEE, 2013.

[64] Borgesen, Peter, et al. "Solder joint reliability under realistic service conditions." *Microelectronics Reliability* 53.9-11 (2013): 1587-1591.

[65] Jaradat, Younis, et al. "Assessment of solder joint fatigue life under realistic service conditions." *Journal of electronic materials* 43.12 (2014): 4472-4484.

[66] Hamasha, Sa, and Peter Borgesen. "Effects of strain rate and amplitude variations on solder joint fatigue life in isothermal cycling." *Journal of Electronic Packaging* 138.2 (2016).

[67] Su, Sinan, et al. "Solder joint reliability in isothermal varying load cycling." *2017 16th IEEE Intersociety Conference on Thermal and Thermomechanical Phenomena in Electronic Systems (ITherm)*. IEEE, 2017.

[68] Al Athamneh, Raed, et al. "Effect of aging on the fatigue life and shear strength of SAC305 solder joints in actual setting conditions." *2019 18th IEEE Intersociety Conference on Thermal and Thermomechanical Phenomena in Electronic Systems (ITherm)*. IEEE, 2019.

[69] Kanchanomai, C., et al. "Influence of frequency on low cycle fatigue behavior of Pb-free solder 96.5 Sn–3.5 Ag." *Materials Science and Engineering: A* 345.1-2 (2003): 90-98.

[70] Kanchanomai, Chaosuan, and Yoshiharu Mutoh. "Effect of temperature on isothermal low cycle fatigue properties of Sn–Ag eutectic solder." *Materials Science and Engineering: A* 381.1-2 (2004): 113-120.

[71] Lee, Hwa-Teng, and Kuo-Chen Huang. "Effect of solder-joint geometry on the low-cycle fatigue behavior of Sn-xAg-0.7 Cu." *Journal of Electronic Materials* 45.12 (2016): 6102-6112.

[72] Lee, Hwa-Teng, et al. "Reliability of Sn–Ag–Sb lead-free solder joints." *Materials Science and Engineering: A* 407.1-2 (2005): 36-44.

[73] Fu, Nianjun, Jeffrey C. Suhling, and Pradeep Lall. "Long term isothermal aging effects on the cyclic stress-strain behavior of Sn-Ag-Cu solders." *2017 16th IEEE Intersociety Conference on Thermal and Thermomechanical Phenomena in Electronic Systems (ITherm)*. IEEE, 2017.

[74] Park, Tae-Sang, and Soon-Bok Lee. "Low cycle fatigue testing of ball grid array solder joints under mixed-mode loading conditions." (2005): 237-244.

[75] Li, J. F., P. A. Agyakwa, and C. M. Johnson. "Effect of trace Al on growth rates of intermetallic compound layers between Sn-based solders and Cu substrate." *Journal of alloys and compounds* 545 (2012): 70-79.

[76] Chuang, Chiang-Ming, and Kwang-Lung Lin. "Effect of microelements addition on the interfacial reaction between Sn-Ag-Cu solders and the Cu substrate." *Journal of Electronic Materials* 32.12 (2003): 1426-1431.

[77] Ma, Xin, Yiyu Qian, and F. Yoshida. "Effect of La on the Cu–Sn intermetallic compound (IMC) growth and solder joint reliability." *Journal of alloys and compounds* 334.1-2 (2002): 224-227.

[78] Wang, Y. W., C. C. Chang, and C. R. Kao. "Minimum effective Ni addition to SnAgCu solders for retarding Cu3Sn growth." *Journal of Alloys and Compounds* 478.1-2 (2009): L1-L4.

[79] Zhang, Liang, et al. "Effects of rare earths on properties and microstructures of lead-free solder alloys." *Journal of Materials Science: Materials in Electronics* 20.8 (2009): 685-694.

[80] Law, C. M. T., et al. "Microstructure, solderability, and growth of intermetallic compounds of Sn-Ag-Cu-RE lead-free solder alloys." *Journal of Electronic Materials* 35.1 (2006): 89-93.

[81] Zhang, Liang, et al. "Interface reaction between SnAgCu/SnAgCuCe solders and Cu substrate subjected to thermal cycling and isothermal aging." *Journal of Alloys and Compounds* 510.1 (2012): 38-45.

[82] Tu, Xiaoxuan, et al. "Influence of Ce addition on Sn-3.0 Ag-0.5 Cu solder joints: thermal behavior, microstructure and mechanical properties." *Journal of alloys and compounds* 698 (2017): 317-328.

[83] Xujing, Nan, et al. "Effect of Pr addition on properties of Sn-0.5 Ag-0.7 Cu-0.5 Ga lead-free solder." *Journal of Electronic Materials* 45.10 (2016): 5443-5448.

[84] Zeng, Guang, et al. "Properties and microstructure of Sn–0.7 Cu–0.05 Ni solder bearing rare earth element Pr." *Journal of Materials Science: Materials in Electronics* 22.8 (2011): 1101-1108.

[85] Xiao, Zhengxiang, et al. "Properties and microstructure of Sn-9Zn lead-free solder alloy bearing Pr." *Journal of Materials Science: Materials in Electronics* 22.6 (2011): 659-665.

[86] Wang, He, Songbai Xue, and JianXin Wang. "Study on the microstructure and properties of low-Ag Sn–0.3 Ag–0.7 Cu–0.5 Ga solder alloys bearing Pr." *Journal of Materials Science: Materials in Electronics* 28.11 (2017): 8246-8254.

[87] Gao, Lili, et al. "Effect of praseodymium on the microstructure and properties of Sn3. 8Ag0. 7Cu solder." *Journal of Materials Science: Materials in Electronics* 21.9 (2010): 910-916.

[88] Li, Bo, et al. "Effect of rare earth element addition on the microstructure of Sn-Ag-Cu solder joint." *Journal of Electronic Materials* 34.3 (2005): 217-224.

[89] Gao, Lili, et al. "Effects of trace rare earth Nd addition on microstructure and properties of SnAgCu solder." *Journal of Materials Science: Materials in Electronics* 21.7 (2010): 643-648.

[90] Liu, Ping, Pei Yao, and Jim Liu. "Evolutions of the interface and shear strength between SnAgCu–xNi solder and Cu substrate during isothermal aging at 150 C." *Journal of alloys and compounds* 486.1-2 (2009): 474-479.

[91] Gao, F., T. Takemoto, and H. Nishikawa. "Effects of Co and Ni addition on reactive diffusion between Sn–3.5 Ag solder and Cu during soldering and annealing." *Materials Science and Engineering: A* 420.1-2 (2006): 39-46.

[92] Laurila, T., V_ Vuorinen, and J. K. Kivilahti. "Interfacial reactions between lead-free solders and common base materials." *Materials Science and Engineering: R: Reports* 49.1-2 (2005): 1-60.

[93] Cheng, Hsi-Kuei, et al. "Interfacial reactions between Cu and SnAgCu solder doped with minor Ni." *Journal of Alloys and Compounds* 622 (2015): 529-534.

[94] Tay, S. L., et al. "Influence of Ni nanoparticle on the morphology and growth of interfacial intermetallic compounds between Sn–3.8 Ag–0.7 Cu lead-free solder and copper substrate." *Intermetallics* 33 (2013): 8-15.

[95] El-Daly, A. A., et al. "Influence of Zn addition on the microstructure, melt properties and creep behavior of low Ag-content Sn–Ag–Cu lead-free solders." *Materials Science and Engineering: A* 608 (2014): 130-138.

[96] El-Daly, A. A., et al. "Properties enhancement of low Ag-content Sn–Ag–Cu lead-free solders containing small amount of Zn." *Journal of alloys and compounds* 614 (2014): 20-28.

[97] Cho, Moon Gi, et al. "Effects of minor additions of Zn on interfacial reactions of Sn-Ag-Cu and Sn-Cu solders with various Cu substrates during thermal aging." *Journal of Electronic Materials* 36.11 (2007): 1501-1509.

[98] Mayappan, Ramani, et al. "The effect of adding Zn into the Sn–Ag–Cu solder on the intermetallic growth rate." *Journal of Materials Science: Materials in Electronics* 25.7 (2014): 2913-2922.

[99] Kotadia, H. R., et al. "Intermetallic compound growth suppression at high temperature in SAC solders with Zn addition on Cu and Ni–P substrates." *Journal of Alloys and Compounds* 511.1 (2012): 176-188.

[100] Kotadia, H. R., et al. "Reactions of Sn-3.5 Ag-based solders containing Zn and Al additions on Cu and Ni (P) substrates." *Journal of electronic materials* 39.12 (2010): 2720-2731.

[101] Yang, S. C., et al. "Massive spalling of intermetallic compounds in solder-substrate reactions due to limited supply of the active element." *Journal of applied physics* 101.8 (2007): 084911.

[102] El-Daly, A. A., et al. "Microstructural modifications and properties of low-Ag-content Sn–Ag–Cu solder joints induced by Zn alloying." *Journal of Alloys and Compounds* 653 (2015): 402-410.

[103] Tang, Y., et al. "Effects of Sb addition on grain ripening growth at interface of Sn-Ag-Cu-xSb/Cu in wetting reactions." *2012 13th International Conference on Electronic Packaging Technology & High Density Packaging*. IEEE, 2012.

[104] Chen, B. L., and G. Y. Li. "Influence of Sb on IMC growth in Sn–Ag–Cu–Sb Pb-free solder joints in reflow process." *Thin Solid Films* 462 (2004): 395-401.

[105] El-Daly, A. A., A. M. El-Taher, and S. Gouda. "Development of new multicomponent Sn–Ag–Cu–Bi lead-free solders for low-cost commercial electronic assembly." *Journal of Alloys and Compounds* 627 (2015): 268-275.

[106] Zhao, Jie, et al. "Kinetics of intermetallic compound layers and shear strength in Bi-bearing SnAgCu/Cu soldering couples." *Journal of alloys and compounds* 473.1-2 (2009): 382-388.

[107] Perkins, Leslie S., and Andrew E. DePristo. "The influence of lattice distortion on atomic self-diffusion on fcc (001) surfaces: Ni, Cu, Pd, Ag." *Surface science* 325.1-2 (1995): 169-176.

[108] Qi, Lin, et al. "The effect of Bi on the IMC growth in Sn-3Ag-0.5 Cu solder interface during aging process." *Proceedings of 2004 International Conference on the Business of Electronic Product Reliability and Liability (IEEE Cat. No. 04EX809)*. IEEE, 2004.

[109] LI, Guo-yuan, and Xun-qing SHI. "Effects of bismuth on growth of intermetallic compounds in Sn-Ag-Cu Pb-free solder joints." *Transactions of Nonferrous Metals Society of China* 16 (2006): s739-s743.

[110] Choi, Won Kyoung, and Hyuck Mo Lee. "Effect of soldering and aging time on interfacial microstructure and growth of intermetallic compounds between Sn-3.5 Ag solder alloy and Cu substrate." *Journal of Electronic Materials* 29.10 (2000): 1207-1213.

[111] Manson, S. S. "Fatigue: a complex subject—some simple approximations." *Experimental mechanics* 5.4 (1965): 193-226.

[112] Lv, Zhiqiang, et al. "A modified nonlinear fatigue damage accumulation model." *International Journal of Damage Mechanics* 24.2 (2015): 168-181.

[113] Wilkins, E. W. C. "Cumulative damage in fatigue." *Colloquium on Fatigue/Colloque de Fatigue/Kolloquium über Ermüdungsfestigkeit*. Springer, Berlin, Heidelberg, 1956.

[114] Borgesen, Peter, et al. "Solder joint reliability under realistic service conditions." *Microelectronics Reliability* 53.9-11 (2013): 1587-1591.

[115] Jaradat, Younis, et al. "Assessment of solder joint fatigue life under realistic service conditions." *Journal of electronic materials* 43.12 (2014): 4472-4484.

[116] Zhang, Junhong, et al. "Study on damage accumulation and life prediction with loads below fatigue limit based on a modified nonlinear model." *Materials* 11.11 (2018): 2298.

[117] Corten, H. T., and T. J. Dolan. "Cumulative fatigue damage." *Proceedings of the international conference on fatigue of metals*. Vol. 1. Institution of Mechanical Engineering and American Society of Mechanical Engineers, 1956.

[118] Zhu, Shun-Peng, et al. "A practical method for determining the Corten-Dolan exponent and its application to fatigue life prediction." *International Journal of Turbo & Jet-Engines* 29.2 (2012): 79-87.

[119] Coffin Jr, L. Fo. "A study of the effects of cyclic thermal stresses on a ductile metal." *Transactions of the American Society of Mechanical Engineers, New York* 76 (1954): 931-950.

[120] Solomon, Harvey. "Fatigue of 60/40 solder." *IEEE Transactions on Components, Hybrids, and Manufacturing Technology* 9.4 (1986): 423-432.

[121] Shi, X. Q., et al. "Low cycle fatigue analysis of temperature and frequency effects in eutectic solder alloy." *International Journal of fatigue* 22.3 (2000): 217-228.

[122] Engelmaier W, Attarwala A I. Surface-mount attachment reliability of clip-leaded ceramic chip carriers on FR-4 circuit boards[J]. IEEE transactions on components, hybrids, and manufacturing technology, 1989, 12(2): 284-296.

[123] Norris K C, Landzberg A H. Reliability of controlled collapse interconnections[J]. IBM Journal of Research and Development, 1969, 13(3): 266-271.

[124] Syed A. Predicting solder joint reliability for thermal, power, and bend cycle within 25% accuracy[C]//2001 Proceedings. 51st Electronic Components and Technology Conference (Cat. No. 01CH37220). IEEE, 2001: 255-263.

[125] Monkman F C. An empirical relationship between rupture life and minimum creep rate in creep rupture tests[C]//proc. ASTM. 1956, 56: 91-103.

[126] Miner M A. Cumulative fatigue damage[J]. Journal of applied mechanics, 1945, 12(3): A159-A164.

[127] Syed A. Accumulated creep strain and energy density based thermal fatigue life prediction models for SnAgCu solder joints[C]//2004 Proceedings. 54th electronic components and technology conference (IEEE Cat. No. 04CH37546). IEEE, 2004, 1: 737-746.

[128] Manson S S, Halford G R, Hirschbere M H. Creep-fatigue analysis by strainrange partitioning[J]. 1973.

[129] Kariya Y, Morihata T, Hazawa E, et al. Assessment of low-cycle fatigue life of Sn-3.5 mass% Ag-X (X= Bi or Cu) alloy by strain range partitioning approach[J]. Journal of Electronic Materials, 2001, 30(9): 1184-1189.

[130] Bevan M G, Wittig M. Complex fatigue of soldered joints-comparison of fatigue models[C]//1997 Proceedings 47th Electronic Components and Technology Conference. IEEE, 1997: 127-133.

[131] Stowell E Z. A study of the energy criterion for fatigue[J]. Nuclear Engineering and Design, 1966, 3(1): 32-40.

[132] Kujawski D. Fatigue failure criterion based on strain energy density[J]. Journal of Theoretical and Applied Mechanics, 1989, 27(1): 15-22.

[133] Oldham J, Abou-Hanna J. A numerical investigation of creep-fatigue life prediction utilizing hysteresis energy as a damage parameter[J]. International journal of pressure vessels and piping, 2011, 88(4): 149-157.

[134] Morrow J D. Cyclic plastic strain energy and fatigue of metals[M]//Internal friction, damping, and cyclic plasticity. ASTM International, 1965.

[135] Solomon H D, Tolksdorf E D. Energy approach to the fatigue of 60/40 solder: Part I—Influence of temperature and cycle frequency[J]. 1995.

[136] Shi X Q, Pang H L J, Zhou W, et al. A modified energy-based low cycle fatigue model for eutectic solder alloy[J]. Scripta Materialia, 1999, 41(3): 289-296.

[137] Shi, X. Q., Pang, H. L. J., Zhou, W., and Wang, Z. P., 2001, "Low Cycle Fatigue Analysis of Temperature and Frequency Effects in Eutectic Solder Alloy," Int. J. Fatigue, 22, pp. 217–228.

[138] Solomon, H. D., and Tolksdorf, E. D., 1995, "Energy Approach to the Fatigue of 60/40 Solder: Part I-Influence of Temperature and Cycle Frequency," ASME J. Electron. Packag., 118, pp. 130–135.

[139] Palmer, M. A., Redmond, P. E., and Messler Jr., R. W., 2000, "Thermomechanical Fatigue Testing and Analysis of Solder Alloys," ASME J. Electron. Packag., 122, pp. 48–54.

[140] Cortez, R., Cutiongco, E. C., Fine, M. E., and Jeannotte, D. A., 1992, "Correlation of Uniaxial Tensio-Tension, Torsion, and Multiaxial Tension-Torsion Fatigue Failure in a 63Sn-37Pb Solder Alloy," Proc 42nd Electronic Components and Technology Conf., pp. 354–359.